

NASA CR-

132897

Harvey Astron

Final Report

for

The Multispectral Point Scanner Study

(1 February 1969 to 1 December 1969)

Contract Number: NAS5-11653

Prepared By:

The Hycon Company
700 Royal Oaks Drive
Monrovia, California

for

Goddard Space Flight Center
Greenbelt, Maryland

(NASA-CR-132897) THE MULTISPECTRAL POINT
SCANNER STUDY Final Report, 1 Feb. - 1
Dec. 1969 (Hycon Mfg. Co.) 230 p

N74-71037

00/99 Unclass
27603

Final Report
for
The Multispectral Point Scanner Study
(1 February 1969 to 1 December 1969)

Contract Number: NAS5-11653

Goddard Space Flight Center

Contracting Officer: Joe Sperty

Prepared By:

The Hycon Company
700 Royal Oaks Drive
Monrovia, California

Project Manager: Warren Shaw

for

Goddard Space Flight Center
Greenbelt, Maryland

ABSTRACT

Hycon submitted its proposal, HPA 9803-39A, on 12 September 1968 to NASA-Goddard in response to Request for Proposal 733-98747/216 for a design feasibility for a Multispectral Point Scanner (MSPS). Volume I of this document proposed the development of an MSPS with an all-reflective (catoptric) optical system to cover electromagnetic radiation in the wavelength range from 0.5 to 15.0 microns. Volume II, submitted with Volume I, proposed an alternate technical approach which uses a reflective/refractive (catadioptric) optical system to cover four spectral bands between 0.5 and 1.1 microns.

In January 1969, Hycon received NASA/GSFC contract NAS5-11653 to perform a design study on a multispectral scanning system in accordance with Hycon's alternate proposal, Volume II. This system is to sample the radiation from a 100-nautical mile-wide swath of the earth's surface along the orbital path of a satellite at a nominal 500-nautical mile altitude. Solar radiation reflected from terrain will be collected simultaneously in four spectral channels (0.5 to 0.6, 0.6 to 0.7, 0.7 to 0.8, and 0.8 to 1.1 microns). Data from all channels (including housekeeping) are to be in a form suitable for recording and/or transmission to ground in real time.

In March 1969, Hycon was requested by NASA to redirect its effort towards a hardware program in accordance with a schedule that would enable it to meet the Earth Resources Technical Satellite (ERTS), a launch date requirement of the last quarter of 1971. In June 1969, modification of the subject contract, which documented the redirection of the program and provided funding to allow Hycon to continue with its redirected efforts through July 1969, was received by Hycon.

At the beginning of July 1969, Hycon notified NASA/GSFC that the total authorized funding would be expended on or about 20 July 1969, and Hycon requested additional funds. Hycon was notified that NASA did not currently have funds to carry on the program. Therefore, on 18 July 1969, Hycon notified GSFC that current authorized funding had been expended and that, effective 20 July 1969, Hycon would stop work in accordance with the Limitation of Funding clause of the contract.

At this point in time, the study phase was nearing completion, and a rough draft of the final study report was being prepared. In a review with NASA/GSFC and NASA headquarters following the stop work order, some additional funding was provided for Hycon to include in the study report the following two new concepts, both of which were outside of the original scope of work.

The tilted wheel concept was developed by Hycon engineers immediately after the stop work order. This concept was developed as a direct result of Hycon's efforts to decrease the size and weight of the scanner system.

A catoptric optical system became practical with the development of a new all-reflective scanning probe concept, and is discussed in the Probe Design paragraph. The study contract specified a catadioptric optical system which could not collect the thermal infrared radiation. The all-reflecting system allows wideband operation, i. e., from 0.5 to 15 microns.

System performance is predicted, scene characteristics defined, a system is recommended for fabrication, and items requiring additional study are discussed in this final report.

TABLE OF CONTENTS

	Page
ABSTRACT	ii
INTRODUCTION AND SUMMARY	1
Summary and Conclusions	1
Recommendations	5
Organization of the Report	7
OPERATIONAL AND ENVIRONMENTAL FACTORS	9
Scene Characteristics	9
Atmospheric Model and Radiant Energy	11
Spacecraft Motion Tolerances	20
Radiation Environment	21
OPTICAL DESIGN STUDY	25
Primary Collecting Optics	26
Probe Design	35
Spectrometer	40
Summary of Optical Design Studies	42
DATA CHANNEL STUDY	45
Data Channel Frequency Response	45
Data Channel Noise	54
Detector Evaluation and Selection	63
Gain, Offset, and Calibration	73
Multiplexing-Demultiplexing	77
MECHANICAL ANALYSIS	95
Preliminary Description of MSPS Mechanical System	95
Thermal Study	98
Materials Study	104
Structural Study and Dynamic Analysis	113
SYSTEM PERFORMANCE	147
Signal-to-Noise Ratio and Noise Equivalent Reflectance	147
System Performance with Parameter Variations	153
BIBLIOGRAPHY	161
GLOSSARY	163
APPENDIX I	I-1
APPENDIX II	II-1
Theory	II-1
Summary	II-10

TABLE OF CONTENTS (CONTINUED)

	Page
APPENDIX III	III-1
Thermal Study	III-1
APPENDIX IV	IV-1
Isotropic System Dimensional Scaling (24-Probe System)	IV-1
Isotropic System Dimensional Scaling (Tilted Wheel System)	IV-4
Isotropic System Response to Variable Solar Heating (24-Probe System)	IV-5
APPENDIX V	V-1
Scan Wheel Dynamics	V-1
24-Probe Tapered Aluminum Scan Wheel Design Outline	V-6
APPENDIX VI	VI-1
General Spherical Imaging	VI-1
Tilted Wheel Geometry	VI-2
Ground Scan Geometry	VI-6

LIST OF ILLUSTRATIONS

Number	Title	Page
Figure 1.	Average Spectral Reflectance of Various Crop Types and Soil	10
Figure 2.	Distribution of Spectral Reflectance Data for Vegetation	12
Figure 3.	Distribution of Spectral Reflectance Data for Soils	13
Figure 4.	Distribution of Spectral Reflectance Data for Snow	14
Figure 5.	Sea Level Extinction Coefficient for Rayleigh and Clear Standard Atmospheres	15
Figure 6.	Comparison of Tabulated Data and Least Mean Squares Fit for Solar Zenith Angle Dependence of Backscatter for Rayleigh Atmosphere at Wavelength of 0.5 Micron (with Previous Models 1 and 2)	17
Figure 7.	Total Radiant Power Imaged on Detector and Resolvable Levels (Band 1 is 0.5 to 0.6 Microns)	18
Figure 8.	Total Radiant Power Imaged on Detector and Resolvable Levels (Band 2 is 0.6 to 0.7 Microns)	19
Figure 9.	Total Radiant Power Imaged on Detector and Resolvable Levels (Band 3 is 0.7 to 0.8 Microns)	20
Figure 10.	Total Radiant Power Imaged on Detector and Resolvable Levels (Band 4 is 0.8 to 1.1 Microns)	21
Figure 11.	Geometrical Distortion Resulting from Spacecraft Roll and Pitch Errors	22
Figure 12.	Geometrical Distortion Resulting from Spacecraft Yaw and Orbit Height Errors	22
Figure 13.	Simple Bouwers Concentric System	27
Figure 14.	F/1.0 Bouwers System	28
Figure 15.	Eight-Inch, f/1.67 Bouwers with Achromatic Corrector	29
Figure 16.	Ray Intercept Curves for 8-Inch f/1.67 Bouwers (at Primary Image)	30

TABLE OF CONTENTS (CONTINUED)

LIST OF ILLUSTRATIONS

Number	Title	Page
Figure 95.	Tilted Wheel Scan Geometry	125
Figure 96.	Scan Wheel Tilt Angle	126
Figure 97.	Scan Wheel Diameter	127
Figure 98.	Scan Wheel Rotation Speed	128
Figure 99.	Scan Curvature	129
Figure 100.	Resolution Element Dwell Time	129
Figure 101.	Scan Efficiency	130
Figure 102.	Thermal Path Length	130
Figure 103.	Scan Wheel Centrifugal Acceleration	131
Figure 104.	Scan Wheel and Momentum Compensation Rotary Drive System . . .	132
Figure 105.	Fundamental Natural Frequency for Momentum Compensated Belt Coupled System Due to Magnetic Motor Compliance	134
Figure 106.	Ratio of Scan Wheel Angular Rotation Error to Bearing Generated Disturbing Torque	135
Figure 107.	Speed Ratio Change Due to a Variable Thickness Belt	136
Figure 108.	Momentum Compensation	139
Figure 109.	Oil Lubricated Bearing Power Loss	145
Figure 110.	Effect of S/N on Analog Signal (Left) and Reproduced Imagery (Right)	148
Figure 111.	Effect of S/N on Analog Signal (Left) and Reproduced Imagery (Right)	149
Figure 112.	Effect of S/N on Analog Signal (Left) and Reproduced Imagery (Right)	150
Figure 113.	Effect of Multiple Traces on Ability to Distinguish Signal in Presence of Noise	151
Figure 114.	NE Δ R for Band 1	153
Figure 115.	NE Δ R for Band 2	154
Figure 116.	NE Δ R for Band 3	155
Figure 117.	NE Δ R for Band 4	155
Figure 118.	Variation of Scanner Performance with Overall Length, f/Number, Field-of-View, (FOV) and Number of Detectors per Channel	156
Figure 119.	Variation of Parameters Relative to 200-Foot Field-of-View	157
Figure 120.	Variation of Parameters with Objective Diameter	157
Figure 121.	Variation of Parameters with Number of Detectors per Channel . .	158
Figure 122.	Variation of Parameters Quantum Efficiency Relative to 0.25 Percent (Band 4)	158
Figure 123.	Variation of Parameters Orbit Height Relative to 500 Nautical Miles	159
Figure 124.	Relative S/N vs. Field-of-View for Various Aperture Diameters . .	159
Figure 125.	Burch Microscope Objective	II-2
Figure 126.	Burch Microscope Objective (Reversed)	II-4
Figure 127.	Catoptric MSPS Configuration	II-5
Figure 128.	Spherical Aberration Cubic	II-8
Figure 129.	Two Acceptable Insulation Systems	III-2
Figure 130.	Exterior Surface Temperatures of HPI Surfaces 1, 2, and 3	III-5
Figure 131.	Exterior Surface Temperatures of HPI Surfaces 4, 5, 6, and 7 . . .	III-5
Figure 132.	Interior Surface Temperatures of HPI Surfaces 1, 2, and 3	III-6
Figure 133.	Interior Surface Temperatures of HPI Surfaces 4, 5, 6, and 7	III-6

TABLE OF CONTENTS (CONTINUED)

LIST OF ILLUSTRATIONS

Number	Title	Page
Figure 134.	Exterior HPI Surface Temperature Averaged	III-7
Figure 135.	Isotropic System Dimension Scanning	IV-2
Figure 136.	Shortened Thermal Path of Tilted Wheel System	IV-5
Figure 137.	Simplified Element of the Passive Thermal Control Circuit for One HPI Wall Zone Pair	IV-6
Figure 138.	Principal Thermal Path	IV-7
Figure 139.	Focal Shift Due to Axial Thermal Flux for an Isotropic Gradient Controlled System	IV-11
Figure 140.	Scan Wheel Precessional Deformation	V-2
Figure 141.	One Spoke Plus Hub Segment	V-7
Figure 142.	Stress and Deflection for Tapered Aluminum 24-Probe Scan Wheel, 1-Inch Wide	V-8
Figure 143.	Hub Forces	V-10
Figure 144.	Spherical Imaging	VI-3
Figure 145.	Scan Wheel Geometry	VI-4
Figure 146.	Scan Rotation Axis	VI-7
Figure 147.	Ground Scan Ellipse Geometry	VI-8
Figure 148.	Geometrical Constructions	VI-9

LIST OF TABLES

Number	Title	Page
Table 1.	Recommended MSPS Specifications	6
Table 2.	Estimated Characteristic Reflectance Difference of Seven Different Common Crop Types (Wheat, Oats, Corn, Barley, Alfalfa, and Sugar Beets)	11
Table 3.	Proton Flux	23
Table 4.	Electron Flux	23
Table 5.	Solar Cosmic Ray Protons	24
Table 6.	Catoptric Scanner Prescription	38
Table 7.	Visual Band Spectrometer Prescription	43
Table 8.	Opticle Design Trade Matrix	44
Table 9.	Noise and Resolvable Levels for Analog Devices Type 180 Amplifier, Band 4	67
Table 10.	Nominal PMT Gain for 1 Microamp Maximum Anode Current	73
Table 11.	PMT Supply Voltage	73
Table 12.	Bandwidth Required for Analog Multiplexing	83
Table 13.	Signal, Noise, Gain, and S/N Levels	84
Table 14.	Equal Quantizing Level	85
Table 15.	Unequal Quantizing Levels	85
Table 16.	Spectrum Occupancy Comparisons	86
Table 17.	Sinusoidal Vibration	96
Table 18.	Random Vibration	97
Table 19.	Material Properties	106
Table 20.	Preload vs. Torque (Single Bearing)	142
Table 21.	Preload vs. Torque (Duplex Pair)	142

TABLE OF CONTENTS (CONTINUED)

LIST OF TABLES

Number	Title	Page
Table 22.	Thrust Load vs. Axial Deflection (Single Bearing)	143
Table 23.	Thrust Load vs. Axial Deflection (Duplex Pair)	143
Table 24.	Radial Load vs. Radial Deflection (Single Bearing)	144
Table 25.	Radial Load vs. Radial Deflection (Duplex Pair)	144
Table 26.	Parameter Change vs. Weight Change	154
Table 27.	12-Inch, f/1.5 Primary Catoptric MSPS	II-9
Table 28.	Thermal Input to Spacecraft, Btu/hr-ft ²	III-3
Table 29.	Orbit Average Temperature Ranges vs. Surface Coating	III-4

INTRODUCTION AND SUMMARY

NASA/GSFC contract NAS5-11653 was issued to investigate the feasibility of a four-channel radiometric scanner for orbital use. The contract was later modified to initiate equipment design. At the time of contract termination, the study and much of the analysis for a preliminary design were nearly complete. The results of both the study and the design effort are recorded in this report.

Included in this report is additional coverage on a tilted wheel concept and an all-reflecting optical system that were outside the scope of the original study.

Summary and Conclusions

Requirements. -The purpose of the Multispectral Point Scanner (MSPS) Study was to investigate the feasibility of a four-channel point scanner for orbital use. The baseline approach, for study purposes, proposed a 12-inch, f/1.0 Bouwers concentric optical system with a multiprobe scanning wheel to scan the first image plane. Energy from the scanning probes is split into four discrete spectral channels by a prism spectrometer, and sensed by a single detector appropriate for each channel.

The design parameters of the system are:

Orbit	500 nautical miles, sun synchronous 8:30 to 9:20 a.m. descending node
Ground coverage	+50 nautical miles normal to the orbit path
Ground instantaneous field-of-view	0.067 milliradian (later changed to 0.076 milliradian)
Spectral bands	0.5 to 0.6 micron 0.6 to 0.7 micron 0.7 to 0.8 micron 0.8 to 1.2 microns (later changed to 0.8 to 1.1 microns)
Calibration	At least three levels on every scan line
Data rate	Within the real-time transmission capabilities of the telemetry system
Weight	Less than 65 pounds
Power	Less than 55 watts
Spacecraft constraints and environment	Nimbus D Handbook (as a guide only)

No specification of additional spectral bands was given when the analysis of all-reflective optics was authorized. An arbitrary selection of radiation bands between 0.5 and 15.0 microns is assumed.

Investigations and Conclusions. -During the study, several conclusions were formed concerning MSPS design factors that were beyond the scope of the contract but pertinent to future ERTS type missions. These conclusions concern:

- a. Image vs. object space scanning.
- b. Single detector per spectral channel vs. multiple detector arrays.
- c. Linear (great circle) vs. curvilinear (tilted wheel) image surface scanning.
- d. Catadioptric vs. catoptric optical systems.

The last two items became part of the study and are reported as such. Analysis related to the first two items are summarized as follows:

Image Plane Scanners. -The image plane scanner recommended in this report results in a smooth, low speed uniform rotary motion scan mechanism. Some of its advantages are:

Collecting Aperture. -The collecting aperture can be increased for narrow scan angles if size and weight limitations permit. This can be accomplished without introducing undue spacecraft reactions. This is a growth feature for future systems where better ground resolution and/or narrower spectral bands are desired, or where greater signal-to-noise ratio (S/N) is needed.

Scan Efficiency. -A scan efficiency of 90 percent can be achieved using slightly curved scans for an 11.4-degree scan angle. Calibration occupies about 8 percent of the scan, while the other 2 percent is the mechanically unusable portion due to optical switching from one probe to the next.

Instantaneous Field-of-View (Optical Resolution). -The optical system geometrical ray trace exceeds the diffracting limit. The system resolution is limited only by mechanical tolerances of the moving optical probes, and the ability to fabricate the optical parts.

Registration (Successive Scans). -Accuracy is limited only by clock frequency precision, accuracy of maintaining uniform motion, and platform stability.

Bandwidth. -A high efficiency scan results in the narrowest possible electrical noise bandwidth. This is reflected in improved S/N.

Multiple Detector Arrays. -Assuming equal scan efficiency for all scanners, the decision of whether to use a single detector per spectral channel or an array of detectors is independent of scanner type.

An array of detectors is justified under only two conditions: (1) when it is necessary to improve S/N, or (2) when the scanning technique is such that it is mechanically impossible to scan at the rate required for a single detector.

The S/N improvement obtainable by use of an array over that of a single detector is \sqrt{N} , where N is the number of detectors in the array. The number of parts required for an array increases directly as the number of detectors.

Optical problems increase with the number of detectors per spectral channel. The field-of-view must be larger (increasing design complexity) and the various spectrometer parts increased in size. Image rotation also may become a serious problem, depending on the scanning mechanism.

The most serious problem in using an array of detectors is in the characteristics of the detectors themselves. It is almost impossible to exactly match the electrical characteristics of two detectors, much less several. Even when they have been aligned as closely as possible they change with time. The drift is completely random and different for each detector. Precise radiometric measurements are extremely difficult to make because of this drift.

Finally, the problem of multiplexing and demultiplexing the data for transmission becomes more complex as the number of detectors per channel increase.

The scanning technique used in the Hycon approach is not only a high efficiency scan, its very design ensures that the required scan rate for a single detector (or even a much higher

scan rate for overlap) can be achieved without mechanical limitations. Thus, the decision to go to multiple detector arrays must be based on a careful weighing of the advantages against the problems that such use creates.

Operational and Environmental Factors. -The analyses of scene and atmosphere characteristics, and solar radiation models have been completed for the needs of the MSPS design. This investigation showed that usable reflectance measurements can be made from space by the MSPS conceived by Hycon. The effects of sun angle and atmosphere conditions were included.

The basic design was developed to maintain geometric image distortion below 1 percent of a measured distance, or 230 feet on the ground (whichever is larger). The resulting tolerances imposed on orbital platform pointing accuracy were tight, but were considered feasible for some existing spacecraft (e.g., some of the Nimbus series).

The effect of the radiation environment on possible refractive elements for the MSPS primary optics (catadioptric system) was determined. The elements considered will not brown or fluoresce excessively during the anticipated mission. An all-reflective optical system will not appreciably degrade due to radiation.

This investigation provided data for system design. However, the tradeoff between spatial resolution and radiometric accuracy is sufficiently sensitive that the selection of an arbitrary set of specifications must remain an option for a data user.

Optical Design. -Several optical systems for forming spherical scannable images were designed. The original concept (12-inch, f/1.0 Bouwers) was not satisfactory. Variations on this approach were then considered. To minimize spherical aberration and thus to relieve the optical correction burden of the scanning probe optics, large refractive correctors could not correct zonal (0.7 semiaperture) spherical aberration unless thick, heavy elements were used. These thick elements produced chromatic aberrations.

The large refractive corrector in the primary optics (e.g., Bouwers element) was eliminated by a new probe optics design by Paul Sugino of the Te Company. Refractive probe elements in the convergent beam preceding the primary image surface helped to create a higher quality first image. Another design approach was then followed leading to an all-reflective MSPS optical system (for collecting 0.5 to 15 micron radiation). Reflective probe optics (of the Burch microscope type) provide optical performance comparable to that of a dioptric system with some increased light blockage.

A folded system was conceived to reduce the lens occlusion problem. Further investigation of the folded system suggested a tilted optical probe wheel (one that does not scan a great circle of the spherical image surface). The tilted probe wheel reduced the number of probes required (from 24 to 8), improved scan efficiency, and substantially simplified fabrication and operation of the scanning mechanism.

A prism has been tentatively selected for spectral separation in the visible and near infrared bands. A dichroic filter would be used to separate the infrared bands from the visual bands when a broader band MSPS is required. The prism provides efficient, selective separation of the spectra. The spectrometer entrance slit determines both the spectral and spatial resolution.

Other approaches for spectral band separation, not investigated as part of this study, include the use of dichroic filters or diffraction grating. These approaches should be considered in any future MSPS design.

Signal Detection and Data Transmission. -Photomultiplier tubes (PMT's) were selected for radiation detection in bands 1, 2, and 3. This decision was based on an analysis of noise and responsivity of existing detectors in the three spectral regions.

The analysis of a detector for band 4 (0.8 to 1.1 microns) is not complete due to lack of data on new detectors. An S-1 photocathode PMT has tentatively been selected for this band. Avalanche diodes are available and have interesting characteristics. Those tested were found to be inferior to the S-1 photocathode PMT. At the conclusion of the study, information was received that advanced avalanche diodes are available. Further analysis should be made of these advanced avalanche diodes before a final choice is made.

Data transmission analysis showed that MSPS signals can be contained within a 20 MHz transmission bandwidth using quadrature phase pulse code modulation/phase shift keying (PCM/PSK) multiplexing. This assumes a single detector for each of four channels. If a fifth (thermal) channel is to be included, a new analysis must be made.

Mechanical and Thermal Analyses. -The most difficult design problems inherent in the MSPS requirements are mechanical tolerances that must be maintained with a limited weight system. These tolerances must be maintained through the launch environment and through the rather wide thermal excursion encountered in space. The thermal environment proved to be the most troublesome source of mechanical misalignment.

Analysis indicated that a thermally isotropic system solution would theoretically maintain focus for all mean temperatures provided there were no thermal gradients. The existence of thermal gradients led to a modified isotropic solution unique to an image surface scanner. Since the image is always on axis, there exists a material distribution solution that allows an optical system to stay in focus for both thermal gradient and nongradient conditions.

A thermally isotropic solution can be achieved with either an all-metal or a hybrid invar-fused silica system. Each system has certain design advantages. The latter system has the advantage of having been proven in space for the gradient solution.

Two basic design approaches were investigated: (1) a great circle scanner, and (2) a tilted wheel scan. The tilted wheel scan has the advantage of using fewer probes and has shorter thermal paths. Folded alternatives for both approaches were investigated and found feasible. Folding does not necessarily reduce the maximum dimensions. It changes the direction of this dimension. The main advantage in folding is to reduce blockage caused by the scanning wheel.

The scan drive system, with momentum compensation, was analyzed and modeled to establish the magnitude of scan velocity shifts, residual scan nonlinearity, and bearing friction and tolerances. In all cases, the mechanical requirements are within the current state-of-the-art.

System Performance Study. -The primary system performance factor, S/N was studied to show the effect of system noise on spatial resolution and radiation measurements. It was shown that usable imagery can be obtained even at low S/N's at the expense of spatial resolution. Such conditions can exist at low sun angles or in the presence of a hazy atmosphere.

A sensitivity analysis of system performance was made. It shows the effects of varying some of the parameters and indicates the direction of possible future modifications of the specifications.

Recommendations

Hycon Company recommends to NASA the development of image-surface scanning MSPS equipment. This approach has growth potential and offers a unique capability for radiometric measurement from space that will be needed in the immediate future. The need for this form of MSPS is expected to become critical when more precise measurements, hence larger apertures, are demanded for the ERTS program.

This MSPS development program should be continued in two major successive phases. The first will produce a MSPS to satisfy the needs of ERTS A and B. The second phase will produce a large aperture system to satisfy future requirements for high spatial and spectral resolution radiometry from space.

The first phase will include completion of the additional analyses recommended in this report, the preliminary design and fabrication of a prototype MSPS, and the construction of a working model. The model should be built to demonstrate feasibility, proven theoretically in this study, of the optical, electronic, and mechanical systems.

Recommended System. -Based on this study, the recommended MSPS design would meet the specifications in table 1.

The recommended structure at the conclusion of this study was a hybrid of fused silica and invar. This is based on theoretical analyses and prior space performance of such an approach. A most intriguing approach from the mechanical design view is an all-metal system. An all-metal system will satisfy all of the thermal requirements and will allow the designer more freedom on the manner of mounting, joining, etc. The main drawback to an all-metal system is whether the metallic substrate will be sufficiently stable for the optical elements. If the optical substrate problem can be successfully handled, an all-metal system would result in a lighter system for the same aperture.

The spectrometer section should be analyzed for optimum operation over the suggested wide spectral range. It may prove that diffraction gratings and/or dichroic filters may prove more efficient than the method tentatively selected.

Further analysis of the exact positioning of spectral band 7 (thermal band) is needed. The parameter that best describes performance is the S/N as related to noise equivalent performance. Positioning this band in a wider, narrower, or different center pass could well improve performance.

All detectors should be further investigated. The detector for band 4 is in an area of rapidly developing technology (avalanche diodes in this case) that should be exploited. The detector for band 7 is in the same category.

Since the detectors for four of the bands require some form of cooling, and this cooling must interface with the total thermal control problem, the entire thermal control should be investigated further. The analysis to date is sufficient for preliminary design purposes, but a detail design is necessary before an iterative computer thermal analysis design can be made.

The present study developed a method of digitizing the data and transmitting it to the ground within a 20 MHz bandwidth. The inclusion of three additional bands requires reexamination of the bandwidth requirements.

Table 1. Recommended MSPS Specifications.

Folded Optical System

Collecting Lens Construction	8 inches diameter, f/1.67 mirror Fused silica with invar structure *
Second surface image quality	20×10^{-6} radians
Scan efficiency	greater than 90 percent
Type of scanning probe optics	Reflective - Burch microscope objectives
Number of probes (tilted scan wheel)	8
Magnification of probe	(Afocal)
First surface depth of focus	± 0.00075 inch
Blocking	37 percent
Overall optical efficiency	54 percent
Spectrometer (bands 1, 2, 3, 4)	BK-7 glass prism (dichroic * filters and diffraction gratings will be evaluated)

Spectrometer (bands 5, 6, 7)

<u>Spectral bands</u>	<u>Wavelength (Microns)</u>	<u>Detector</u>
1	0.5 to 0.6	S-20 or S-25 PMT
2	0.6 to 0.7	S-20 or S-25 PMT
3	0.7 to 0.8	S-25 PMT
4	0.8 to 1.1	S-1 PMT (cooled) or silicon avalanche diode (cooled)
5	1.55 to 1.75	Germanium diode *
6	2.2 to 2.4	InSb (passive cooling) *
7	10.4 to 12.6	HgCdTe (passive cooling) *

Signal Processing

Bandwidth	0.5 cycles/resolution element, 187.5 KHz/ channel at 3 db corner frequency
Filter type	Bessel, 30 db/octave
Multiplexing:	
Type	Quadrature PCM/PSK, 7 bits per word plus word and line signal
Bandwidth	20 MHz (for Bands 1, 2, 3, and 4 only) *

Mechanical System

Construction	Fused silica - invar *
Thermal control	Passive *
Momentum compensation	Counter rotating mass, belt coupled
Size:	
Length	25 inches
Width	20 inches
Depth (less folding sunshade)	20 inches
Weight	less than 65 pounds (for four-channel MSPS)

System

Spatial Resolution	0.076 milliradian
NE Δ R	1 percent
NE Δ T	0.5° K

*Areas where further study and analysis is recommended. These areas were incomplete due to lack of time, or are areas of rapidly developing technology.

As part of this examination of bandwidth, the ground resolution, atmospheric transmission, and S/N of the three additional bands must be investigated in a manner similar to the analysis of the original four bands. This would include the gain and offset settings required and the number of digits required to adequately perform the tasks.

Hardware. -The success of the ERTS program depends on the successful performance of all experiments. The following is recommended to ensure the performance of a 7-channel point scanner:

A full scale operating model of the MSPS system, described in this report, should be fabricated. This would be identical to a space version, as far as form, fit, and function are concerned, but would not necessarily carry the same level of components as for space.

This unit, although designed for space, would be suitably configured for use in a high flying (above 50,000 feet) aircraft. This change in configuration would be to facilitate use in an aircraft and would in no way compromise the space version.

A set of necessary equipment for supporting an aircraft test program should also be fabricated.

Finally, a comprehensive series of high flying aircraft tests should be made with this unit.

This approach will supply NASA the following:

- a. Proof that a high efficiency image surface scanner can be built and operated.
- b. Proof of the validity of the assumptions made as to atmospheric transmission and S/N.
- c. Proof that the data obtained are useful to prospective users. This also will give data reduction stations opportunity to develop software and techniques for handling this data when it ultimately comes from space.
- d. Proof that the various detectors will operate in the manner predicted.

If design changes are found necessary as a result of this flying model, they can be made prior to an orbital mission rather than to have the user withstand the disappointment of marginal or faulty operation. The cost effectiveness of this approach should be large.

Organization of the Report

This report covers all work done on the MSPS project as a design study. To achieve greater ease in relating study results, project redirection (e.g., elimination of the need for proposed feasibility breadboard and initiation of an early design stage) has not been detailed in the report of technical results. Discussion of the two additional study areas, the tilted wheel concept and the all-reflective optical system, are included in the introductory and summary material, and in individual sections of this report.

The analysis of scene radiation and space operational environment, discussed in section on Operational and Environmental Factors determines the basis for analysis and design tradeoffs discussed in succeeding sections. Optical design, signal detection and transmission, and mechanical system analyses are reported in detail in section titled Optical Design Study, Data Channel Study, and Mechanical Analysis. Summary of expected system performance and the overall effect of parametric changes are reported in section titled System Performance.

OPERATIONAL AND ENVIRONMENTAL FACTORS

This section presents the results of the analysis of those parameters which establish the conditions under which a multispectral point scanner must operate and which ultimately determine sensor performance. The most important parameters are terrain reflectance distributions, and atmospheric transmittance and backscatter.

Terrain reflectance distributions define the spectral characteristics of the scene while atmospheric transmittance and backscatter spectrally attenuate the radiant energy incident on and reflected from the scene. Both of these subjects received considerable attention early in the study. Tables and graphs of the spectral reflectance of a wide range of surface features were compiled from existing sources. Several atmospheric models were investigated and combined and a computer program was written to allow rapid evaluation of signal and background energy collected for the complete range of mission parameters. For purposes of feasibility and design evaluation, this portion of the study is complete.

The geometrical accuracy of images reconstructed from scanner data will mostly depend on the motion stability of the orbiting platform carrying the scanner. For this reason, a brief analysis was conducted to define the spacecraft motion tolerances required to maintain geometrical accuracy within limits set by the system requirements.

The results of this analysis indicate maximum permissible rates within the capabilities of advanced Tiros-Nimbus type spacecraft. This portion of the study is complete.

The effect of prolonged exposure to the radiation environment of a 500-nautical mile polar orbit must be considered in the design of the proposed scanner system. Estimated flux levels for such an orbit have been compiled and some conclusions drawn regarding effects on components. Additional effort is required to more fully define the possible degrading effects on electrical components and optical surfaces of the radiation, particularly the lower Van Allen belt levels and recommend appropriate shielding.

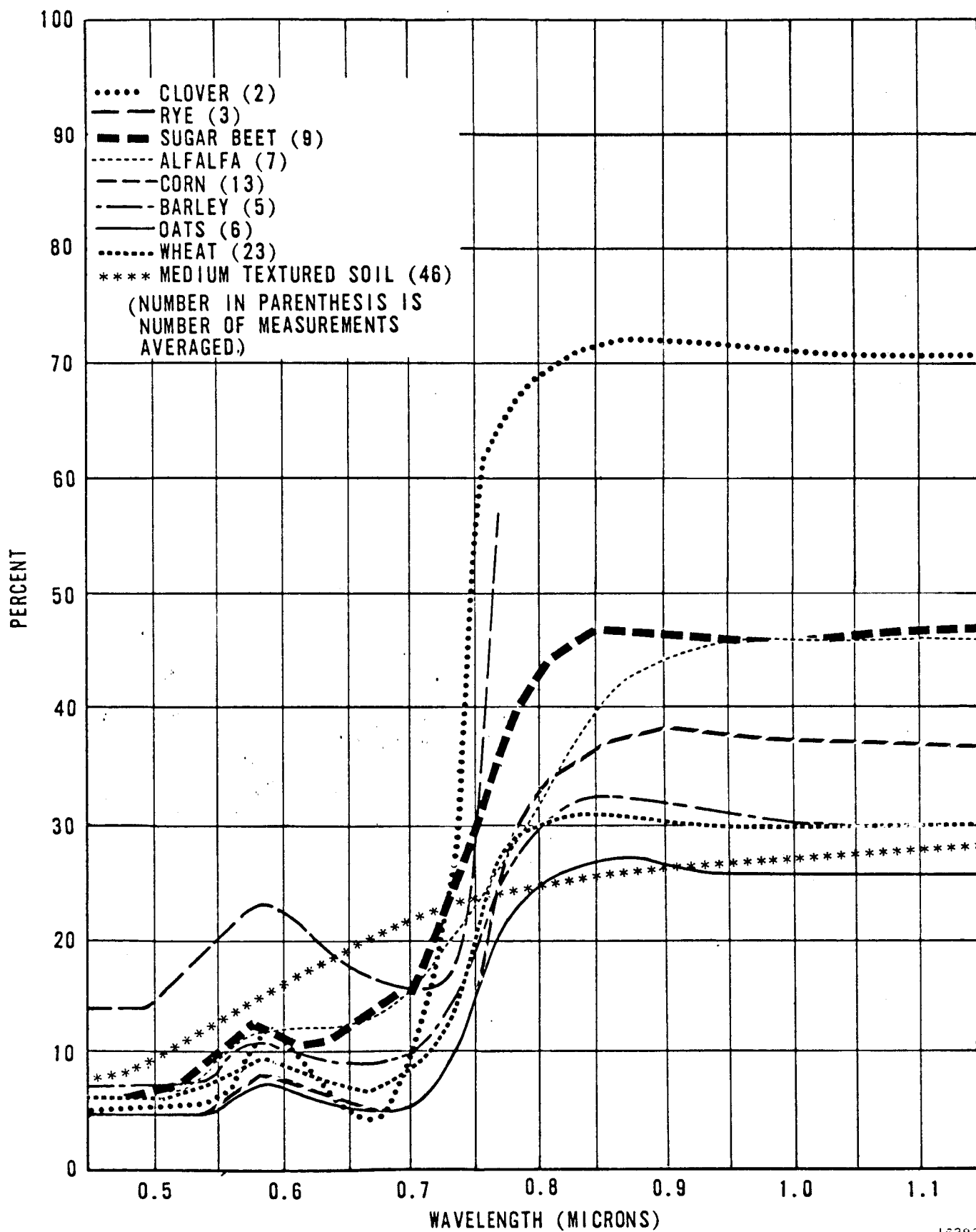
Scene Characteristics

Terrain spectral reflectance distribution and reflectance differences are the parameters that must be reduced from the data collected by a multispectral scanner operating in the visible and near infrared spectral regions. It is these parameters which ultimately set the operating levels and sensitivity requirements for the sensor.

A compilation of available⁽¹⁾ spectral reflectance data was made to determine probable reflectance values for targets of interest in each of the four specified spectral bands. Over 270 different vegetation targets and 100 different soil targets were included in the analysis. Reflectance measurements for each type of target were tabulated and the maximum, minimum, and median values of reflectance calculated at each wavelength used. In addition, the reflectances below which 5 and 95 percent of the measurements fell were computed, since these two limits encompass 90 percent of all the reflectance measurements for that specific target at that wavelength.

Figure 1 shows the resulting average spectral reflectances for a few selected crop and soil types. This figure shows that different crop types are characterized by differences in reflectance which increase as the wavelength increases.

Estimates of the characteristic reflectance differences between seven different common crop types are shown in table 2. This table gives an indication of the general range of



16383

Figure 1. Average Spectral Reflectance of Various Crop Types and Soil.

Table 2. Estimated Characteristic Reflectance Differences of Seven Different Common Crop Types (Wheat, Oats, Corn, Barley, Alfalfa, and Sugar Beets).

Spectral Band (Microns)	Estimated Characteristic Reflectance Differences (Percent)
0.5 to 0.6	0.7
0.6 to 0.7	1.0
0.7 to 0.8	2.0
0.8 to 1.1	3.0

reflectance difference resolution required of a multispectral scanner. These numbers should not be taken to represent rigorous requirements since several other factors, such as reflectance distributions, overlap, and sophistication of data reduction techniques, influence the ability to distinguish between various target types.

In addition to data for specific crop types, reflectance distribution information is required for agricultural targets as a group in order to estimate the range of expected signal

levels. For this purpose, terrain features were divided into three major categories; vegetation, soil, and snow. The resulting spectral distribution curves for these three categories are shown in figures 2, 3, and 4.

These distributions of reflectance data, and especially the range encompassing 90 percent of all measurements, will be used throughout this report to estimate signal levels.

Atmospheric Model and Radiant Energy

To determine required scanner parameters, such as collecting aperture, overall efficiency, and to estimate performance of various candidate designs, the radiant energy input to the collecting optics must be determined.

For the reflected energy spectral bands, the radiant signal at the collecting optics is composed of two components; solar energy, which has traversed the atmosphere and been reflected by the terrain, and solar energy backscattered by the earth's atmosphere. These two components are assumed to be independent. No significant error is expected from this assumption. Since the solar radiant flux outside the atmosphere is relatively well known and values of terrain reflectance have been compiled in the previous section, the primary task in calculating expected energy levels is to quantify the effects of the atmosphere. To this end, an atmospheric model is required.

The primary reference for the model atmosphere is the Air Force "Handbook of Geophysics and Space Environments" published in 1965. This reference contains an optical model clear standard atmosphere. The model is in the form of a tabulation of optical extinction coefficients versus altitude and wavelength for the conditions of Rayleigh scattering, aerosol scattering, and ozone absorption respectively.

The extinction coefficient, τ , is a convenient parameter to describe atmospheric transmission, which is defined by:

$$T = e^{-\tau M}$$

where,

- T = transmission of a thickness of atmosphere characterized by air mass M
- τ = extinction coefficient for air mass 1.
- e = natural log base (2.718)

The convenience of the parameter τ is that extinction coefficients for different attenuation phenomena can be added to find a composite transmission.

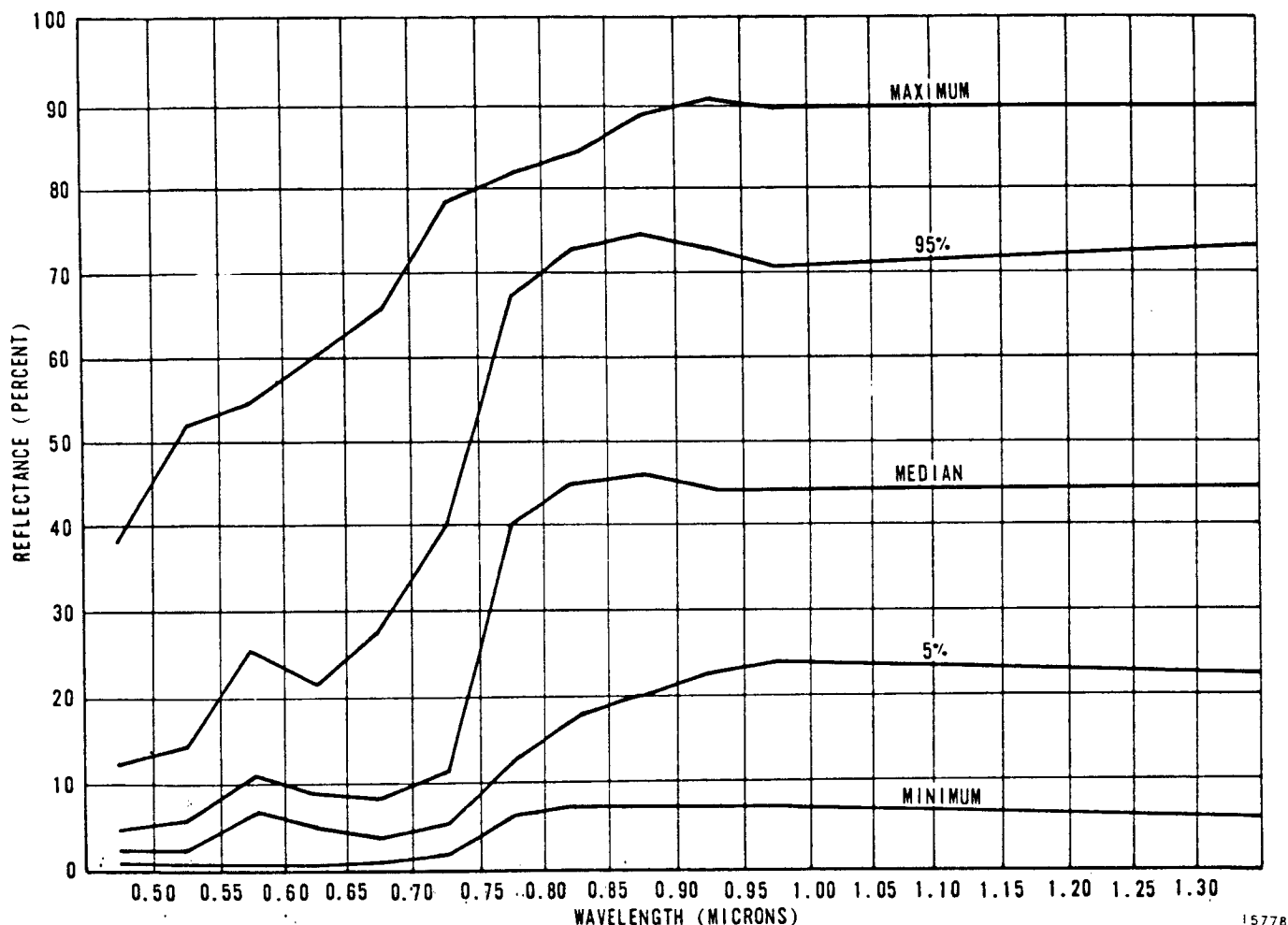


Figure 2. Distribution of Spectral Reflectance Data for Vegetation.

Experimental measurements of extinction coefficients for real atmospheres at three sites around the world⁽²⁾ indicate values lying between those for Rayleigh and for Rayleigh plus Aerosol plus Ozone (composite) atmospheres. For this reason, the extinction coefficients for a Rayleigh and for a composite atmosphere are thought to bracket a realistic estimate of atmospheric parameters. Figure 5 is a plot of extinction coefficient versus wavelength for the two types of atmosphere, for a vertical path from sea level to infinite height. Since these coefficients are tabulated for various altitudes and wavelengths, inclusion of the effects of changes in terrain altitude is possible.

Based on the extinction coefficient shown in figure 5, the radiant energy due to backscatter and terrain reflectance can now be calculated. Let $W_s(\lambda, \theta)$ represent the radiant power at the collecting aperture due to 100 percent terrain reflectance, but excluding backscatter.

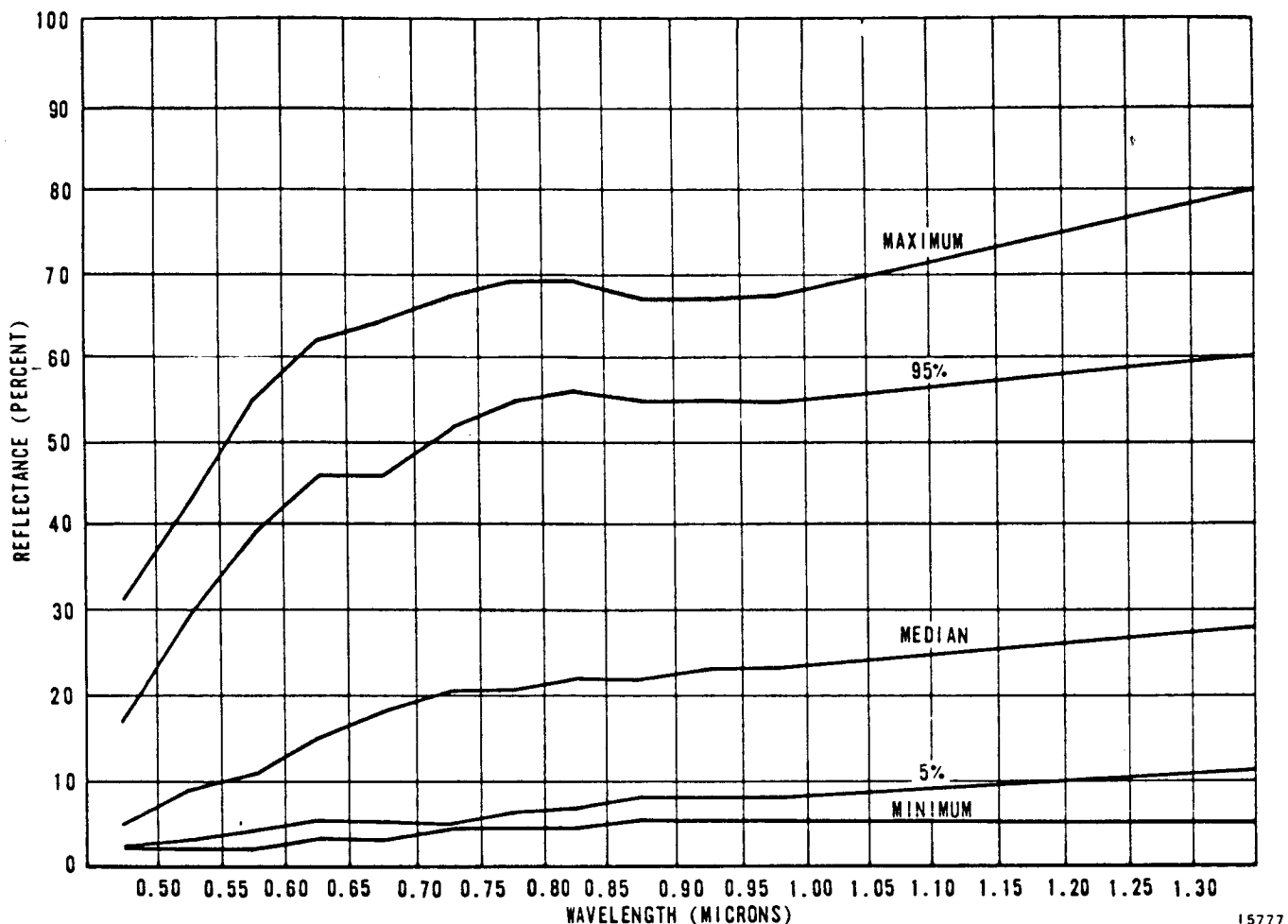


Figure 3. Distribution of Spectral Reflectance Data for Soils.

Then,

$$W_s(\lambda, \theta) = \frac{H_\lambda T_o T_\theta \cos \theta}{\pi} \text{ (watt/m}^2\text{-micron-steradian)}$$

where a Lambertian reflection at the surface has been assumed, and

H_λ = solar spectral irradiance outside the atmosphere (watt/m²-micron)

θ = solar zenith angle

T_o = transmission of the atmosphere for air mass 1 = $e^{-\tau_t(\lambda)}$

T_θ = transmission of the atmosphere for a path at

angle $\theta = e^{-\tau_t(\lambda) \sec \theta}$ (air mass = $\sec \theta$)

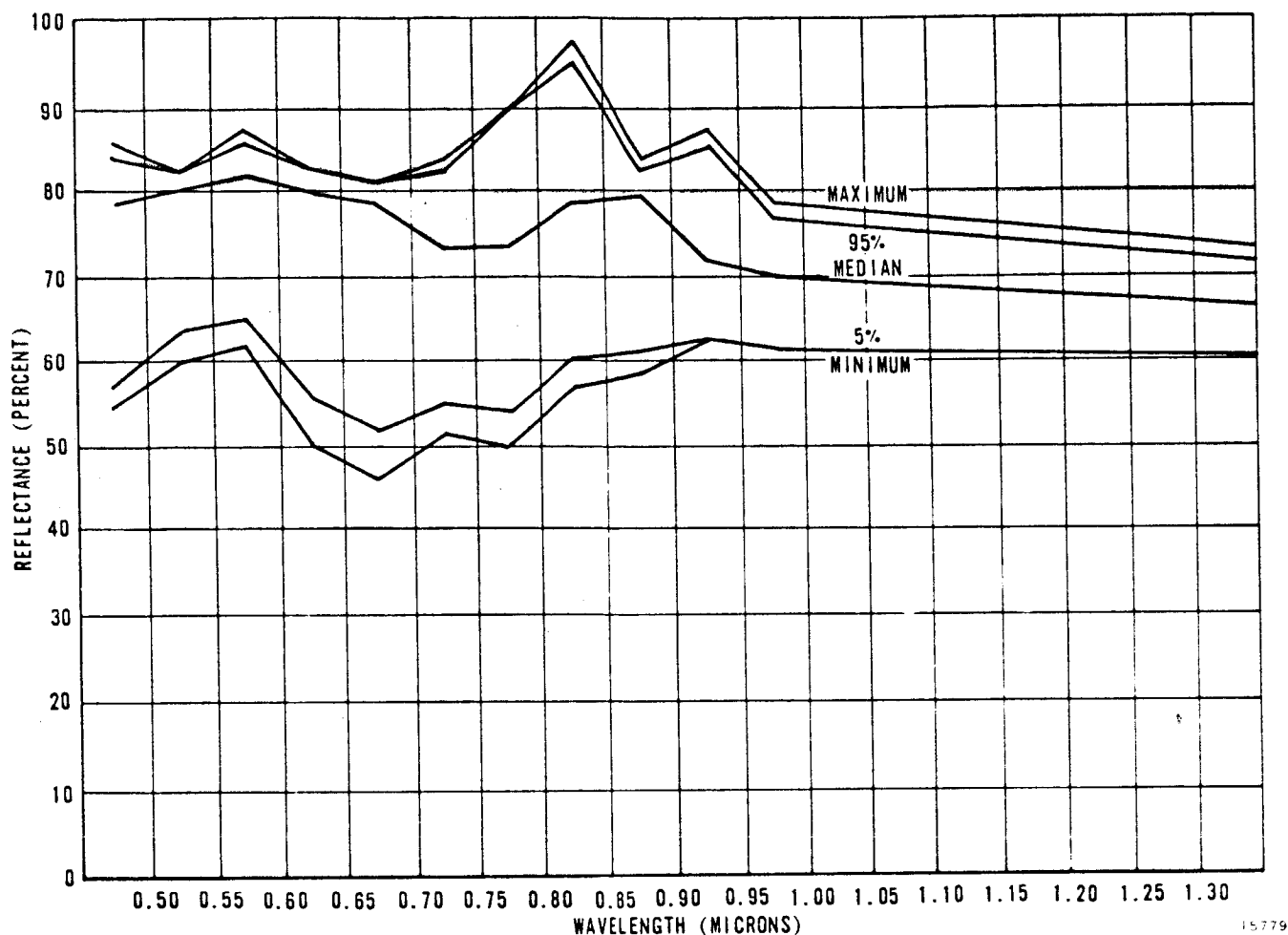


Figure 4. Distribution of Spectral Reflectance Data for Snow.

τ_t = total atmospheric extinction coefficient for air mass 1

so that,

$$W_s(\lambda, \theta) = \frac{H_\lambda \cos \theta e^{-\tau_t(\lambda)(1 + \sec \theta)}}{\pi}$$

To calculate backscatter, it is assumed that all the energy which is not absorbed and which does not reach the ground is scattered in Lambertian fashion into both hemispheres, i.e., into 2π steradians. Although probably not correct, this assumption leads to results very close to those based on estimates of total atmospheric albedo quoted by Robinson⁽³⁾

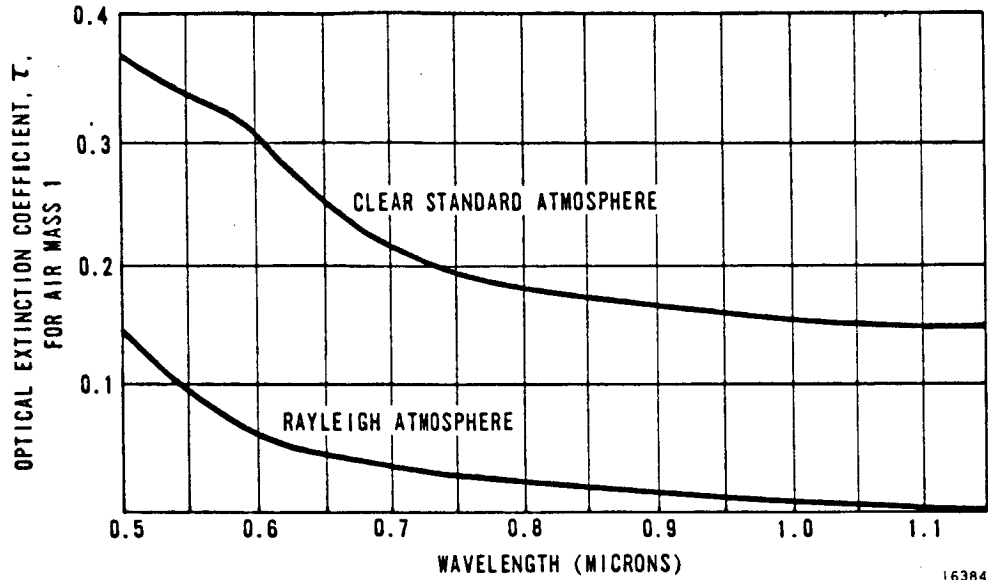


Figure 5. Sea Level Extinction Coefficient for Rayleigh and Clear Standard Atmospheres.

and used in previous calculations. Thus, if $W_B(\lambda, \theta)$ represents the radiant power at the collecting aperture due to backscatter only,

$$W_b(\lambda, \theta) = [W_b(\lambda, 0^\circ)] [R(\lambda, \theta)]$$

where $W_b(\lambda, 0^\circ)$ represents an expression for the magnitude of backscatter at 0° solar zenith angle and $R(\lambda, \theta)$ represents a function of wavelength expressing the rate at which backscatter falls off with solar zenith angle. From the assumption above,

$$W_b(\lambda, 0^\circ) = \frac{H_\lambda (1 - e^{-\tau_t(\lambda)})}{2\pi}$$

An expression for $R(\lambda, \theta)$ must now be found. Data is available on the variation of backscatter with solar zenith angle based on calculations assuming a plane parallel Rayleigh atmosphere⁽⁴⁾ for selected wavelengths and solar zenith angles. Rather than trying to reproduce these complex calculations, it is sufficient for present purposes to simply fit the data available with a smooth polynomical curve. That curve is then used to extrapolate to needed points not included in the tables.

The procedure used was to list the magnitudes of backscatter from the tables for each of the four wavelengths and seven solar zenith angles contained in them. Each value was normalized to unity at $\theta = 0^\circ$. The four sets of seven data points each were fitted by a least

mean squares second-order fit resulting in four sets of coefficients for those curves, each for a different wavelength. The set of coefficients was then fitted by a second curve expressing the wavelength dependence of the coefficients. The following equation resulted:

$$R(\lambda, \theta) = (C_1) 10^{-4} \theta^2 + (C_2) 10^{-2} \theta + 1$$

where,

$$C_1 = -2.11\lambda^2 + 4.05\lambda - 2.12$$

$$C_2 = 1.02\lambda^2 - 1.91\lambda + 0.415$$

λ = wavelength in microns

θ = solar zenith angle in degrees.

Figure 6 shows these results graphically for wavelength of micron, 0.5 where the solid line represents the exact tabulated values and the dashed line represents the values derived from the above equation. Also shown for reference are the results which would have been obtained assuming a $\cos \theta$ falloff. Similar results were obtained for other wavelengths.

Given $W_S(\lambda)$ and $W_B(\lambda)$, the power imaged on the detector for each spectral band is found by multiplying by the collecting area, field-of-view (steradians), and optical efficiency, and integrating over the wavelength band of interest:

$P_S(1)$ = signal power imaged on detector for spectral band 1

$$= \frac{\pi D^2 E F^2 R}{4} \int_{\lambda_1}^{\lambda_2} W_S(\lambda) d\lambda$$

$P_B(1)$ = backscatter power imaged on detector spectral band 1

$$= \frac{\pi D^2 E F^2}{4} \int_{\lambda_1}^{\lambda_2} W_B(\lambda) d\lambda$$

where,

D = aperture diameter

E = optical efficiency including blockage

F = field-of-view (radians)

R = terrain reflectance

$\lambda_2 - \lambda_1$ = wavelength range for band 1.

Using the equations above for backscattered power and terrain reflected power, the amount of radiant power imaged on the detectors for each of the four spectral bands was

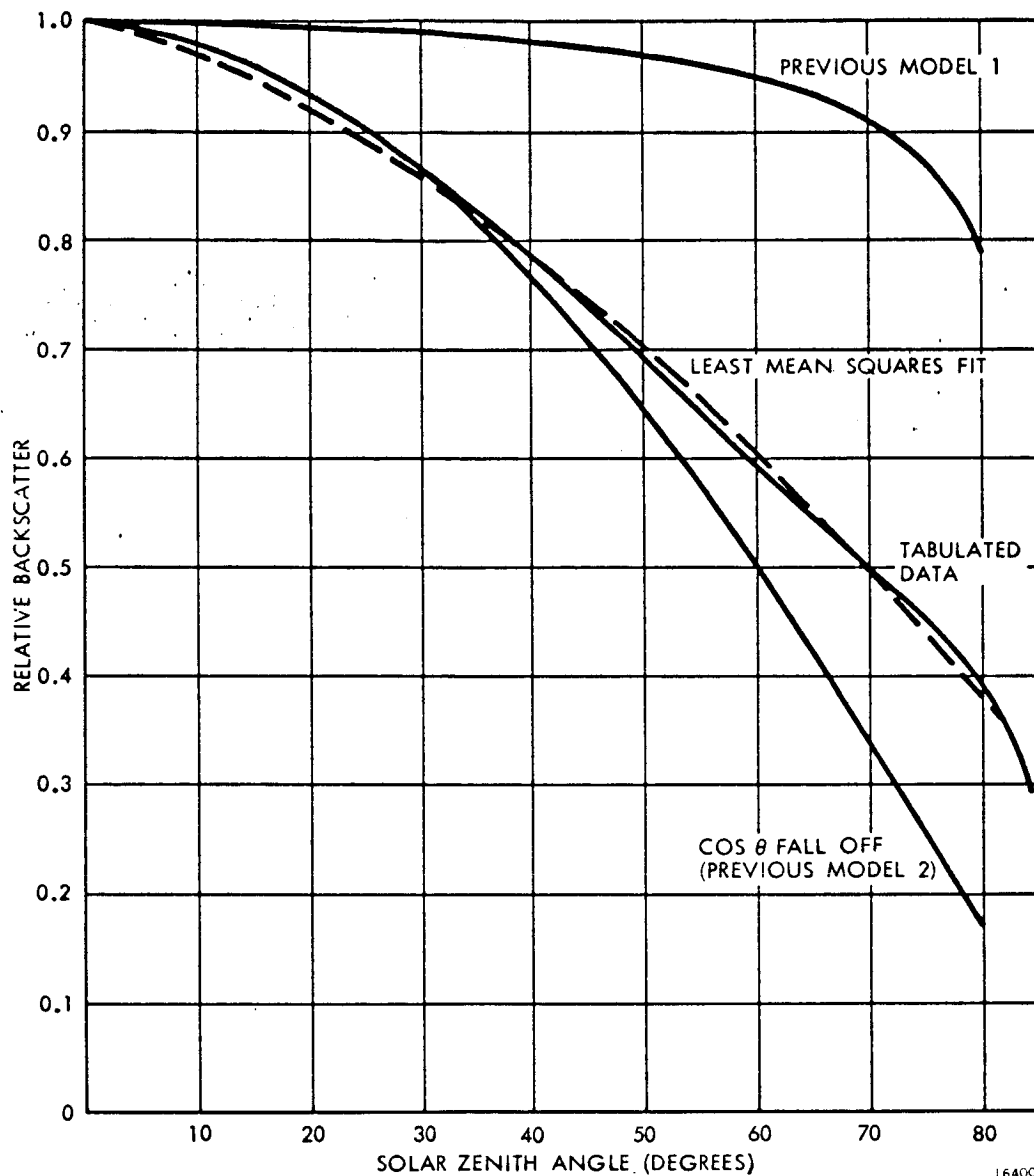


Figure 6. Comparison of Tabulated Data and Least Mean Squares Fit for Solar Zenith Angle Dependence of Backscatter for Rayleigh Atmosphere at Wavelength of 0.5 Micron (with Previous Models 1 and 2).

calculated assuming a Rayleigh atmosphere. An 8-inch collecting aperture, 60 percent optical efficiency, and 66-microradian field-of-view were used as representing best estimates of system parameters at that time. Figures 7 through 10 are plots of the total radiant power (terrain plus backscatter) as a function of solar zenith angle for various terrain reflectances. Linear scales are used so the plots visually indicate the conditions a linear detector and amplifier would experience. The top curve in each case is the peak signal expected from bright, high altitude cloud tops (100 percent reflecting, no atmospheric attenuation). The broad line below that represents the range of powers for 100 percent terrain reflectance, plus backscatter for a Rayleigh atmosphere and terrain altitudes between sea level and 2 kilometers. The broad line at the bottom of each figure represents backscatter power for the same range of altitudes.

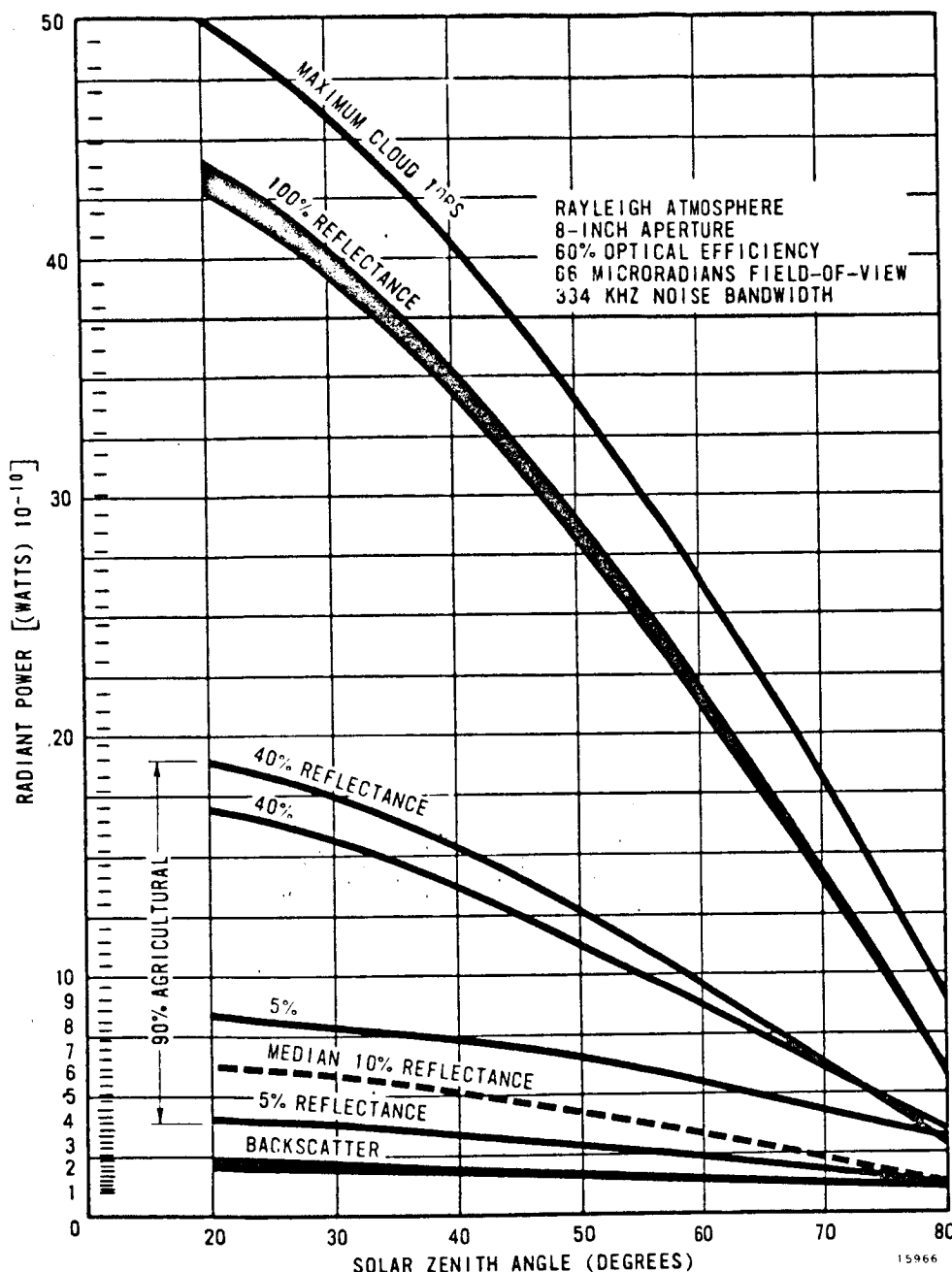


Figure 7. Total Radiant Power Imaged on Detector and Resolvable Levels (Band 1 is 0.5 to 0.6 Microns).

The curves described set the limits to expected signal amplitude under extreme conditions. Primary interest, is not on extreme conditions, but on those typical of agricultural and geological targets. As reported in the previous section of this report, an analysis of available spectral reflectance data has been made to determine probable reflectance values for targets of interest in each of the spectral bands. The curves in figures 7 through 10 identified as 90 percent soils and vegetation, were drawn using these reflectance data distributions. These curves show the radiant power levels which 90 percent of all vegetation and soil targets are expected to fall. As atmospheric haze increases, the dynamic range of these powers will decrease but will always lie within the limits shown. This is the range of power levels of primary concern to the present feasibility study. Also shown in the figures is a dashed line indicating the expected median power level for agricultural targets.

As will be pointed out in the section of this report on System Performance for a given set of scanner parameters, the

rms output noise level is fixed for a fixed radiant power level regardless of how that power level was generated, i.e., the scanner cannot distinguish between backscatter and signal, or between low terrain reflectances and high solar zenith angles so long as the total radiant power imaged on the detector is the same. Using the technique described in the section on System Performance, the rms equivalent noise input can be computed as a function of radiant power level. Assuming that at a given power level the next resolvable power level is at a distance equal to the rms noise amplitude, it is possible to calculate a series of steps each

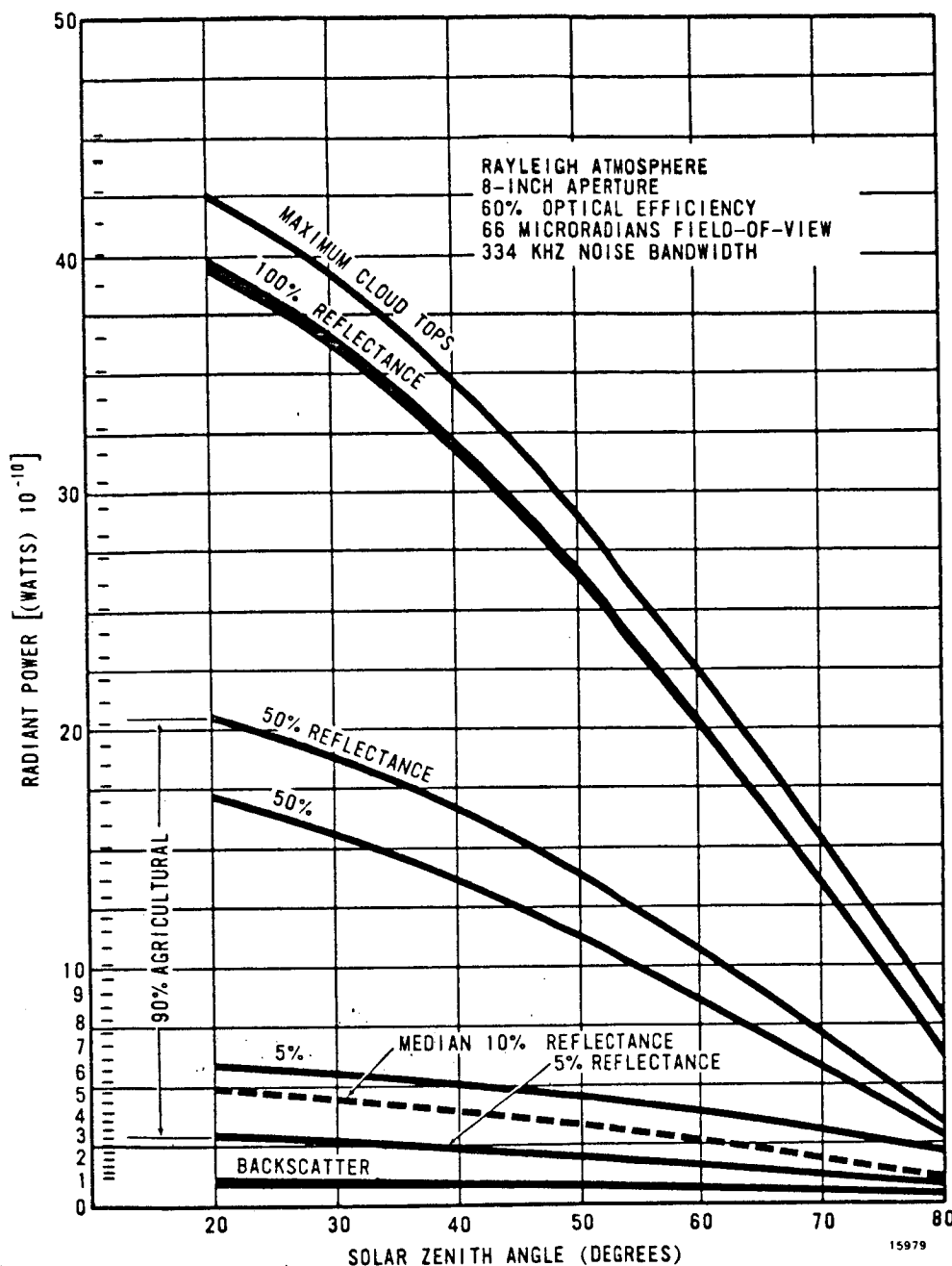


Figure 8. Total Radiant Power Imaged on Detector and Resolvable Levels (Band 2 is 0.6 to 0.7 Microns).

agricultural targets will, without changes of gain or offset, be capable of retaining all the resolvable information available for all atmospheric conditions and all solar zenith angles greater than 20 degrees. Conversely, a system designed for the requirements of some typical atmospheric conditions would be found lacking in quality under good seeing conditions. This is the reason for concentrating on Rayleigh atmospheres in the course of this study. Gain and offset controls will still be required to cover those signal levels outside the range of agricultural targets, e. g., snow or clouds.

separated from its neighbor by the rms noise level, and representing just resolvable increments of power. This was done for each spectral band assuming a 335 KHz noise bandwidth and PMT detectors.

The series of just resolvable levels is indicated by the tick marks up the left edge of figures 7 through 10. Although these resolvable levels are fixed (they extend horizontally across the page), their meaning, in terms of NE Δ R, depends on solar Zenith angle, atmospheric conditions, and other parameters. For example, as solar zenith angle increases, the range of radiant power associated with a given change of terrain reflectance decreases. But the resolvable levels remain fixed so that equivalent NE Δ R increases with solar zenith angle. It is the range of signals which is changing and not the resolvable power levels. A system design of sufficient quality to retain all the resolvable information available for a Rayleigh atmosphere at 20 degrees solar zenith angle and over a range of powers equivalent to 90 percent at expected

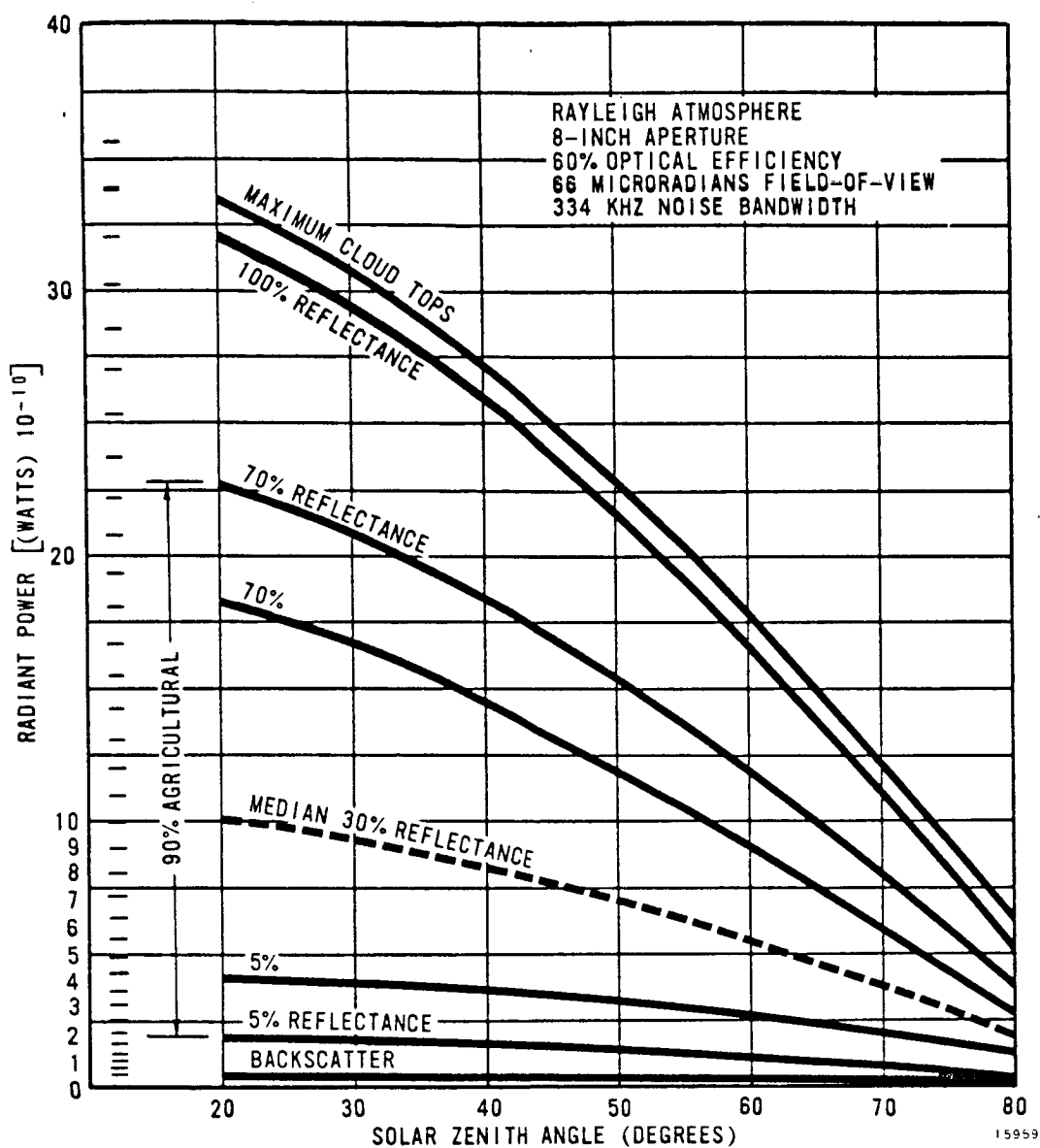


Figure 9. Total Radiant Power Imaged on Detector and Resolvable Levels (Band 3 is 0.7 to 0.8 Microns).

Spacecraft Motion Tolerances

An ideal orbiting platform for a point scanning sensor would have a fixed roll and yaw attitude, and have a pitch rate just sufficient to maintain a nadir pointing sensor. Unfortunately, existing spacecraft are not ideal. A brief first order analysis of maximum permissible spacecraft attitude and attitude rate errors was conducted to prove the feasibility of maintaining geometrical distortion in the image reconstructed from point scanner data to less than 1 percent. The results of this study indicated that most of these limits were within current practical limits for attitude stabilization and all were within the capabilities of advanced Tiros-Nimbus type spacecraft.

Figures 11 and 12 demonstrate the types of distortion resulting from spacecraft attitude errors and list the maximum permissible, uncorrectable attitude and attitude rate errors

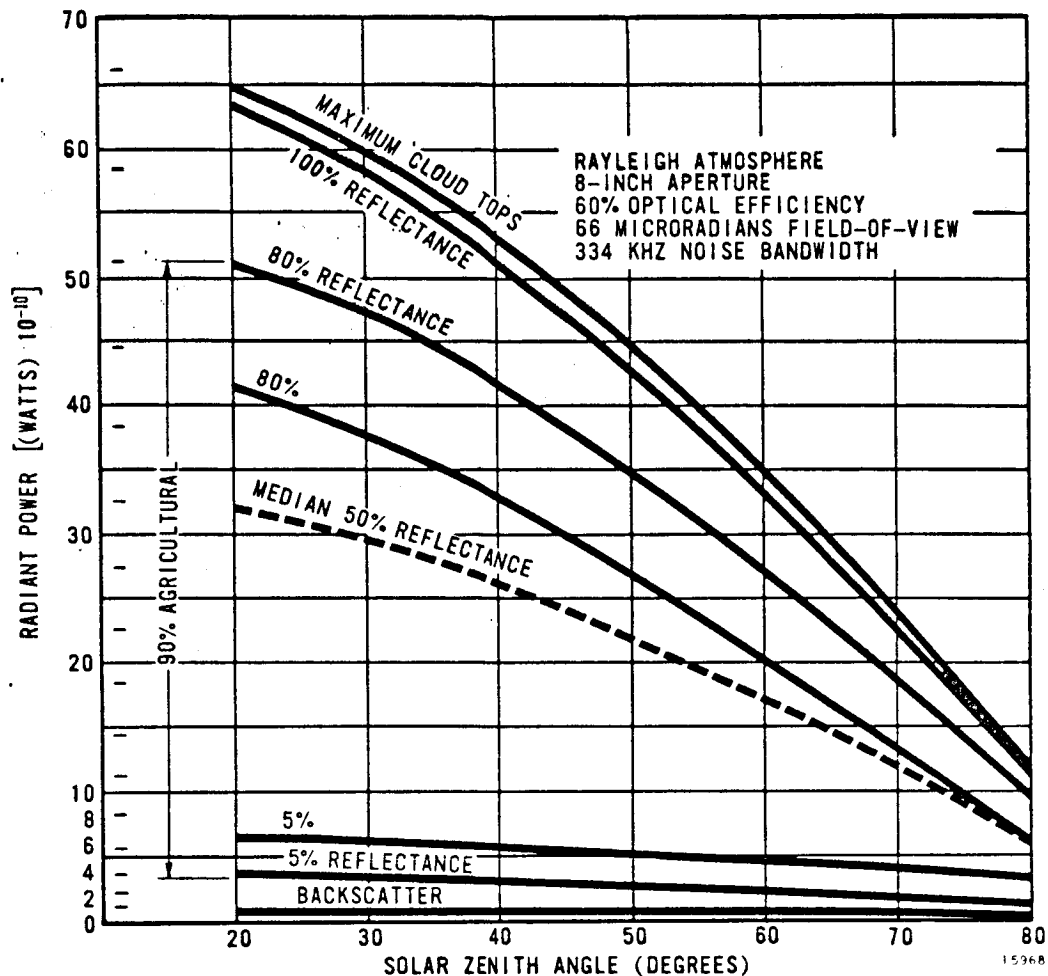


Figure 10. Total Radiant Power Imaged on Detector and Resolvable Levels (Band 4 is 0.8 to 1.1 Microns).

that can be allowed and still prevent mapping errors due to each individual source from exceeding $\pm 1/2$ percent, or $\pm 1/10$ resolution element, whichever is greater. The combined rms error, when all sources are operating simultaneously, is expected to be less than ± 1 percent, or ± 0.03 resolution element. Assuming some method of correcting the printout could be devised, errors exceeding those listed would be permissible, providing the uncertainty in applied correction did not exceed the limits shown. In each case, the most critical dimension, i. e., the one causing the most stringent limitation, is shown. The largest format considered is a square 100 nautical miles on a side which requires 30 seconds to scan.

Radiation Environment

The charged particle radiation environment to which a satellite in a 494-nautical mile altitude circular polar orbit would be exposed is described in this section. The specified altitude for scanner operation is 914 kilometers. Rather than make a new orbit trace computer run, a previous run for a 1000-kilometer altitude was used. Since this will be given integrated particle intensities similar to, but slightly larger than those in the specified orbit,

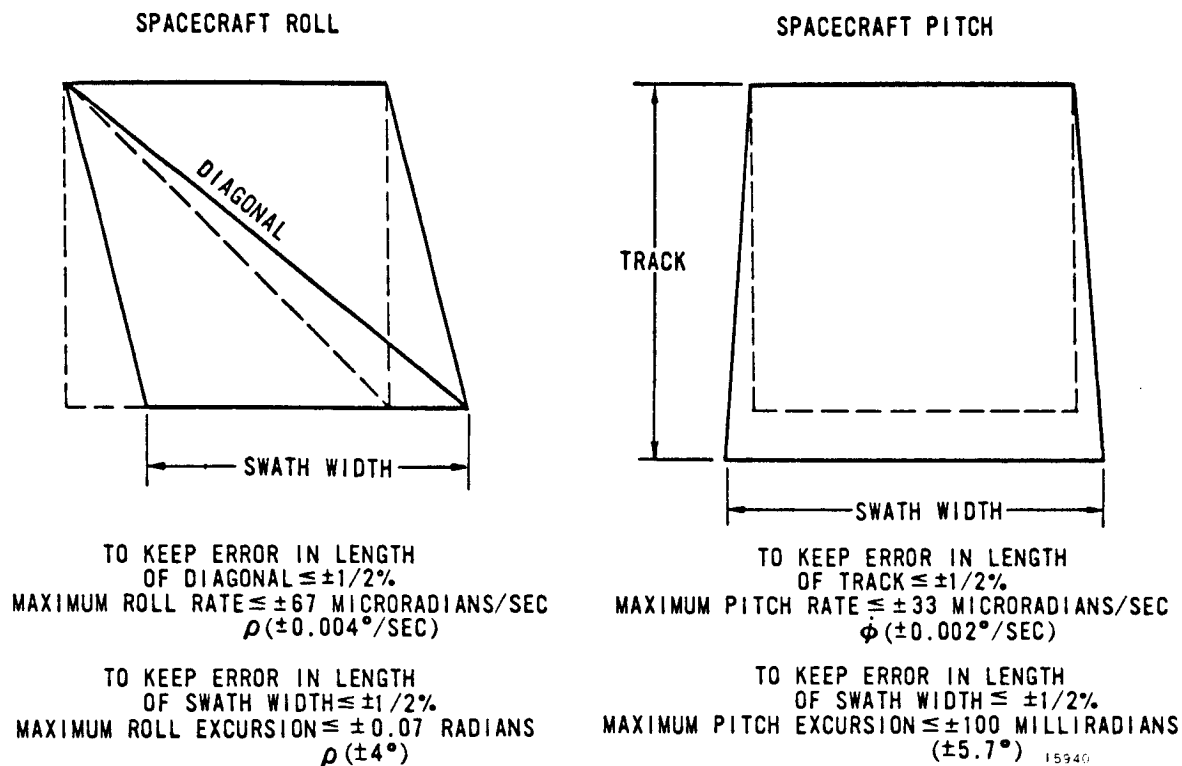


Figure 11. Geometrical Distortion Resulting from Spacecraft Roll and Pitch Errors.

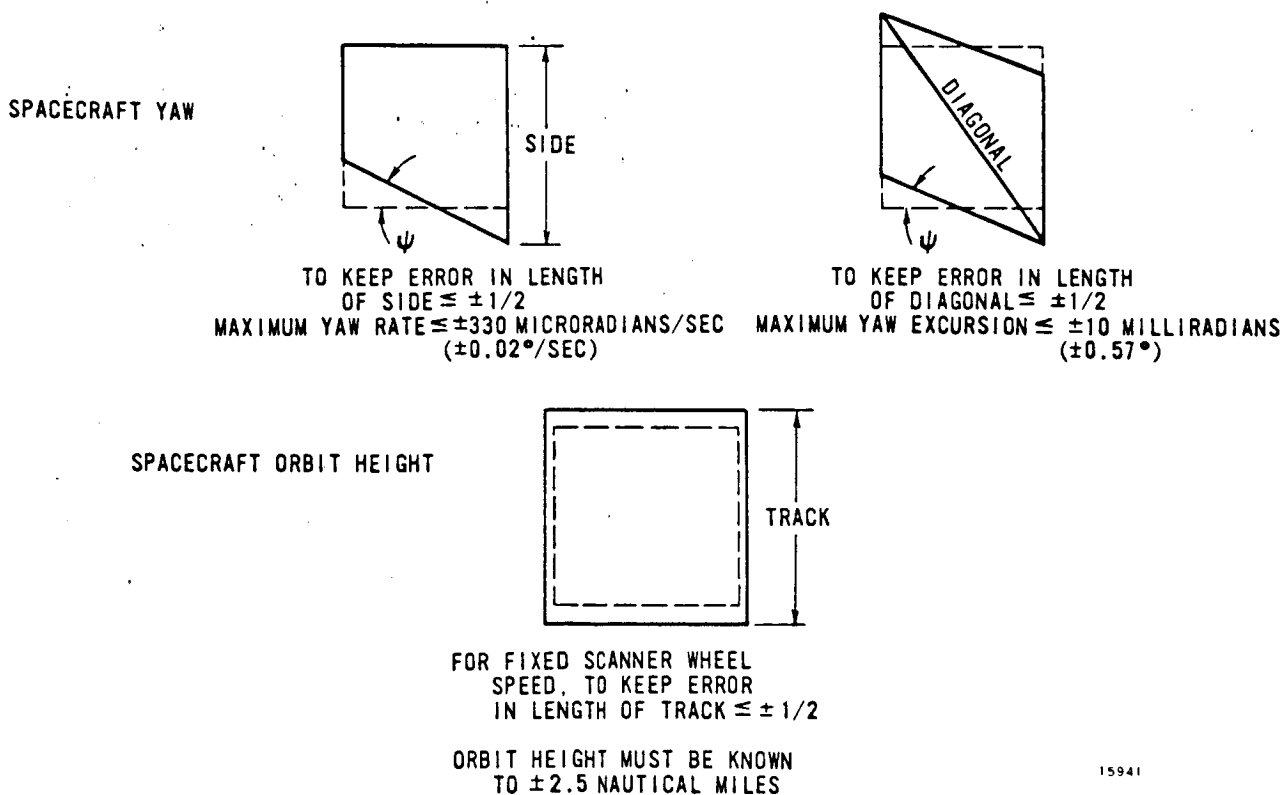


Figure 12. Geometrical Distortion Resulting from Spacecraft Yaw and Orbit Height Errors.

Table 3. Proton Flux.

Total proton flux ($40 < E < 700$ MEV) = (6.9) 10^9 per year	
E (MEV)	Protons/cm ² -year-MEV
45	(9.5) 10^7
55	(7.7) 10^7
65	(6.4) 10^7
75	(5.5) 10^7
85	(4.7) 10^7
95	(4.0) 10^7
125	(2.7) 10^7
175	(1.4) 10^7
225	(8.1) 10^6
275	(4.8) 10^6
325	(2.8) 10^6
375	(1.7) 10^6
425	(1.05) 10^6
475	(6.5) 10^5
525	(4.1) 10^5
575	(2.6) 10^5
625	(1.6) 10^5
675	(1.0) 10^5

MEV = million electron volts

appeared by 1972. Thus, the intensities listed should be considered to be upper limits. The differential energy spectrum again is shown.

Table 4. Electron Flux.

Total electron flux greater than 0.5 MEV = (2.5) 10^{14} per year Total electron flux greater than 5.0 MEV = (7.0) 10^{12} per year	
E (MEV)	Electron/cm ² -year-MEV
0.75	(1.7) 10^{14}
1.25	(1.1) 10^{14}
1.75	(7.3) 10^{13}
2.25	(4.8) 10^{13}
2.75	(3.2) 10^{13}
3.25	(2.2) 10^{13}
4.25	(9.8) 10^{12}
4.75	(6.6) 10^{12}
5.25	(6.3) 10^{12}
5.75	(3.7) 10^{12}
6.25	(2.0) 10^{12}
6.75	(1.0) 10^{12}
7.25	(5.1) 10^{11}
7.75	(2.4) 10^{11}

the results will be adequate to determine if there will be a problem due to the charge particles. A more thorough analysis can be made if these results indicate a possible hazard.

The tables give the integrated particle intensities and energy spectra expected. The year for which these calculations were made, 1963, was near solar minimum. The trapped proton results will be similar in 1972, again approaching solar minimum. The first column of table 3 for trapped protons is particle energy, and the last column is differential proton omnidirectional intensity. These two columns define the proton differential energy spectrum.

The trapped electron data in table 4 includes an appreciable contribution from the electrons produced by the Starfish high altitude nuclear test in 1962; this component will have essentially disappeared by 1972. Thus, the intensities listed should be considered to be upper limits. The differential energy spectrum again is shown.

Table 5 is for solar cosmic ray protons. This is the integrated intensity and differential energy spectrum for the large single event of November 12, 1960. These intensities would be appropriate if one event, similar to the November event, occurred during satellite lifetime. This is a fairly pessimistic assumption, so the omnidirectional intensities given should be considered upper limits. The duration of a typical solar cosmic ray event would be a few days.

A search of the literature of potential effects of this environment on the refractive optics was made through the facilities of Battelle Memorial Institute.

Table 5. Solar Cosmic Ray Protons.

Total solar cosmic ray flux > 0.2 MEV = $(7.0) 10^{10}$ Total solar cosmic ray flux > 3.0 MEV = $(3.8) 10^9$	
E (MEV)	Particles/cm ² -MEV
0.1	$(2.9) 10^{12}$
0.2	$(3.8) 10^{11}$
0.3	$(1.1) 10^{11}$
0.5	$(2.5) 10^{10}$
0.7	$(9.3) 10^9$
1.0	$(3.2) 10^9$
2.0	$(4.3) 10^8$
3.0	$(1.3) 10^8$
5.0	$(1.5) 10^9$
7.0	$(1.0) 10^9$
10.0	$(6.8) 10^8$
20.0	$(3.0) 10^8$
30.0	$(2.0) 10^8$
50.0	$(4.5) 10^7$
70.0	$(1.7) 10^7$
100.0	$(3.2) 10^6$
200.0	$(1.1) 10^5$
300.0	$(1.5) 10^4$
500.0	$(6.9) 10^3$
700.0	$(1.1) 10^3$
1000.0	$(1.8) 10^2$
2000.0	(4.6)
3000.0	$(5.5) 10^{-1}$
5000.0	$(3.9) 10^{-2}$

Although no information was available on the specific glasses selected, the following conclusions can be made:

a. Since all refractive elements on the proposed system are protected from direct radiation, the effect of browning will be minimal for the radiation levels encountered.

b. Lens cements are more sensitive than glass to browning, but there are no cemented elements.

c. A more serious problem, change in index of refraction could occur.

d. Because all elements cannot be shielded, the effect of change in index can be minimized. Further investigation of the magnitude of the effect, and the effect of shielding, is indicated.

OPTICAL DESIGN STUDY

The Hycon multispectral scanner utilizes the image-surface scanning technique. Since scanning is more easily accomplished by a free-running rotation than a translational or oscillatory motion, the primary collecting optics must provide a spherical (or cylindrical) image surface. Further, image quality along this surface must be uniform over the full 15° (11.4° active) cross-track scan so that the optical system generates no scan-angle-dependent signal modulation. All optical systems considered in this study meet these requirements by using, as the primary collector, a spherical mirror which produces a spherical image surface.

Signal invariance with scan is assured by forcing the entrance pupil, which is the image of the aperture stop as imaged by the front of the optical system, to lie at the center of curvature of the primary mirror. The position of the aperture stop depends on the particular probe design. When the aperture stop is fixed, i.e., does not rotate, then there is a slight modulation due to the change in area with scan. Since the area of the stop is proportional to the cosine of the scan angle, the error is a maximum of only 0.5 percent at 5.7° .

The spherical image surface is scanned by a rotating wheel with optical probes as spokes. The probes are essentially microscope objectives which relay the primary image to the secondary image at the entrance pupil of the spectrometer. In addition, the probe optics are designed to correct, as much as possible, the aberrations of the primary optical system. Probes operating at 10:1 and 20:1 magnifications were considered.

Spectral range determines many of the optical design features and parameters. One requirement, strictly adhered to during this study, is that energy in all spectral bands from a resolution element or calibration source be presented to the photodetectors (or the entrance pupil of the spectrometer) simultaneously. If both the thermal infrared and visible spectral bands are to be used, then the collecting optics, including the probes, must be catoptric, i.e., all-reflective.

Several catadioptric primary systems, especially the Bouwers concentric system and its derivatives, were designed to furnish good primary image quality. Also, a new probe configuration (called the "Sugino"), which uses zero-power refractive corrector elements in the converging beam in front of the primary image surface, was designed for this purpose.

None of the catoptric systems considered produces good primary image quality, as all of the reflective probe elements are placed downstream from the primary image. For these systems, synchronization can be provided by a shaft encoder on the axle of the probe wheel or, perhaps, by using suitable pulse-shaping electronics on the video signal from a blurred image of a point source. Calibration sources placed at the primary image do not present as much a problem. They can be made sufficiently large so that calibration will be unaffected by aberrated edge effects. Alternatively, it might be possible to inject the timing and calibration light signals through an optical system which has the same aberrations as the primary collecting optics.

Two visual-band catadioptric systems and one wide band catoptric system were investigated in detail. Due to the way the study program developed, the visual systems were great-circle scanners with 24 probes, while the catoptric system was a tilted plane scanner with 8 probes. Actually the design concepts for both types of scanners can be extended to encompass either catadioptric or catoptric optics. This section also includes discussion of the spectrometers for each of the two systems.

Designs were aided by the automatic design programs POSD for the IBM 1130 and System/360 Model 30, the Optical Research Associates (ORA) program CODE IV for the IBM System/360 Model 44, and by a number of Hycon programs. The design process was simplified

because the system is essentially a point imager even when multiple detectors are used. Only third and higher order spherical aberrations are important and need to be corrected. The primary design considerations for the optical system include size, weight, aperture, and spatial and spectral resolution. As is the usual case, the main emphasis in the initial stages of design was placed on spatial resolution. Once adequate resolution was obtained, then the other factors could be examined more closely and compromises made.

Initially, all designs were evaluated on the basis of the ray intercept data and geometric spot size. An initial design goal was that 90 percent of the geometric rays should be contained in an angular blur circle 25 microradians in diameter.

The image quality was investigated for two different conditions; first, or primary, surface and second surface. First surface image is that image formed by the primary collecting optics. The second surface image is that formed by the entire optical train of the scanner and is the image at the entrance pupil of the spectrometer.

The independent optimization of these two images was motivated by mechanical considerations. If an adequate first surface image could be obtained, the instantaneous field-of-view could be mechanically defined at this point by a field stop. This approach had certain advantages in apportioning the mechanical tolerances for maintaining geometric fidelity. As the study progressed, various problems developed in obtaining good first surface image quality while the mechanical advantages were not as real as they first appeared.

Primary Collecting Optics

The simplest form of collector is a spherical mirror. When the aperture stop is at the center of curvature of a spherical reflector, the image is free from coma and astigmatism of all orders. For distant objects, the spherical mirror does have undercorrected spherical aberration. Even though it has only one-eighth that of an equivalent glass lens (at "minimum bending"), the spherical aberration would be intolerable in those systems requiring good first surface image quality.

The angular blur diameter, B, produced by a spherical mirror can be approximated by:

$$B = \frac{7.81}{F^{\#3}} \text{ milliradians}$$

where $F^{\#}$ is the relative aperture of f/number given by:

$$F^{\#} = \frac{r}{2d}$$

with the radius of curvature, r, and aperture diameter, d. The expression is accurate for third-order spherical aberrations at slow speeds but is not so reliable for speeds faster than f/2.0. For instance, at f/1.0, B is actually 9.1 milliradians instead of the predicted 7.8 milliradians.

Another f/number dependent quantity is the depth of focus, which is proportional to the square. For fast systems, the small depth of focus is reflected in tight mechanical tolerances

on the axial position of a stop at the primary image, and of the first element in the probes. Fast systems are characterized by large spherical aberrations, which have to be corrected, and by tight mechanical tolerances. Slow systems are ungainly; they do not fit into small packages. Hence, some compromise must be made.

The specification for spatial resolution was initially given as 67 microradians and later relaxed to 76 microradians. To have primary image quality of comparable value, using only a spherical reflector would require an f/number slower than $f/4.68$. An 8-inch mirror of this f/number has a radius of curvature of 76 inches. This leads to a great-circle scanner wheel 76 inches in diameter, which is too large.

Systems with refractive correctors for the spherical mirror were investigated. In these systems, the major tradeoff concerned the relative amount of correction to be afforded by the probe and the correcting element(s) placed before the mirror. The best of these systems seemed to be the system using the Sugino probe. Here three refractive elements in the converging beam correct the primary image quality to about 40 microradians. Correction to 25 microradians is accomplished by six refractive elements aft of the primary image. No correctors in front of the primary mirror are needed with the Sugino probe system.

Bouwers Concentric System.—The Bouwers concentric system (figure 13), consisting of a thick miniscus refractive corrector and spherical mirror appears to be an ideal choice for an image-plane scanner, since it is not subject to off-axis aberrations. All objects at infinity are viewed on-axis. This is achieved by requiring that the spherical surfaces of the corrector and the mirror be concentric to the aperture stop. Under this condition, the focal surface is also a sphere, centered at the stop, with radius equal to the focal length of the system.

The corrector, which has low negative power, produces over-correct spherical aberration which compensates for the under-correct spherical aberration of the concave spherical mirror. Coma and astigmatism are identically zero because of the concentricity. The only remaining aberrations of the Bouwers concentric system are residual zonal spherical aberration and longitudinal chromatic aberration. The latter is an unfortunate consequence of the refractive corrector, since the front surface mirror has no chromatic problems.

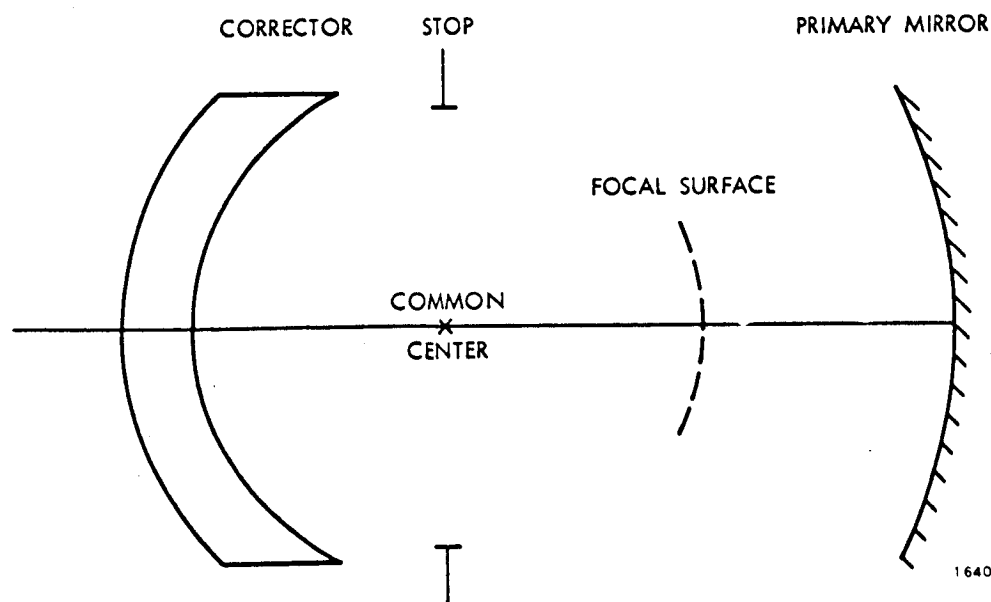


Figure 13. Simple Bouwers Concentric System.

In the basic Bouwers system, the axial separation of the corrector from the stop (hence, the radius of one of the surfaces) and the thickness of the corrector are essentially the only two variable parameters which can be used to control the residual zonal spherical and longitudinal chromatic aberrations. In general, as corrector thickness increases, zonal spherical aberration is reduced while longitudinal chromatic aberration is increased. In addition, secondary spectrum will be a problem, because of the wide spectral range at 0.5 to 1.1 microns.

Twelve-Inch Aperture, f/1.0 Bouwers. -As a first approach, a 12-inch aperture, f/1.0 system was investigated (figure 14).

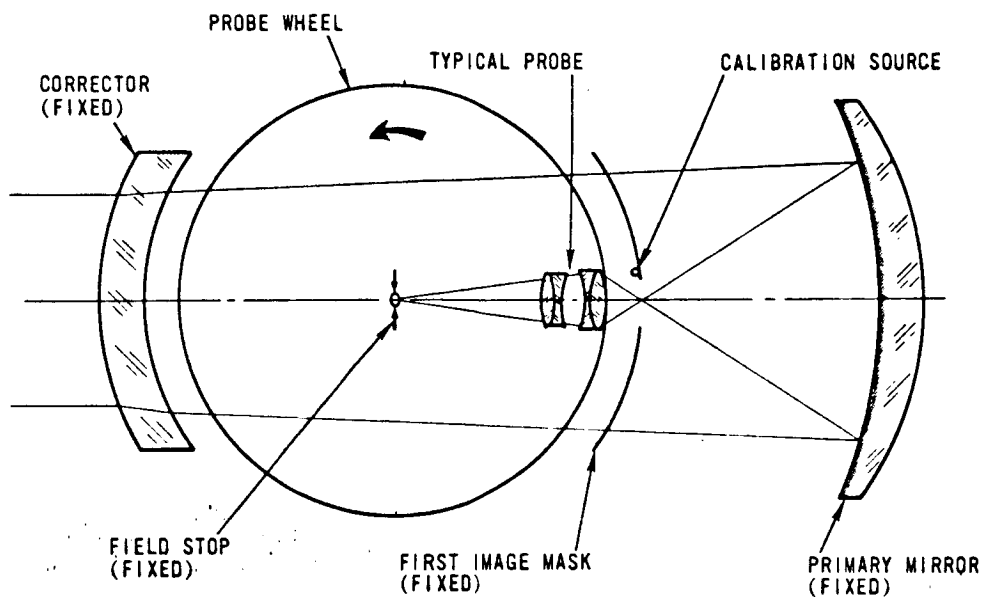


Figure 14. F/1.0 Bouwers System.

Early in the design, it became apparent that this system would be too heavy and too large for existing representative spacecraft because of the thick corrector. Preliminary analysis of the 12-inch, f/1.0 system also showed that the spherical aberration was too large to conveniently correct.

Weight considerations preclude the optically concentric configuration. Hence, it was decided to limit the fused silica corrector thickness to 1.5 inches. At the monochromatic (C-light, 656.3 nanometers) best focus the primary image quality is about 0.7 milliradian in angular blur circle diameter. Considering the chromatic aberration of the same order leads to broadband imagery of about 1 milliradian quality. This is too large if a field stop, (76 microradians) is to be placed at the primary image.

A preliminary analysis of the probe action indicates that a minimum of nine elements would be required to simultaneously correct the zonal spherical and secondary spectrum to obtain a broadband image of the order of 76 microradians. Even then, aspherization of one surface might be necessary.

There are several approaches in the literature for increasing the resolution at the primary image surface. Most of these approaches assume a thicker corrector element. Color and zonal spherical aberration can be decreased by allowing a slight departure from the concentric requirement. This improvement is achieved at the expense of the chromatic and astigmatic

aberrations. Another approach would be to achromatize the corrector by making it a doublet. Concentricity would be preserved at 1 wavelength if glasses with the same index (at one color), but with differing values, were employed. The chromatic aberration would vary with obliquity, i.e., with field angle. All off-axis aberrations lead to signal modulation as a function of scan angle, which is intolerable.

Since the major cause of the poor primary image is the extreme speed of the $f/1.0$ system, it was decided to investigate systems with f /numbers up to $f/1.75$ so that the optimum Bouwers corrector thickness would be less than 2 inches.

Eight-Inch Aperture, $f/1.67$ Bouwers with Achromatic Corrector. -In investigating Bouwers systems with varying f /numbers, it was found that an $f/1.67$ system furnished a good compromise between physical size and optical image quality. Even with a system this slow, it was found that an additional corrector, an achromatic element at the stop, was needed to provide primary quality of the order of 67 microradians.

This zero power achromatic corrector contains two thin elements, one of KzFS-N4 and the other of SK-4. These two glasses have catalog C-indices of 1.60924 and 1.60954, respectively. This system is shown in figure 15.

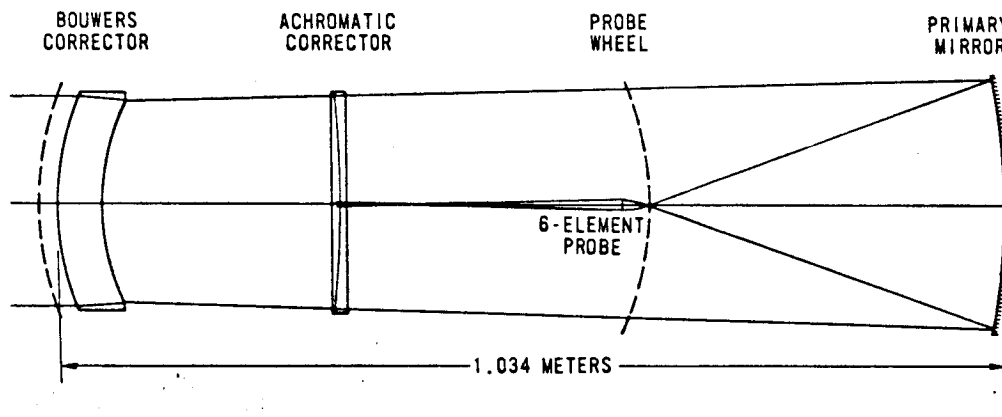


Figure 15. Eight-Inch, $f/1.67$ Bouwers with Achromatic Corrector.

The outer two surfaces of the corrector are plano while the inner two have the same curvature. The placement of the corrector at the stop, with its essentially zero power, permits partial correction of the chromatic aberrations, both primary and secondary, while introducing negligible astigmatism and coma. Since the zonal spherical aberration remains the same with this configuration, it must be corrected in the probe.

The most completely investigated Bouwers system consists of a 2-inch miniscus corrector, a 1/2-inch thick achromatic corrector at the stop, and the spherical mirror. The probe wheel effectively cuts in half the Bouwers corrector and, with the axle, cuts into quarters the achromatic corrector. The low power of these elements makes the alignment of the separate pieces noncritical.

For this system, 90 percent of the geometric energy falls within 40 microradians. This high quality primary image helps simplify the probe design. It will be shown that six refractive elements provide better performance than the nine needed for the $f/1.0$ system. The ray intercept curves for this primary system are shown in figure 16. Zonal spherical, longitudinal chromatic aberrations, and secondary spectrum problems are evident. The most important item is that the axial and off-axis images are virtually identical.

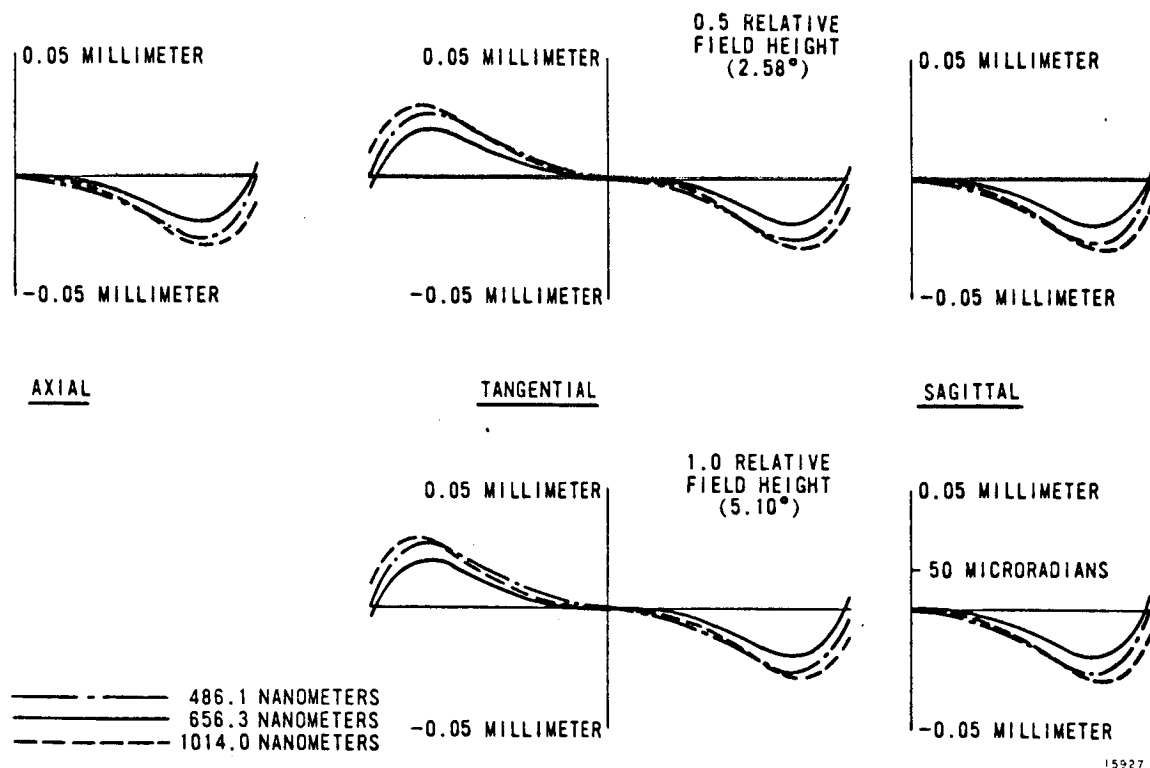


Figure 16. Ray Intercept Curves for 8-inch, $f/1.67$ Bouwers (at Primary Image).

Eight-Inch, $f/1.67$ Bouwers-Schmidt.—One approach to correct the zonal spherical aberration in the primary image is to aspherize the first surface of the achromatic corrector, i.e., at the stop. This produces a type of Bouwers-Schmidt configuration.

The previously discussed 8-inch $f/1.67$ Bouwers was modified and computer optimized to produce the ray intercept curves of figure 17. There is a great improvement in curve shape over the unaspherized versions. The straightness of the aberration curves indicates that the residual is mostly longitudinal (axial) chromatic aberration, each color simply having a different best focus. There is also some spherochromatism, the chromatic variation of spherical aberration.

The chief disadvantages of this solution are with the aspheric plate. Fabrication of this plate is routinely accomplished, but it is a time-consuming procedure. The aspheric achromatic corrector must be split for the axle and wheel. Aligning the four quadrants and maintaining the alignment of an aspheric is a difficult mechanical problem. A probe could be designed to compensate for the axial color.

Schmidt System.—In an effort to reduce the weight of the corrector elements, a classic Schmidt system was investigated. The classic Schmidt system (figure 18) consists of a spherical reflector with an aspheric corrector at its center of curvature, which is also the aperture stop. Third-order spherical aberration and coma are nonexistent. In addition, the troublesome zonal spherical aberration of the Bouwers system can be corrected. The residual aberrations consist of spherochromatism and certain high order forms of astigmatism or oblique spherical. Since the action of the aspheric plate is different in the tangential and sagittal planes, astigmatism results.

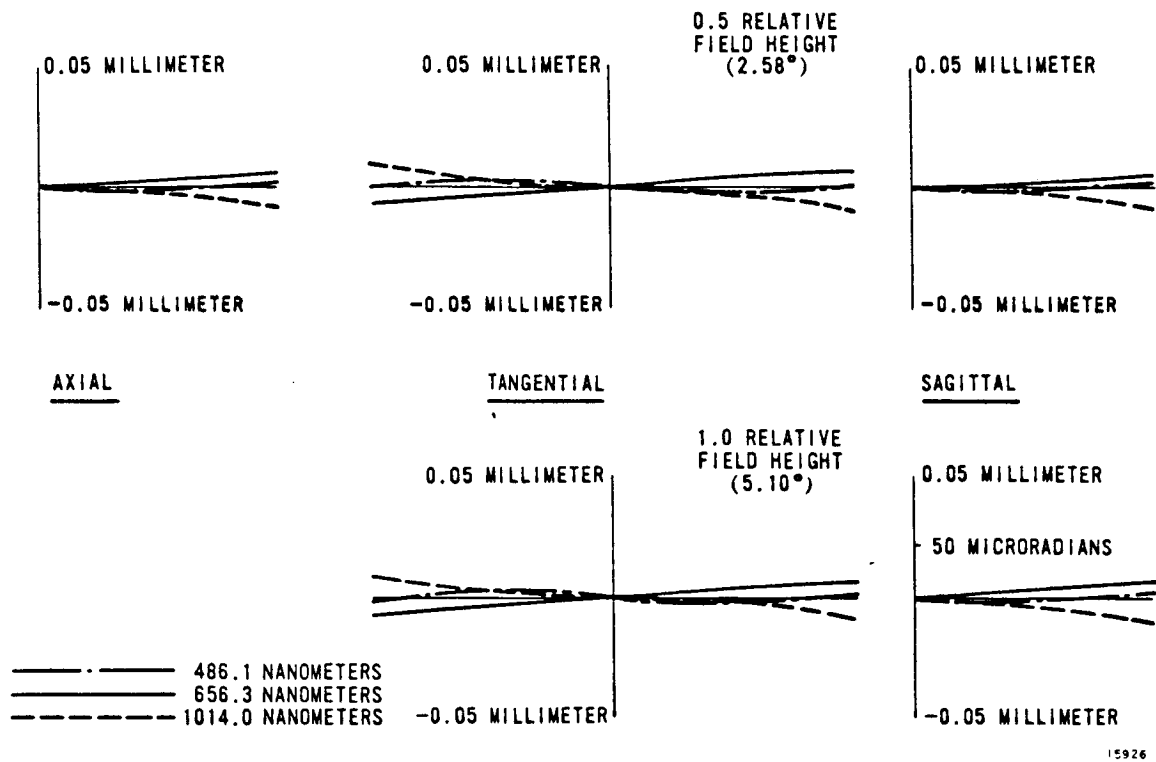


Figure 17. Ray Intercept Curves for Bouwers-Schmidt (at Primary Image).

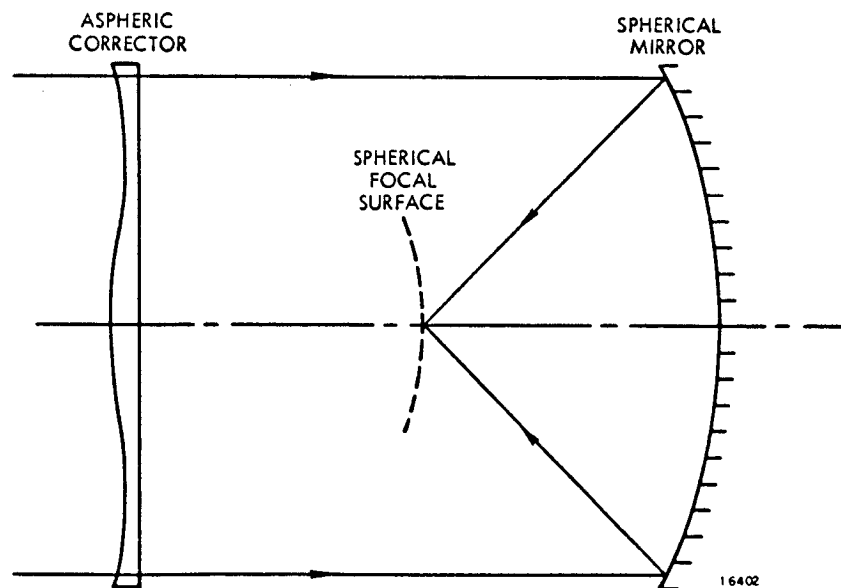


Figure 18. Classic Schmidt System.

For this scanner application, the primary advantages of a Schmidt system would lie in size and weight. The aspheric corrector is more centrally located in the system than the Bouwers corrector and is much thinner.

The thinner aspheric corrector leads to smaller chromatic aberrations. One difficulty is in the fabrication alignment of the aspheric plate which must be split into fourths. The chief problem is optical because the astigmatism makes it impossible to maintain image quality through the probe across the field. This would lead to signal modulation as a function of scan angle.

An 8-inch, $f/1.5$ Schmidt system was designed using ORA program CODE IV. The departures from the classic Schmidt are the inclusion of up to the tenth-order aspheric coefficient and a slight bending of the corrector. The ray intercept curves are plotted in figure 19.

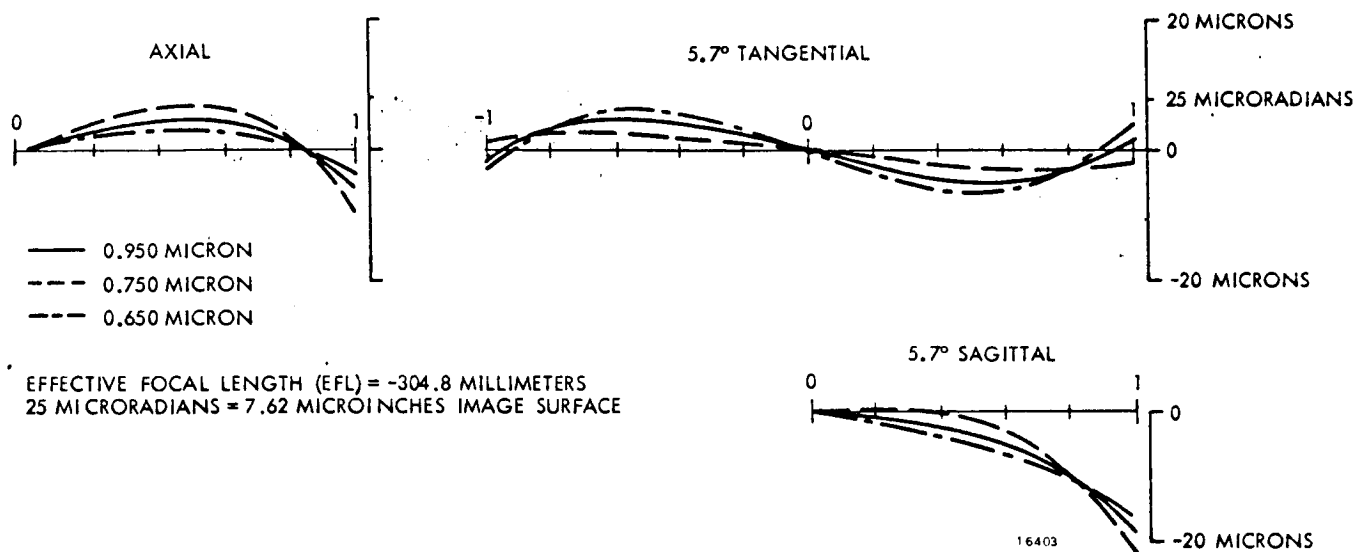


Figure 19. Ray Intercept Curves for 8-Inch $f/1.5$ Bouwers.

These show primary image quality superior to the 8-inch, $f/1.67$ Bouwers system. The tangential curves at 5.7 degrees and the axial curves have reversed form. Note the sagittal fan data at the 5.7 degree field position. The astigmatism is clearly shown. The focal plane could be moved to provide a better balance between the tangential and sagittal directions, but at the expense of tangential performance.

The high, but varying, image quality across the field presents an impossible problem in probe design. A rubber probe is needed. A probe was designed to work on-axis with the resulting image quality of 25 microradians. At the 5.7-degree field position, image quality deteriorated to a blur circle of about the microradians for a resolution element.

Eight-Inch, $f/1.67$ Primary, Sugino Probe.—One of the main objections to the Bouwers system described previously in this section is the heavy refractive corrector required. Also, the Bouwers and the achromatic corrector had to be split for the probe wheel. A new approach, conceived by Paul Sugino of the Te Company, avoids these disadvantages (see figure 20). In this approach, the first level of optical correction is moved from the parallel beam ahead of the primary mirror to the converging beam ahead of the first image surface. This required the addition of a three-element, zero-power corrector to each probe, but did eliminate the large heavy refractive correcting elements. This system always operates on-axis.

ALTERNATE - FULL SYSTEM

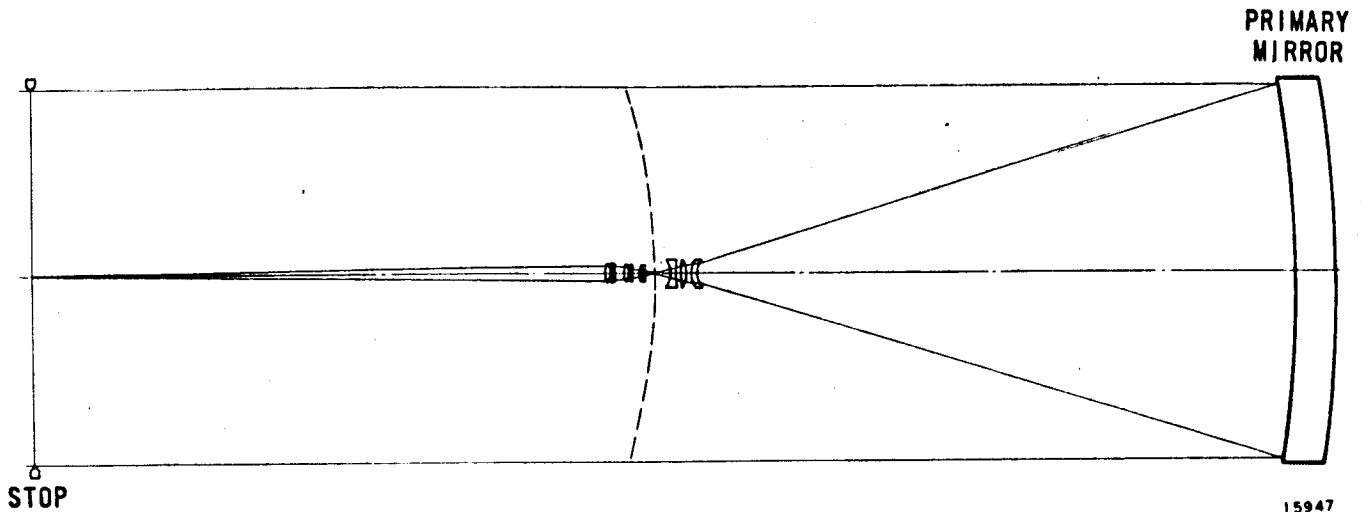


Figure 20. Sugino Probe System.

Calibration and synchronization point sources would be inserted into the system via a U-shaped circular channel in the probe wheel. There is sufficient room between the third and fourth elements of the Sugino probe to accommodate such a channel without compromising the mechanical strength of the wheel.

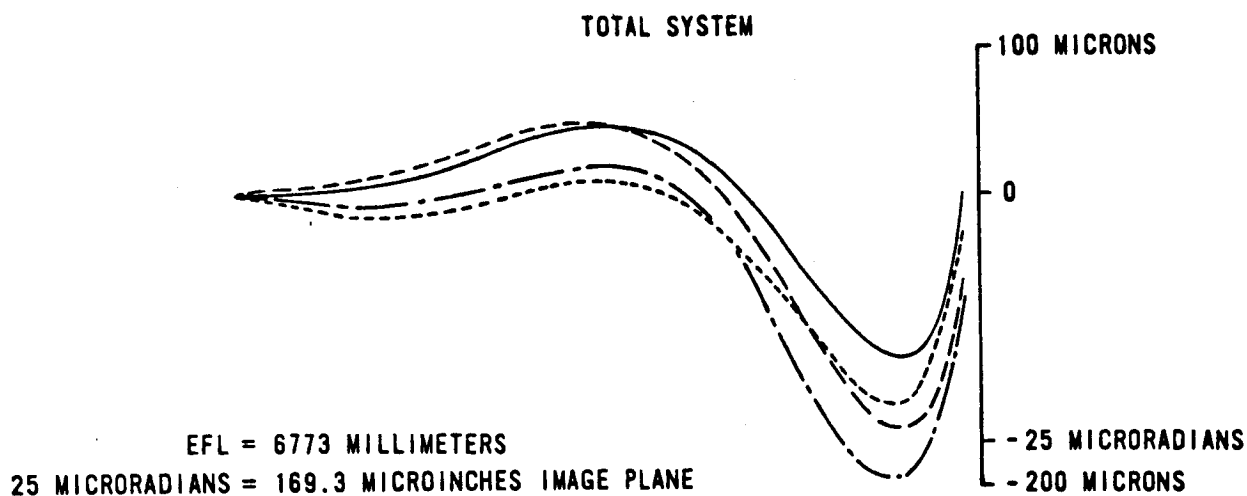
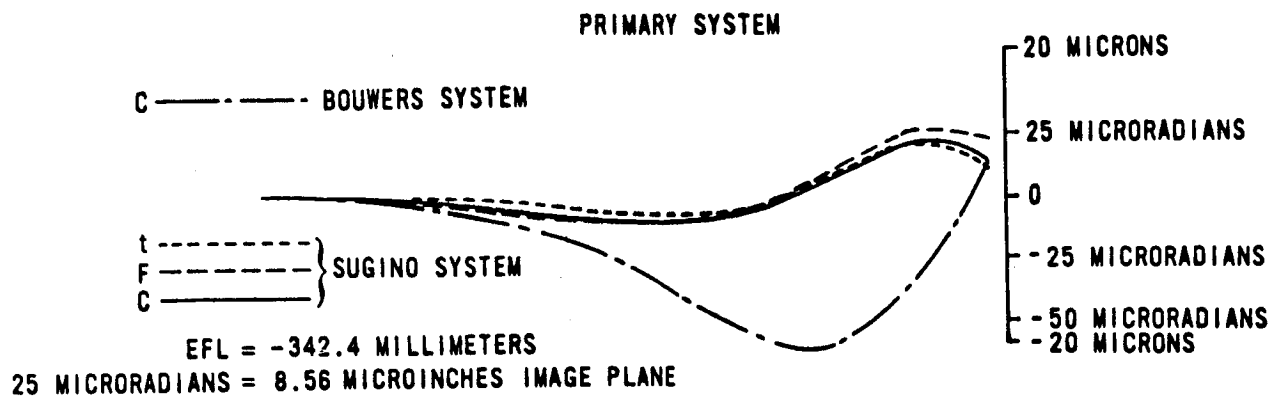
The ray trace of this system indicated that it had better image quality, at both first and second image surfaces, than any of the previously discussed systems. A comparison of the ray trace image quality of this approach with the image quality of the $f/1.67$ Bouwers with achromatic corrector is given in figure 21.

Nine-Inch $f/1.5$ Primary, Sugino Probe.—Increasing system S/N can be accomplished by increasing aperture. The extension properties of the Sugino probe system was investigated. The design process, applied to a 9-inch, $f/1.5$ primary, furnished an excellent insight into the modus operandi of the system.

Primary image quality was first optimized using the constructional parameters of the first three elements of the Sugino probe as variables. With this optimization, 90 percent of the geometric rays fell in a blur circle of 26 microradians diameter. Note the form of the ray intercept curves in figure 22, particularly the three zero cross points. These higher order aberrations make it difficult to relay the good primary image quality to the second image (the entrance slit to the spectrometer). The best image quality achieved with the six elements aft of the primary image was 41 microradians. Thus, the probe was not even able to maintain the primary image quality much less improve it.

The next step was to relax the primary image requirement by allowing the elements before the primary image to take part in the optimization. Doing this, a final image quality of 17 microradians was achieved. This quality was obtained at the expense of the primary image whose blur circle radius had increased to 67 microradians. Although this is very large, it should be compared to the 2310 microradians of an uncorrected $f/1.5$ spherical primary.

It is obvious that compromises can be made. For instance, one system with a primary image quality of 76 microradians and overall quality of 35 microradians was designed. With the lessening of the requirement for first surface image quality, the Sugino probe becomes



15948

Figure 21. Ray Intercept Curves for $f/1.67$ Sugino vs. $f/1.67$ Bouwers.

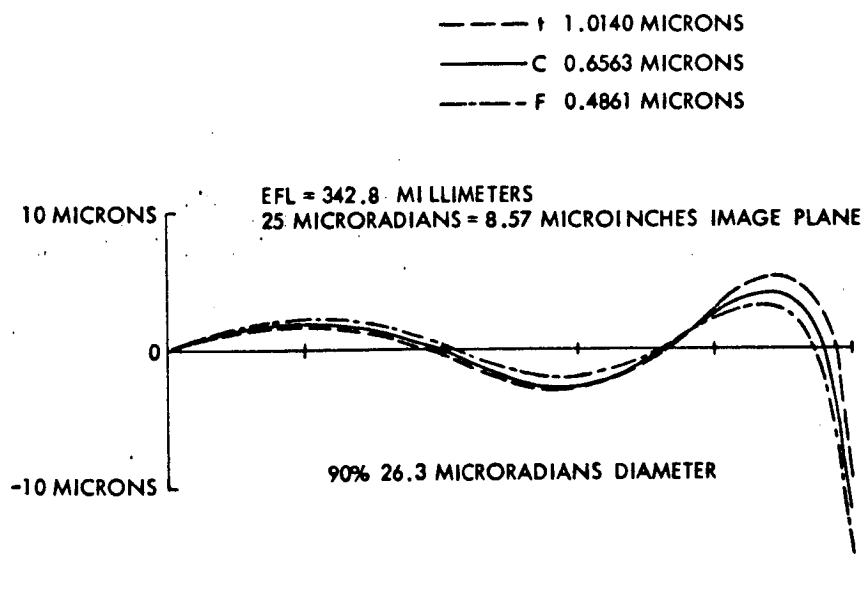


Figure 22. Ray Intercept Curves at Primary Image of $f/1.5$ Sugino.

a very usefully configuration for fast systems. With a nine-element probe, speeds faster than $f/1.5$ are readily achievable. At these speeds, mechanical tolerances, particularly those relating to primary-secondary separation, are very important.

Probe Design

In addition to relaying the primary image to the entrance pupil of the spectrometer, the probe must correct, at least partially, the aberrations of the primary, particularly the zonal spherical and the secondary color in the Bouwers systems. In the Sugino probe, the delicate balance between the corrective power before and after the primary image has been previously discussed.

Initially in the program, only dioptric (all refractive element) probes were considered and these on the basis of a 24-probe wheel in the great circle configuration. The design of these refractive microscope objectives proved straightforward and the resulting prescriptions appeared reasonable to fabricate and align. Also, they would pass the required spectral range, 0.5 to 1.1 microns. If this range were expanded to include the ultraviolet, or the thermal infrared, then an all-reflective system would be mandatory. In fact, a catoptric probe would seem to be ideal, since mirror systems are generally, light in weight and introduce no chromatic aberrations of their own.

All-reflective systems were not originally considered because of two drawbacks, both of which are minimized in the folded, tilted wheel scanner. A two-mirror configuration to meet the resolution requirement requires precision high order aspheric surfaces, particularly on the secondary (first probe mirror). Fabricating a matched set of 24 aspheric small mirrors is a formidable task. Though lightweight, mirror probes would tend to be bulky, far bulkier than dioptric optics. This would lead to mounting problems and increased obscuration, since 24 probes are involved.

With the tilted wheel approach, the number of probes decreases from 24 to 8. The wheel is removed from the direct optical path by the folding flat, and the size of the reflective elements is limited only by the size of the wheel. Hence, a catoptric design becomes feasible.

Dioptric Probes. -All dioptric probes considered in this report are the same type, namely six-element microscope objectives. (The Sugino probe has nine elements, but only six after the primary image.) Three different Schott glass types, KzFS N4, SK 16, and FK 50, are used to minimize secondary spectrum. A typical probe of this type is shown in figure 23. The design of the dioptric probes was accomplished using program POSD, controlling the axial marginal and zonal rays in three colors.

Initially it was decided, somewhat arbitrarily, to go to a 10:1 probe system for the Bouwers systems. Later analysis showed that a probe operating at a magnification of 20:1 would be advantageous as it results in a smaller probe diameter, decreased obscuration, and lower probe-wheel moment of inertia. The change from 10:1 to 20:1 in the probe does not materially change the spectrometer design. The two probes are very similar. The Sugino probes considered operate at 20:1.

The aberration curves for the 10:1 probe in the $f/1.67$ Bouwers system for the axial field position are shown in figure 24. Image quality was found to be similar within a few micro-radians at all field positions. The ray intercept curves for the 8-inch $f/1.67$ system with Sugino probe are shown in figure 21. For this system, the object is always on-axis, so there can be no field position modulation.

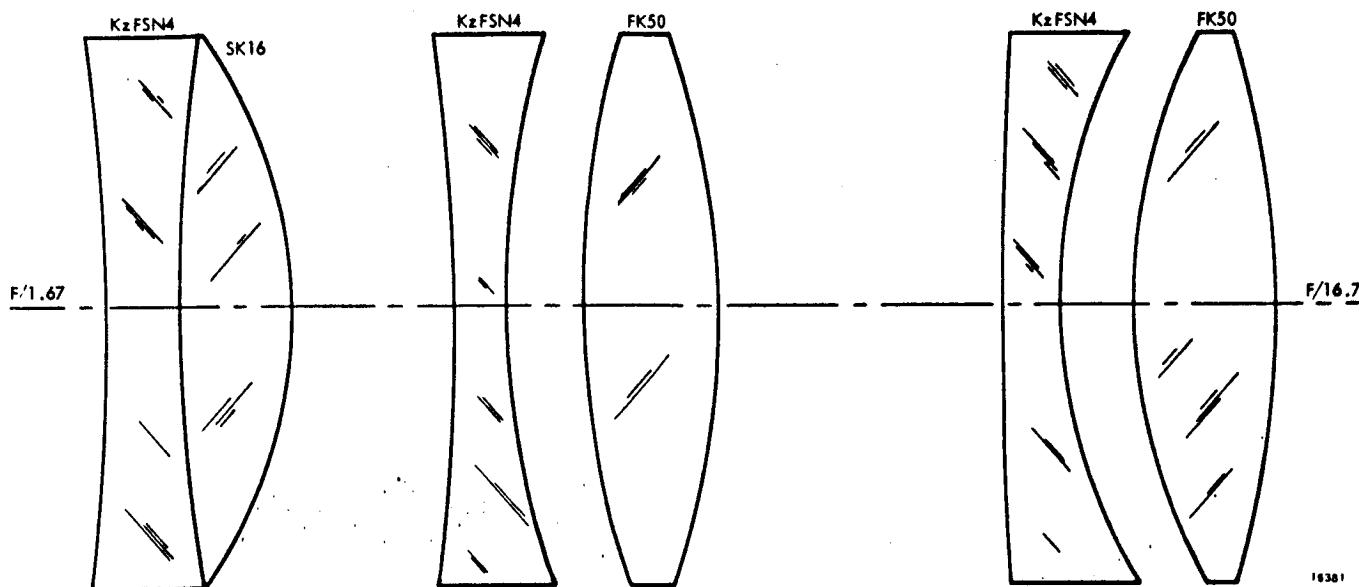


Figure 23. Dioptric Probe (10:1).

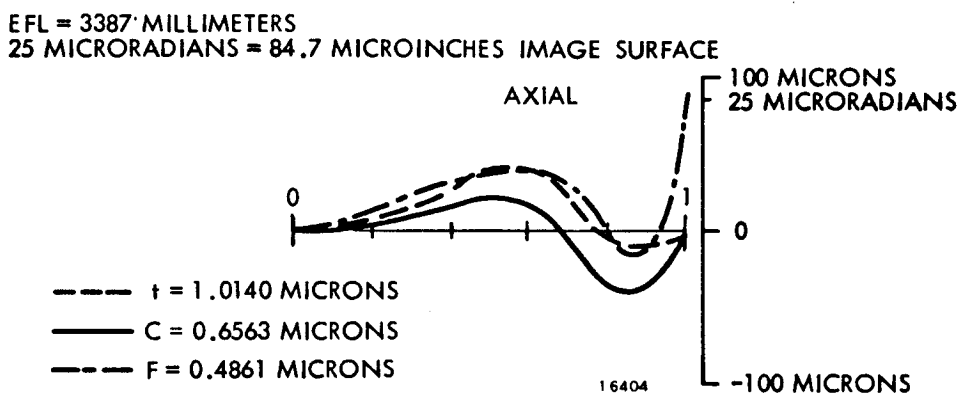


Figure 24. Ray Intercept Curves for 8-Inch, $f/1.67$ Bouwers with 10:1 Probe.

Catoptric Probes (Additional Study Area).—This study establishes the feasibility of incorporating a reflective probe into the tilted wheel scanner configuration. All probes considered in this paragraph are of the Burch microscope type, i.e., having two reflecting surfaces (with power) and are designed for use with an $f/1.67$, 8-inch primary mirror. No correction of the primary image was attempted. The small wheel of the tilted plane scanner and the resulting decreased mechanical deformation mitigate the requirement for a stop at the primary image surface.

With the tilted wheel scanner, an arc of 45 degrees is scanned, compared to the 15 degree scan (11.4 degrees active) of the great circle scanner. The 15 degree scan motion can be absorbed in the spectrometer without derotating the image. The 45 degree scan motion dictates a derotation system. Otherwise the spectrometer collimator lens would have an incident cone faster than $f/0.5$. To simplify the derotation process, it was decided to make the probe afocal, i.e., the exiting beam from the tertiary is collimated.

The basic idea of the derotator is to prevent the images of square resolution elements from rotating during the scan. This is mandatory if multiple detectors are used. This

condition establishes the basic optical matrix function that must be satisfied by the particular configuration of folding mirrors. This function of mirror normal and ray directions is discussed in detail in appendix I.

An algebraic solution for the constructional parameters of Burch microscope objectives that produce any specified spherical aberration is presented in appendix II. The analysis for a complete three-mirror system (figure 25) shows that the tertiary mirror has a negligible corrective leverage, even when aspherization is considered. Hence, the tertiary mirror was held spherical in all cases and the secondary mirror was allowed to assume a conic section and then a more general aspheric shape.

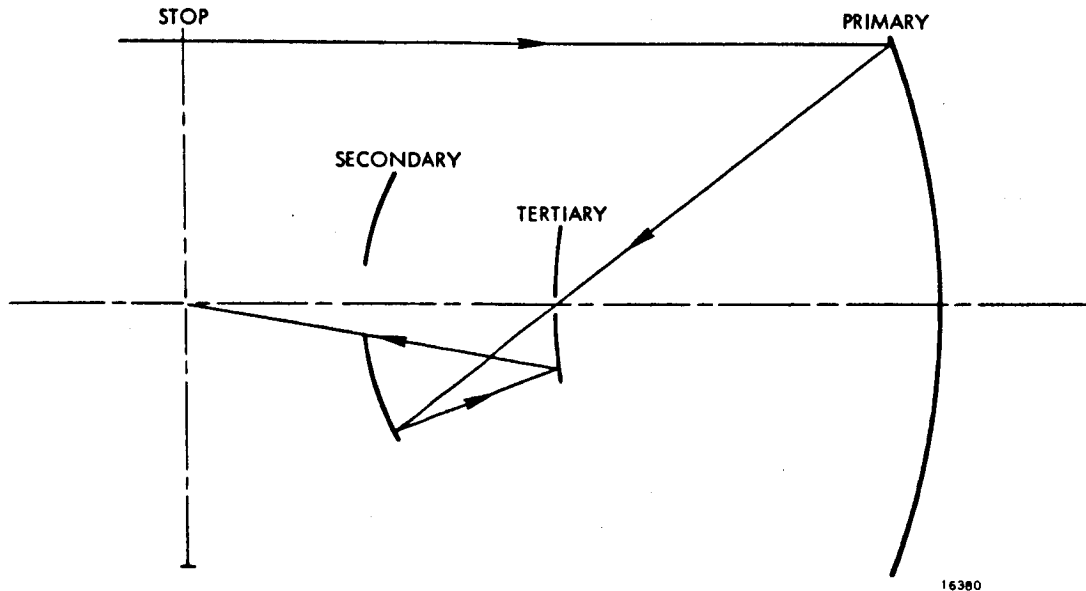


Figure 25. Catoptric System.

The variable parameters for design optimization are the two curvatures and axial separations, and the conic constant and aspheric deformation coefficients of the secondary. The conic constant is the negative square of the eccentricity. The relation between the primary image secondary separation, conic constant, and overall resolution quality is graphically shown in figure 26. As the distance from the primary image point to the secondary mirror increases, the conic constant approaches zero (surface becomes a sphere) and the resolution approaches 50 microradians. Since, in a diverging light beam, the diameter of the secondary mirror varies directly as the distance from the primary image point, the consequences of this large diameter on packing in a tilted wheel with fixed parameters must be considered. If a secondary mirror diameter which would yield a 76 microradian image could be tolerated, packing on the probe wheel would reduce the number of probes permissible from eight to five.

Taking the maximum secondary diameter which would yield a wheel with eight probes, the resultant conic solution gives an image quality of about 120 microradians which cannot be substantially improved in the spectrometer optics.

Assuming that the imagery leaving the probe optics must satisfy the 76-microradian criterion, the forcing function becomes the deformation coefficients of the conic base. The final

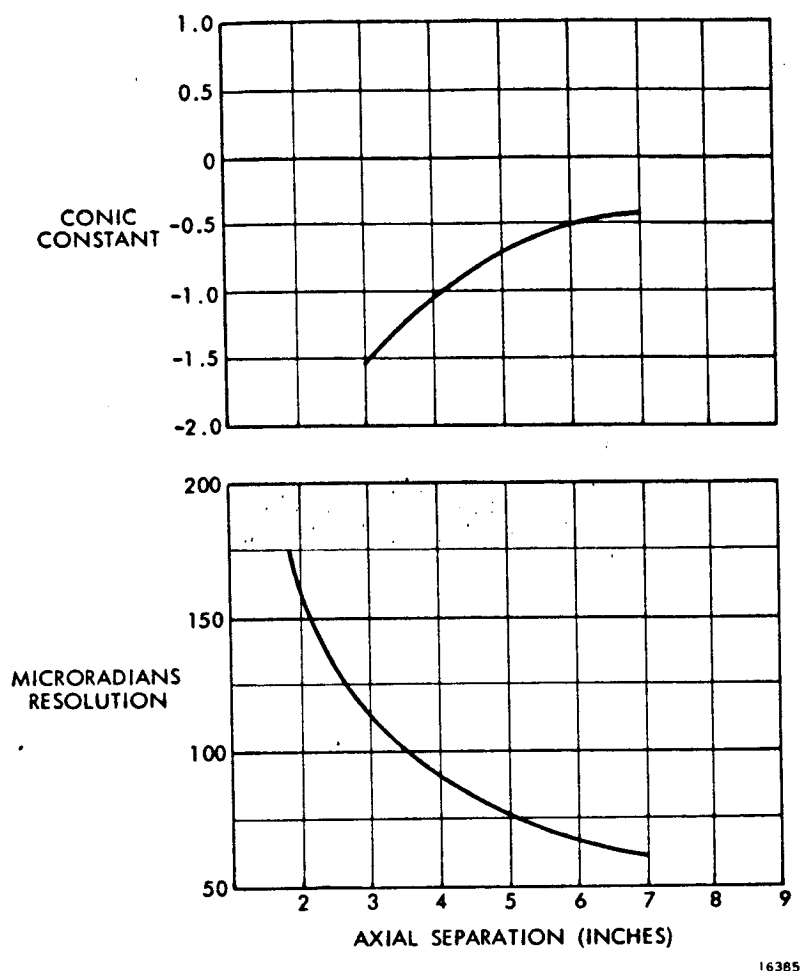


Figure 26. Primary Image to Secondary Mirror Separation.

Table 6. Catoptric Scanner Prescription.

Axial separation from primary image		3.00 inches
Secondary Mirror:	Radius	4.269 inches
	Conic Constant	-1.626 inches
	Deformation Coefficients	$-0.000234^4 + 0.0001731^6$
Axial separation to tertiary		9.004 inches
Tertiary mirror:	Radius	-3.289 inches
	Conic Constant	0
	Deformation coefficients	---

assessment of the all-reflective scanner optics is made using a parabolic mirror with numerical aperture selected to yield an overall system equivalent focal length of 267 inches. Using two of the aspheric coefficients (the fourth and sixth order), image quality for the system of table 6 was found to be an excellent 4.7 microradians.

This system is typical of those investigated. (A complete folded system, including spectrometers, is shown in figure 27.)

Fabrication of eight identical aspheric mirrors will be a formidable task, particularly since the signs of the two coefficients are different. In a final design it may be expedient to relax the image quality to about 25 microradians and ease the optician's burden. Testing the mirror is simplified by its concavity. It can be tested by itself using a null lens in the system with the spherical primary and testing mirrors.

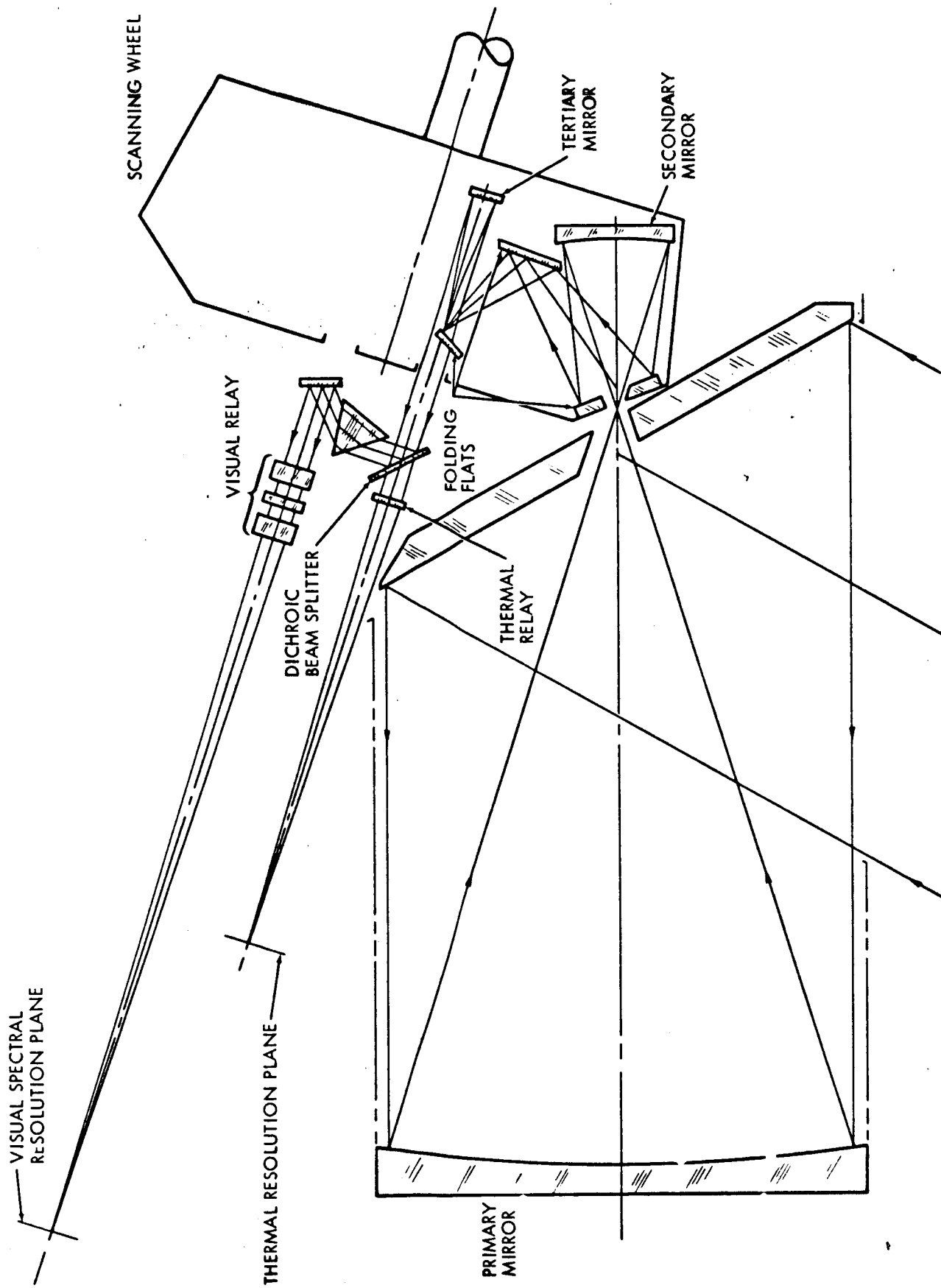


Figure 27. Optical Schematic of Catoptric Scanner and Spectrometers.

Spectrometer

Two separate spectrometers were designed during the program. The first, for use with a great circle scanner, covers the 0.5 to 1.1 micron spectral band. The second includes the 8 to 11 micron thermal infrared band, in addition to the 0.1 to 1.1 micron band, and is for the tilted wheel scanner.

Great Circle Spectrometer (0.5 to 1.1 Microns). -The conceptual design of this narrow band spectrometer is presented in this paragraph. Figure 28 shows a plane view sketch of the optical layout of the spectrometer. In an actual system, all optical flat would probably be introduced to fold the spectrometer through 90 degrees to conserve space. The mechanical layout is shown in figure 29.

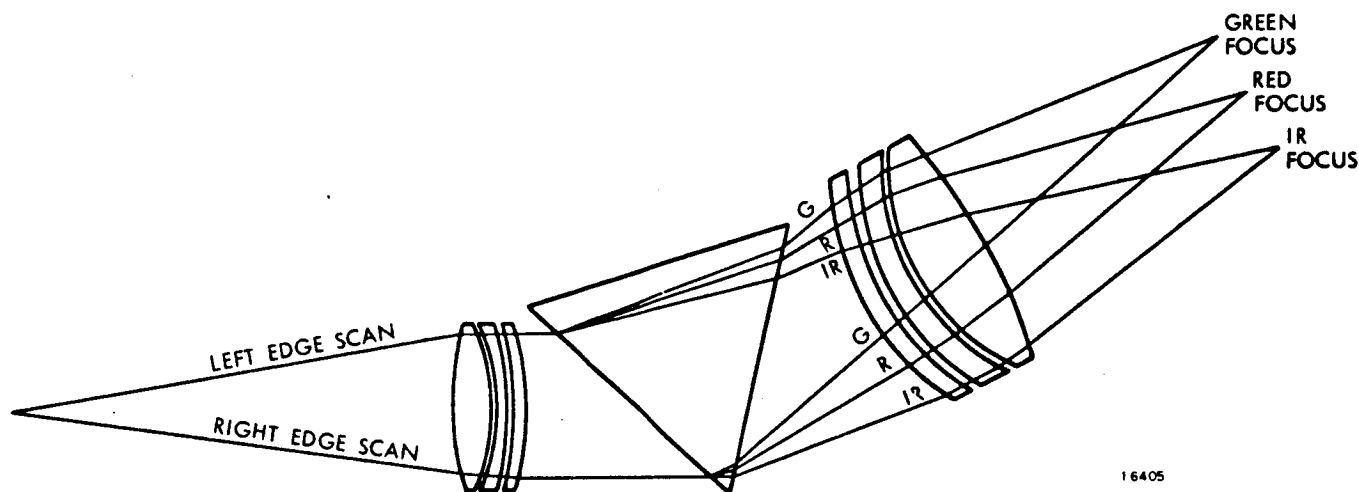


Figure 28. Spectrometer Layout, Plane View.

The entrance aperture is square, 0.076 milliradians on a side referenced to the scanning optics. With a 267-inch focal length optical system, the entrance aperture is a square approximately 0.02 inch on a side. This aperture is located at the axial focal point of a collimating lens, which will be an air-spaced triplet, well corrected for spherical and axial chromatic aberrations. Its aperture will be large enough to pass all the radiation entering the entrance aperture as a result of the active scan (11.4 degree half-angle) of the probe optics. The radiation will emerge from the collimating lens as a collimated beam, traverses the aperture of the lens horizontally as the probe scans, but which will always be parallel to the optical axis of the lens. This beam strikes an equilateral prism which disperses the light in angles depending on its wavelength. This prism can be BK-7 glass, but other choices are available. The dispersed beam of radiation is then reimaged by a second lens identical to the collimating lens. Since radiation of each wavelength enters this lens at a fixed angle different from that of radiation of any other wavelength, each wavelength will be brought to a focus at a different point in the focal plane of the second lens.

A set of four quartz light pipes, whose faces are properly sized to accept radiation across the desired wavelength interval, are located in the focal plane of the second collimator and conduct the radiation to the proper detector. This would be strictly true if the collimating lens were perfectly free of aberration and if the entrance aperture were a geometrical point. For all practical purposes, the first assumption is true. Lens aberrations should cause the nominal boundary between wavelength bands to shift no more than 1 or 2 nanometers.

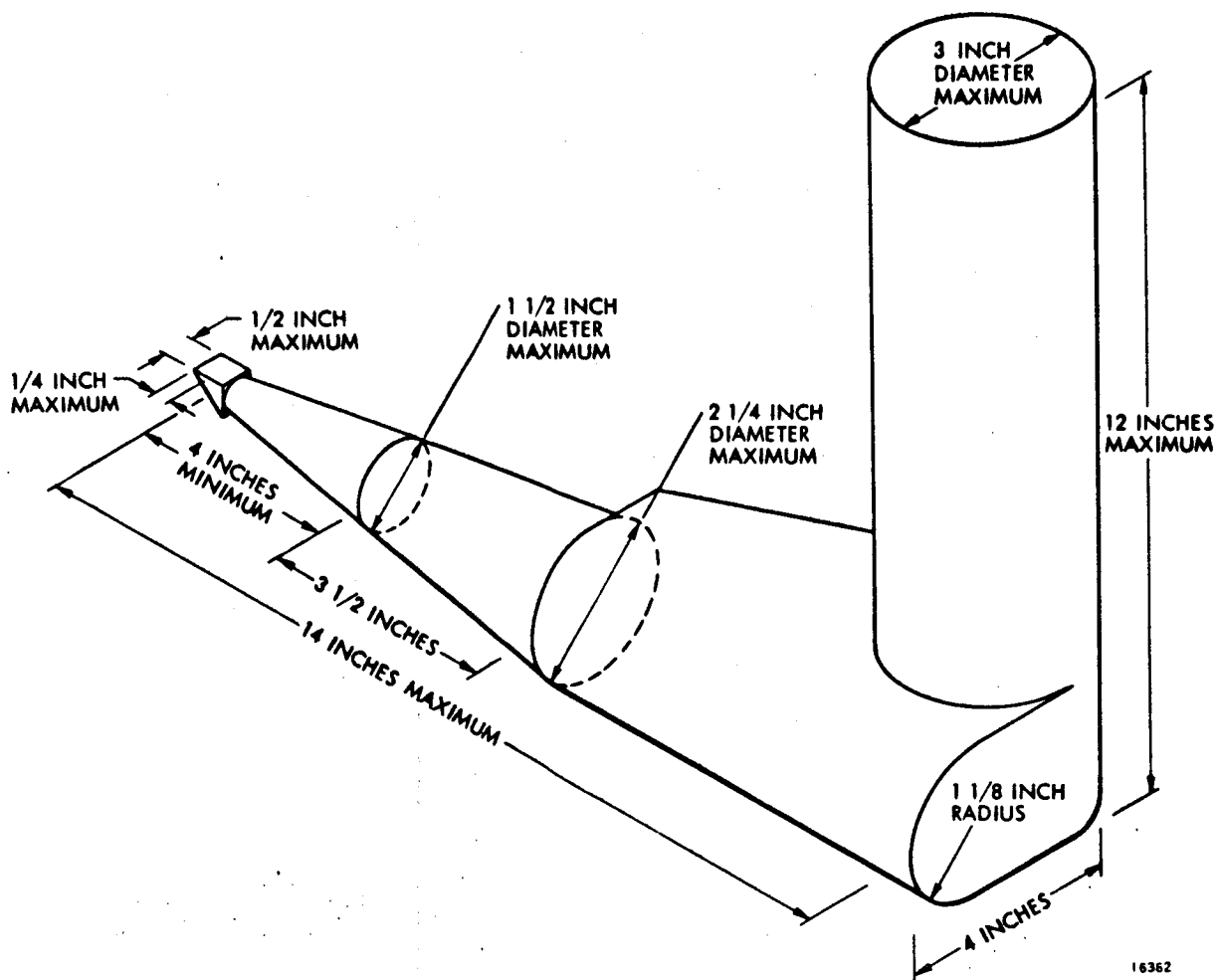


Figure 29. Spectrometer Mechanical Configuration.

Inhomogeneities in the prism will cause only small shifts. The entrance aperture is a finite size and contributes significantly to the spectral resolution of the spectrometer. In effect, the radiation of any given wavelength will form an image of the entrance aperture at the focal plane of the second lens. If the boundary between wavelength bands is chosen to pass through the center of this image at the nominal boundary wavelength, some radiation from closely adjacent wavelengths will also fall on the opposite side of the boundary from that on which its center lies. Figure 30 shows the spectral distribution of energy reaching the four light pipes, assuming a 7.5-inch focal length collimating lens and a BK-7 prism.

Tilted Wheel Spectrometer (0.5 to 1.1, 8 to 11 Microns). The basic feature of the tilted wheel spectrometer is the parallel beam exit of the energy from the scanner. This beam translates over the entrance apertures of the dichroic beam splitter, which separates the visual and infrared channels. The visual channel is further split by a prism. Adding other dichroic beam splitters to split off other channels is easily accomplished because of the collimated nature of the incidence beam. The complete tilted wheel, all-reflective scanner with spectrometer is shown in the optical schematic of figure 30.

The basic requirement of the spectrometer optics is to produce the required image for the visual and thermal channels. The effect of the circular tilted wheel scan is a translation of the beam in a small arc in a plane perpendicular to the parallel exit bundle from the scanner assembly. The magnitude of this distance included with the instantaneous aperture of

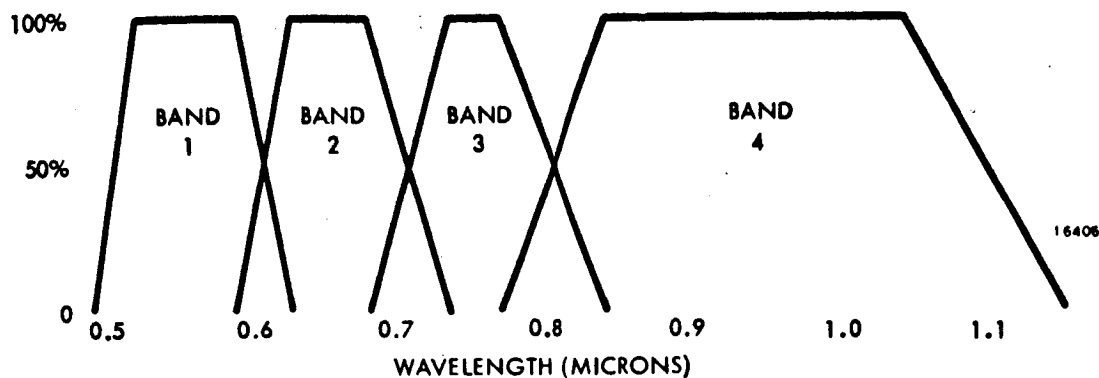


Figure 30. Spectral Distribution of Energy.

0.4-inch diameter is about 1 inch. The design goals on the spectrometer optics are that for any 0.4-inch diameter parallel beam within a 1-inch diameter aperture the resultant imagery relative to the overall equivalent focal length must be equal to or better than 150 microradians for the thermal band, and 76 microradians for the visual band.

Thermal Band Optics. -Taking the dynamic aperture requirement of the spectrometer as 1 inch, the optimization of the objective is a matter of evaluating the performance of a 13.333-inch objective. Using a single-element objective of Eastman Kodak Irtran-6 with an index of refraction of about 2.6, the optimum shape produces minimum spherical aberration (to the third-order) approximately equal to $8/N^3$ milliradians, where N is the f /number of the system.

In this case, the spherical aberration is $8/10^3$ radians, or 3 microradians. The lens prescription designed for this application is: $R_1 = 12.99$ inches, $t = 0.150$ inches, and $R_2 = 27.267$ inches. The performance in the thermal channel was verified by ray tracing the entire system.

Visual Band Optics. The requirements with respect to dynamic aperture are unchanged from those of the thermal band. The additional factor which has to be considered is the wide spectral range of 0.5 to 1.1 microns. The design problem for the spectrometer (referred to in paragraph titled "Great-Circle Spectrometer"), is one of optimizing spherical aberration, coma, and chromatic aberration, both primary and secondary. The field angle requirements are those associated with the angular dispersion of the prism itself over the above spectral interval.

The final design parameters, for the particular solution analyzed in detail, are presented in table 7.

Performance of the complete system, including visual spectrometer, was verified by ray trace.

Summary of Optical Design Studies

A comparison of the design of seven optical systems is contained in table 8. Most of the items are self explanatory. The only precaution concerns the resolution values. None of the designs listed can be considered fully optimized. Hence, further improvement is possible.

Table 7. Visual Band Spectrometer Prescription.

Object distance-- Equivalent focal length		Infinity 13.33 inches	
Surface	Radius	Axial Separation (Inches)	Glass
1	6.272	0.350	PSK 52
2	-7.267	0.250	air
3	-5.632	0.150	F1
4	10.913	0.350	air
5	-48.400	0.350	BaF 4
6	8.430	12.279	air

It is also possible that detailed tolerance analyses may show it necessary to back off and accept decreased performance.

Of the three catadioptric systems only the $f/1.67$ Bouwers (with achromatic corrector) and the two systems with the Sugino probe are acceptable insofar as optical quality is concerned. Because of physical differences in the approaches of these two contenders, final selection must take into account other than optical parameters.

An $f/1.67$ catadioptric system appears to be about as fast as can be built if first surface image quality is of paramount importance. The Sugino probe offers the best possibility for faster systems if the requirement for good primary image quality (76 microradians) is relaxed.

Several folded configurations were tried to shorten the catadioptric system. Seemingly, the only one of merit used a simple 45-degree flat at the primary image. The chief advantage of this folded system is the decreased obscuration produced by removing the probewheel from the direct optical path. The saving in size is more apparent than real since the aperture stop must remain at the center of curvature (after folding). The folded system would be shorter but thicker.

Wide spectral range can be achieved only with all-reflective optics. A two-element probe system is shown to need an aspheric secondary, which will be difficult to fabricate, particularly in matched sets. The primary and tertiary mirrors are spheres. Further, the secondary is concave for easy testing. Final aspheric touchup can be done using knife edge (or better yet, interferometrically) testing of the whole system to gauge the desired profile on the secondary.

The salient feature of the design proposed for this application is the afocal nature of the probe. The entering $f/1.67$ cone of light is converted to a collimated bundle existing from the tertiary. This greatly simplifies spectrometer design.

Table 8. Opticle Design Trade Matrix.

Optical Design Approach	Aperture (Inches)	First* Surface Image Quality (Microradians)	Second Surface* Image Quality 5.7° off-axis (Microradians)		Probe Optics	Advantages	Disadvantages
f/1.0 Bowers (f/20 system)	12	1000	70	70	8 to 10 elements Probably 1 asphere	Largest possible aperture for the available space.	Difficult probe design. Poor performance. Probably too heavy. Calibration problems. Tight mechanical Tolerances. Limited spectral range.
f/1.5 Schmidt (f/30 system)	8	28	18	51	6-elements	Short system. Good quality first image.	Change in resolution with scan angle.
f/1.67 Bowers/Schmidt (f/33.3 system)	8	48	Not computed		--	Acceptable first surface image quality.	Split aspheric corrector difficult to align. Limited spectral range.
f/1.67 Bowers with achromatic corrector (f/33.3 system)	8	53	20 (f/33.3) 26 (f/16.7)	31 (f/33.3) 27 (f/16.5)	6-elements	Good resolution at all scan angles.	Heavy corrector elements. Both correctors must be split to accommodate the scanner wheel. Split aspheric corrector element would be difficult to build and align. Limited spectral range.
f/1.67 Sugino probe (f/33.3 system)	8	37	17	17	9-elements	No large, heavy split corrector elements. Good resolution; always on-axis.	More elements in probe. Scan wheel must be larger causing more blockage. Limited spectral range.
f/1.5 Sugino probe (f/30 system)	9	76	35	35	9-elements	Larger aperture.	Same as for f/1.67 Sugino probe.
f/1.67 Catoptric system (afocal)	8	1680	4.7	4.7	2-mirrors	Virtually unlimited spectral range. Good final image quality.	Poor primary image quality. One probe element is a difficult-to-fabricate aspheric.

*Based on blur circle diameter containing 90 percent of the geometric rays.

DATA CHANNEL STUDY

This section presents the results of studies into the requirements and properties of a multispectral scanner data channel from detector to data multiplexing, and demultiplexing at the ground station. The telemetry system was not a part of the study.

The first item studied was the required analog bandwidth, since this affects performance of the entire data channel. The principal design factors influenced are system noise and telemetry bandwidth. The effect of the data channel frequency response on video signal output was studied and a criterion for selecting optimum bandwidth was developed. A 3db bandwidth of about 180 kHz is required for a 76-microradian field-of-view. A 5-pole transitional Butterworth-Thompson filter with a response providing 1 to 2 percent overshoot is suitable for the present application. Direct coupling at the low signal frequencies prevents calibration level drop during one line time.

System noise was considered next. All significant sources of data channel noise were analyzed and overall system noise was calculated for appropriate detectors in each spectral band. The results of these calculations were used throughout this study to evaluate various detector types, requirements on the telemetry system, and overall system performance. For the first three spectral bands, photomultiplier tubes are considered as having the lowest noise of all detectors currently available. For the fourth band, the decision between PMT's and solid-state silicon detectors is not straightforward. Primary interest in detector evaluation and testing during this study was centered on the fourth band. Current state-of-the-art silicon detectors were tested. On the basis of the test results, it is concluded that without further detector development the advantages of the silicon detectors is not significant enough to warrant their use over the older and more completely understood photomultiplier detectors. Gain levels, appropriate for avoiding saturation and fatigue of the dynode multipliers, were calculated based on the use of PMT's in all bands.

Attention was next directed to the selection of gain, offset, and calibration levels for the video amplifier string of each channel. High and low gain settings will be required for the first three channels but a single fixed gain will be adequate for the fourth band. The use of switchable offset levels does not appear to be necessary. A consistent set of calibration levels was shown to be feasible using a tungsten source operating at 2400° K with appropriate filtering to provide three calibrate points and black levels in each band.

The final subject considered in this portion of the study was the multiplexing and demultiplexing system required to transmit the data collected by the scanner. Numerous methods of analog and digital multiplexing were considered. A differentially coherent quadrature phase shift keying (PSK) transmission scheme, after digital encoding and time division multiplexing, is the best choice for the present application. An rf bandwidth of 20 MHz will be adequate. Block diagrams of a specific approach are presented.

Data Channel Frequency Response

The combined system bandwidth is limited largely by three system components: (a) the resolution limit of the collecting aperture, (b) the ac transfer characteristics of the field stop, and (c) the electrical signal.

Optical Modulation Transfer Function (MTF). -For purposes of preliminary estimates, a diffraction limited optical system was assumed.

The on-axis MTF of a diffraction limited clear circular aperture is:

$$\text{MTF}(\theta) = \frac{2}{\pi} (\varphi - \cos \varphi \sin \varphi)$$

where,

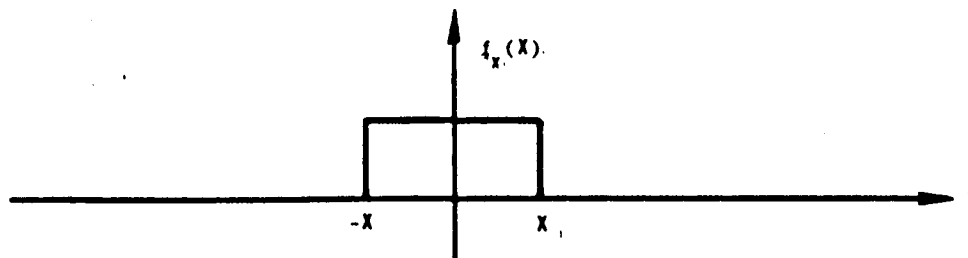
- θ = angular period of object (radians per cycle)
- $\varphi = \cos^{-1} (\lambda/\theta D)$
- λ = wavelength
- D = objective diameter (measured in the same units as λ).

The resulting MTF of a clear circular aperture versus the period of a sine-wave ground target is plotted in figure 31 for 8- and 12-inch objective diameters and a wavelength of 1 micron. This shows the percent response (normalized to 100 percent at dc) of the primary collecting aperture to a periodic sine-wave target of variable frequency. Occlusion of the central portion of the aperture (by the scan wheel and axle) will reduce the modulation of the system at low and intermediate spatial frequencies. Computation of the MTF of a circular aperture occluded by an arbitrarily shaped obstruction is ordinarily done numerically (a closed form solution does not exist in the general case) by either a convolution process or the fast Fourier transform (FFT) method.

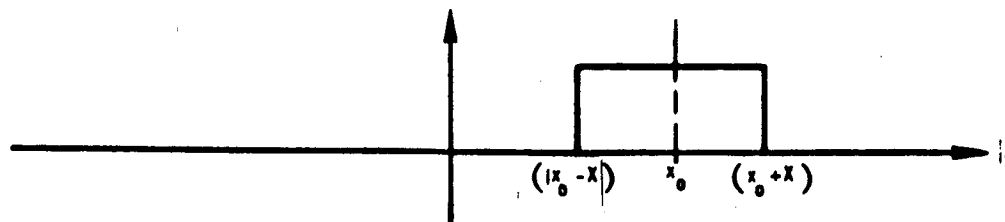
To estimate the degradation in MTF caused by blockage, the occluded aperture shown in figure 31 was analyzed. This configuration is based on preliminary estimates of the scanner wheel and axle blockages. The resultant MTF calculated using the FFT method is also shown in figure 31, again normalized to 100 percent at zero frequency. Since the collecting aperture is no longer circularly symmetric, neither is the transfer junction. The MTF for spatial frequencies oriented parallel to the wheel or axle, and at 45 degrees, are shown. The principal effect of the blockage on MTF occurs for ground periods in the range 25 to 250 feet. At spatial frequencies corresponding to a ground period of 460 feet, the obscuration decreases the response from 95 percent (unobstructed aperture) to the 89 to 91 percent range, depending on direction.

Scanning Aperture MTF. - The field stop also limits high frequency response or resolution, since the detector output is proportional to the integrated radiant flux passing through the field defining aperture. Thus, high frequency signals of a period smaller than the field-of-view tend to be integrated out.

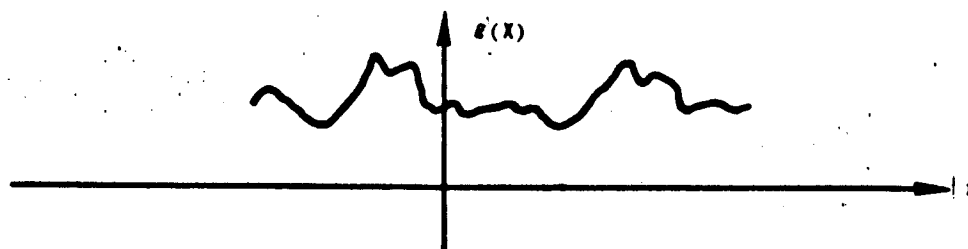
If we define a field stop function, $f_X(x)$, corresponding to a square field-of-view referred to the ground as shown:



then $f_X(x - x_0)$ is:



where the displacement x_0 is caused by the scanning action along the ground. Consider a ground target intensity given by $g(x)$:



The flux output of the scanner, o_{x_0} , imaged onto the detector as a function of x_0 , will be:

$$o_{x_0} = \int_{x_0 - X}^{x_0 + X} g(x) dx = \int_{-\infty}^{\infty} [g(x)] f_X(x - x_0) dx = g(x) * f_X(x).$$

* denotes convolution

According to the convolution theorem, this convolution in the spatial domain is equivalent to multiplication in the frequency (spatial) domain, i.e., $F(o) = F(g) \cdot F(f)$, where F denotes the Fourier transform and the subscripts have been dropped for convenience. If the ground target is considered to be the input and the integrated flux the output, the transfer function for the field stop is:

$$\frac{F[o(x)]}{F[g(x)]} = F[f_X(x)],$$

i.e., the Fourier transform of the field stop function.

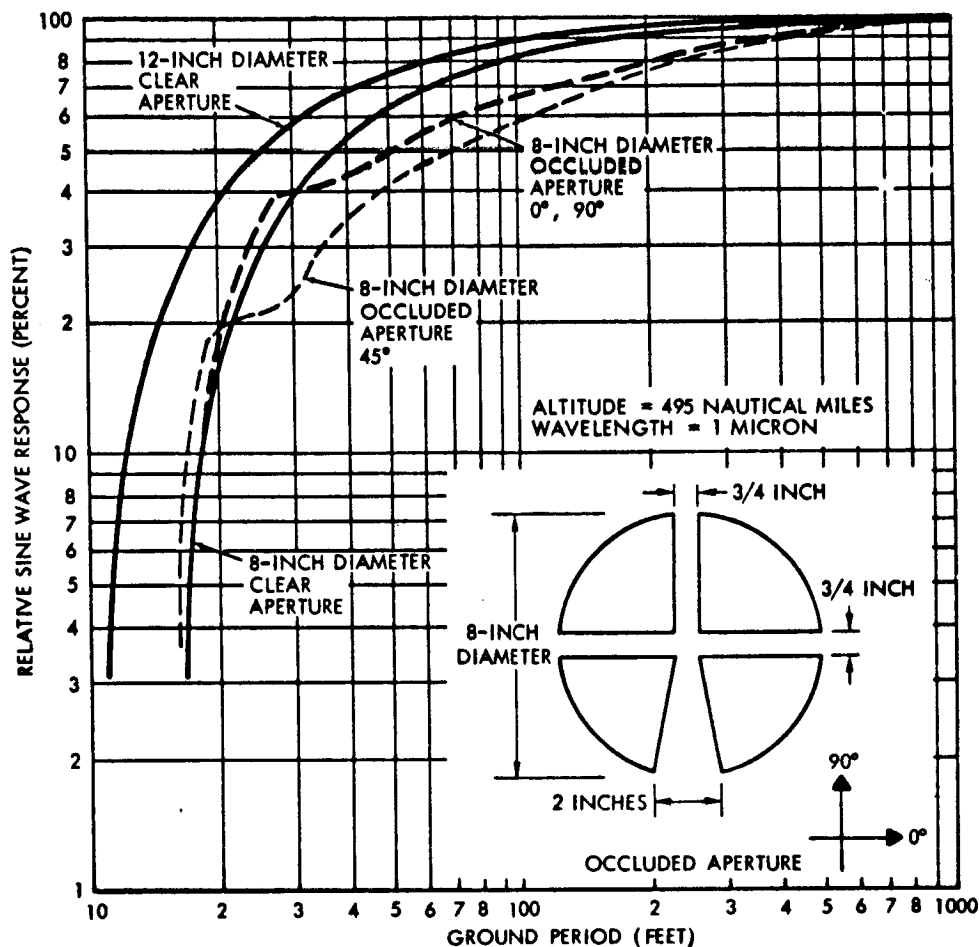


Figure 31. Optical MTF for Diffraction Limited On-Axis Systems.

For a square field stop, the Fourier transform normalized to unity at dc is the sine function, $\text{sine}(W)/W$, where W is $2\pi fX$, f is spatial frequency in the direction of scan, and X is the half slit width.

For a circular field stop, the same argument holds except that two dimensions must be considered. The resulting transfer function is given by: $2J_1(W)/W$, J_1 is the first order Bessel function of the first kind and W is $2\pi f\rho$, where ρ is the radius of the stop. The factor 2 ensures that the transfer function is unity at zero spatial frequency.

The MTF's for a square and circular aperture are plotted in figure 32. It is apparent that the field stop limits high frequency response or resolution for more than the rest of the optical system. Achieving diffraction limited operation is not mandatory to maintain system performance. The MTF's shown in figure 32 represent the response of the scanning aperture to

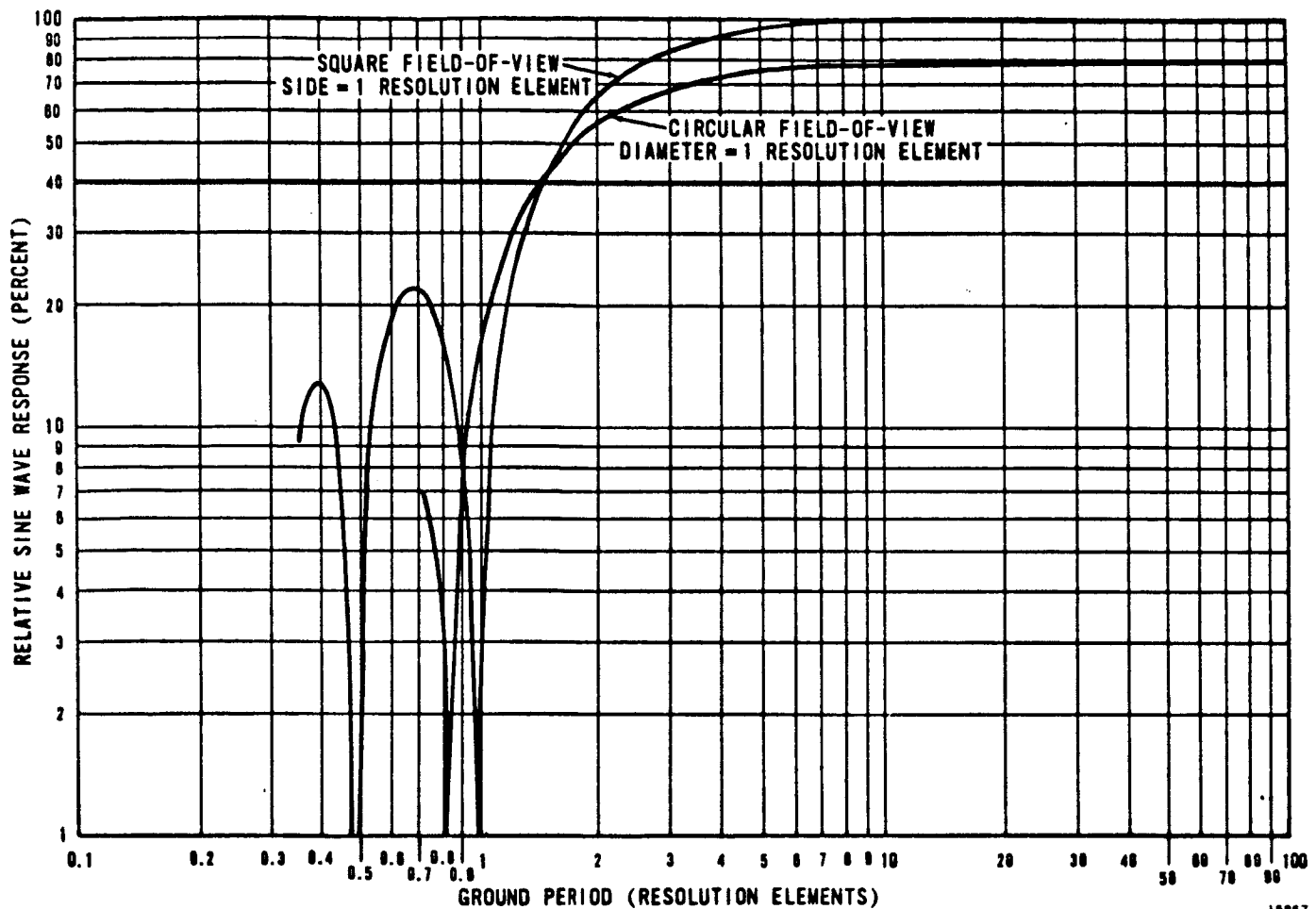


Figure 32. Aperture MTF for Square and Circular Field-of-View.

periodic sine-wave targets on the ground. The MTF for the circular aperture has been normalized by $\pi/4$ so as to account for the difference in areas between the square and circle.

For targets with periods shorter than 1.5 resolution elements, the circular aperture has an advantage of high modulation response but, for the majority of targets, it suffers in comparison to a square aperture because of its reduced area for the same linear dimension.

Electrical Frequency Response. -The shape of the electrical system transfer function and the bandwidth limit has an important effect on video output. For purposes of reducing total bandwidth occupancy, a rapid roll-off for frequencies above the corner frequency is desirable. In the following, a roll-off rate of 30 db per octave (5-pole) is assumed to be typical. With this constraint, it is still possible to select various bandpass shapes. If maximum flatness of frequency response within the passband is desired, a Butterworth or maximally flat magnitude characteristic is chosen. Butterworth filters, especially those with fast roll-off rates, suffer from overshoot and ringing when driven by transient inputs. If good transient response is desired, a Bessel or maximally flat delay characteristic is chosen. These two types of bandpass characteristics are considered as bounds to the actual system response which will lie somewhere between the two.

Figure 33 is a comparative plot of the frequency characteristics of 5-pole Bessel and Butterworth type filters yielding equal noise bandwidths and roughly comparable noise

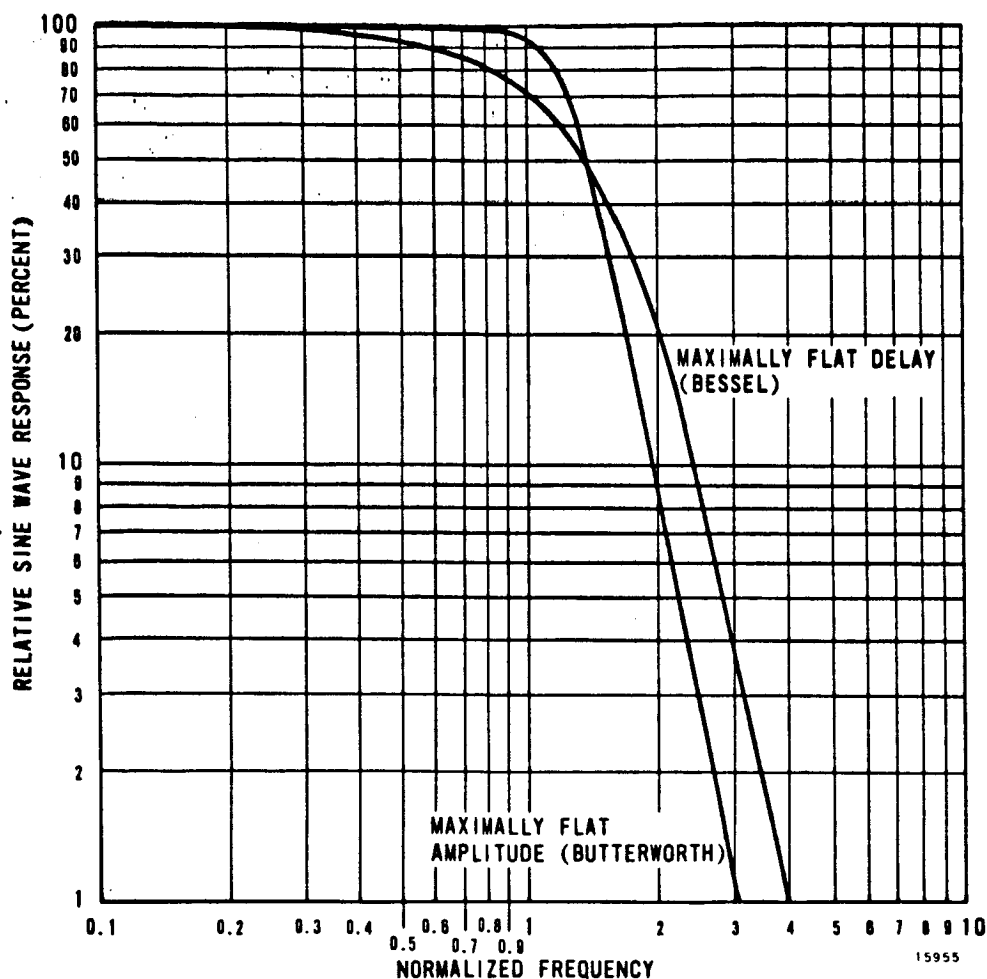


Figure 33. Comparison of Amplitude Characteristics of 5-Pole Bessel and Butterworth Filters.

performance. Note that the 3 db frequencies are not the same. In the following, whenever Bessel and Butterworth designs are compared, it will be on the basis of equal noise bandwidths, the 3 db frequencies being appropriately adjusted. The slow roll-off of the Bessel filter shown in figure 33 is responsible for the lack of overshoot, but also causes some loss in high frequency response within the passband.

To compare the performance of these two types of filters, and also estimate system performance as a function of bandwidth, system response to other than sine-wave patterns was investigated. Target selection is arbitrary. Isolated bar targets of variable width probably represent a close approximation to conditions likely to occur when scanning agricultural features.

To compute the output of the video amplifier characteristic for a given terrain target, two approaches are possible. The target can be convolved with the optical system point spread function, aperture function, and impulse response of the electrical filter, or the equivalent operation of multiplication can be performed in frequency space. This second approach was judged simpler for present purposes.

The overshoot characteristic of Butterworth response is clearly indicated in figure 33. A modest amount of overshoot is sometimes desirable in a visual display since this tends to

make edges appear sharper than they are, but extreme values produce undesirable ghosts and represent erroneous results if accurate quantitative data is desired. On the other hand, the time delay and slight loss in amplitude for equal noise bandwidth of the Bessel response is also shown. The time delay does not appear to be a serious disadvantage since all signals, possibly including optically generated line sync pulses, will be delayed by an equal time. The presence of a time delay should not be detectable at the video output, providing the delays for all four channels are equal, thereby preserving spectral registration.

The Fourier transform of the ground target, in this case a rectangular bar (or pulse in time), was multiplied by the Fourier transform of a square aperture (figure 32), and also by the frequency response of the selected filter (with appropriate phase shift). This yielded the frequency spectrum of the resulting video channel output. The inverse transform was then taken to produce the shape of the output pulse as a function of ground distance in relation to the size of one resolution element. Figures 34, 35, 36, and 37 are plots of these results for isolated bars of widths 0.5, 1, 2, and 4 resolution elements. Plots for Butterworth corner frequencies equivalent to 1.0, 0.75, 0.50, and 0.25 cycles per resolution element and Bessel corner frequencies equivalent to 1.0, 0.75, 0.50, and 0.25 cycles per resolution element and Bessel corner frequencies yielding equal noise bandwidths are shown and are indicated by the number identifying each curve. In each case, the triangular or trapezoidal pulse represents the ideal output if infinite bandwidth were available.

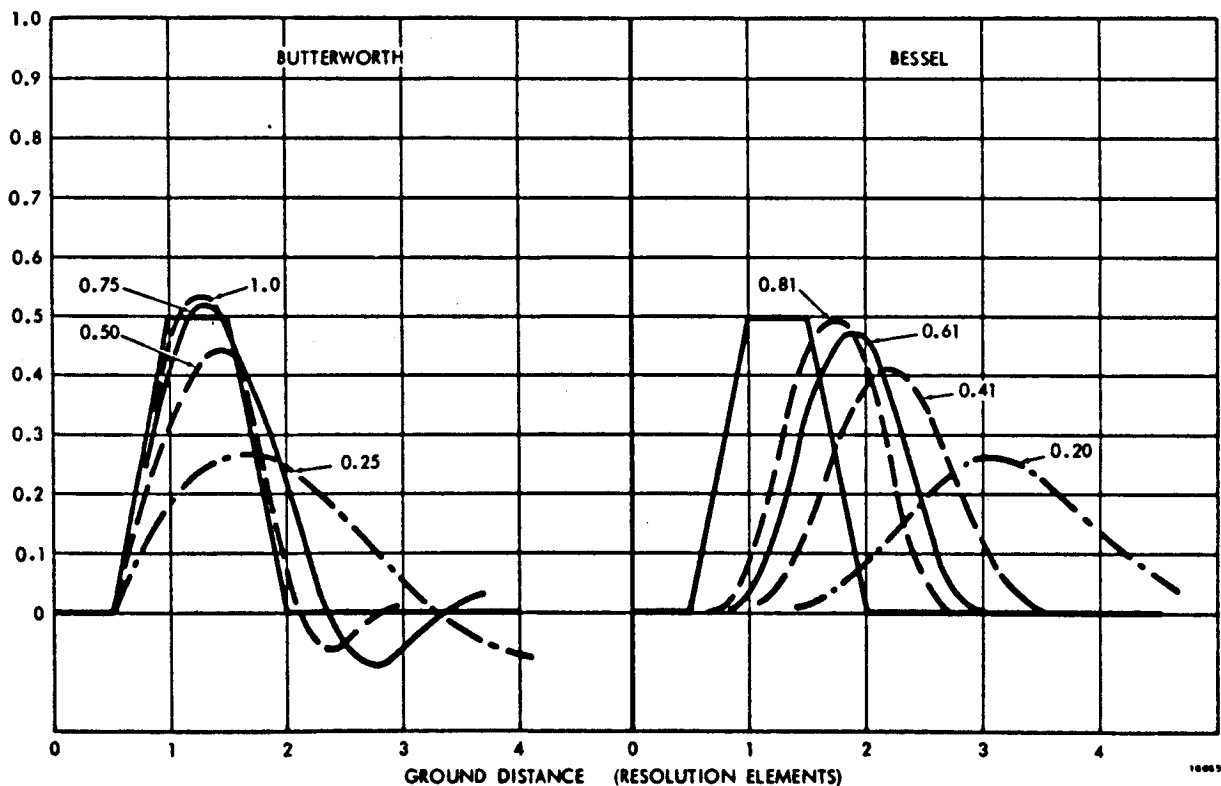


Figure 34. Video Output for Isolated Bar Width, 0.5 Resolution Element.

Figure 38 summarizes the results of figures 34 through 37 by showing the peak output of each type of filter as a function of bandwidth and bar width.

Selection of Optimum Data Channel Frequency Response. -Referring to the plots of figures 34 through 37, it is clear that to obtain an accurate video representation of a terrain

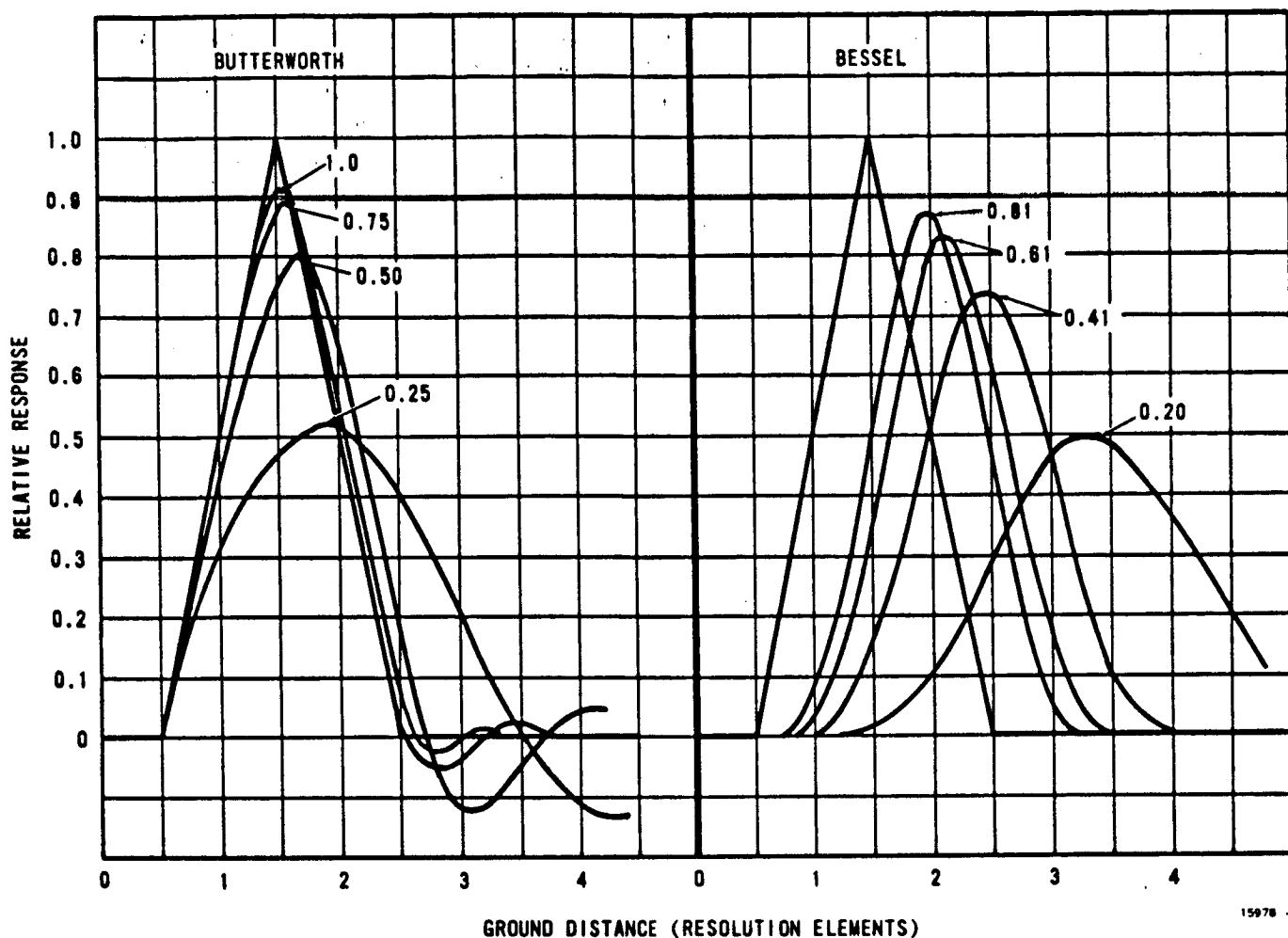


Figure 35. Video Output for Isolated Bar Width, 1 Resolution Element.

feature, a very wide bandwidth is used. This would be true were it not for noise which increases as the bandwidth increases and tends to make the video output a less accurate rather than more accurate representation of the true signal. In fact, noise would appear to be a more serious degrader of image quality than lack of high frequency response, since it obscures all signals equally whereas the latter only affects small or transient objects.

As an example of a possible criterion for selecting the video bandwidth, consider the problem of detecting an isolated bar equal in width to 1 resolution element with the highest possible accuracy and interpret accuracy to mean (S/N). As the bandwidth is increased from some low value, S/N is increased due to the higher signal amplitude. Noise is also increasing as the square-root of the bandwidth and eventually will cause a reduction in S/N even though the signal amplitude is still increasing.

To quantify these ideas, a relative S/N can be calculated using the results from figure 35 or 38 and assuming white noise. Referring to figure 39, the peak signal amplitude is shown to increase with bandwidth in agreement with figure 38. Assuming a relative value of noise amplitude equal to 0.5 at a bandwidth of 0.25 cycles per resolution element and increasing as the square-root of bandwidth, the curve shown results. Note that the noise amplitude increases more slowly than the signal amplitude at first, but soon increases much more rapidly. The product of these two curves is a plot of relative S/N. The S/N for Butterworth and Bessel filter characteristics is a maximum for an equivalent Butterworth bandwidth of 0.4

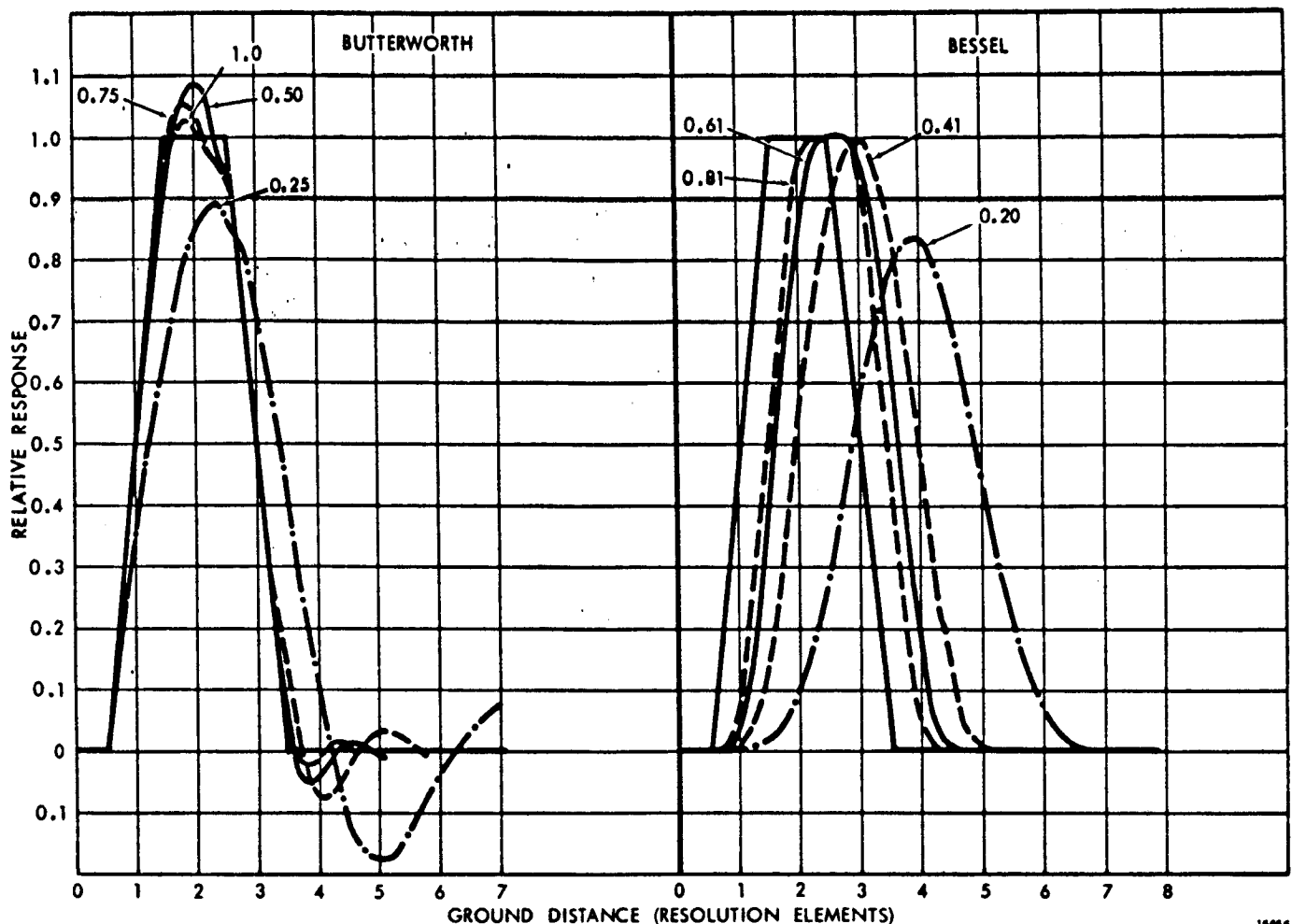


Figure 36. Video Output for Isolated Bar Width, 2 Resolution Elements.

to 0.5 cycles per resolution element. This is probably a much lower bandwidth than would have been selected on the basis of signal amplitude only, and points out the importance of considering loss in accuracy due to noise and decreased signal amplitude.

These results are applicable to a Bessel type response, but using such a low bandwidth with a Butterworth response would lead to large errors due to the overshoot mentioned previously. The overshoot of the Butterworth filter can be reduced by increasing the bandwidth as shown in figure 37, but again this will increase the error due to noise. Figure 40 shows the relative rates at which overshoot decreases and noise increases for a 5-pole Butterworth response, indicating the large penalty in S/N to be paid for a very small reduction in overshoot.

From the previous discussion, it is apparent that neither the pure Butterworth nor pure Bessel response is completely satisfactory and that a compromise between the characteristics of each would be desirable. A class of realizable response functions possessing characteristics intermediate between the two pure types, the transitional Butterworth-Thompson family, is obtainable by linear interpolation of pole position between the two original response functions. Such a compromise, with pole position chosen to yield a noise bandwidth equivalent to a Butterworth 3 db frequency of 0.6 cycles per resolution element and a damped overshoot of 1 to 2 percent, would appear to be ideal for the present application. A bandwidth

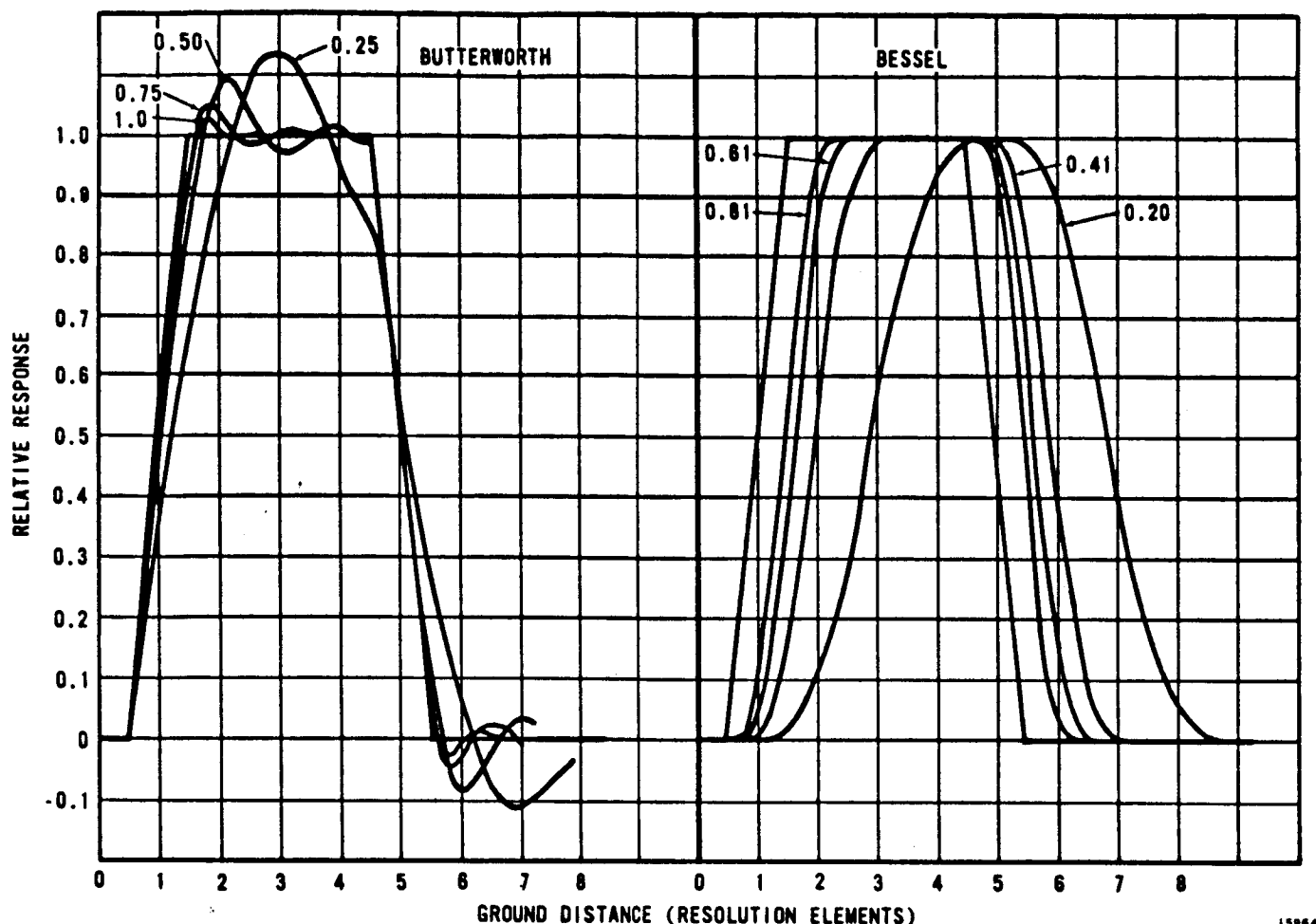


Figure 37. Video Output for Isolated Bar Width, 4 Resolution Elements.

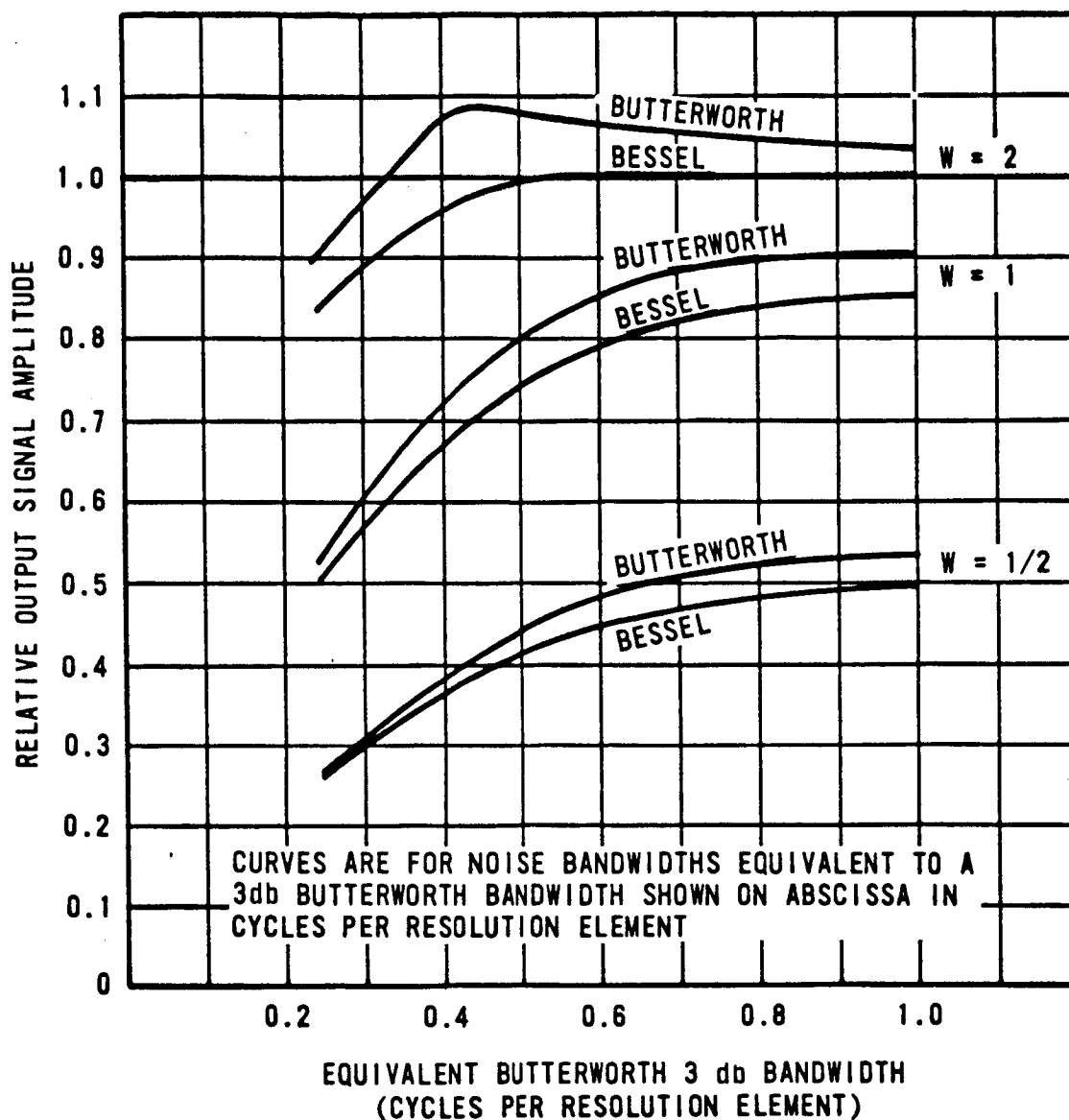
slightly above that yielding optimum S/N can be chosen to improve edge response without significantly degrading S/N because of the relatively broad optimum.

Data Channel Noise

Total data channel noise consists of that due to the detector, thermal noise in the detector load, amplifier noise, noise due to the random arrival of photons (photon noise), and quantization noise introduced by analog-to-digital (A/D) conversion of the final video signal. All other noise sources should be negligible.

Video Channel Noise. -The mean square noise current due to the detector alone appearing at the detector output can be assumed to be due to detector dark leakage current for detector types suitable for the visible and near infrared spectral region. It is given by:

$$(i_d)^2 = (3.2) 10^{-19} (i_{dc}) (GAIN)^2 (BWN) (ENF)^2$$



15973

Figure 38. Peak Video Output.

where,

i_d = dark current

i_{dc} = primary or cathode dc dark current

GAIN = detector gain prior to output

BWN = noise bandwidth

ENF = an excess noise factor due to the detector gain mechanism.

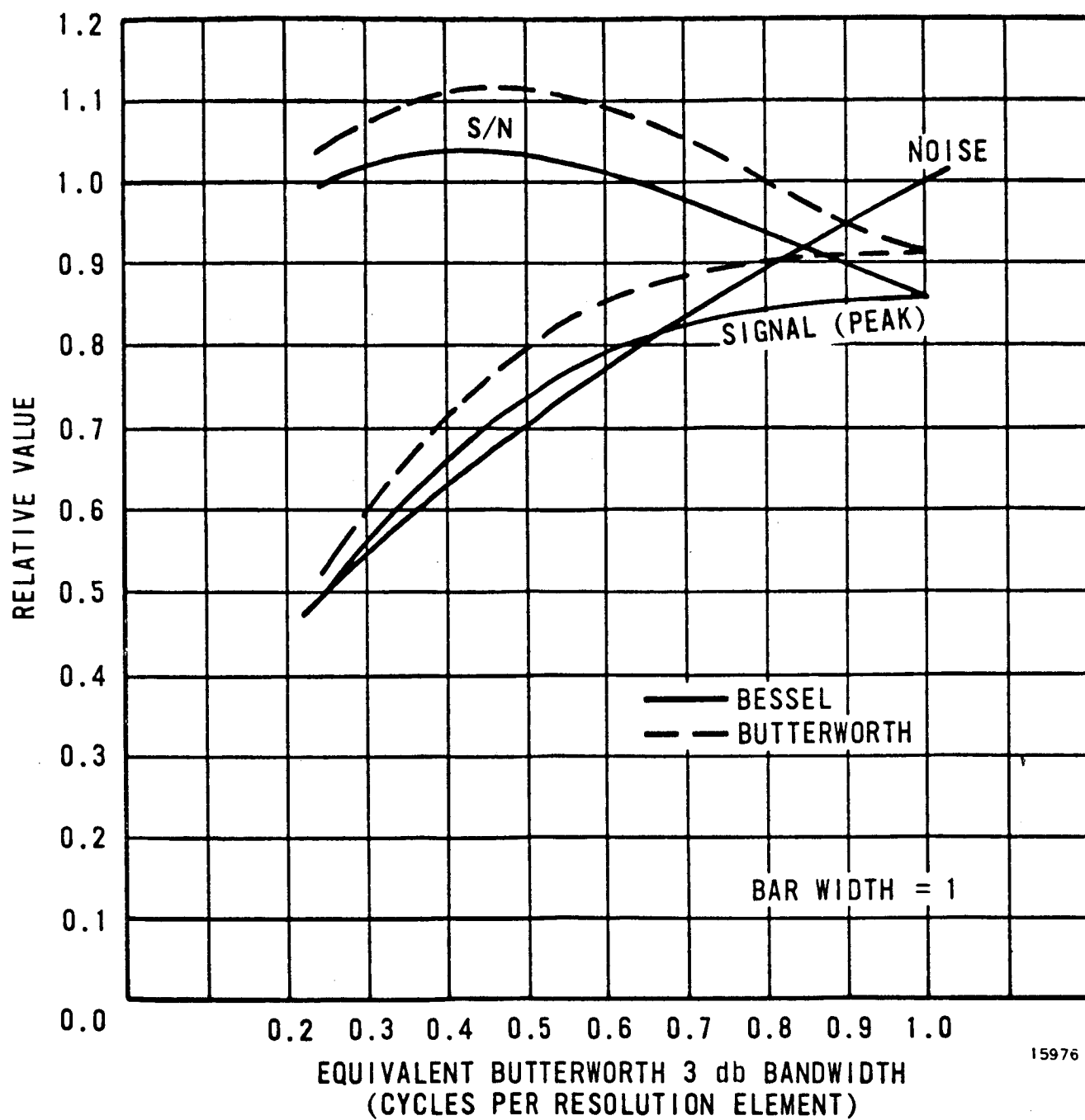


Figure 39. Tradeoff of Signal Amplitude for S/N.

For calculating thermal and amplifier noise (figure 41), the following equivalent noise circuit is assumed:

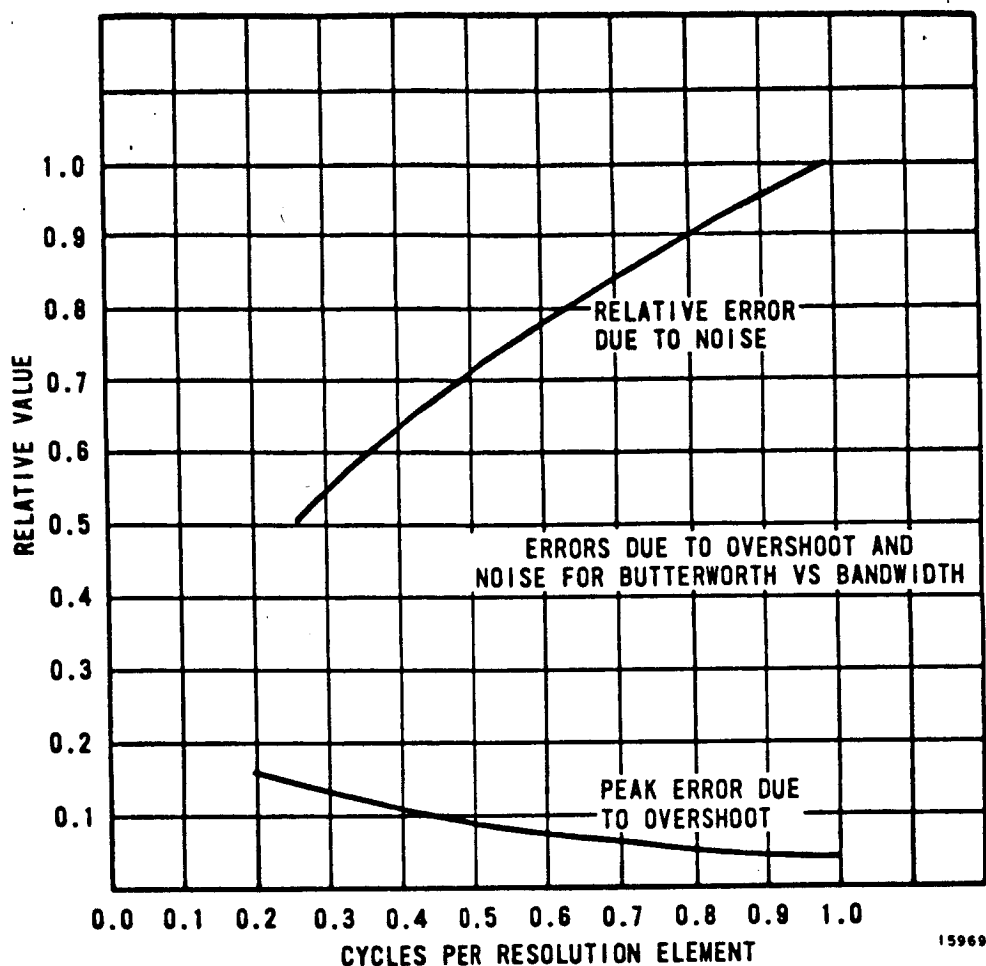


Figure 40. Tradeoff of Errors Due to Overshoot and Noise.

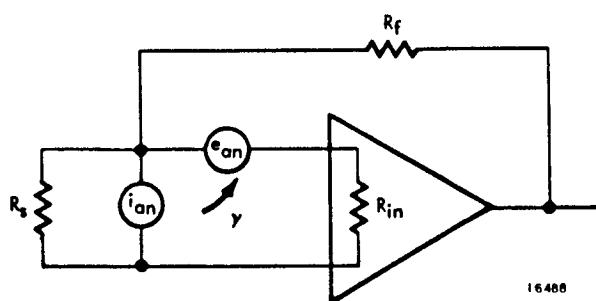


Figure 41. Equivalent Noise Circuit for Calculation of Thermal and Amplifier Noise.

R_s represents the source resistance of the detector, and load resistance if one is used. R_f and R_{in} represent the feedback resistance and amplifier input resistance. Amplifier noise is represented by current noise generator, i_{an} , and voltage noise generator, e_{an} , with a correlation between them of γ . Using this model, the mean square thermal noise current referred to the detector output is:

$$\overline{(i_t)^2} = (1.63) 10^{-20} (\text{BWN}) \left(\frac{1}{R_f} + \frac{1}{R_s} \right)$$

and the mean square noise current due to the amplifier is:

$$\overline{(i_A)^2} = \left\{ i_{an}^2 + \left(\frac{e_{an}}{R_t} \right)^2 + 2\gamma \left(\frac{i_{an} e_{an}}{R_t} \right) \right\} (BWN)$$

where,

R_t = parallel resistance of R_s , R_f , and R_{in} .

These three noise sources (detector, thermal, and amplifier) are independent of the presence of a signal and represent fixed system noise. In addition to this fixed noise, an additional noise appears at the detector output in the presence of a signal, due to the random arrival rates of photons. The mean square noise current at the detector output due to this source is:

$$\overline{(i_p)^2} = (3.2) 10^{-19} (i_k) (GAIN)^2 (BWN) (ENF)^2$$

where,

i_k = cathode photocurrent = P (SENS)

and,

P = radiant power imaged on detector (watts)

SENS = sensitivity of detector cathode (amps per watt) = $\frac{Q_\epsilon \lambda}{124}$

and,

Q_ϵ = quantum efficiency prior to gain (percent)

λ = wavelength of radiation (microns).

The total rms noise current at the detector output due to all these sources acting at random is then:

$$i_{rms} = \sqrt{(i_d)^2 + (i_t)^2 + (i_a)^2 + (i_p)^2}$$

The input radiant power equivalent to this noise current, ENI, is:

$$ENI = \frac{i_{rms}}{(SENS) (GAIN)} \text{ rms watts .}$$

Note that for a given set of detector and circuit parameters, the total noise depends only on the total radiant power imaged on the detector and does not depend on the origin of the radiant power, i. e., it does not depend on whether the radiant power was due to backscatter or terrain reflectance or any combination of these factors. For this reason, it is possible to calculate noise and apparent S/N performance separately from any consideration of atmospheric and scene characteristics provided that the general range of radiant power levels is known. Apparent S/N means the total radiant input power divided by the total equivalent noise input without removing that portion of the total radiant power due to terrain reflectance. To calculate NE Δ R, such a separation is necessary and requires a knowledge of, or assumptions about, atmospheric conditions and terrain reflectance. For present purposes which are directed toward design criteria, it is convenient to handle noise performance separately from considerations of scene parameters, since a number of useful conclusions can be drawn from noise levels alone without confusing the issue with solar zenith angles and other scene characteristics.

Figures 42 through 45 are plots of total equivalent noise input versus total radiant power imaged on the detector for the four spectral bands of interest, and for detectors appropriate to each band. Results for noise bandwidths equivalent to Butterworth 3 db frequencies of 112 kHz, 200 kHz, and 300 kHz are shown. Using a log-log presentation, photon noise limited performance is indicated by a straight line sloping up to the right with a slope of one-half. Conversely, system noise limited performance is indicated by a horizontal straight line showing that noise level is independent of radiant power level. In each of these plots, the solid lines represent the total noise using the noise parameters for an Analog Devices 120 operational amplifier, selected as being representative of currently available high speed, low noise designs. Also shown, as a dashed line, are the results assuming the noise parameters typical of an Analog Devices 165 operational amplifier. This is an economy grade general purpose amplifier and is included to show the relative sensitivity of total noise to amplifier quality. PMT's, because of their high gain, are relatively insensitive to amplifier noise degradation.

Also shown in the figures are sloping lines indicating apparent S/N's. The intersection of the total noise curves with the S/N = 1 line indicates the minimum detectable radiant power. In bands 1 and 2, radiant power levels above 10^{-10} watts are expected so that apparent S/N in the 5 to 50 range will result. In band 3, lower power levels and lower S/N but still about 10:1 for typical signal levels, are expected. In band 4, because of the poor performance of available detectors, S/N performance is lower than in the other bands.

Referring to figure 45 for band 4 performance, note the departure of the uncooled S-1 photocathode line from the photon noise limited performance indicated for the cooled detector. The line for a cathode dark current of $(3) 10^{-13}$ amps, which is typical of a relatively large area S-1 photocathode at room temperature, exhibits degraded low signal performance due to the high dark current. This indicates the desirability of reducing the dark current for this detector either by using a small area photocathode or by cooling, or both. Data from RCA⁽⁵⁾ indicate that dark current can be reduced by about two orders of magnitude by cooling to -20° C so that extreme cooling is not required to achieve substantial improvement in S/N. Because of the relatively poor performance of the S-1 photocathode in band 4, other types of detectors should be investigated.

Figure 45 shows the estimated performances of two of the solid-state detectors studied. The two detectors in figure 45 are an ordinary Schottky barrier silicon diode without gain and a prototype GE avalanche gain silicon detector. Both detectors are clearly system noise limited but for different reasons. The major sources of noise in the gainless diode are thermal noise in the load resistance and amplifier noise, since the dark current is very low in this device. There is not much opportunity for substantial reduction of either of these noise

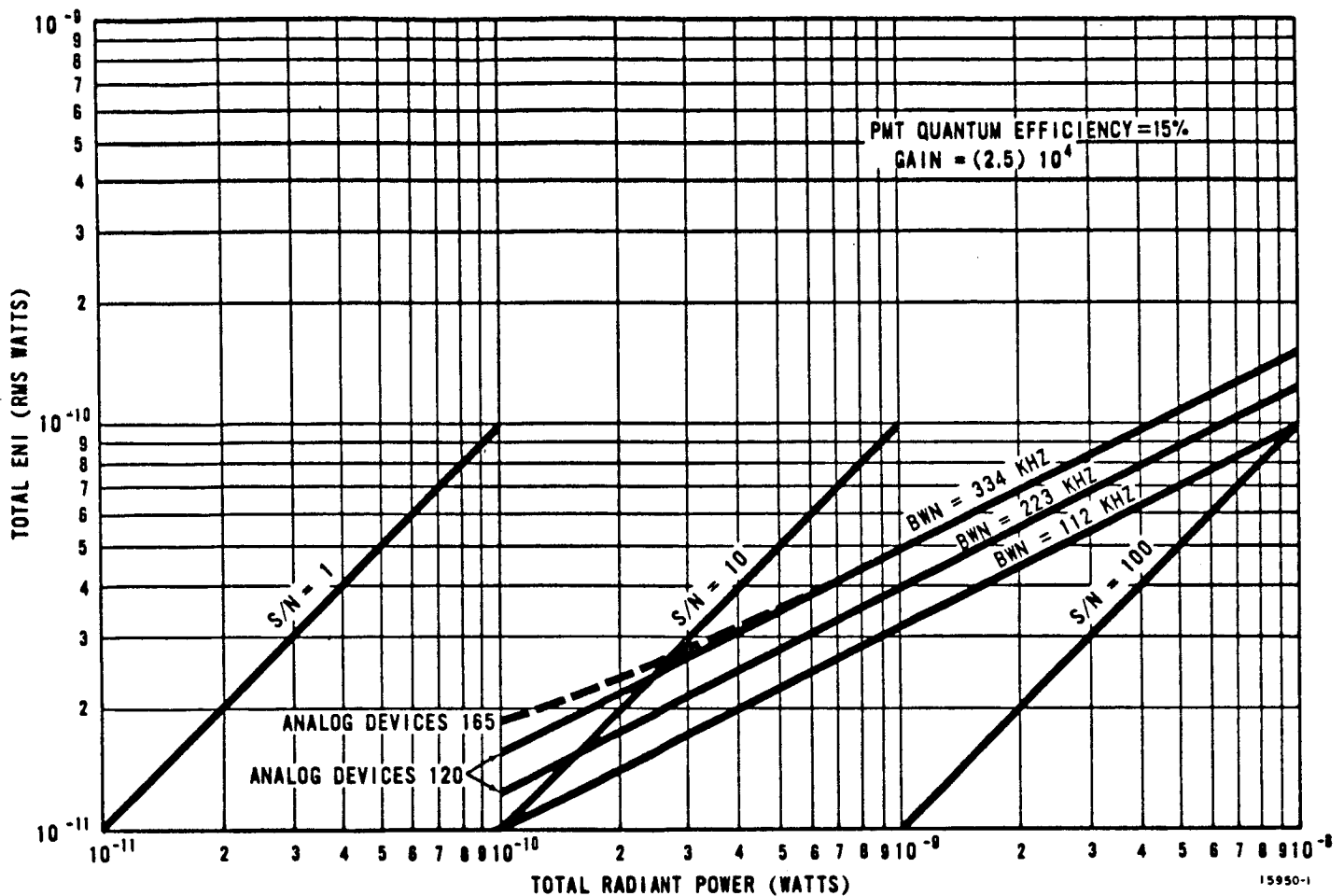


Figure 42. Noise Input vs. Radiant Power, Band 1.

sources except by reducing the electrical bandwidth sufficient to permit higher impedance and lower thermal noise levels. Gainless diodes do not appear to offer improved performance over the S-1 cathode for the range of radiant power levels of interest at the current electrical bandwidth for one detector per channel. The major source of noise for the GE avalanche gain detector is due to the large dark current, which was 5 microamps in the one detector tested. There is considerable hope for reduced dark current and higher gains for this type of device so that improved performance can be expected, but the extent of that improvement cannot be predicted yet. Noteworthy is the dashed line indicating the performance of this detector with the relatively noisy model 165 operational amplifier showing that because of the low gain available, this device is considerably more sensitive to amplifier design than a PMT. It is also evident that if the noise level of this detector cannot be reduced by at least a factor of four, the PMT will be superior over part of the range of power levels expected and the avalanche gain silicon device will be superior over the remainder. A judgement may then be necessary as to the relative importance and occurrence of high and low signal levels.

Another useful feature of the graphs shown in the figures is that an estimate of resolvable signal levels can be made. For example, refer to figure 40 for $f = 300$ kHz. At a radiant power level of 10^{-10} watts, the equivalent rms noise is about $(0.05) 10^{-9}$ watts so that the next resolvable signal level is at about $(1.05) 10^{-9}$ watts.

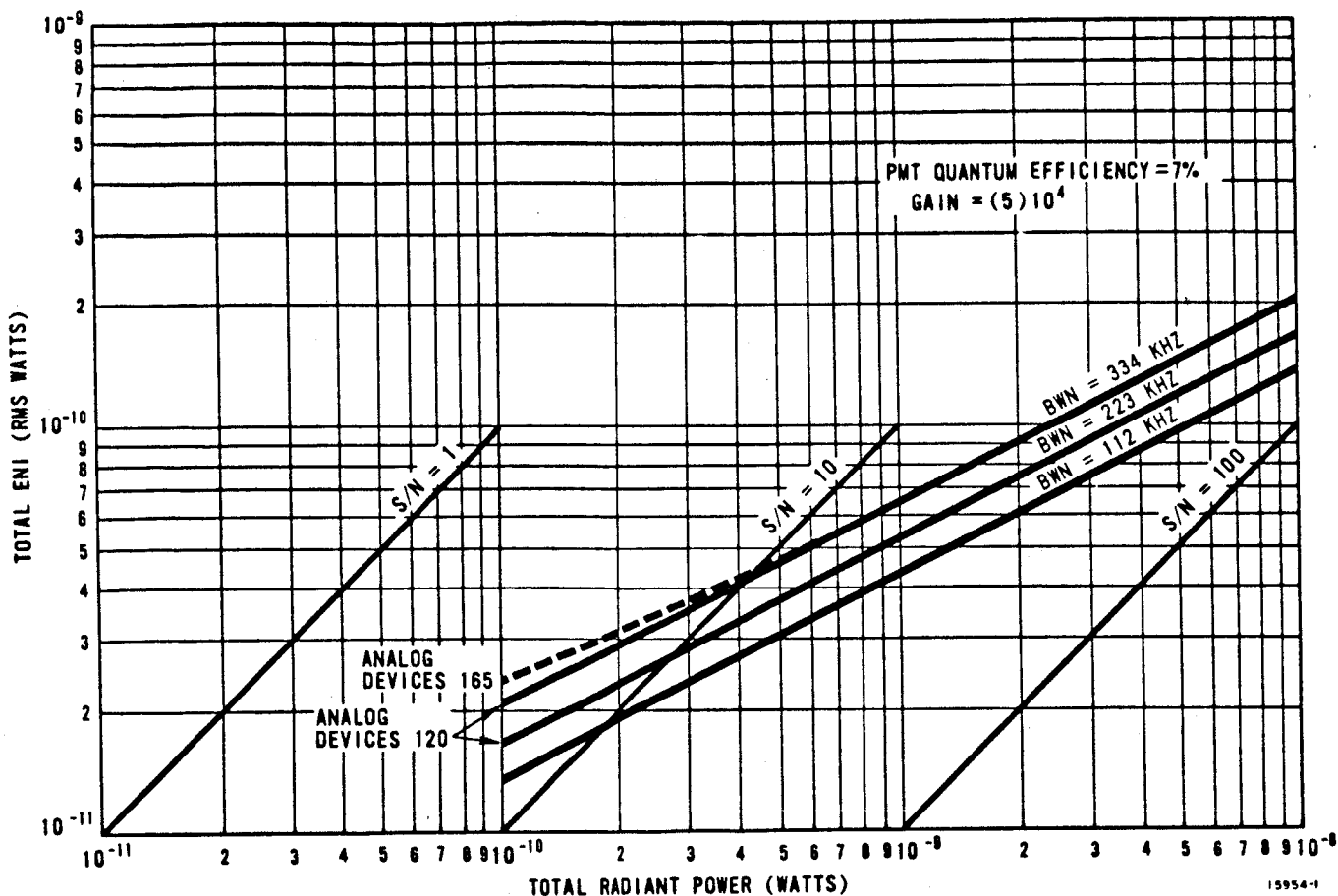


Figure 43. Noise Input vs. Radiant Power, Band 2.

Quantization Noise. -If an analog signal with an rms noise level ϵ , is sampled and quantized using a quantization step size q , the rms noise or error in the resulting quantized signal will be larger than ϵ . This added error arises from the fact that regardless of what the true signal amplitude is, if it lies anywhere within q , it will be reported to be exactly in the middle of the quantization step. If it is equally likely that the true signal lies anywhere within the quantization interval (uniform rectangular error distribution). Then the rms quantization error will be $\pm q/\sqrt{12}$. Regardless of the error distribution, the rms quantization error must be less than $\pm q/2$. Now assuming that the signal error and quantization error are independent, and adding in an rms fashion results in:

$$\epsilon_{\text{total}} = \sqrt{\epsilon^2 + \frac{q^2}{4}}$$

for the case of maximum quantization error.

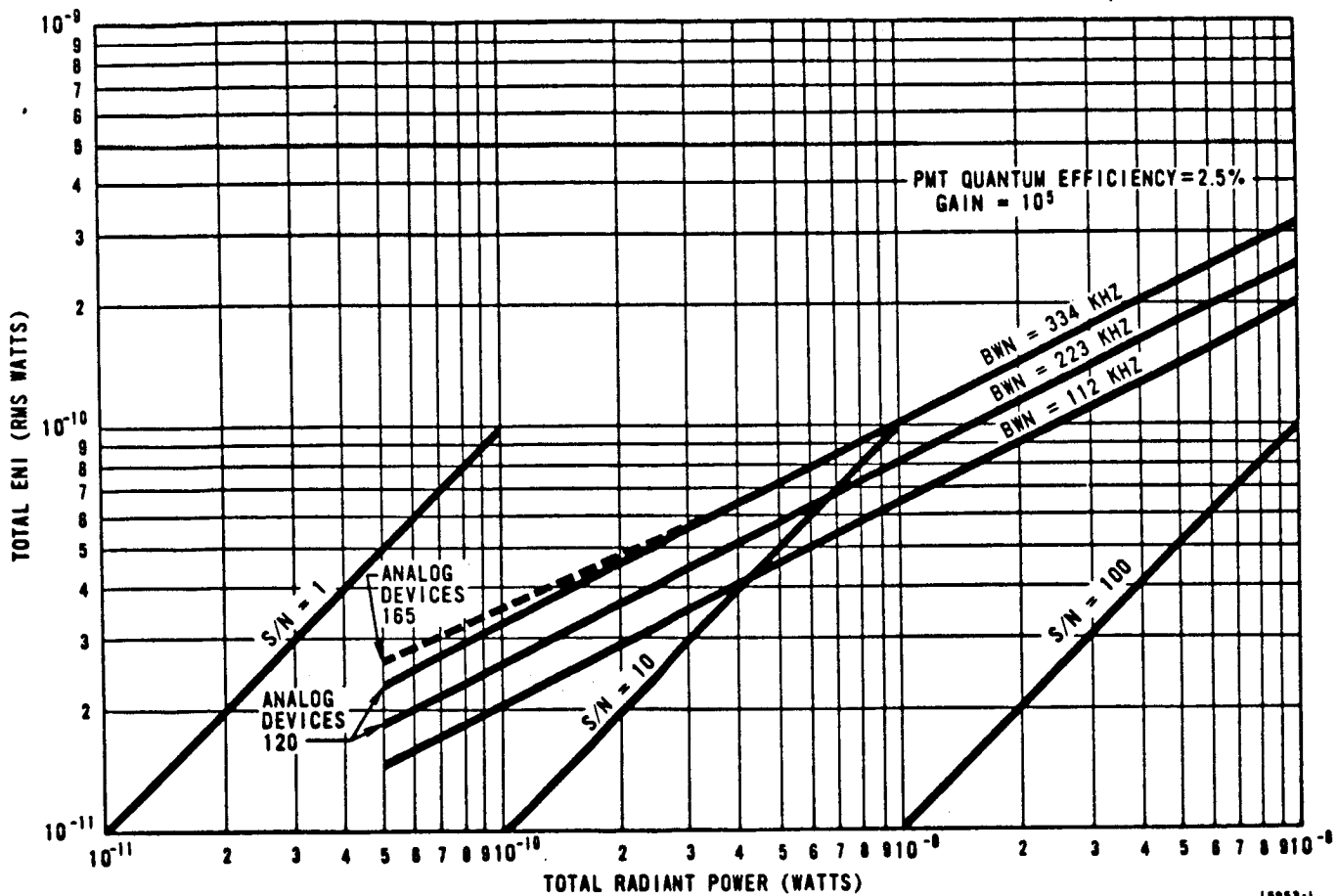


Figure 44. Noise Input vs. Radiant Power, Band 3.

If it is desired that the quantization error should not increase the total error level by more than a fraction, ρ , then:

$$\sqrt{\epsilon^2 + \frac{q^2}{2}} = \epsilon_{\text{total}} \leq (1 + \rho) \epsilon$$

$$q \leq 2 \rho^2 + 2\rho\epsilon$$

This equation is plotted in figure 46 for added error in the range of 1 to 10 percent. Also shown are similar results assuming a uniform error distribution. These graphs show that analog-to-digital conversion does not degrade overall S/N by more than 5 percent if a quantization step size in the range 0.6 to 1.0 times the rms analog noise level is used. This result will be used later in the paragraph on Multiplexing - Demultiplexing.

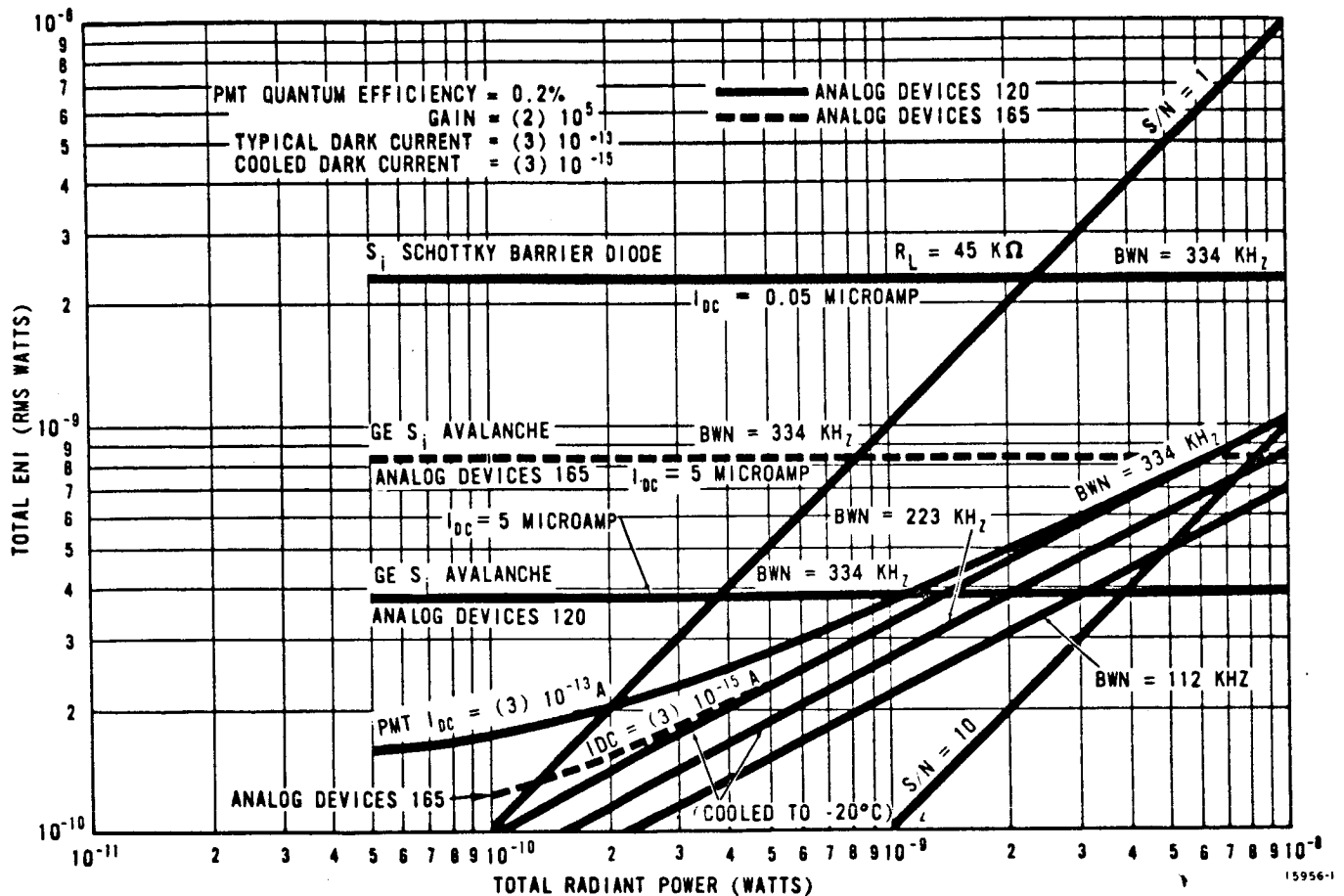


Figure 45. Noise Input vs. Radiant Power, Band 4.

Detector Evaluation and Selection

One of the primary tasks in detector evaluation concerned the selection of alternate detectors to the S-1 photocathode for operation in band 4. As pointed out in the previous paragraph on noise calculations, there is little probability of reducing thermal and amplifier noise to levels sufficiently small to permit operation of a detector in this band without an internal gain mechanism. For this reason, interest was centered on silicon detectors with avalanche gain. Preliminary evaluations of the G&G AV-102 and a prototype avalanche silicon detector from GE were performed. The following paragraphs describe results obtained.

General Electric G-1 Avalanche Diode. -Figure 47 is a copy of the data sheet supplied by GE. This represents essentially all the information available pertaining to the anticipated use of the detector, since the device has been used mainly as a nuclear particle detector or, in the pulse mode, in conjunction with GaAs emitting diodes.

The first parameter of interest was spectral response, since it had been indicated that this was not typical of silicon detectors for short wavelengths. Figure 48 is a plot of spectral sensitivity relative to an Eppley thermopile. Because of the low responsivity of the thermopile, an excessively wide slit width had to be used on the monochromator, which prevented

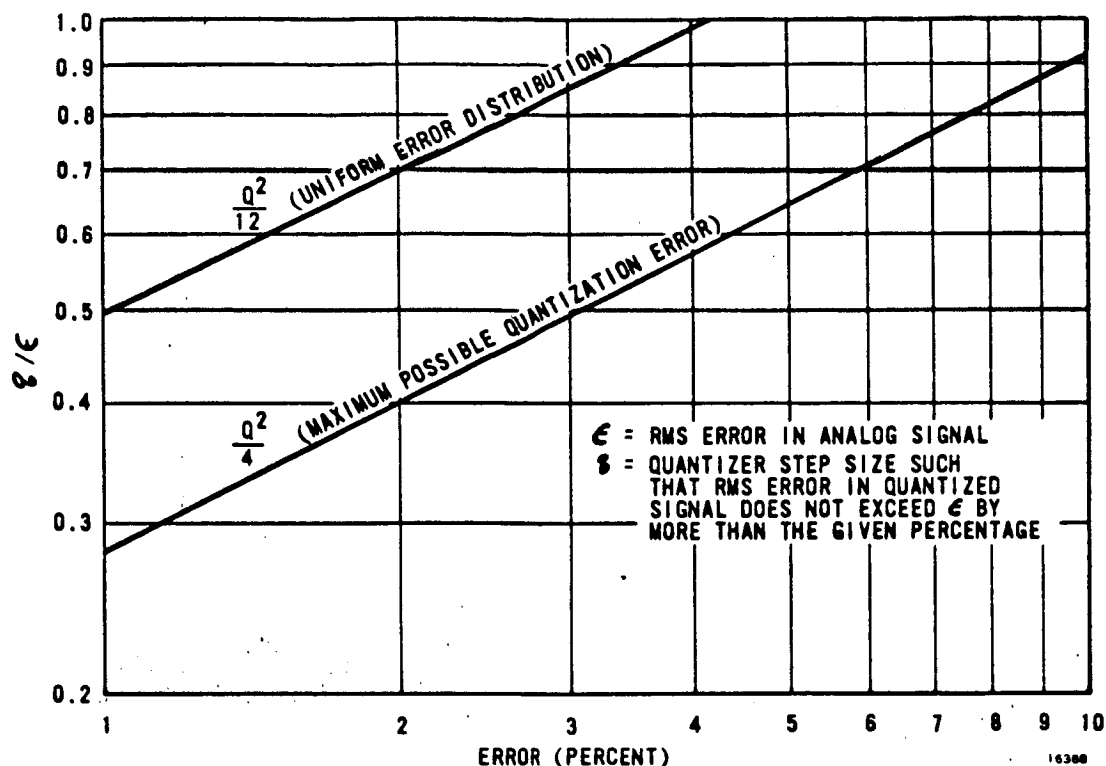
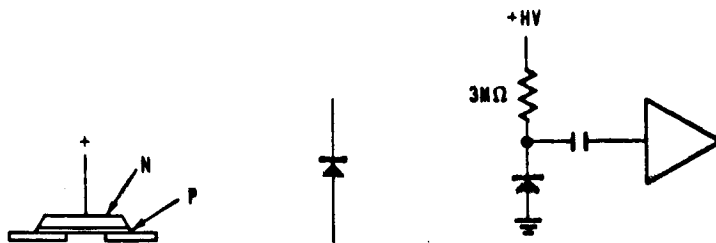


Figure 46. Additional Error Due to Quantization.

high spectral resolution. Response is definitely peaked near 0.9 micron and falls off at the visible end much more rapidly than an ordinary silicon detector. This is due to the presence of a thin layer of silicon at the detector surface which strongly absorbs short wavelength photons. The manufacturer indicates that response may be extended down to 0.7 micron by etching this layer thinner. Comparison of sensitivity at 0.9 micron with that of an ordinary silicon detector indicated approximately equal quantum efficiencies when the avalanche detector was operated at a gain of 1. Responsivity of the detector over band 4 should be about 0.2 amp per watt or better.

The dc dark current was measured as a function of applied voltage and is plotted in figure 49. The dark current measured exceeded that shown on the data sheet, but at the time this was attributed to temperature differences. More about this point later. Note that the dark current increases only by a factor of about 4 as the bias is increased from 500 to 2200 volts. Because of the structure of this device, only part of the dark current is expected to increase more slowly than signal as gain is increased, an important factor in improving S/N performance.

To check this, the device gain was measured as a function of bias voltage by exposing the detector to a constant level of chopped radiant energy and measuring peak-to-peak output voltage versus bias. The results are shown in figure 50 for three values of illumination. The exact illumination values are unknown, but were chosen to produce signal currents in the range of those expected in practice. The plateau between 400 and 700 volts is at a device gain of 1. The avalanche or breakdown point was judged to occur when the oscilloscope display began to jump around noticeably although it is most probable that the noise level had been building up slowly to that point.



DETECTOR NO.: 6-1
 DETECTOR AVALANCHE VOLTAGE: + 2182 VDC
 DETECTOR LEAKAGE CURRENT: < 3 MICROAMPS
 DETECTOR CAPACITANCE: \approx 5 PICOFARADS
 APERTURE SIZE: \approx 2 MILLIMETERS DIAMETER
 GAIN (AVERAGE): 300 AT 2150 VDC WITH 0.9 μ A SOURCE

NOTES:

1. The detector is free of plasma noise events when operated below the rated avalanche voltage.
2. Temperature coefficient of avalanche is approximately 2.16 v./ $^{\circ}$ C.
3. The depletion region is formed at 500V. Here the gain is unity.
4. The gain increases exponentially as a function of voltage with the gain highest when operated close to avalanche.

16422

Figure 47. Silicon Avalanche Detector Data Sheet.

Maximum exhibited gain was 150, a factor of 2 less than claimed. This may be due to differences in measurement technique, since at GE gain was measured in pulse mode using nanosecond pulses as opposed to the nearly dc measurements reported here. In any case, a gain of 100 is probably sufficient for present purposes.

Signal current increases about two orders of magnitude as bias is increased from 500 to 2200 volts, which is considerably faster than dark current increase.

Detector linearity was measured and a maximum deviation of 10 percent was noted over a range of 1000:1 in intensity. This could easily be due to measurement technique but does not represent a serious error.

The last parameter of importance to detector evaluation is the excess noise factor associated with the gain mechanism. During the month it took to assemble equipment to run this test, the detector was unused. When it was used again, the dark current had increased to about 20 microamps, indicating some deterioration had occurred. The detector was returned to GE for examination and it was found that the surface protective resin had crept under one contact.

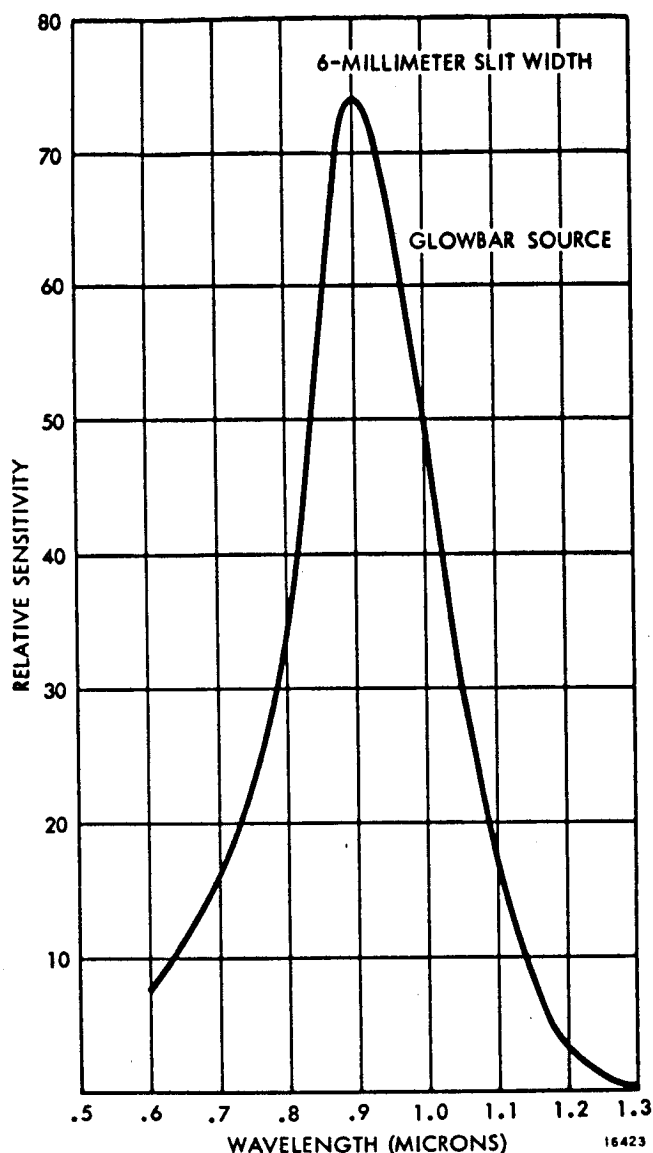


Figure 48. Spectral Sensitivity of GE Detector G1 Relative to Eppley Thermopile.

Several important conclusions can be reached on the basis of data collected so far:

a. As indicated in figure 50, gain is very sensitive to bias voltage at an operating point near a gain of 100. In fact, the gain changes about 70 percent for a 1 percent change in supply voltage. For comparison, a typical PMT, which is noted for sensitivity to voltage variations, changes gain by only about 10 percent for a 1 percent change in supply voltage. Power supply regulation requirements are seven to eight times more stringent for this detector than for a PMT.

b. Since breakdown voltage changes about 2 volts per^o C, a temperature coefficient change of gain of about 7 percent per^o C is to be expected.

c. Output dark current will apparently be in the neighborhood of 1 microamp. Signal currents, due to expected radiant power levels, are in the range 10^{-8} - 10^{-7} amps, between one and two orders of magnitude below the dark current level. Unless some method of suppressing dark current or increasing gain is found, ac coupling, to block the large dark current, will probably be required. Cooling may be some help, although the amount of cooling required to reduce dark current by two orders of magnitude may be excessive.

d. Table 9 is part of a computer print-out of estimated noise contributions for the detector tested. An excess noise factor of 1.2 was used in lieu of any measured data since this is typical of a PMT. If the excess noise factor is actually higher than this, the noise due to dark current will be even larger than shown. It is already the dominant noise source, exceeding both thermal and amplifier noise by over an order of magnitude. The suitability of this detector, depends mainly on reduction of dark current and associated noise.

e. Primary matters for future action are measurements of excess noise factor and investigation of methods to reduce dark current.

EG & G AV-102 Avalanche Diode. -The primary advantage of the EG & G avalanche detector over the GE device is low operating bias voltage (11 volts compared to 2200 volts). As indicated by this difference in bias voltage, the two detectors are the results of completely different design philosophies and their performance is not similar.

The variation of dark current, dark current noise, and signal gain was measured as a function of bias voltage and the results plotted in figures 51, 52, and 53. In figures 51 and 53 the upper curve is an expanded representation of the avalanche region and should be read

**Table 9. Noise and Resolvable Levels for Analog Devices Type
180 Amplifier, Band 4.**

Parameters	Value	Unit
Wavelength	0.80 to 1.10	Microns
Detector	SI Avalanche	
Quantum Efficiency	30	Percent
Gain	100	
Noise Bandwidth	$(3.34) 10^5$	Hz
Cathode Dark Current	$(5) 10^{-8}$	Amp
Output Dark Current	$(5) 10^{-6}$	Amp
Dark Current Noise	$(8.77) 10^{-9}$	Rms Amp at Detector Output
Equivalent Input	$(3.82) 10^{-10}$	Rms Watt
Equivalent Load	9,800	Ohms
Thermal Noise	$(7.41) 10^{-10}$	Rms Amp at Detector Output
Equivalent Input	$(3.23) 10^{-11}$	Rms Watt
Amplifier Noise	$(8.51) 10^{-9}$	Rms Amp at Detector Output
Equivalent Input	$(3.70) 10^{-10}$	Rms Watt
Current Noise	$(4.62) 10^{-9}$	Rms Amp at Detector Output
Voltage Noise	$(5.89) 10^{-9}$	Rms Amp at Detector Output
Combined Noise	$(1.22) 10^{-8}$	Rms Amp at Detector Output
Equivalent Input	$(5.33) 10^{-10}$	Rms Watt

using the upper voltage scale. In this device, output dark current increases just as rapidly as signal current with gain increase. According to the vendor data sheet, the rms noise at the output due to a primary photo current, I_s , is given by:

$$i_{nrms} = \sqrt{2qI_s \Delta f} M^{(1 + x/2)}$$

where,

M = multiplication factor or gain

x = a factor ≈ 0.5 .

This indicates an excess noise factor of $\sqrt[4]{M}$. For a gain of 100, this is about a factor of 3 more rms output noise than an ideal noise free gain would produce. For reference, a PMT introduces only about 20 percent excess output noise due to the gain mechanism. This gain related excess noise is so large that, according to the equation, S/N should decrease as gain is increased.

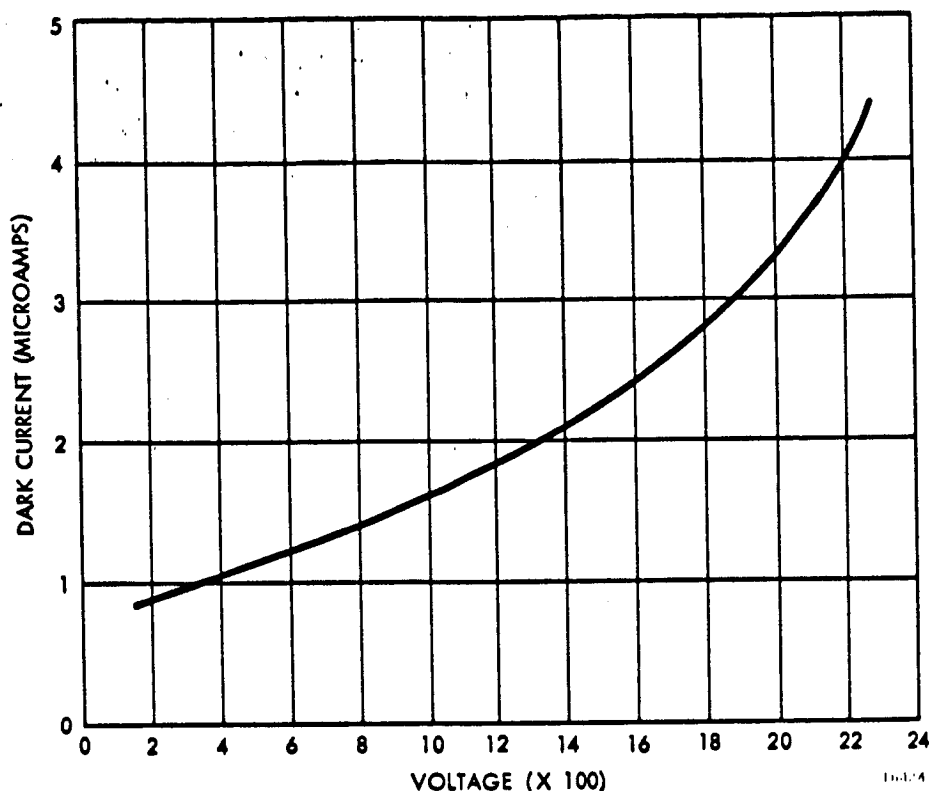


Figure 49. DC Dark Current vs. Bias Voltage for GE S1 Avalanche Detector G-1.

To confirm this conclusion, the S/N of the detector was measured. The signal used was a 500 Hz chopped radiant power sufficient to produce a signal of 50 microvolts peak-to-peak across a 10 kilohm load at a gain of 1. This corresponds roughly to the signal level expected for the highest radiant power to be experienced in band 4 when viewing cloud tops, and was high enough so that noise due to the signal current completely dominated amplifier and dark current noise. The measurement noise bandwidth was 135 kHz. Under these conditions, peak-to-peak signal to rms noise ratio of 11:1 was measured at a bias voltage of 5 volts, corresponding to a gain of 1. Bias voltage was increased to produce a peak-to-peak output of 25 millivolts (gain of 500), and S/N of 5:1 was measured. Under both conditions, detector shot noise was easily visible in the output. These measurements confirm the fact that S/N performance is degraded by increasing gain in this device. The best operating point occurs at a gain just high enough to overcome amplifier and thermal noise, but no higher. Setting detector noise at the output equal to thermal and amplifier noise:

$$\sqrt{2qI_0} M \left(1 + \frac{X}{2}\right) = 1.4 \sqrt{\frac{(1.63) 10^{-20}}{R}}$$

where,

I_0 = detector dark current = 0.25×10^{-9} amp

R = largest resistance which can be used before RC time constant limits bandwidth \approx 50 kilohms.

X = 0.5

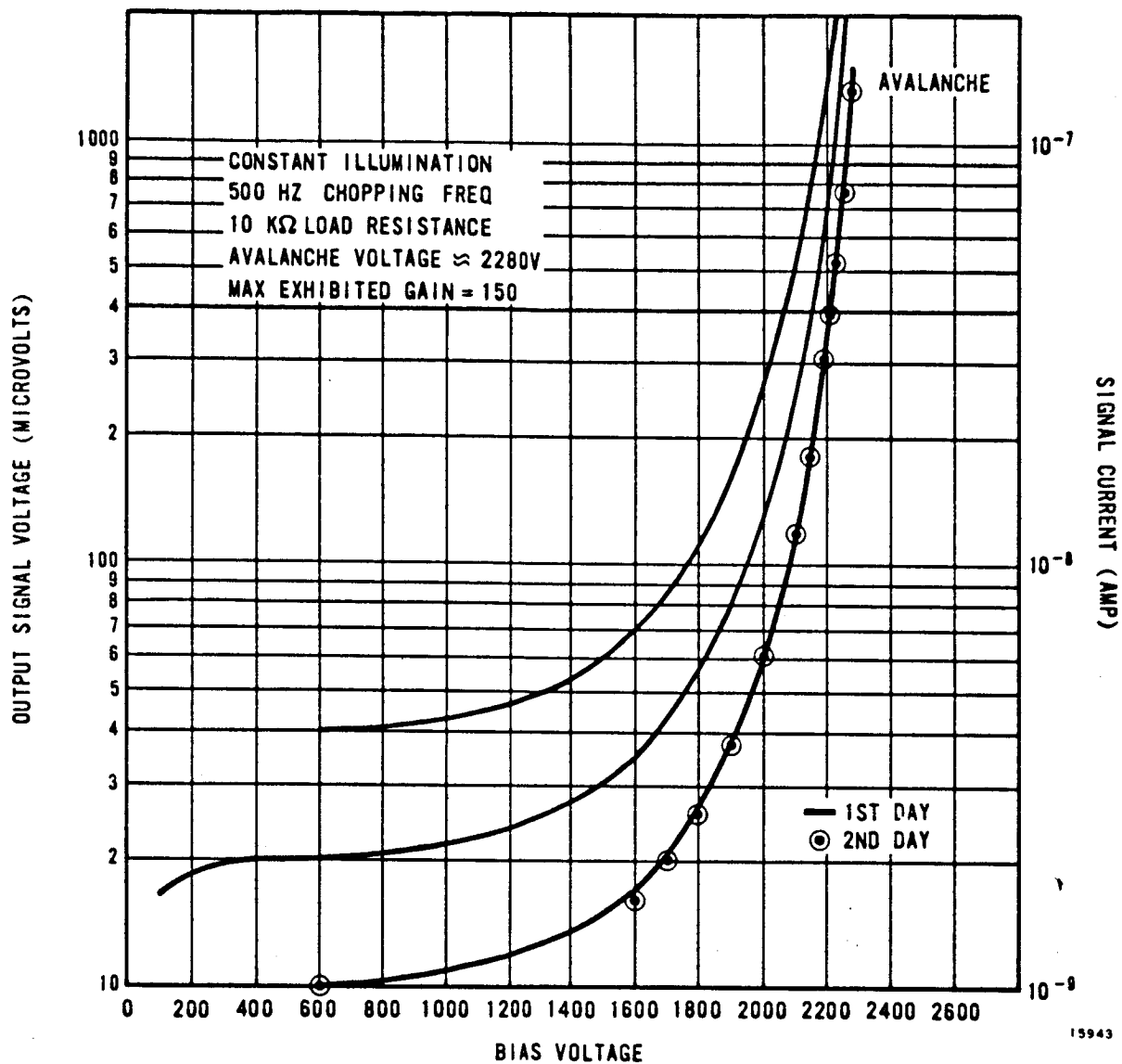


Figure 50. Signal Gain of GE Detector G-1.

the factor 1.4 on the right assumes an amplifier noise about equal to the thermal noise. Solving for M yields:

$$M_{\max} \approx 40.$$

Although this device is capable of gains exceeding 1000, in practice, a gain of over 50 will result in loss of S/N.

Returning to the measured values of $S/N = 11$ at $M = 1$, and $S/N = 5$ at $M = 500$, an increase in noise over signal by a factor of 2.2 is indicated. The value predicted by the term $\sqrt[4]{M}$ is about 4.7. It is believed that the difference by about a factor of 2 is not because the detector is only half as noisy at a gain of 500 as predicted by the equation, but because it is twice as noisy at a gain of 1. Even though the formula predicts no excess noise when $M = 1$, this

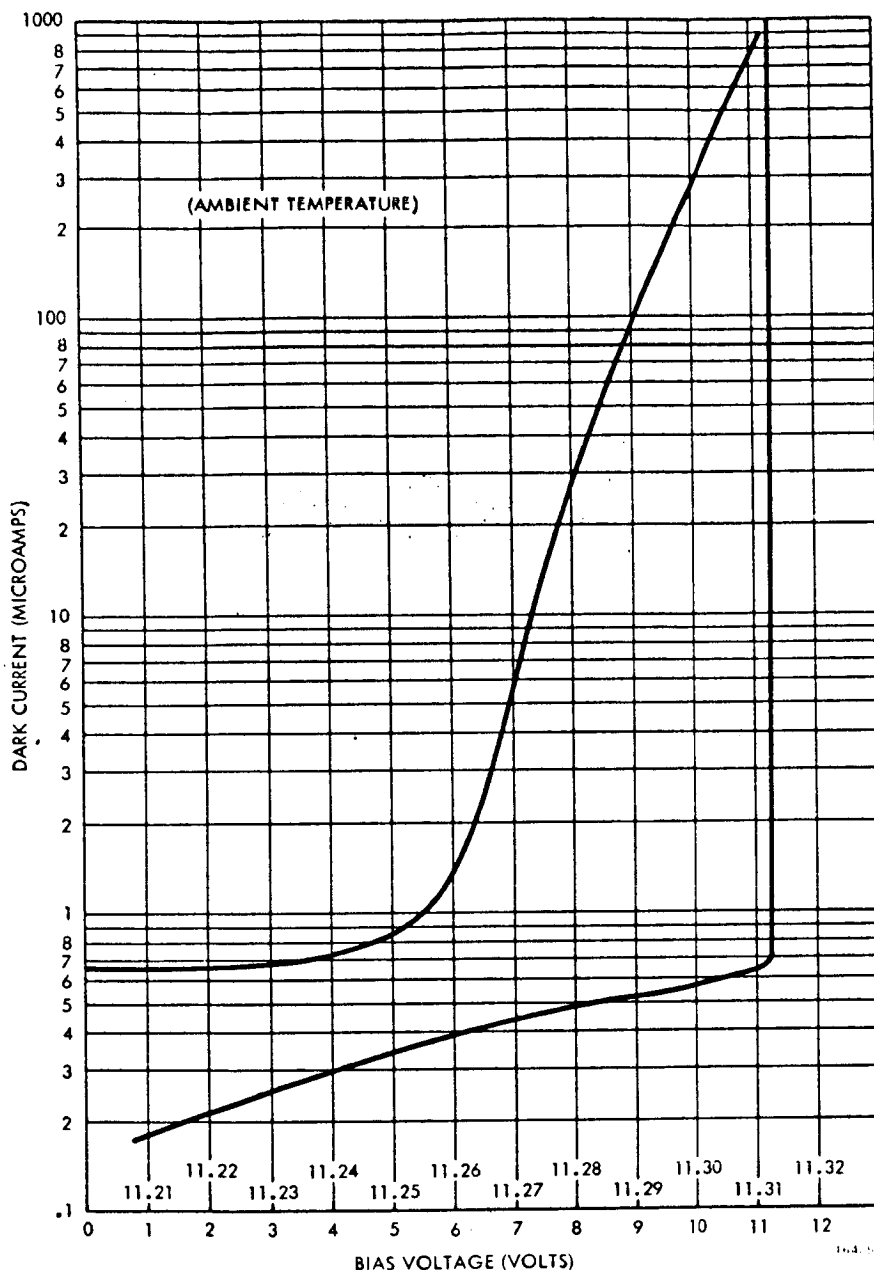


Figure 51. DC Dark Current vs. Bias Voltage for EG and G Detector AV-102.

was not observed to be true. The noise level increased visibly even at bias levels of a few volts, where the gain was still unity.

Based on a limited amount of testing, several conclusions can be drawn:

a. The extremely small detector area (0.01 inch diameter) places severe constraints on the focusing and alignment of the energy from the spectrometer.

b. As indicated in figure 53, the gain is extremely sensitive to bias voltage. A gain change of about 1500 percent per 1 percent change in voltage is indicated. This is some 200 times more sensitive than a PMT or over 20 times more than the GE detector. A voltage stability of about ± 0.004 percent should be required for ± 5 percent gain stability.

c. Bias voltage changes at about 60 millivolts/ $^{\circ}$ C. A temperature stability of $\pm 0.008^{\circ}$ C would be required for ± 5 percent gain stability.

d. Measured S/N under conditions of maximum expected radiant signal were lower than those expected from an S-1 photocathode PMT under

similar conditions. This has not yet been confirmed by direct laboratory comparisons.

e. Due to the long absorption path of long wavelength photons and the very thin structure of this device, red sensitivity is not expected to be as good as the GE detector, which has a very thick structure.

f. This device does not appear suitable for the present application.

Detector Selection. -For the first three spectral bands (0.5 to 0.6; 0.6 to 0.7 and 0.7 to 0.8 microns) photomultipliers with appropriate cathode materials are the best detectors presently available. For the fourth band (0.8 to 1.1 microns), silicon solid-state detectors begin to compete with the S-1 photocathode in terms of S/N performance. However, at the bandwidth required for single detector operation (100 to 300 kHz), impedance levels must be so low that thermal noise in the load resistance completely dominates detector and photon noise for solid-state detectors. There are two ways to overcome this problem; reduce the bandwidth

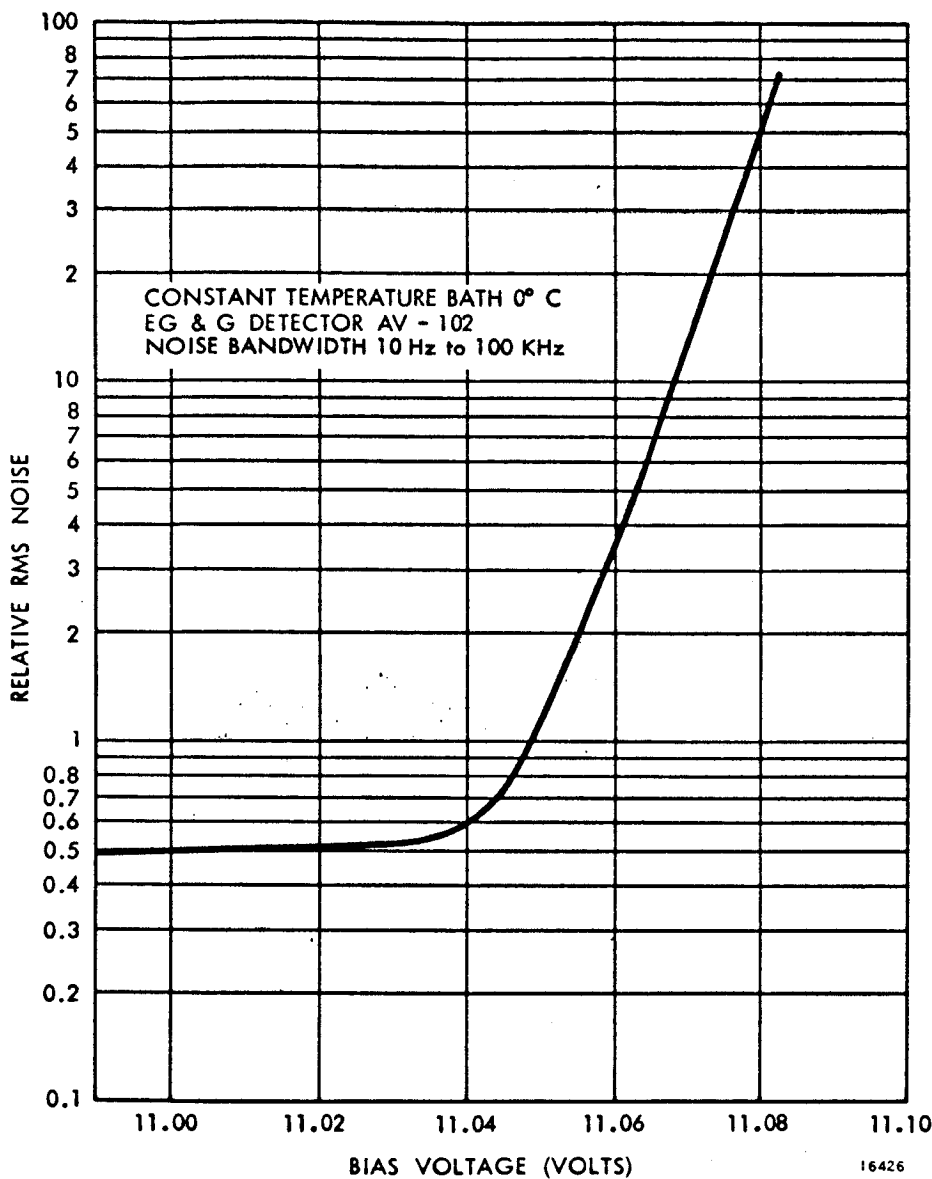


Figure 52. RMS Dark Current Noise.

An estimate of the overall multiplier gain consistent for a maximum sustained anode current of 1 microamp was made. This current level corresponds to the maximum current density at which a typical beryllium-copper dynode can be gain stabilized. It must be anticipated that the scanner will view high brightness cloud tops for extended periods so that gain must be set low enough to produce a maximum anode current of 1 microamp under these conditions. Table 10 was produced using the results of the paragraph on radiant energy.

The indicated gain levels are relatively low compared to typical operation of the multiplier structure. There are two techniques to reduce photomultiplier gain, reduce the voltage per stage, or reduce the number of stages. For low noise operation, reducing the voltage per stage, and the secondary emission ratio, is undesirable since this leads to increased

by using multiple detectors, or introducing a relatively noise free gain mechanism before the sources of thermal noise. If the first approach is taken, i.e., bandwidth reduction, an ordinary silicon photodiode could be used. To retain a single detector per channel, a device with an internal gain mechanism must be used. This is the reason for the interest in avalanche gain silicon detectors indicated in the previous section.

Based on information currently available, the performance of the best of avalanche diode detectors (GE G-1) is still marginal compared to a cooled S-1 photocathode. Further evaluation and development may change this conclusion. It must also be considered that improved performance of the S-1 photocathode is also possible for instance, by means of light trapping by internal reflection. This was not included in the performance estimates for the S-1 PMT.

Use of photomultipliers in all four spectral bands was judged best because positive data indicating the superiority of current silicon avalanche gain detectors was not available.

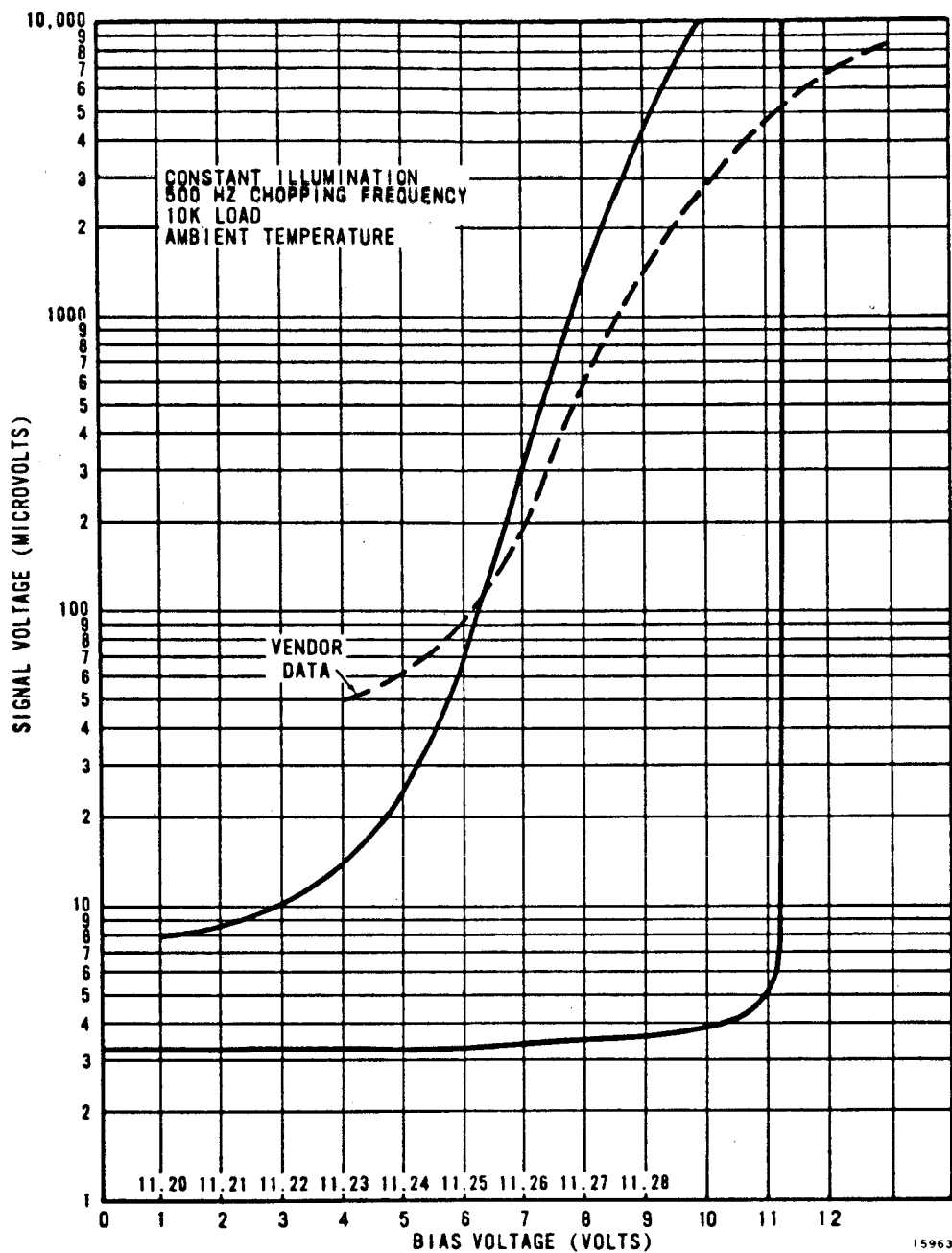


Figure 53. Signal Gain EG and G Detector AV-102.

excess noise. In fact, it is desirable to operate the first two stages of the multiplier at rather high voltages to improve electron collection efficiency and achieve low noise gain.

After the first stages, subsequent noise contributions become less important. For these reasons, the number of active stages of each multiplier tube should be selected to provide proper overall gain. A stage voltage of 135 volts, with a corresponding stage gain of about 2.5, is a suitable operating point for beryllium-copper dynodes. The required number of stages to achieve a given overall gain can then be found from:

$$N = \frac{\log \text{GAIN}}{\log 2.5}$$

Table 10. Nominal PMT Gain for 1 Microamp Maximum Anode Current.

Band	Cloud Top Radiant Power (watts)	Nominal Cathode Current (amps)	Nominal Gain for 1 Microamp Anode Current
1	$(5.75) 10^{-9}$	$(3.62) 10^{-10}$	$(2.8) 10^3$
2	$(4.90) 10^{-9}$	$(1.80) 10^{-10}$	$(5.6) 10^3$
3	$(3.85) 10^{-9}$	$(5.57) 10^{-11}$	$(1.8) 10^4$
4	$(7.45) 10^{-9}$	$(1.15) 10^{-11}$	$(8.7) 10^4$

The photocathode of a PMT is a linear transducer of photons to electrons over a very wide dynamic range. The dynode multiplier likewise has a very wide dynamic range. However, it is possible to destroy the inherent linearity in the dynode multiplier by improper dynode current supplies. Ultimate stability and linearity is achieved by separate regulation of each dynode voltage. This approach is cumbersome.

To determine the suitability of the more simple dynode resistive divider supply commonly used, the overall tube gain was computed as a function of anode current for a fixed supply voltage. Under these conditions, as anode current increases the current in the last few divider resistors decreases, lowering the voltage drop across these stages. Since the overall voltage is fixed, the voltage across the first several stages increases resulting in an overall increase in tube gain.

Using Table 10, the results are as listed in table 11.

Table 11. PMT Supply Voltage.

Band	Number of Stages	Overall Supply Voltage
1	10	1340
2	11	1420
3	12	1620
4	14	1830

The actual calculation of this effect is complicated and was accomplished by using an iterative computer program. The results are plotted in figure 54. Essentially identical results were obtained for all combinations of gain and number of stages anticipated. Two conditions are shown.

In curve 1, all dynode resistors are equal and large enough to limit bleeder current to about 30 microamps at the desired overall gain. In curve 2, the cathode and first dynode resistors have been increased to 6 megohms to produce a higher voltage drop across the first two stages. Supply voltage is adjusted to yield the same overall gain. In addition to higher efficiency and lower noise, this technique also yields slightly improved linearity. In this case, a linearity of better than 1 percent is possible for anode currents less than 1 microamps with a bleeder current of only 30 microamps.

Gain, Offset, and Calibration

The selection of gain, offset, and calibration levels is complicated by their interaction. Ideally, gain levels should be chosen on the basis of the expected dynamic range of signals in each channel and then appropriate calibrate levels established for each gain setting. The complication arises because the same calibration source will be viewed simultaneously in all channels. The spectral distribution of the source prevents calibration levels from being chosen independently for each channel.

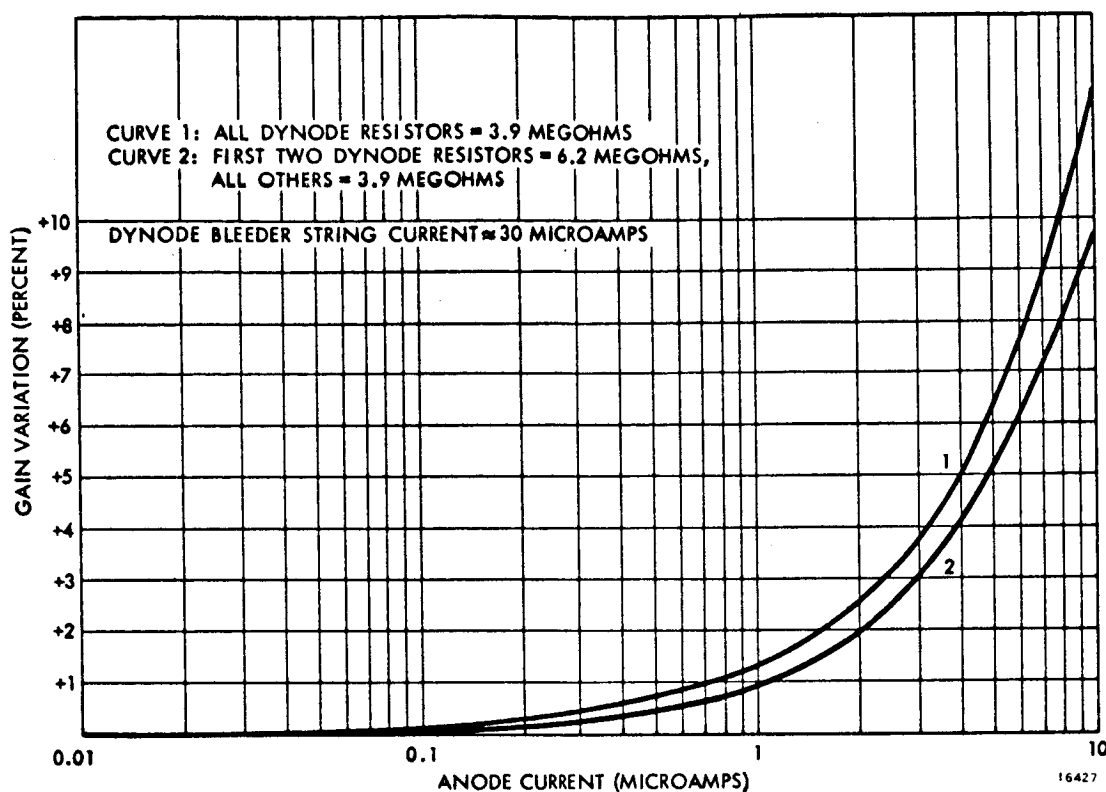


Figure 54. Photomultiplier Tube Gain vs. Anode Current.

The following calibration scheme was assumed to establish the feasibility of selecting a self consistent set of gain and calibration levels based on a realizable source spectral distribution. A tungsten filament, operated at some suitable color temperature, will be filtered to provide a spectral output so the output signal from each channel will be near the maximum expected under operating conditions. Other calibrate levels will then be established by using additional neutral density filters to provide a fixed fraction of full scale signal in all bands. This is only one possible scheme. Colored filters, or additional sources, could be used to alter the ratios of calibrate levels for different bands. The assumed technique is very simple and establishes the feasibility of consistent gain and calibration level selection. It is not required that the calibrate source have the same spectral distribution as the scene viewed, but simply that it produce similar detector output currents.

Figures 55 through 58 summarize, for each spectral band, the range of expected radiant energies for peak highlight areas and the majority (90 percent) of agricultural targets. Also shown are the region expected for the median of agricultural measurements, and the radiant energy corresponding to the average albedo of the earth for that band. As described in the paragraph on Detector Evaluation and Selection, the gain of each photomultiplier will be adjusted to provide 1 microamp of anode current for peak highlight illumination. An anode current scale corresponding to this PMT gain is shown in the figures.

Video channel gain settings, appropriate to each band, are indicated in figures 55 through 58. The low gain setting allows the entire range of expected signals to be accommodated within the dynamic range of the telemetry system. It is assumed that 7-bit, equal level encoding will be used to transmit the data. The tick mark near the bottom of each gain line indicates the level below which the quantizer step size is larger than the rms noise. Below this mark, quantization noise contributes more than 5 percent excess noise. For band 4, the

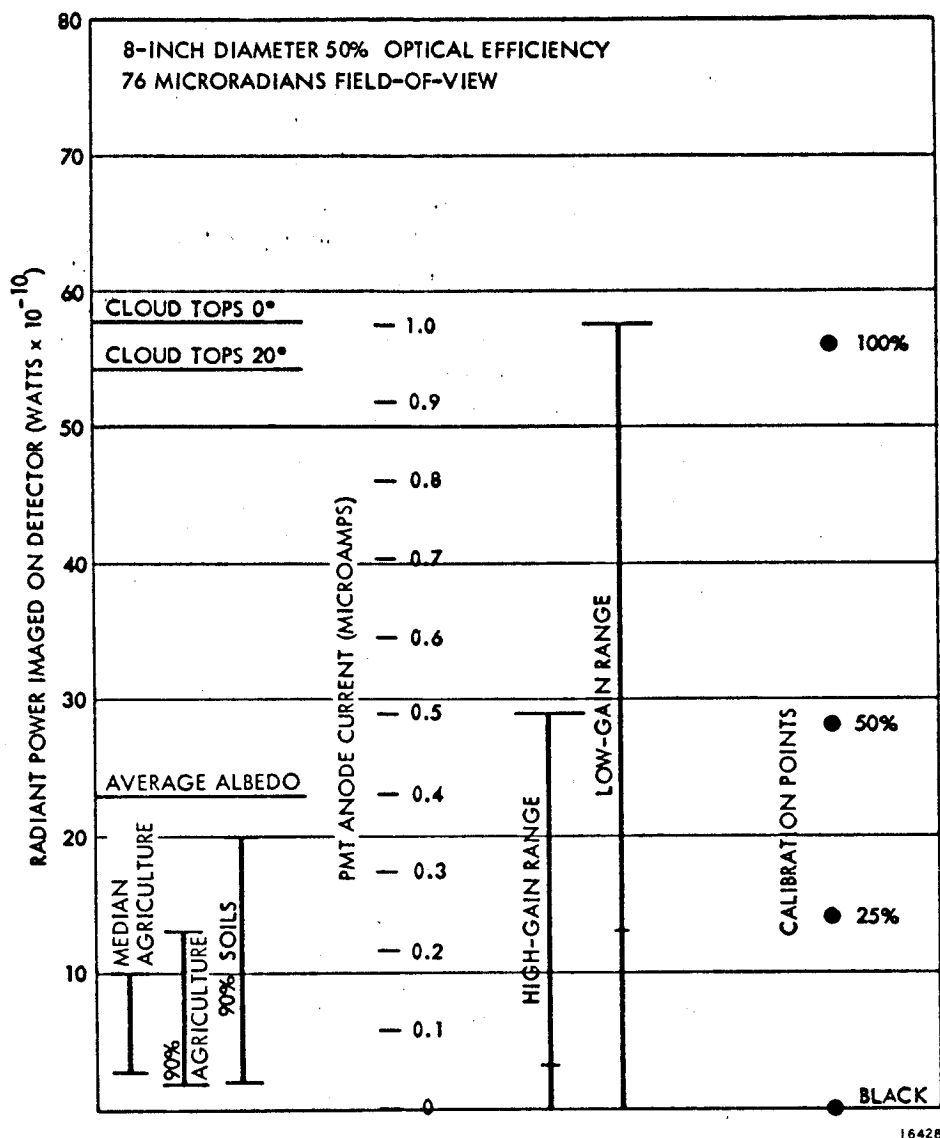


Figure 55. Gain and Calibration Levels, Band 1.

entire range of signals can be covered with one gain setting with sufficiently fine quantization so that quantization noise is negligible. In band 3, the need for a second, higher gain setting is marginal since the low gain setting covers essentially all expected signals with less than 5 percent quantization noise. An improvement in S/N (by increasing collecting aperture size) would require the higher gain shown. In bands 1 and 2, at least one high gain setting is mandatory since, at low gain, quantization noise would be significant over the lower half of the range of agricultural signals. In band 1, a third, even higher gain may be desirable.

The need for offset levels is not clear. The range of signals of primary interest, i. e., those for agricultural targets, can be covered adequately with the high gain setting and no offset. A small offset to gate out backscatter might be convenient but would not improve signal resolution significantly. A relatively large, e. g., half scale, offset would be required to cover high level signals with the same resolution as available for agricultural targets. The figures indicate that sufficient resolution already exists at the low gain setting to cover these signals with less than 5 percent additional quantization noise. The desirability of providing switchable offset would, because of the additional complexity, seem to depend on a particular interest in some range of signals requiring less than 5 percent added quantization noise.

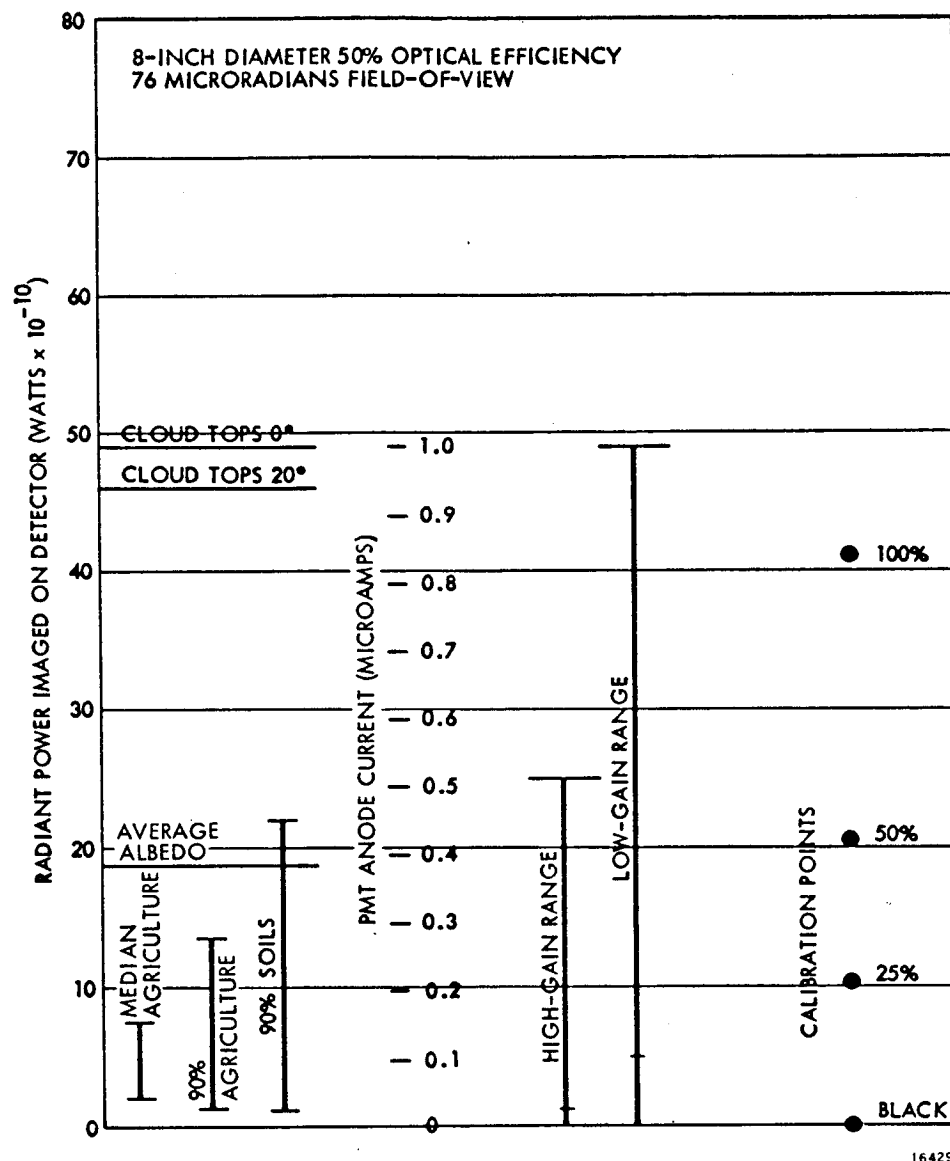


Figure 56. Gain and Calibration Levels, Band 2.

A set of realizable calibration points is also shown in the figures. Three active levels at near full, half, and quarter scale, and a passive black level, are shown. These calibrate levels were computed assuming a tungsten source, with filtering to cause the distribution of signals in the various bands to approximate the distribution of full scale signals.

Figure 59 shows the approximate life versus color temperature for a tungsten filament quartz iodine lamp. At temperatures below which the iodine cycle is operative, the rate of tungsten evaporation is so low as to be negligible. Since a lifetime of 8,000 to 10,000 hours is desirable, an operating temperature of 2400 to 2500° K appears suitable.

It is now necessary to select appropriate filtration for this source to yield detector output currents similar to that produced when viewing a highlight scene element. For this purpose, data in the Schott glass filter catalog (6) was used as being representative of materials currently available. It is possible to choose filter type and thickness to obtain the desired spectral distribution. It was clear that no single filter would adequately correct the tungsten output, so combinations of two filter types were tried. A two dimensional optimization program

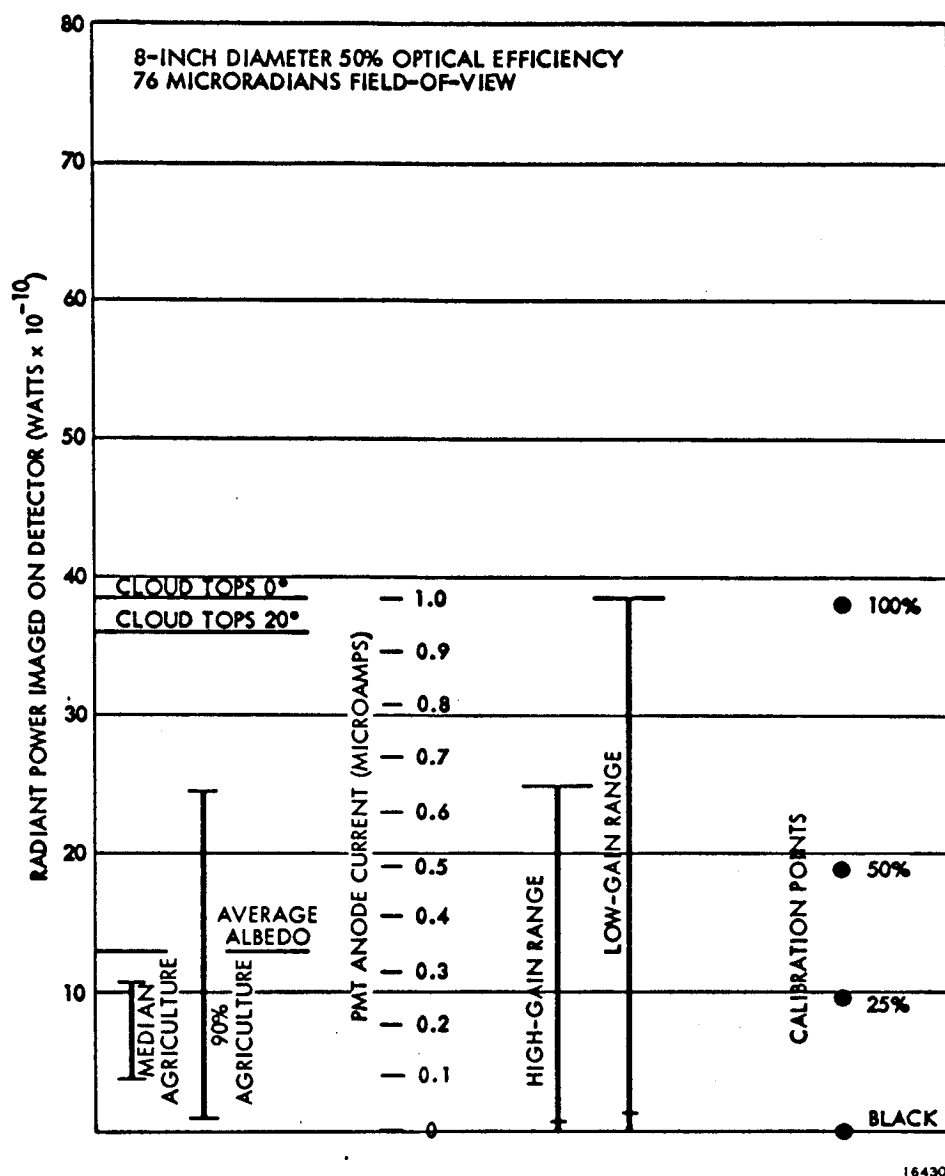


Figure 57. Gain and Calibration Levels, Band 3.

was used to select the best combination of thicknesses for any selection of materials. In doing the calculations, the spectral distributions of filters, source, and detectors were all considered and comparisons made on the basis of output signal current. The calibrate levels shown are for a 2400° K blackbody source with filtration composed of 0.62 millimeter of Schott VG-9 filter glass and 1.26 millimeter of KG-1 glass.

The gain and calibration levels summarized in figures 55 through 58 demonstrate the feasibility of selecting a self-consistent set which meets all system requirements.

Multiplexing-Demultiplexing

Figure 60 shows a typical video channel with an output sample. Timing is for contiguous 230-foot wide lines. Each video signal will be band limited to a frequency spectrum of dc to about 150 kHz, with a 30 to 36 db per octave roll-off.

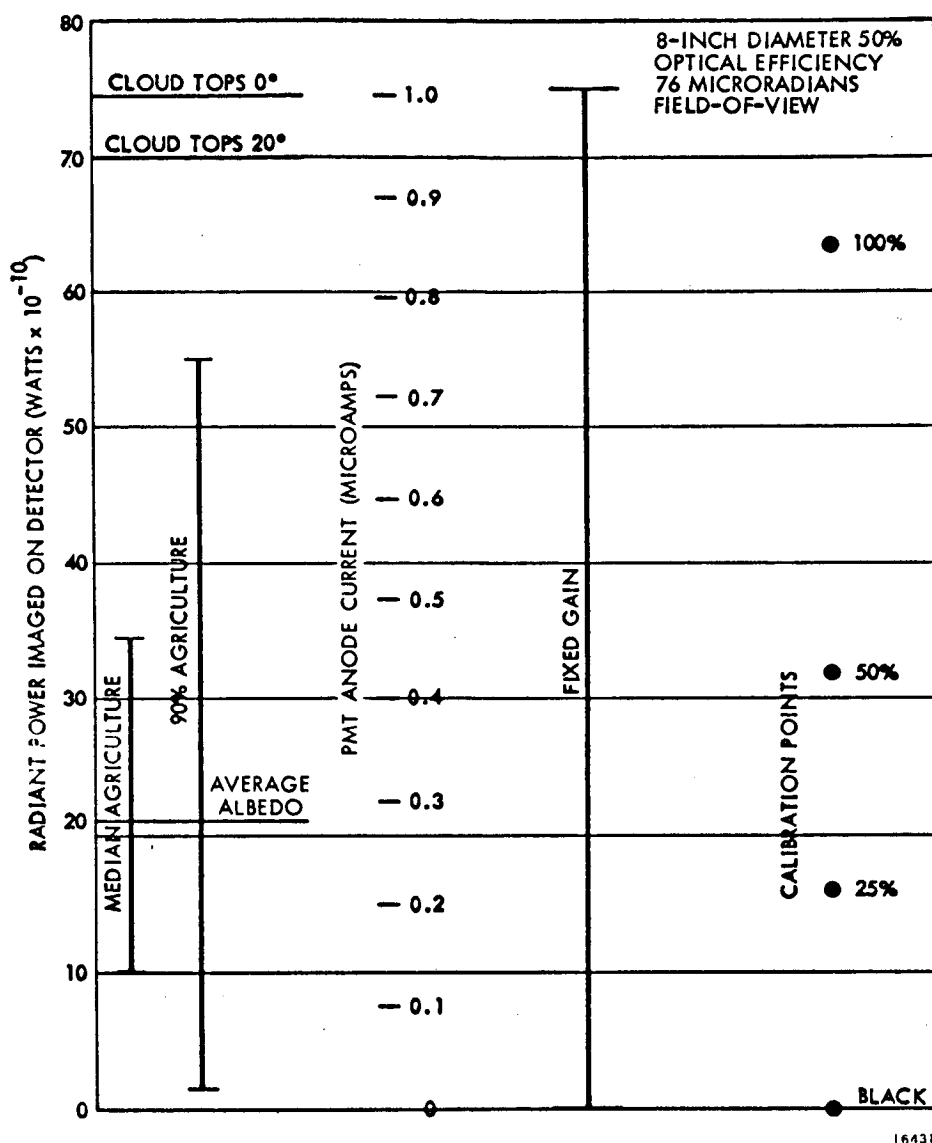


Figure 58. Gain and Calibration Levels, Band 4.

Each line of information will occupy approximately 11.5 milliseconds, of which the last 9 milliseconds will be actual video generated by scanning the ground. The first 2.5 milliseconds of each line will be devoted to line sync and calibration pulses. The uncertainty or jitter in the time between consecutive line sync pulses is caused by small inequalities in the mechanical spacing between scanning probes.

The multiplexer must combine the four parallel video signals into a single composite video signal which can be transmitted over a wideband link to the ground station. There the composite video signal will be demultiplexed back into four parallel video signals. The bandwidth required to transmit the information produced by the scanner to the ground station is of primary concern.

We conclude that digital encoding and multiplexing, and transmission by differentially coherent quadrature PSK, is an acceptable solution to the data transmission problem. The following paragraphs describe the line of reasoning which led to this conclusion with some of the alternate telemetry systems, both analog and digital, which were considered.

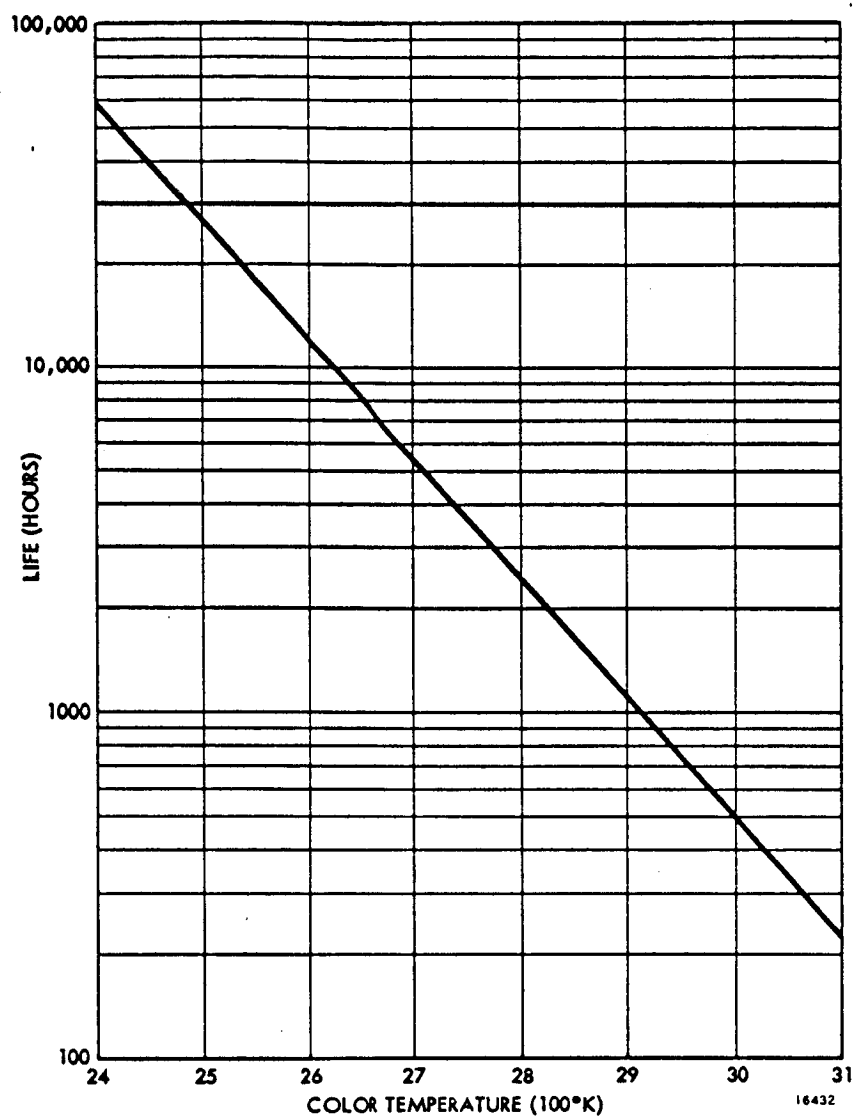


Figure 59. Life vs Color Temperature of Quartz Iodine Lamp.

Analog Multiplexing. - The four video signals can be analog multiplexed in the frequency domain by modulation of subcarriers to yield FM/FM or AM/FM transmission or, in the time domain, by sampling yielding PAM/FM transmission.

FM/FM. - Figure 61 shows plots of the total FM subcarrier bandwidth required to transmit all sidebands with amplitudes greater than the percentage indicated by the parameter γ . The ordinate, β , is the ratio of the total bandwidth to the maximum subcarrier deviation. The curve labeled $\gamma = 0.01$ indicates the bandwidth required to transmit all sidebands containing more than 1 percent of the signal. This is what would be required to ensure signal distortions of less than 1 percent. For a deviation ratio (modulation index) of 1, a subcarrier bandwidth about seven times the baseband signal bandwidth is required. Assuming a video bandwidth of 150 kHz, the required subcarrier bandwidth is about 1 MHz. Allowing a maximum subcarrier deviation of ± 50 percent, the lowest subcarrier frequency which can be used is 1 MHz. Providing 1 MHz guard bands between channels results in a total baseband spectrum occupancy of at least 7.5 MHz. Assuming a carrier modulation index of 1 and requiring that all sidebands with amplitudes over 10 percent be transmitted, a radio frequency (rf) bandwidth of about 32 Mhz is needed (figure 61).

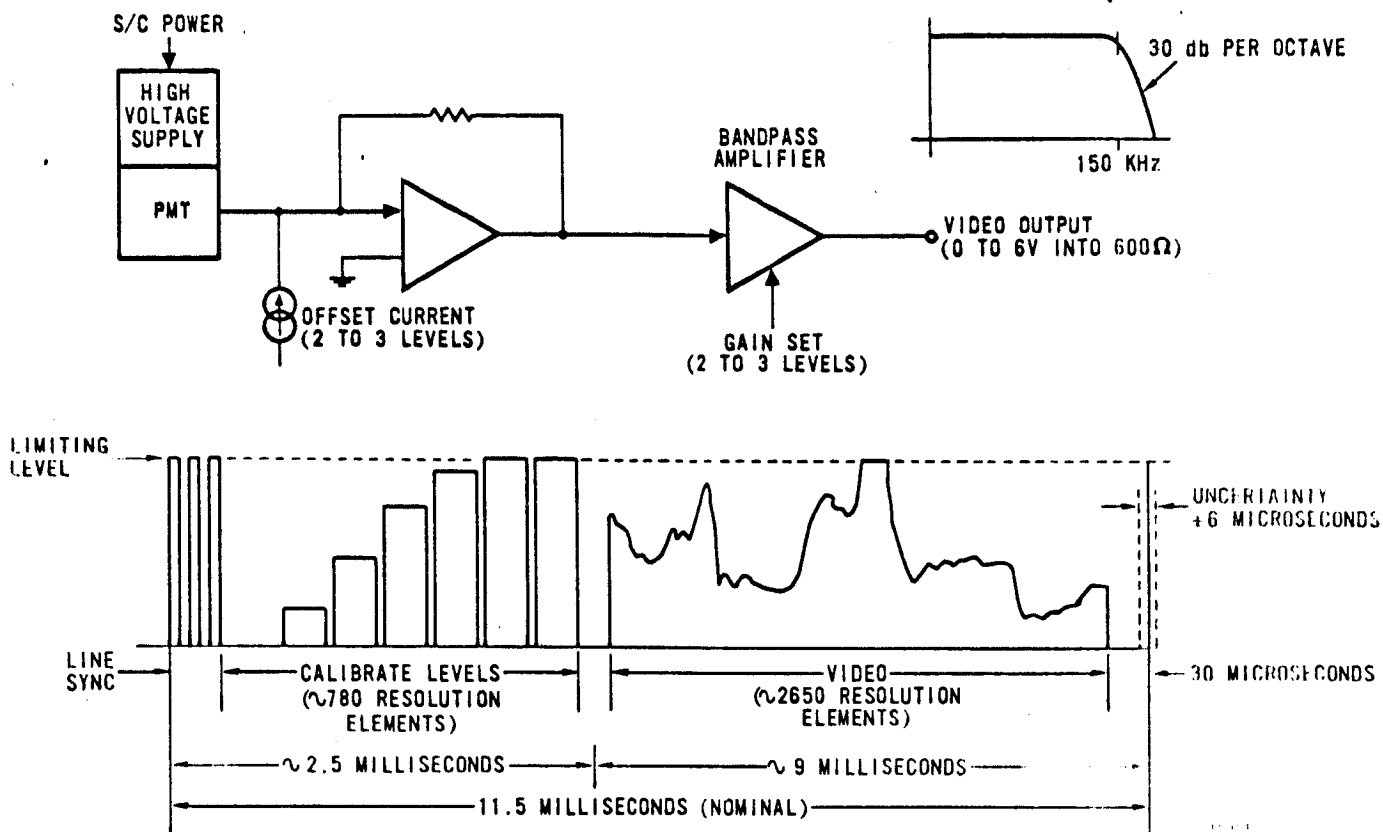


Figure 60. Typical Video Channel.

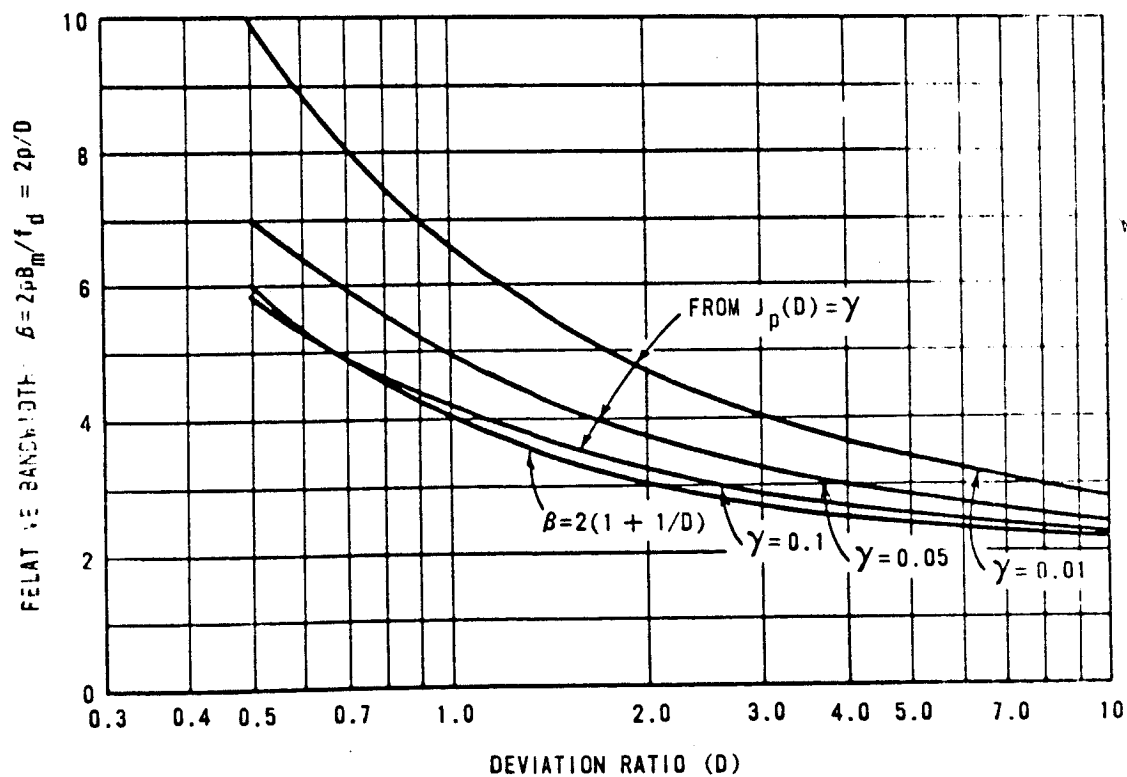


Figure 61. Bandwidth Requirements.

Bandwidth can be reduced by using narrower guard bands, a smaller modulation index, or by transmitting fewer sidebands. All these techniques result in lower S/N and greater intermodulation and other distortions.

AM/FM. -The use of amplitude modulated subcarriers to reduce required base bandwidth was considered. Suppressed carrier, double sideband AM modulation of the four video signals, and a fifth narrow band pilot carrier for demodulation reference were assumed in order to avoid strong subcarriers which would cause intermodulation products. Each subcarrier would have a spectrum occupancy of about 600 kHz. Assuming subcarrier frequencies of 0.5, 1.5, 2.5, and 3.5 MHz, a total spectrum occupancy of less than 4.5 MHz can be achieved.

With the above frequency assignments, only two third-order intermodulation products fall in the occupied spectrum. The FM modulation and demodulation process will produce other products between the signal channels. It is estimated that these intermodulation products can be held to be more than 40 db below the signal level, producing a system with less than 1 percent intermodulation distortion and occupying less than 4.5 MHz of base bandwidth. However, an rf bandwidth of about 31 MHz must be provided to retain 1 percent FM accuracy (figure 61).

PAM/FM. -The four video signals can be multiplexed in the time domain by sequential sampling. It is important that the sampling rate be high enough to adequately define the signal and avoid reconstruction errors.

There are several aspects of sampling rate and accuracy which must be considered. First, regardless of sampling rate, the values of the waveform at the sampling instants will be accurately known. Sampling rate effects the accuracy with which one can reconstruct the values the waveform had between sampling instants. Therefore, the selection of sampling rate depends largely on the requirement for interpolation between sample values during data reduction. In the present case, there are two end uses for the data collected; computer analysis and hard copy photo production. The computer, being a discrete device, operates only on sample values and does not require data concerning the entire intermediate waveform to perform its function. Providing enough samples are taken to cover the area scanned, interpolation will probably not be required for computer analysis. At least one sample per resolution element is required to completely cover the ground area scanned. The value of sampling more than once per resolution element for subsequent computer analysis is uncertain. Unless scan line overlap is used, only one sample per resolution element in the track direction can be obtained. The implications, for computer purposes, of a higher sampling rate in the other direction are not clear.

For hard copy photo production, interpolation between sample values cannot be avoided since the eye of the observer would fill in the gaps between samples, even if an attempt were not made to do so in creating the photo. Therefore it is important to use a high enough sampling rate so that interpolation accuracy can be held to a value commensurate with the requirements of hard copy production. Assuming carefully controlled exposure and processing, the image density on film can be controlled to an accuracy of ± 0.02 to ± 0.04 density units. With a gamma of 1, this corresponds to an equivalent video accuracy of ± 5 to 10 percent. Sampling rate should be selected to provide an interpolation accuracy of at least 5 percent.

Figure 62 shows, on linear scales, the baseband video signal spectrum for a single channel assuming an electrical bandwidth of 150 kHz and a field-of-view of 230 feet. Also shown are the aliased spectra which would be produced if the original signal were sampled at 300,000 samples per second (1 sample per resolution element), 450,000 samples per second (1.5 samples per resolution element), and 600,000 samples per second (2 samples per resolution element). Components of the original waveform at frequencies where the baseband and aliased spectra overlap cannot be accurately reconstructed.

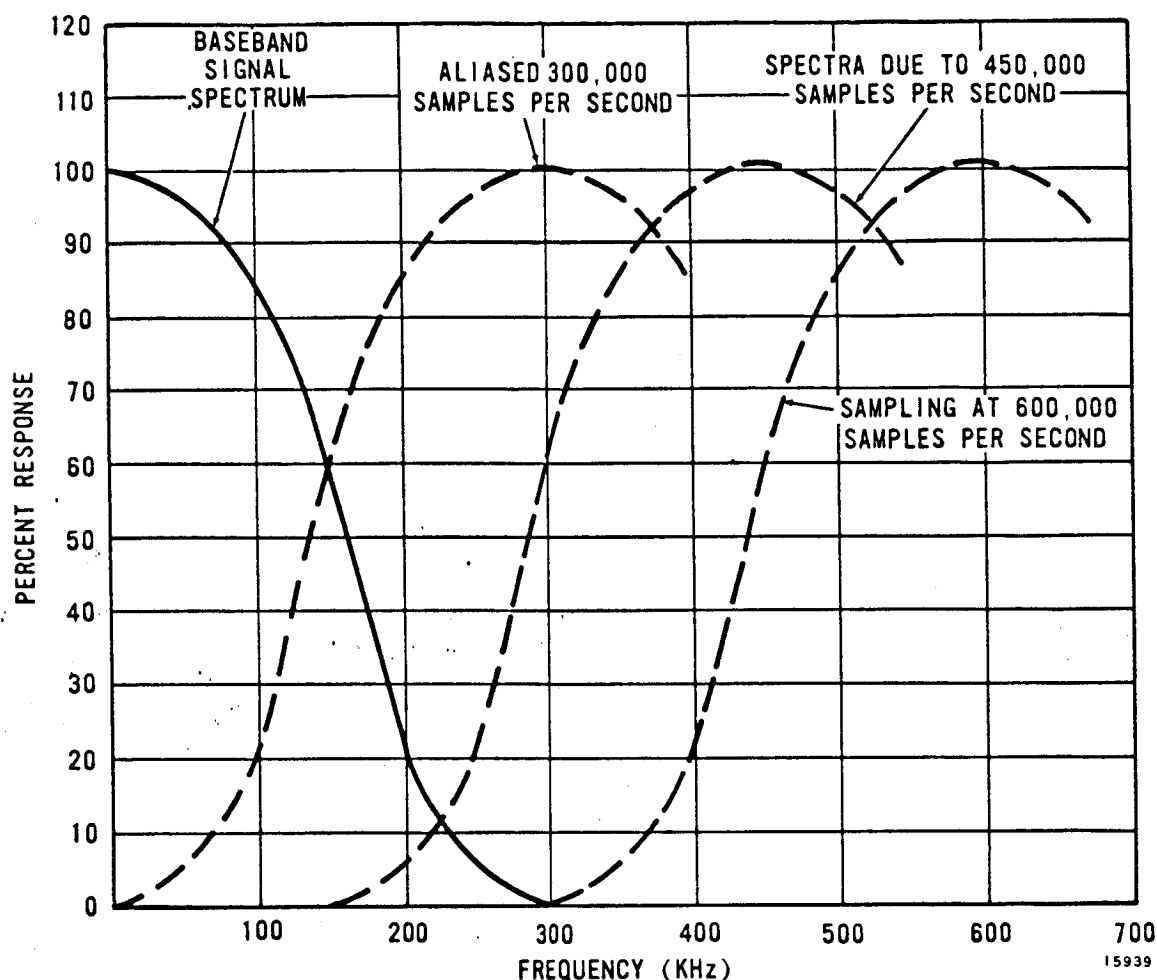


Figure 62. Frequency Folding Due to Sampling.

The magnitude of the loss of accuracy at these frequencies depends on the reconstruction or interpolation technique used. Figure 63⁽⁷⁾ shows the expected rms error in reconstructing the original waveform as a function of the parameter γ , which is equal to the ratio of the sampling frequency to the 3db video frequency. This assumes the use of an optimum realizable interpolating filter. The parameter k indicates the number of poles in the filter which limited the baseband spectrum before sampling. In the present case, $K = 5$. From the graph it is apparent that for 5 to 10 percent reconstruction accuracy, a sampling rate about three times the baseband corner frequency is required. For the assumed case, this works out to be a minimum of 450,000 samples per second per channel (1.5 samples per resolution element).

Given this sampling rate, we can now return to the discussion of bandwidth requirements for PAM/FM. Since each of the four channels must be sampled 450,000 times each second, there results a total pulse rate (excluding frame identification and sync) of 1.8 million pulses per second. Since this is an analog system, adequate bandwidth must be provided to allow the pulse amplitude to stabilize. A bandwidth of at least 0.75 times the pulse rate must be allowed so the pulse amplitude can rise to 99 percent of its final value in one pulse time. This results in a minimum base bandwidth of 1.35 MHz. Referring again to figure 61, an rf bandwidth at least seven times this large, 9.5 MHz, is required to maintain FM accuracy.

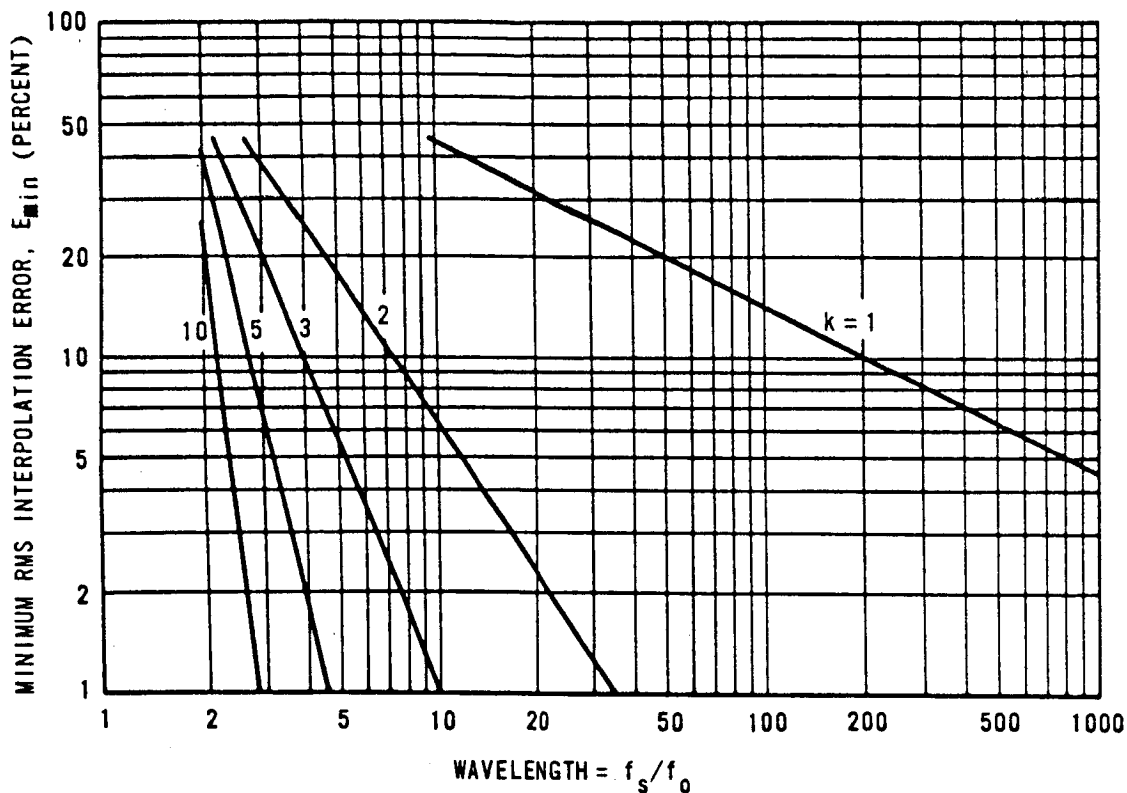


Figure 63. Minimum Interpolation Error vs. Normalized Sampling Frequency.

Summary of Analog Multiplexing. -Table 12 is a summary of the bandwidth requirements for the three types of analog multiplexing considered. In each case, sufficient bandwidth is allowed so that errors due to restricted bandwidth should not exceed 1 percent.

Table 12. Bandwidth Required for Analog Multiplexing.

Type	Base Bandwidth (MHz)	Rf Bandwidth (MHz)
FM/FM	7.5	32
AM/FM	4.5	31
PAM/FM	1.4	9.5

Assuming an rf bandwidth of 20 MHz and a transmitter power of 20 watts, the S/N at the receiver intermediate frequency for maximum slant range (1100 nautical miles) was estimated. Table 13 presents the results for various receiving antennas and noise temperatures.

These S/N's will be improved somewhat due to the use of FM, but even so they are not suitable to a high quality analog link. Even allowing adequate bandwidth and S/N, the accuracy of analog telemetry is questionable because of nonlinearities and drift in each of the modulation, transmission, and demodulation processes. It is generally conceded that without expending a large effort, an overall analog accuracy of about 5 percent is as good as should be expected. This accuracy would greatly limit the dynamic range available to transmit video and would require an increased number of gain and offset levels to accommodate the overall signal dynamic range. For these reasons, digital transmission was investigated.

Digital Multiplexing. -The discussion of sampling rate under PAM/FM is valid for true digital sampling and indicates a minimum sample rate of 450,000 samples per second per

Table 13. Signal, Noise, Gain, and S/N Levels.

Antenna Type	85-Foot Dish		40-Foot Dish		Units
Receiver antenna gain	51.5		45.5		db
Receiver temperature	35	100	35	100	° K
Transmitter antenna gain	0	1.5	0	1.5	db
Receiver antenna temperature	125	125	125	125	° K
Receiver system temperature	160	225	160	225	° K
System noise (20 MHz)	-103.7	-102.2	-103.7	-102.2	dbm
Transmitter power	43	43	43	43	dbm
Space attenuation	-169.5	-169.5	-169.5	-169.5	db
System margin	-6	-6	-6	-6	db
Rf at receiver antenna	-132.5	-131.0	-132.5	-131.0	dbm
Rf at receiver	-81.0	-79.5	-87.0	-85.5	dbm
Receiver intermediate frequency S/N	22.7	22.7	16.7	16.7	db

channel. A consideration of analog noise and resolvable signal levels is necessary to determine the number of bits or quantizer levels required per sample.

For a photon noise limited system, resolvable signal levels are not equally spaced over the range of signal amplitude. The most efficient encoder would be one with unequal quantization intervals. The requirements on an equal level encoder were analyzed to determine whether this degree of sophistication is worthwhile.

In the subparagraph on Quantization Noise, an equation is derived expressing the quantizer step size, q , required so as not to increase an analog signal error, ϵ , by more than a given percentage. For a quantization error contribution of 5 percent, the result is $q \leq 0.64 \epsilon$. Referring to the paragraph on Noise Calculations, the analog signal from the video amplifiers will be photon noise limited and so the equivalent rms error can be given by:

$$\epsilon = k \sqrt{W} \text{ rms watts}$$

where,

W = radiant power on the detector (watts)

k = a constant, different for each band, determined from the plots of noise shown in the paragraph on Noise Calculations and given below:

Band	k
1	$(1.5) 10^{-6}$
2	$(2.1) 10^{-6}$
3	$(3.2) 10^{-6}$
4	$(1.0) 10^{-5}$

For an equal level encoder, the step size, q , must be chosen so as not to degrade the lowest noise level signal. For the 5 percent criterion:

$$q = 0.64 \sqrt{W_{\min}}$$

where, W_{\min} is the smallest radiant power expected in each band. This defines the required size of quantization step. If the range of signals to be quantized is known, the required number of binary quantizer bits can be found. Taking the range of signals to be the range expected for agricultural targets for 20 degrees solar zenith angles shown in the paragraph on Radiant Energy, table 14 results:

Table 14. Equal Quantizing Level.

Band	W_{\max}	W_{\min}	ϵ	q	Number of Equal Levels
1	$(1.88) 10^{-9}$	$(4.0) 10^{-10}$	$(3.0) 10^{-11}$	$(1.9) 10^{-11}$	77 (7 bits)
2	$(2.04) 10^{-9}$	$(2.8) 10^{-10}$	$(3.5) 10^{-11}$	$(2.2) 10^{-11}$	79 (7 bits)
3	$(2.27) 10^{-9}$	$(2.0) 10^{-10}$	$(4.5) 10^{-11}$	$(2.9) 10^{-11}$	72 (7 bits)
4	$(5.10) 10^{-9}$	$(3.5) 10^{-10}$	$(1.9) 10^{-10}$	$(1.2) 10^{-10}$	40 (6 bits)

A 7-bit, equal level quantizer should be capable of digitizing the signals expected from the scanner while not increasing the rms error level by more than 5 percent (this is for an analog noise bandwidth of 335 kHz).

To compare these results with the requirements on an unequal level quantizer and to determine if this degree of sophistication is advantageous, the number of actually resolvable levels between W_{\max} and W_{\min} was determined for each band (the number of levels each separated from its neighbor by the rms noise level). Then assuming the same 5 percent criterion used above, the approximate number of unequal quantizer levels required was found by dividing by 0.64. Table 15 presents the results:

Table 15. Unequal Quantizing Levels.

Band	No. of Actually Resolvable Levels	Number of Unequal Quantizer Levels
1	32	50 (6 bits)
2	30	47 (6 bits)
3	23	36 (6 bits)
4	12	19 (5 bits)

It appears that using an equal level encoder over the range of signals expected will not require more than one extra bit per channel and will have the advantages of contributing less than 5 percent error over most of the range.

We conclude that an equivalent of seven binary bits per sample will not degrade the scanner S/N. Since there are

four channels of video, the total transmitted bit rate, excluding sync bits, is approximately 12,600,000 bits per second.

Frequency Shift Keying (FSK). -It is necessary that the frequencies assigned to the digital levels to be transmitted be orthogonal at the time the demodulator samples to determine which level is being sent to realize the full S/N capability of the data channel. If sampling takes place at the end of a pulse interval, the frequency separation between adjacent digital levels should equal the pulse transmission rate. ⁽⁸⁾ In addition, the digital signal will occupy a spectrum twice the pulse rate wide centered around each of the transmitted frequencies. The total spectrum occupancy of an N-level FSK system is given by:

$$BW = (N + 1) \frac{F_o}{\log_2 N}$$

where,

BW = rf spectrum occupancy

F_o = equivalent binary bit rate

N = number of levels in digital code, i.e., N = 2 for binary.

The results are shown in table 16 for binary, quaternary, and octal FSK systems with $F_o = 12.6$ million bits per second:

Table 16. Spectrum Occupancy Comparisons.

Coding	N	Minimum rf Spectrum Occupancy
Binary FSK	2	28 MHz
Quaternary FSK	4	31.5 MHz
Octal FSK	8	38 MHz

Orthogonal signal conditioning is not required. Reducing the frequency spacing between levels leads to intersymbol interference and increased bit error rate. Bandwidth saving is not very large before bit error rate becomes unacceptable. For this reason, a means of achieving orthogonality without requiring increased bandwidth was sought. Using orthogonality in the phase rather than frequency domain offers such a solution.

Phase Shift Keying (PSK). -If four phase PSK of a single carrier frequency is used to transmit two bit values per pulse, the total rf spectrum occupancy can be reduced by a factor of one-half over that required to transmit individual bits on separate carriers. Assuming a bit rate of 12.6 million bits per second, the rf spectrum required for four phase PSK is 12.6 MHz since only 6.3 million pulses per second are transmitted. This relatively narrow bandwidth is encouraging, however, it must be remembered that no provision for sync and identification bits was made. Since quadrature PSK seemed to offer a feasible approach to the video transmission problem, it was decided to investigate, in greater detail, a practical implementation of this technique.

Word Format and Bit Rate. -As mentioned previously, there are an equivalent of 12.6 million bits of information to be transmitted each second. Extra bit positions must be allowed in any practical system for frame identification and sync. In the present case, a 40-bit word, containing one sample from each of the four spectral channels, and a word sync group is recommended. The word format is in figure 64.

The first seven bits comprise a word sync group consisting of seven 1's (1111111), which is a forbidden data state. Each data sample consists of the 7-bit binary representation of the video amplitude at the sample time. The spacer bits (zeros) are required to prevent a series of seven 1's from occurring in the data section which would be mistaken for a sync

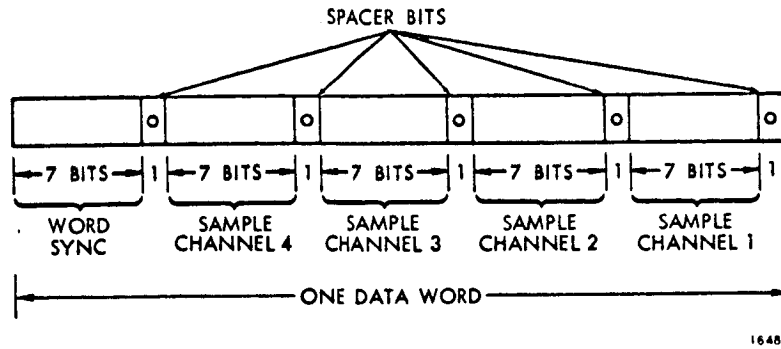


Figure 64. Word Format.

group by the ground equipment. When a new scan line begins, in addition to the normal word sync, a group of seven 1's is also transmitted in the space normally occupied by the channel 4 sample. Thus, ground equipment can recognize word sync by the occurrence of a sequence of seven 1's and line sync by the occurrence of two such groups in sequence.

The combination of 40 bits per word and 450,000 words per second yields a total bit rate of 18 million bits per second for a practical system.

Estimated Bit Error Rate.—Since quadrature is recommended, the pulse rate is 9 MHz and the rf bandwidth for the first lobe is 18 MHz. With a differentially coherent system, the demodulation problem is simplified from that for a coherent system. The error rate for such a system has not yet been determined in closed form, but the error rates for this particular case have been calculated using a computer. (9)

If a matched filter detector is used, the ratio of filter output pulse energy to noise density is given by:

$$\frac{E}{n_o} = \frac{1}{2} \frac{S}{N_{IF}} T (B_{IF})$$

where, T is the pulse duration and B_{IF} is the intermediate frequency bandwidth. The factor $1/2$ occurs here because there are two bits per pulse and the signal energy is split between the bits. It was previously estimated that the worst case intermediate frequency S/N for a 20 MHz bandwidth will be 16.7 db. The pulse energy to noise density ratio for a 16.7 db intermediate frequency S/N is:

$$\frac{E}{n_o} = \frac{1}{2} (SNR_{IF}) T (B_{IF}) = 52 = 17.2 \text{ db.}$$

The required pulse energy to noise density ratio for 10^{-4} error rate is 11.1 db. This gives a S/N margin of 6.1 db.

We conclude that differentially coherent quadrature PSK will provide a first lobe bandwidth of 18 MHz, and a 10^{-4} bit error rate with a 6-db margin, an actual error rate of about 10^{-15} . Limiting the bandwidth to the first lobe does not seriously deteriorate the orthogonality of the signal set or the power of the transmitter. Ideal band limiting will result in a power reduction of 1/2 db (10 percent) if placed after the transmitter. This is in addition to resistive loss associated with this filter, which could be as high as 2 db. This requires further investigation.

Encoder-Multiplexer. -Figure 65 is a block diagram of a system for quantizing the four analog video signals and multiplexing the resultant bits into a pulse stream suitable for input to a quadrature modulator.

All video signals are sampled simultaneously at a rate of 450,000 samples per second by the four dual track and hold amplifiers. These units are arranged so that one circuit is tracking the input while the other is holding the previous sample. An aperture time of about 10 nanoseconds is required to preserve analog accuracy. The held voltages are quantized in parallel by the four 7-bit A/D converters. The output state 111111 is forbidden. (This is further discussed under sync generation.) Each A/D converter performs only 450,000 conversions per second, which is within the state-of-the-art.

After complete conversion, the output of each A/D converter is strobed into a pair of 4-bit shift registers. The eighth bit in each pair is held at the zero level. In addition, a fifth pair of registers holds the sequence 1111110. These additional bits form the sync and spacer groups necessary for reliable decommutation. The contents of all the shift registers are sequentially shifted, two bits at a time, to lines \bar{A} and \bar{B} .

The quadrature encoder determines from the previous phase (lines \bar{C} and \bar{D}) what the new phase should be, based on the current values of \bar{A} and \bar{B} . This decision is gated by the clock into a pair of flip-flops to generate the new \bar{C} and \bar{D} hence, the new phase.

The signals, \bar{C} and \bar{D} , when applied to an appropriate quadrature modulator, to be described later in this section, will cause a phase shift of 0° , 90° , 180° , or 270° from the previous phase. This differential phase shift can be recognized by ground equipment to regenerate the \bar{A} , \bar{B} sets (1.1), (0.1), (0.0), or (1.0), respectively.

System Timing. -The system clock rate is 9 MHz. All gating throughout the system is synchronous with this clock. A 5-bit binary counter and appropriate output gating from it generates all the timing signals required by the system. The counter is reset when the nineteenth state is reached through the upper flip-flop on the right just below the counter (figure 65). This flip-flop is necessary to prevent a race condition in the reset circuit. The numbers on the gates refer to the decimal equivalent state of the counter.

The outputs associated with each such set of numbers is true if the counter is in any of the listed states. Those outputs having a bar over them are false when the counter is in the listed state. All the gates have an enabling input from the clock. The channels are clocked onto the transmitter pulse stream in the order of their channel numbers.

Synchronization. -Synchronizing pulses are provided for word and line separation. A line start pulse (full scale) occurs simultaneously in all four video channels at the beginning of every line. This pulse can be generated by a bright optical point source, which each optical probe scans across before entering the active region of the scan line.

To guarantee recognition of the line start pulse by the on-board circuitry, a fifth independent signal, generated by a magnetic pickup on the scanner shaft, indicates the region of the

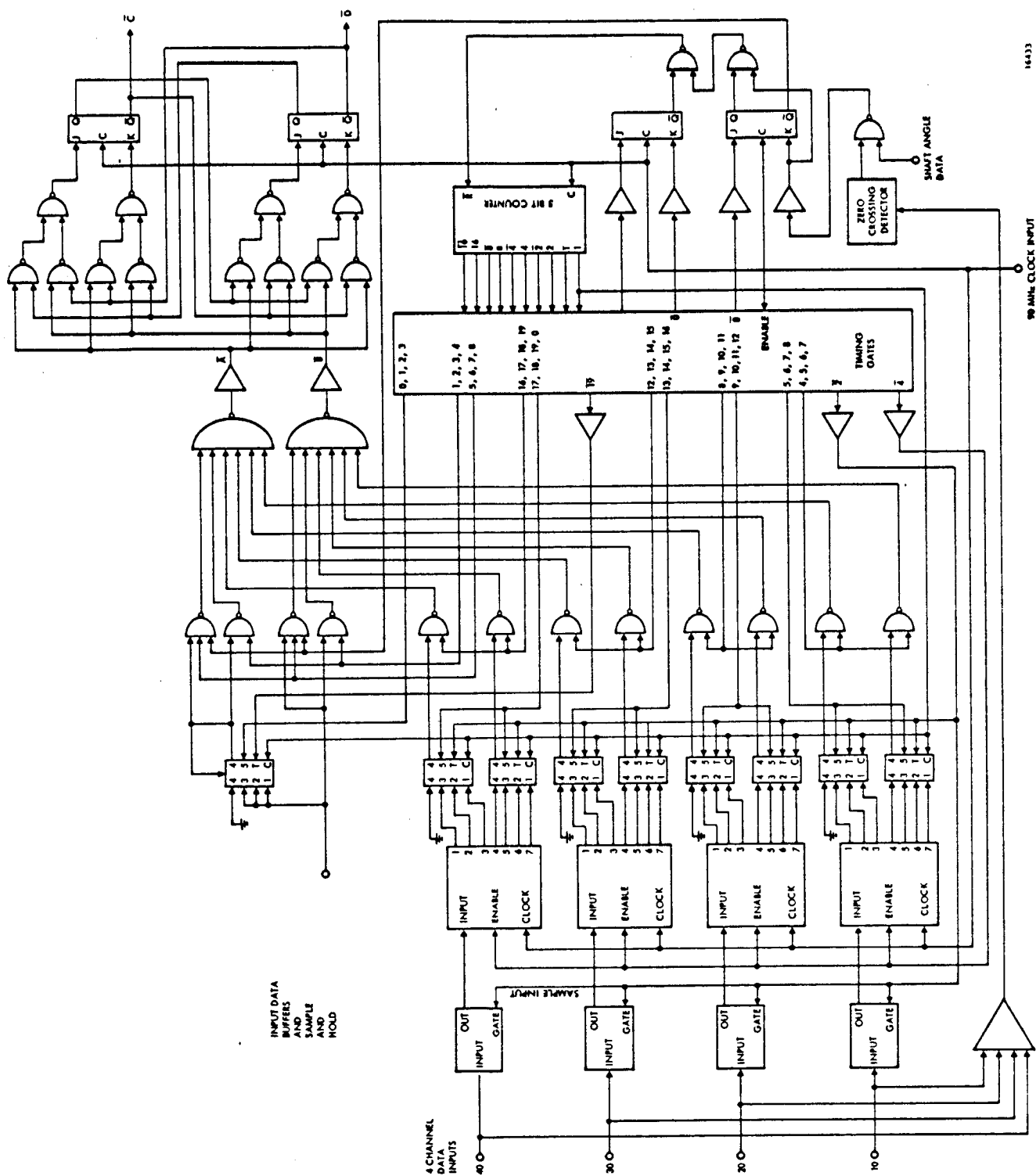


Figure 65. Encoder - Multiplexer Logic Diagram.

scan where a line sync will occur. This pulse does not have sufficient rise time or positional accuracy to act as a sync pulse in itself, but is suitable to gate on the sync recognition circuit.

To improve the S/N of the line sync pulse and to increase reliability, the outputs of all four video channels is added together. The leading edge of the sync pulse is reinforced while noise, being uncorrelated, tends to cancel. The summed voltage is compared with a half scale reference voltage by a zero-crossing detector.

The coincidence of the gating waveform and the sharp pulse from the zero-crossing detector establishes the precise time reference for a line start.

When a line start pulse is recognized, the timing gates are reset to zero, interrupting whatever phase was in process and initiating a new sample cycle on the next clock transition. Thus, sampling will occur within one clock cycle (110 nanoseconds = 0.03 resolution element) of the correct time. The interruption of the process being performed will not be significant. No useful data occurs in the region of the line start time. The pulse transmission rate and phase remains constant so that no loss of bit sync in ground equipment occurs.

The first word transmitted after recognition of a line start pulse consists of a normal word sync (01111111) followed by a second identical sync group in the position normally occupied by the channel 4 sample. This signal consists of A and B sequences of 01110111 and 11111111, respectively. Since this combination corresponds to a data sub word of 01111111, which is a forbidden data sub word, line sync and data will not be confused in the decoder, except for the case when an error is made in decoding due to system noise. This, has a very low probability of occurring within a line as shown by the relation:

$$\begin{aligned} P(E_{\text{line}}) &= P(E_{\text{bit}}) (T_{\text{line}})^{18} (R_{\text{bit}}) \\ &= 10^{-15} (0.0115) (18) 10^6 = (2.07) 10^{-10} \end{aligned}$$

Word sync occurs once every 20 pulses. The last four pulses of each word is the word sync. Word sync consists of A and B sequences of 0111 and 111, respectively. Line sync consists of two consecutive word sync subwords. The first sequence is generated by the upper 4-bit circular shift register. It is connected with end to end feedback so that when shifted it will continually generate the sequence. In addition, it is loaded from voltage sources once each 20-pulse word. The other sequence is generated directly from a constant voltage source. Since the line sync is added to the channel 4 video data during the last half of the line sync sequence, the presence of video data does not cause an error in the line sync code. This adding is done by the six input AND gates, whose outputs are labeled A and B identification. The inputs are negative logic.

The line sync generation is inhibited when the lower right flip-flop is set by the $\bar{8}$ output from the timing gates. Under this condition, only word sync is generated at the beginning of each word.

Quadrature Modulator. -Figure 66 is a block diagram of a quadrature modulator suitable for transmission of the pulse train generated by the encoding logic. A 180 MHz pilot is phase shifted 0° , 90° , 180° , or 270° , depending on the values of the two binary bits (A and B) being transmitted. The pilot frequency (180 MHz) must be an integral multiple of the pulse rate (9 MHz) to provide an integral number of cycles per pulse to aid ground phase recognition circuitry.

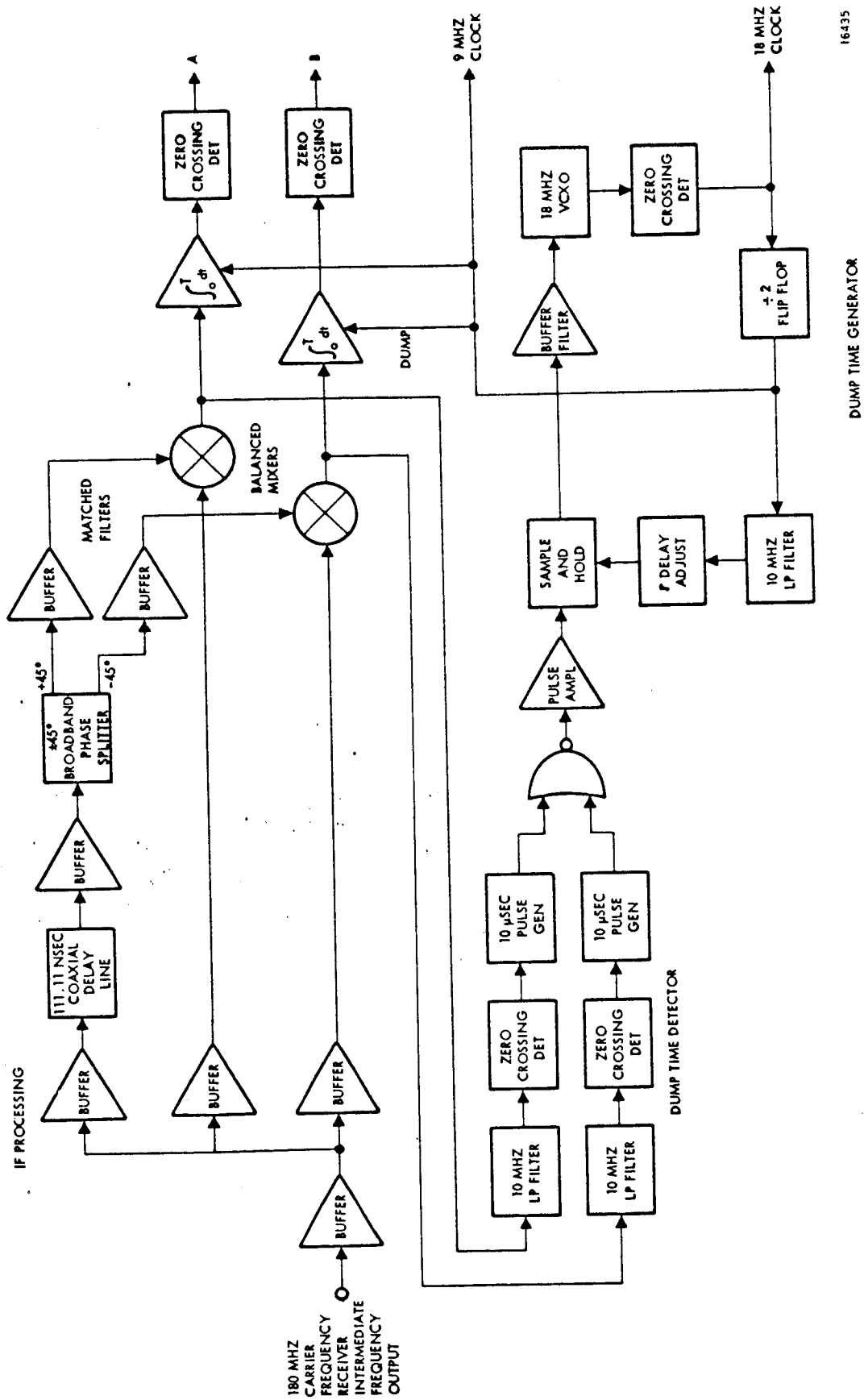
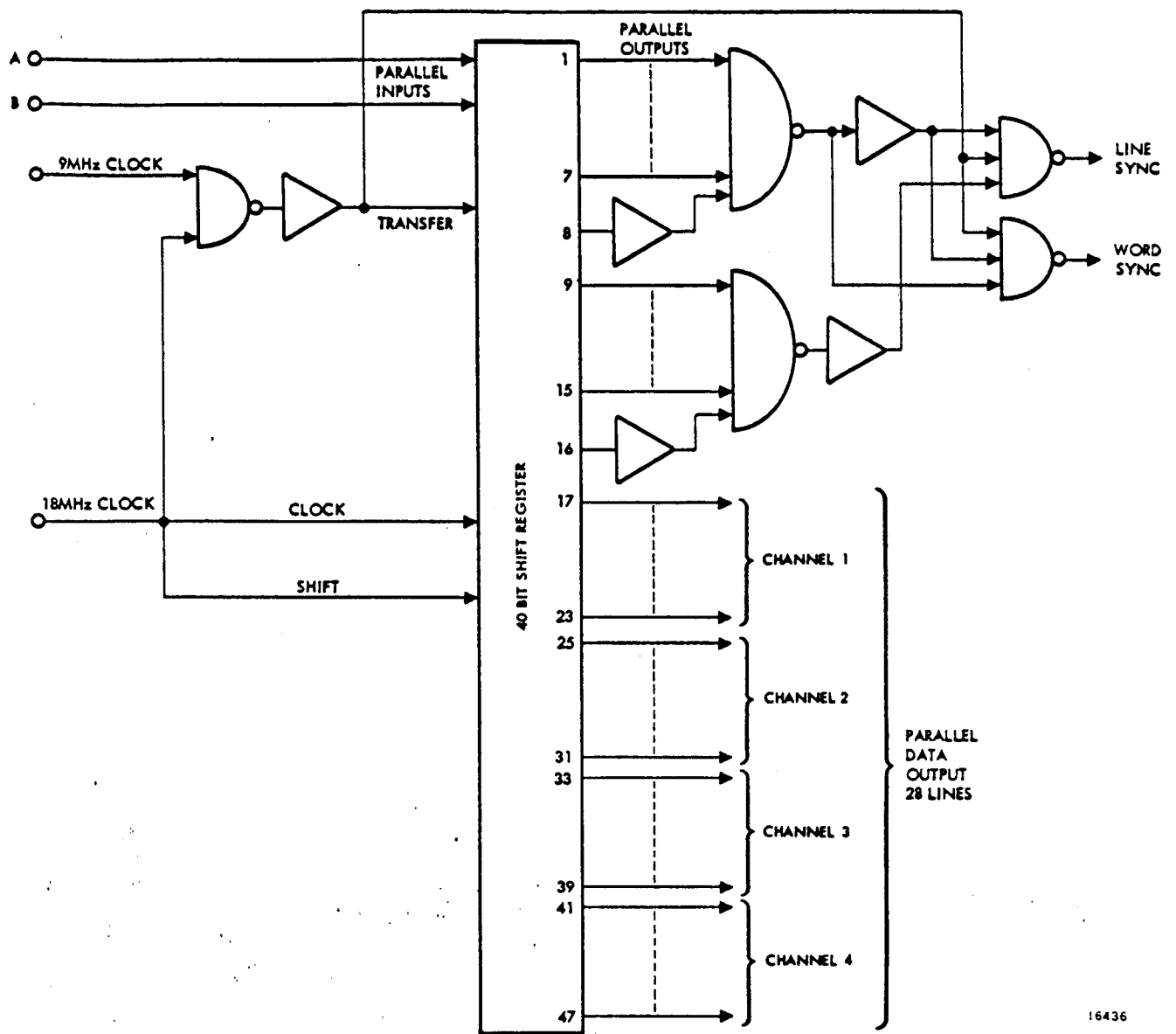


Figure 67. Receiver Demodulator.



16436

Figure 68. Demultiplexer.

MECHANICAL ANALYSIS

The physical size, weight, and precision requirements of the proposal MSPS system presented difficult mechanical design problems. The theoretical solutions and compatible hardware concepts generated to solve those problems will be discussed in this section. A description of a folded system which circumvents problems associated with the original system is also included. The extension of analysis performed for the original unfolded system will be noted with the resulting improvements in calculated performance.

The thermal study outlines a passive radiation control system and presents the orbital analysis used to verify system performance. In the materials study section, orbital environmental effects are studied and an optimum material system determined. It is found that with proper material selection, a thermally isotropic system can be made insensitive to axial gradients and mean temperature changes.

The structural study determines the configuration needed to satisfy the stress, dynamic, and thermal requirements.

The rotary drive systems study describes solutions to the basic scan and momentum compensation system problems including bearing and lubricant selection.

The folded tilted wheel system is described in the scan wheel systems section of the Structural Study. Examples comparing the folded system to the original system will be found in most paragraphs of this section.

Supporting equations and derivations for this section are in appendices III, IV, V, and VI.

Preliminary Description of MSPS Mechanical System

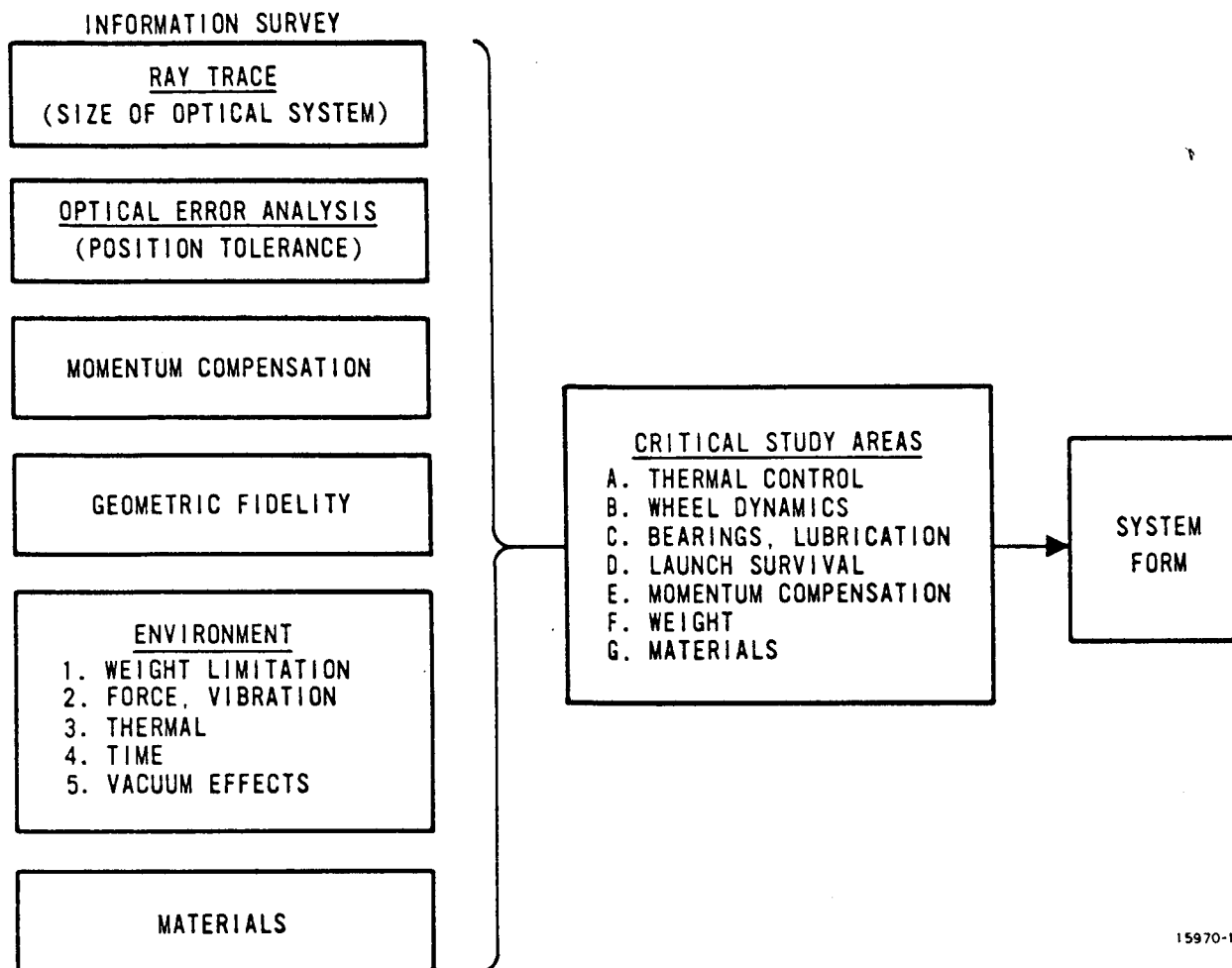
The proposed mechanical system evolved from an iterative systems analysis. Problem areas indicated by initial system studies indicated tentative solutions. These design approaches assisted in the development of the proposed mechanical system. Study areas leading to mechanical system definition are illustrated in figure 69.

The initial optical system was physically large (figure 70). The optical error analysis indicated a depth of focus of only ± 0.0004 inches at the primary image. The 26-inch diameter scan wheel had to scan the primary image with the above radial accuracy while maintaining a lateral runout of less than ± 0.0001 inches, to maintain 1/10 of an image resolution element width.

Total scanner system weight was limited to 65 pounds. An initial weight estimate, figure 71, indicated that the initial design approach would result in an overweight system even if low density materials were used. Other design approaches were necessary.

The system was designed to meet the Nimbus D environmental test specifications. The vibration specifications are presented in tables 17 and 18.

In addition to vibration, the system must survive a thrust axis centrifuging at 30g for 5 minutes, and three thermal cycles from +23 to +113° F.



15970-1

Figure 69. Mechanical Systems Analysis.

Table 17. Sinusoidal Vibration.

Frequency Range (Hz)	Acceleration Amplitude 0 to Peak (g)	
	Thrust Axis	Transverse Axis
10 to 70	6.0*	-
70 to 150	10.0	-
150 to 2000	7.5	-
5 to 40	-	6.0*
40 to 2000	-	7.5

*Exposure limited to 1/2-inch double amplitude.
Sweep rate - 1 octave per minute.

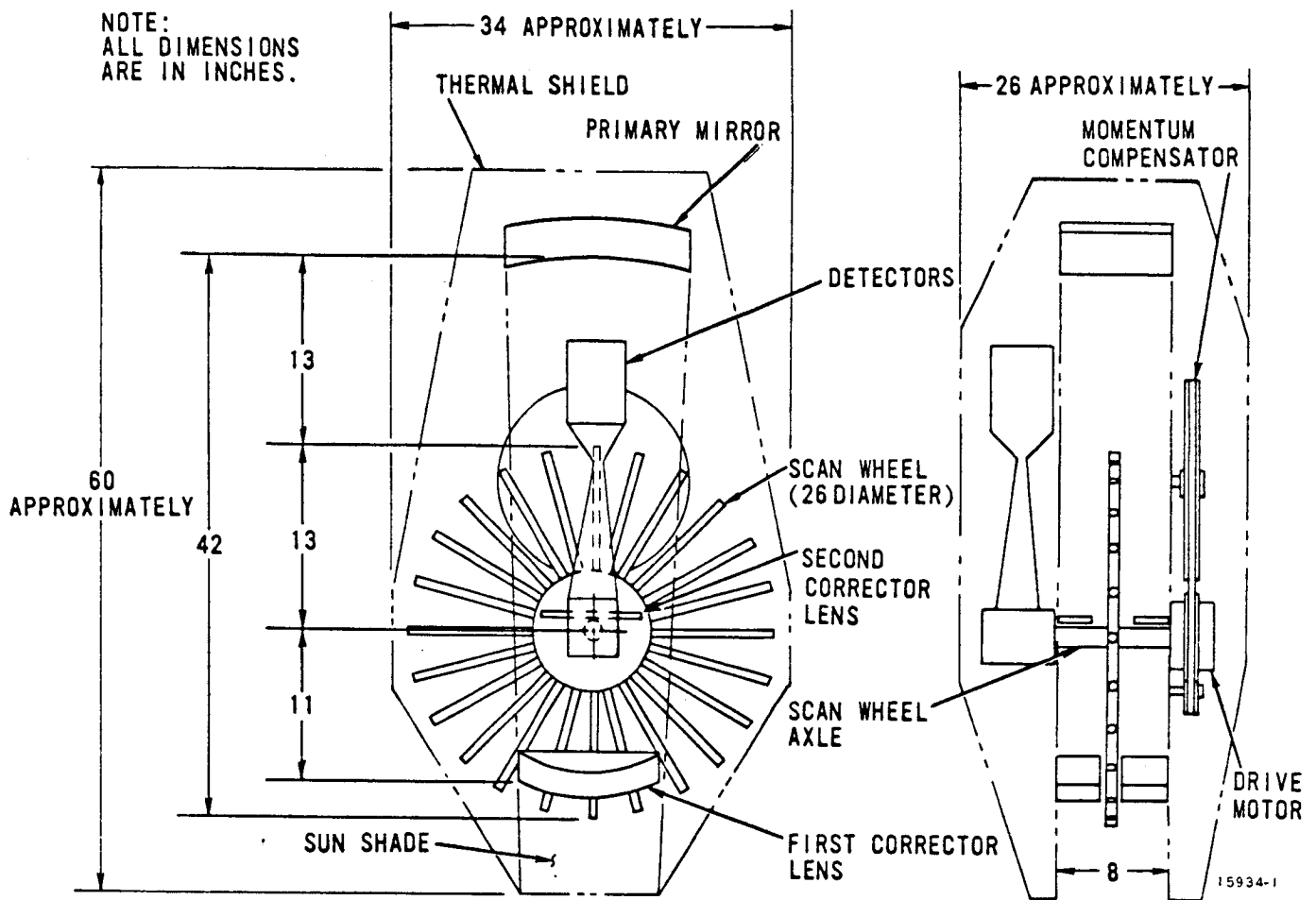


Figure 70. Initial Bouwers Achromat.

Table 18. Random Vibration.

Direction (4 minutes duration)	Frequency Band (Hz)	PSD (g^2/Hz)	Max g-rms
Thrust axis	20 to 2000	0.11	15
Transverse axes	20 to 2000	0.11	15

Angular momentum compensation was required to limit scanner momentum unbalance to the spacecraft to 0.06 inch-pound-seconds. This figure represented about 0.1 percent of the probable scan wheel momentum.

The following analyses resulted in a workable design for a slightly modified version of the initial system of figure 70. In addition, a folded tilted wheel scan system was established which would considerably reduce the size and substantially increase the reliability of the initial design.

Thermal Study

The thermal analysis was one of the most critical portions of the mechanical study. This is the result of the very small primary image depth of focus (± 0.0004 inch).

Passive thermal control was dictated by the low scanner weight and power allotments. The preliminary scanner weight allocation, figure 71, which gave 5 pounds for thermal control showed that it was still necessary to reduce total scanner weight by 30 percent over a light beryllium system.

A radiative passive control scheme, figures 72 and 73, was chosen for analysis because it was estimated that conduction in a low density structure would not be a predominant transfer mechanism. The initial materials study paragraph showed that the thermal control system was required to maintain primary mirror, structure, and scan wheel random mean temperature variations of less than 2° F of each other to maintain required focus over a structural length of 40 inches. A conceptual open-grid uniform structure (figure 72) was placed within a closed blanket shell of aluminized mylar high performance insulation (HPI). This shell was held away from the scanner by insulated standoffs. To a first approximation, the structure should present a low radiation resistance between the hot and cold insulation shell walls with resulting low structural temperature gradients.

In addition, if the shell walls are sufficiently removed from the uniform structural elements, the resulting similarities in geometrical shape factors should reduce the intensity of localized irradiation, i.e., hot spots.

The equivalent steady-state circuit for one HPI wall zone pair is shown in simplified form in figure 73. Reduction of R_2 would reduce the internal temperature difference between the

PREDETERMINED WEIGHTS:

WEIGHT (POUNDS)

DETECTORS	4
THERMAL CONTROL	5
1ST CORRECTOR	20
2ND CORRECTOR	3
TOTAL BEARINGS	2
SPECTROMETER	5
ELECTRONICS + MOTOR	9
	48

MATERIAL - DEPENDENT WEIGHTS:

WEIGHT (POUNDS)

	BERYLLIUM	ALUMINUM
PRIMARY MIRROR	8	21
SCAN WHEEL + PROBES	6	12
MOMENTUM COMPENSATOR	4	9
BODY STRUCTURE + CELLS	11	34
SPACE CRAFT MOUNTING	7	8
TOTAL	36	84
SYSTEM TOTAL	84	132

15958-1

Figure 71. Initial Weight Estimate.

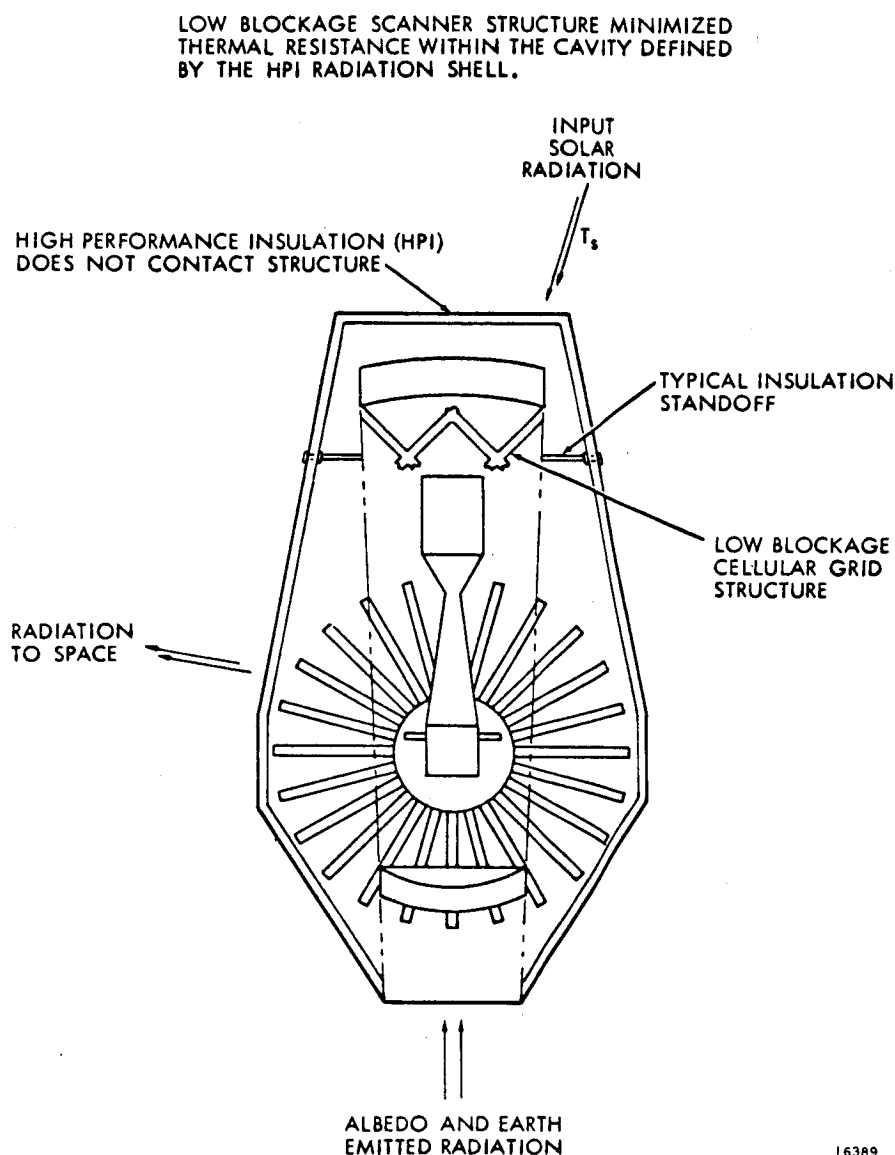


Figure 72. Passive Thermal Control System.

insulation shell surface, and the corrector lens (for the Bouwers concentric configuration) for the orbit of figure 76.

Blockage by the Nimbus D spacecraft's solar panels and central mounting torus was neglected as was the precession error of the orbit plane during the 1 year orbit life. The program showed that the large corrector lens received direct solar radiation for approximately 10 minutes while entering and leaving the Earth's shadow. A baffle was added to the bottom of the insulation shell to shield the lens from direct solar flux.

An average internal system temperature near room temperature was desired to simplify hardware testing in the laboratory. The input fluxes from the orbital analysis were averaged over the orbit and were used to calculate the external temperature effects of varying the absorptivity, α , and emissivity, ϵ , of the outer Kapton layer of the insulation shell. The corrector lens, surface 8, was not included in this calculation since it was connected directly

I-th and J-th wall zones. Increasing the coupling resistances, R_3 , -- R_9 , -- R_n , with respect to the mirror, structure, and scan wheel resistances, would reduce the temperature differences between the structural components. These differences result from inequalities between R_3 , R_4 , R_5 , -- R_n , and would be proportional to the wall zone temperature differences.

The potential simplicity and low weight of this system warranted investigation even though the primary mirror shadow, noninsulated scan window, and limited insulation standoff space would complicate the analysis.

An orbit model for evaluating the thermal control concept was generated using the McDonnell - Douglas Astronautics Corporation (MDAC) Orbital Thermal Environment Computer Program (F-872) and the insulation shell model of figure 74 and 75. The program computed the incident components of direct solar, reflected solar, and Earth emitted radiation for each

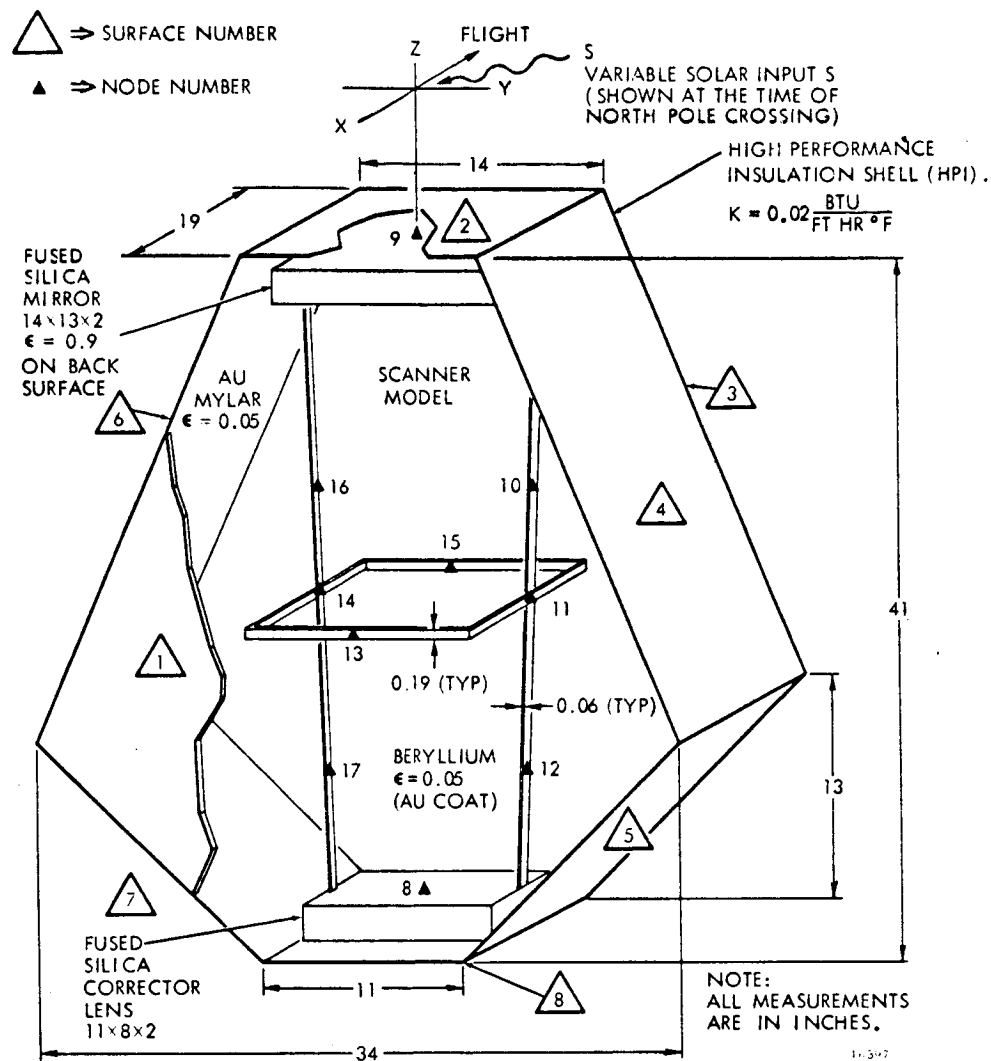


Figure 74. Simplified Model for Preliminary Thermal Calculation.

programmed into the interior of the HPI shell, figure 74. The eight-element structure was connected to the central corrector and mirror nodes through a fused silica path quasi-representative of an actual lens cell. The assembly was programmed into the MDAC, JA26-3D-Heat Transfer computer program. This program was not suited to transient calculations involving low heat capacity insulation systems, so the external surface temperatures were first calculated for an empty insulation shell using the F-872 orbital program, and then inputted to the JA26 program. Due to a coordinate rotation programming error, the insulation shell of figure 74 was rotated 90° in the $-Z$ direction. This effect tended to exaggerate the XY structural temperature gradients but did not affect the Z gradients. Plots of the insulation surface temperature are in appendix III. The model element temperatures for the fifth orbit are shown in figure 75.

After five orbits, the lens was still cooling the structure which would otherwise have come to equilibrium around 95°F . It was estimated that at least 20 orbits would have been necessary to achieve equilibrium. Once the equilibrium times are known for a system, it would

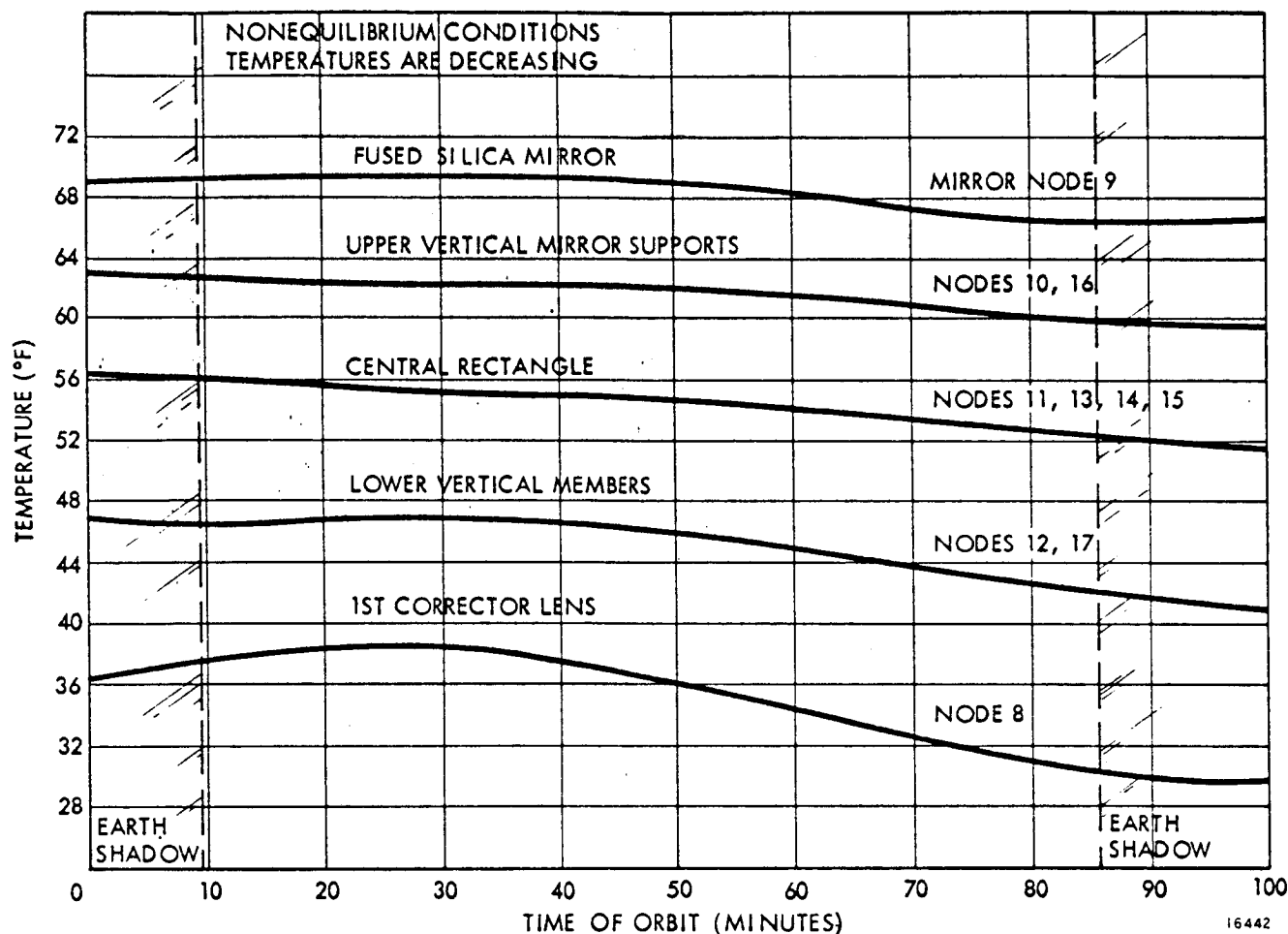


Figure 75. Element Temperatures for the Simplified Model of Figure 74 for the Fifth Orbit.

be sufficient to use steady-state gradient calculations to greatly reduce computer time. There was not sufficient time in the MSPS program to continue the gradient calculations.

It was apparent that a low system mean temperature would result from direct connection to the high emissivity corrector lens. The low mean was judged to be far more acceptable than would be the gradients if the mean were raised by increasing the solar input energy transfer through the HPI shell.

The corrector lens also appeared to control the temperature oscillations shown in figure 75. The structure and mirror oscillations were never out of phase by more than 3°F along the vertical optical axis. It was apparent that the control system could be improved sufficiently to reduce the gradients to the 2°F range by increasing the lens coupling resistance (R_G , figure 73). The lateral temperature gradients in figure 75 were so small that laterally symmetric nodes at the same vertical portion were plotted as one temperature. This meant that the radiation control concept for a low blockage direction in the structure was very effective, even for the highly nonsymmetrical side heating in the HPI shell. (Plots are given in appendix III.) This degree of efficiency cannot be realized in an actual structure due to higher blockage, but the efficiency would never be much less than that exhibited by the

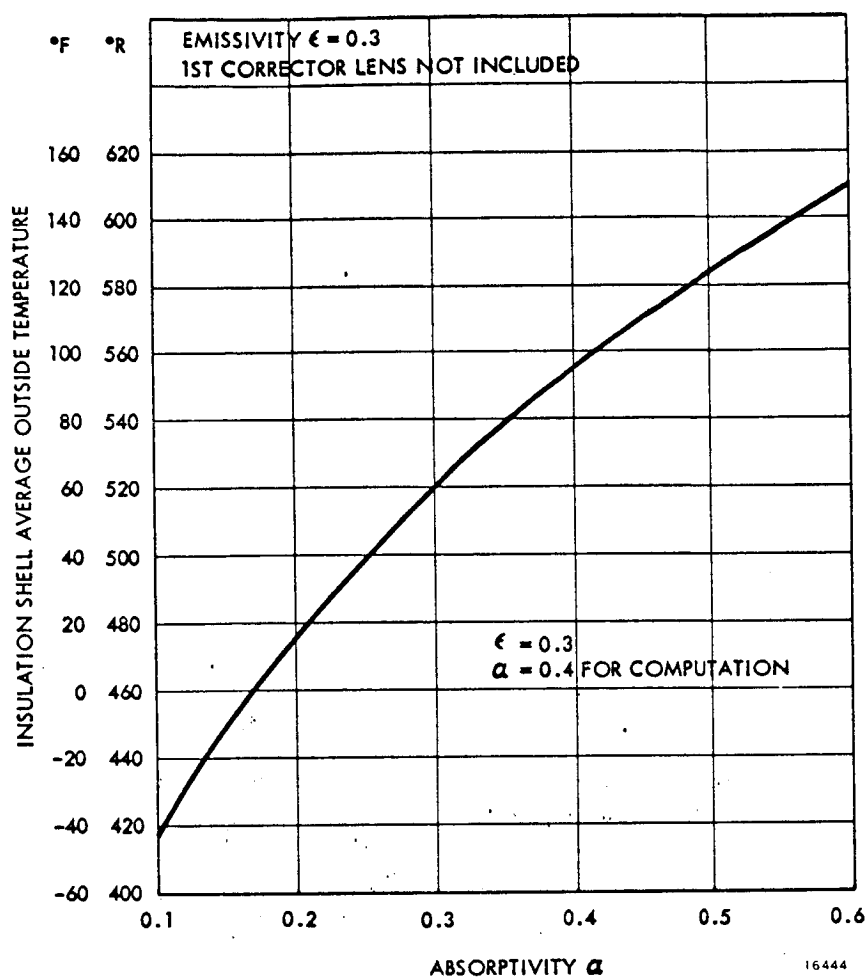


Figure 77. Orbital Average.

During the material study, it was determined that defocusing due to gradients, resulting from steady-state heat flow through the structure, could be reduced approximately by the cube of a structural size reduction at constant weight. This fact, and a vehicle interface size problem, led to the adoption of a third, and final modification of the original spherical scanning system. The final system, discussed in the paragraph on tilted wheel scanning, reduced the optical axis thermal path length by a factor of 2.5. This new tilted wheel system will be considerably less sensitive to changing orbital conditions than the preceding approach. Thermal analysis of the tilted wheel system is a task that must be performed before a final detail design can be made. Time did not permit this task within the present scope of work.

Materials Study

Scanner construction materials must be compatible with the scanner physical requirements and orbital environment. Initially we

knew that weight restrictions and the large scanner structural size would require emphasis on launch survival properties. In particular, a shallow depth of focus of the primary image sphere (± 0.0004 inch) sets a prime requirement for thermal and temporal dimensional stability.

To minimize the complexity of the optical system, there were no provisions for post launch adjustment of focus and alignment. Therefore, the launch survival criteria included preservation of mechanical tolerances. The orbital thermal environment could consume all of the focal tolerance so the initial mean focal length had to be preserved within a few micro-inches through launch, and subsequent 1 year orbit life.

Material dimensional stability during launch will depend on environmental vibration amplitude and vehicle acceleration bias, and the state of material residual stress. Cumulative plastic strains can result from a residual or acceleration bias stress potential if there is sufficient noncumulative plastic activity present during launch. Vibration stresses, sufficient to produce plasticity, can provide the necessary energy to induce secondary cumulative yielding. It was thus necessary to choose materials which could be stress relieved to levels below their microyield stresses (MYS). In addition, material with high gross yield strengths will be necessary to limit the noncumulative vibration plasticity which will otherwise trigger the bias induced cumulative strains. In general, launch acceleration bias stresses of less than 5000 psi are expected. Such stresses would induce slip on the order of 1 microinch per

inch of stressed material during the first few vibration plastic half cycles for a material having a MYS equal to 5000 psi. Subsequent creep during the remaining launch time should be negligibly small.

Vibration stresses were found to be inversely proportional to the ratio of elastic modulus to density. Referring to table 19A, beryllium has an E/ρ value six to nine times greater than the other materials. From table 19B, each of the materials listed has acceptable MYS values with the possible exception of magnesium. Additional material properties are listed in table 19C. Data for Invar were not available.

It was estimated that a locally stressed system of the type and size in question would survive launch if the following conditions were met.

- a. Bias stresses should be less than the MYS.
- b. Vibration stresses at points of maximum bias stress should be less than the gross yield stress.
- c. The material should not be in a state of metastable phase or stress equilibrium. This can be accomplished by relieving stress to the microyield stress (MYS) level, and vibrating per launch specifications prior to final focus.
- d. Appropriate distribution of material should be made to limit strains in the sensitive tolerance directions.
- e. Plated coatings having nonzero bonding stresses must have tensile and bond strengths in excess of the vibration stress level.

Long term dimensional stability in orbit will depend on the phase stability of the material, since the residual and working stress levels will be negligible. Phase stability is maximum in the unalloyed materials, beryllium and the glasses. The precipitation hardened aluminums and magnesium will have marginally acceptable microstability. The stability of Invar was studied. It was estimated that the required stability could be achieved after aging treatments of approximately 1 month duration. It will be necessary to carefully limit the post treatment temperature exposure of an Invar or super Invar system to the approximate range at 20 to 130° F. This range was within the required vehicle exposure cycle.

The effects of thermal expansion were considered and a simplified model was developed to guide the initial hardware design effort.

Thermal gradient control in orbit is to be obtained by passive means. However, the mean system temperature cannot be controlled by passive techniques due to uncontrolled environmental changes. The simplest material solution known to be compatible with various uniform mean temperatures is the so-called "isotropic" system. In an isotropic system, all of the materials have the same thermal expansion coefficients, ϵ , within the specified operating range. The system shown in figure 78 will remain in focus at any condition which provides a solution to equation (1):

$$\frac{L_m}{2} - L_s + L_w = 0 \quad (1)$$

where

- L_m = primary mirror radius
- L_s = structure length
- L_w = scan wheel radius

Table 19. Material Properties.

A

Material	Thermal Expansion $\xi \times 10^6$ (1/° F)	$\frac{K}{\xi \rho} \times 10^{-6}$ (BTU IN ³) (FT-HR-LB)	Matsukov Coefficient $\frac{EK}{\rho \xi C_p} \times 10^{-14}$ (IN-LB ° F) (FT-HR)	$\frac{E}{\rho} \times 10^{-6}$ INCHES	Material	MYS (PSI)	Elastic Limit (PSI)
Beryllium	6.42	248	237	667	Beryllium* I-400	5,000	60,000
Tenzalloy	13.4	58	27	103	Tenzalloy	--	22,000
Aluminum 356	11.8	85	41	108	Aluminum 356	12,000	23,000
Invar 36	0.56	38	68	75	Invar 36	--	20,000
Titanium	4.67	9.6	11	88	Titanium 6A1-40	70,000	100,000
Magnesium	14.4	71	19	103	Magnesium AZ31	3,000	33,000
Cer-vit	< .08	> 166	> 101	147	Cer-Vit	--	--
Fused Silica	0.28	35	23	132	Fused Silica	--	--
Super Invar (C.D.)	0.29	73	130	75	Super Invar	--	20,000
Bearing Steel 52100	6.4				Bearing Steel 52100	40,000	100,000
Bearing Steel 440C	5.6				Bearing Steel 440C	75,000	150,000
Electroless Nickel	7.2				Electroless Nickel	--	--

B

* After Stabilization Heat Treat

C

Material	Youngs Modulus $E \times 10^{-6}$ (PSI)	Weight Density ρ (LB/IN ³)	Thermal Conductivity K (BTU)/(FT-HR ° F)	Heat Capacity C_p BTU/LB ° F
Beryllium	44.0	0.066	105	0.46
Tenzalloy	10.3	0.100	78	0.22
Aluminum 356	10.5	0.097	97.6	0.22
Invar 36	21.4	0.286	6.05	0.12
Titanium	14.3	0.163	7.3	0.13
Magnesium	6.5	0.063	64.4	0.25
Cer-Vit	13.4	0.091	1.21	0.22
Fused Silica	10.5	0.080	0.78	0.17
Super Invar	21.4	0.286	6.05	0.12

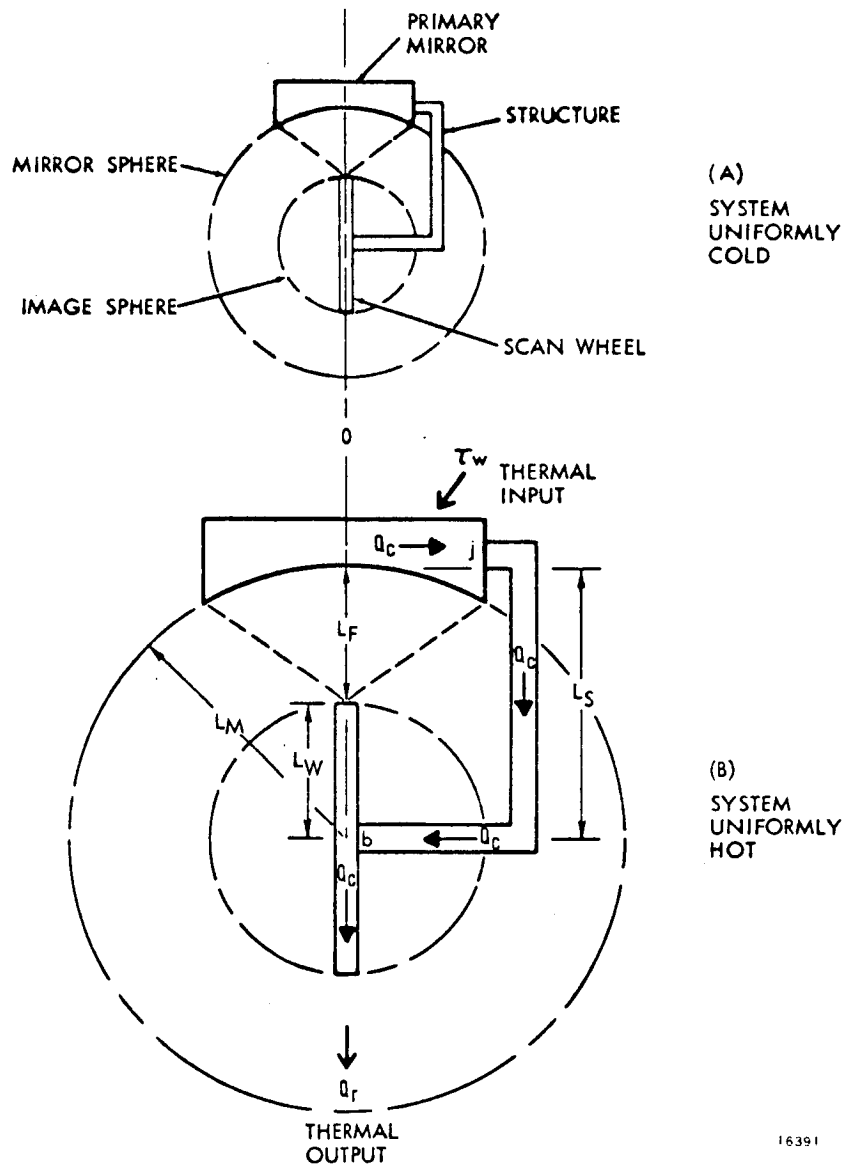


Figure 78. Isotropic System, Dimension Scaling.

It was apparent from figure 78 that an isotropic system will change scale without defocusing for a uniform change in volume. All expansions will be uniform and equation (1) will be satisfied for that condition. Equation (1) was rewritten to include the effects of temperature and expansion coefficients on the component lengths for a three component model:

$$\Delta F = C_1 \frac{L_m}{2} - C_2 L_s + C_3 L_w = 0 \quad (2)$$

$$\Delta F = \epsilon_m \Delta T_m \frac{L_m}{2} - \epsilon_s \Delta T_s L_s + \epsilon_w \Delta T_w L_w \quad (3)$$

where,

ΔT = change in component mean temperature

ϵ = thermal expansion coefficient.

For a perfectly isotropic structure:

$$\epsilon_m = \epsilon_s = \epsilon_w$$

and,

$$\Delta F = \Delta T_m \left(\frac{L_m}{2} \right) - \Delta T_s L_s + \Delta T_w L_w = 0. \quad (4)$$

One solution to (2) is $C_1 = C_2 = C_3$. From (4) it is apparent that $\Delta T_m = \Delta T_s = \Delta T_w$ implied zero focus change for an isotropic system subjected to a uniform change in component mean temperatures. Since the simple solution above was not the only solution to (2), it is possible to incorporate the more sophisticated gradient controls discussed later.

Focal shifts for the mean change condition, due to errors in matching ΔT 's and ϵ 's, were apparent from (3). Equation (3) was rewritten to show that mean temperature error effects are linear in system size for a given system:

$$\Delta F = L_m \left[\frac{E_m \Delta T_m}{2} - E_s \Delta T_s + \frac{E_w \Delta T_w}{2} \right] \quad (5)$$

An example of a 24-probe aluminum system showed that three-fourths of the ± 0.0004 -inch focal tolerance will be absorbed by an arbitrary 2° F zero flux gradient. A representative gradient pattern was chosen which displaced the scan wheel and mirror 1° F from the structure in opposite directions. The same fixed gradient conditions were applied to an aluminum tilted wheel system, figure 79. The defocus was found to be only three-eighths of the focal tolerance, due to the shorter thermal path lengths. The magnitude of the defocusing depended on the particular regions affected by the gradients and the temperature ratios. For zero flux gradients, the defocusing is proportional to the first power of the physical system size.

Initial results from the thermal analysis indicated that the relative phase of arbitrary cycling gradients can be controlled to 2° F. These gradients are of the transient phase lead or lag type resulting from the day/night orbital cycling and nonzero heat capacities of the various material zones. However, the passive control system cannot limit the mean spread of the average zone temperatures to 2° F at equilibrium. In addition, the spread can change due to variable insulation surface properties and solar angle during orbit life. The principal thermal flux in the structure, which causes the spread in the mean component temperatures along the optical axis, comes from solar input near the mirror. This flux can be conducted parallel to the axis and dissipated through the scan wheel to the open scan window. Since focus is most sensitive to gradients along the optical axis, it is sufficient to generate material solutions applicable to that axis, and not necessarily applicable for other directions.

The representative circuit of figure 73 (paragraph on thermal study) was used for an axial analysis of the effects of thermal flux. Considering the I-th wall to be the hot surface near the mirror and the J-th wall to be the scan window, the applicable axial thermal path was $R_1 - R_5 - R_m - R_j - R_s - R_b - R_w - R_8 - R_j$. The radiative coupling resistances R_4, R_6 ,

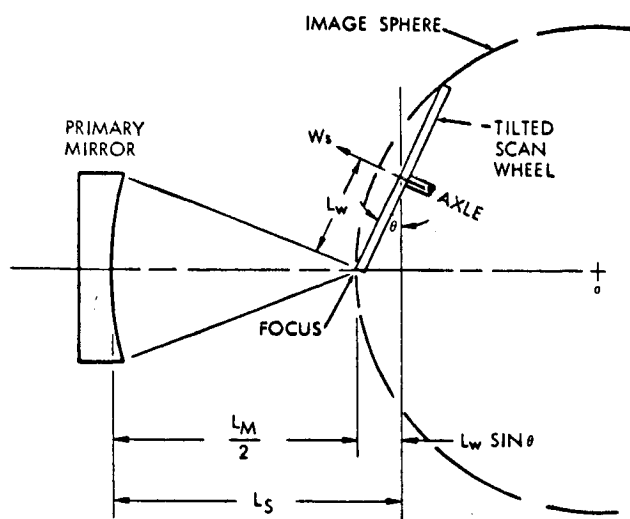


Figure 79. Shortened Thermal Path of Tilted Wheel System.

etc. were neglected to simplify the resulting equations. The resulting series circuit, figure 80, included scan wheel bearing and mirror mounting resistances, but not heat capacities. The subsequent equations thus represented steady-state flux conditions. This approach is justified by the thermal analysis, which has shown that the temperature phase lags during any orbital period are less than 2°F . The phase lags resulted from slowly changing the flux values in components with small but nonzero heat capacities. On this basis, it was decided that an isotropic solution for any uniform temperature change, plus the knowledge that phase differences would be less than 2°F , plus an isotropic solution for any reasonable optical axis flux, will suffice to approximate invariant focus.

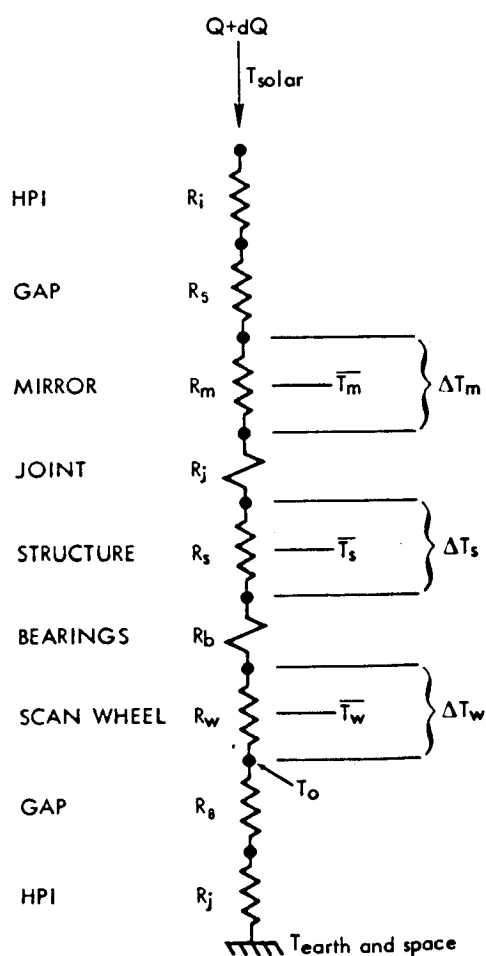


Figure 80. Principal Thermal Path.

The isotropic solution for thermal flux was determined. From appendix IV, equation (8), for the 24-probe three-component model, the change in focus due to a constant flux, Q , was:

$$dF = Q \left\{ \frac{1}{2} L_m \epsilon_m \left[\frac{L}{KA_w} + \frac{L}{KA_s} + \frac{1}{2} \left(\frac{NL}{KA_m} \right) + R_b + R_j \right] + \right. \\ \left. - L_s \epsilon_s \left[\frac{L}{KA_w} + \frac{1}{2} \frac{L}{KA_s} + R_b \right] + L_w \epsilon_w \left[\frac{1}{2} \frac{L}{KA_w} \right] \right\} \quad (6)$$

where,

Q = steady thermal flux (Btu/hr)

L = component length (ft)

ϵ = component thermal expansion coefficient (inch/inch $^{\circ}\text{F}$)

K = component thermal conductivity (Btu/ft hr $^{\circ}\text{F}$)

A = component cross sectional area (ft 2)

N = thermal path length equivalent fraction for mirror

R_b = combined scan wheel bearing resistance (hr $^{\circ}\text{F}$ /Btu)

R_j = mirror mount resistance (hr $^{\circ}\text{F}$ /Btu)

L_m = mirror radius (inch)

For a perfectly isotropic system:

$$\epsilon_m \equiv \epsilon_s \equiv \epsilon_w ; K_m \equiv K_s \equiv K_w$$

Solving equation (6) for $dF = 0$ yields the condition for invariant axial focus for an isotropic system subjected to an axial thermal flux (figure 81):

$$\frac{NL_m}{A_m} - \frac{L_w}{A_w} + 2K (R_j - R_b) = 0 \quad (7)$$

This model can be extended to any number of components in a final design effort.

Equation (3) related the length to area ratios of the system components in terms of the joint and bearing resistances. A number of valid solution combinations exist for equation (3), any of which would yield a system whose axial focus was insensitive to steady axial thermal flux to the first approximation. In actual practice, since the thermal flux through the mirror is in part radial, there would be small secondary effects on mirror figure beyond the simple scale response to mean temperature.

The mechanism of solution (7) is different from that found in the simple isotropic solution for the uniform temperature change. In equation (7), the C's of equation (2) were unequal. Solution (7) maintained focus only on the structural axis. A pure scale change can occur only for equal C's. As a result, the scan wheel diameter is no longer equal to the mirror radius during an applied flux, even though the upper wheel periphery is constrained to remain at the primary focus. The wheel center is displaced (by the flux) from the image sphere center by an amount, δ_L :

$$\delta_L = \frac{1}{2} \Delta L_m - \Delta L_w. \quad (8)$$

From figure 81,

$$\text{focal shift} = \Delta F = \delta_L \left(1 - \cos \frac{\varphi_s}{2} \right) \quad (9)$$

where,

$$\frac{\varphi_s}{2} = \text{scan half angle}$$

Apply condition (7) to equation (8) after substituting values from (6):

$$\Delta F \left(1 - \cos \frac{\varphi_s}{2} \right) Q L_m \epsilon \left[\frac{R_w}{2} + \frac{R_s}{2} + R_b \right] \quad (10)$$

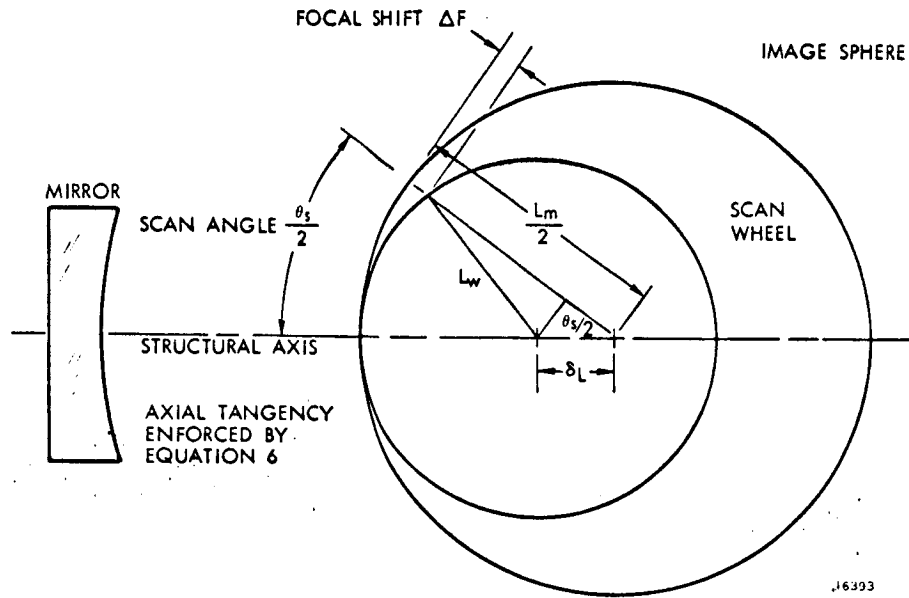


Figure 81. Focal Shift Due to Axial Thermal Flux for Isotropic Gradient Controlled System.

For a constant weight independent of material type:

$$\Delta F = \left(1 - \cos \frac{\phi_s}{2}\right) Q L_m^3 \left[\left(\frac{\rho \epsilon}{K}\right) \left\{ \frac{1}{8 W_w} + \frac{1}{2 W_s} \right\} + \frac{\epsilon R_b}{L_m^2} \right] \quad (11)$$

where,

W_w = scan wheel weight effective in instantaneous conduction path

W_s = structural weight effective in conduction path.

This is the change in focus for an isotropic probe system which conforms to control equation (7).

Equation (11) indicates that focus shift for a gradient condition at constant weight is proportional to the cube of the system size.

An example was generated from equation (11) to determine the best choice of material properties. A weight of 10 pounds was assumed to be thermally effective over the 40-inch path for the 24-probe system. The results for four materials are plotted against scan wheel bearing resistance in figure 82. The term, K_D , is a function of material distribution.

A tradeoff between bearing resistance (also joint resistance per equation (6)) and material thermal properties is evident. It was estimated that total bearing resistance would be near 70 hr °F/Btu. The superiority of Invar is apparent. Super Invar is approximately 20 times

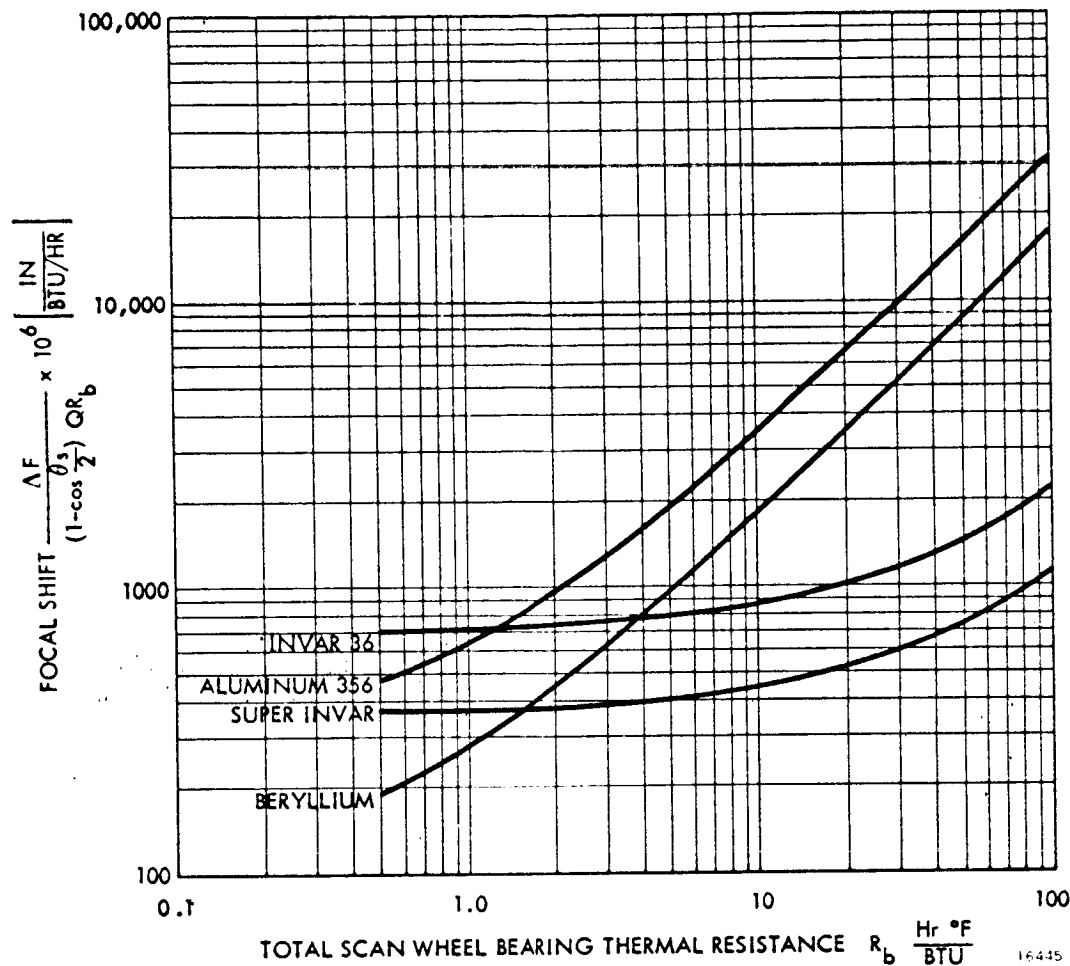


Figure 82. Total Scan Wheel Bearing Thermal Resistance.

better than aluminum 356 in the range of interest, where joint and bearing resistances are predominant over structural resistance.

For a super Invar 24-probe system, a 15° F gradient will result in a flux, Q , of about 0.06 Btu/hr. From figure 82 for a maximum scan half angle of 7.5° , the maximum defocus for a 60° truss configuration system ($K_D = 1.33$) will be:

$$\Delta F = (1000) (1 - 0.9914) (0.06) (1.33) 10^{-6} \text{ inches}$$

$$\Delta F = 0.000,000,7 \text{ inch.}$$

The control provided by a perfect solution to equation (7) is in excess of the requirements. There will thus be room for structural approximations to (7). Most of the approximations will probably be absorbed by the mirror and mirror mount, since the mirror will not actually be constructed from Invar, but from a thermally matched glass, such as fused silica, to obtain an adequate optical substrate. Control of the thermal path in a fused silica mirror will be only approximate due to the difficulty of shaping the mirror blank to obtain an exact solution to equation (7).

Comparison of the Matsukov coefficients of the various materials, table 19A, showed that fused silica will ordinarily be a poor choice for a mirror material subjected to a variable

thermal environment. The ability of fused silica to resist deformation and to recover from local thermal gradients is inferior to most of the metals and to Cer-Vit. However, the thermal analysis indicated that the local thermal uniformity in the insulation shell will permit the use of fused silica if the glass were coated all over with a low emissivity material, such as gold or aluminum.

The choice of Invar and fused silica will also hold for the tilted wheel system, since its bearings and joints will be similar to those in the 24-probe system. The advantages of the threefold decrease in size for the tilted system over the original 24-probe scanner are inferred from the above equations. It was estimated that the tilted system will be less than half as sensitive to heat capacity induced cycle gradients and a quarter as sensitive to axial flux.

A preliminary structural design iteration should be made using the above simplified system model and the equations in appendix II. The model should then be expanded to include active heat sources, such as motor and bearings. Additional control zones should be incorporated as components are added.

Structural Study and Dynamic Analysis

The structural study established a way to distribute structural materials in the various scanner components. The distribution was subordinate to the weight, size, and thermal requirements determined in paragraphs on thermal study and materials study.

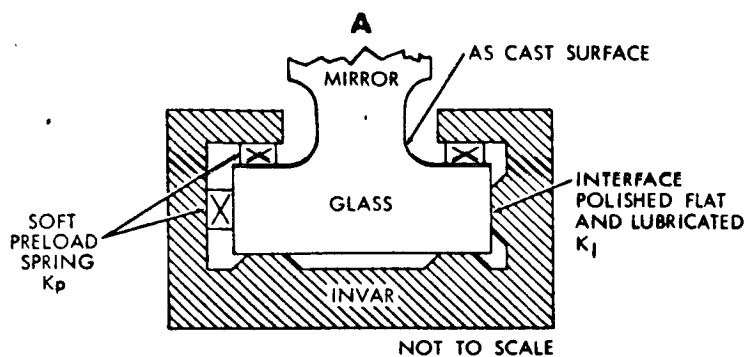
The study consisted of stress and dynamic analyses. Where the material constants used in examples were not those pertaining to Invar or quartz, the applicability is noted.

Scanner Body Structure. -The basic forms of the body and primary mirror were determined first, since these were considered to be the most difficult areas of the body assembly. Detailed design of smaller components was not undertaken due to lack of time.

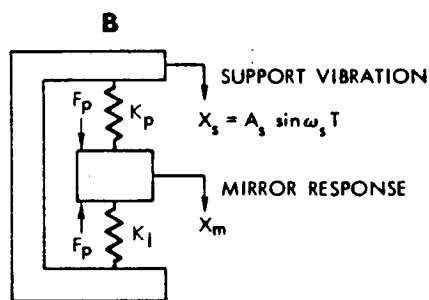
Mirror Mounting. -The primary mirror is fused silica weighing about 10 pounds. The requirement for maintaining focus in the presence of system axial gradients and varying mean temperatures meant that finite lateral thermal strain differences had to be accommodated between the mirror and body structure. At the same time, the optical axis alignment and vertical indexing of the mirror against its mounts has to be maintained to at least one-tenth of the total ± 0.0004 tolerance. The remaining tolerance is required by the thermal system.

The mirror is supported at three points. The location points would be optimized during the mirror design. Each of the three mounting locations will consist of a glass extension from the mirror and an Invar preload fixture. One of the fixtures will index the mirror to the structure in all three translation axes. The second unit will fix two rotation directions, and the third will stabilize the remaining rotation.

A typical preload fixture for two translation axes is shown in figure 83 view A. The glass extension will be preloaded against three surfaces of the Invar fixture by soft springs of spring constant K_p . The glass/Invar interface, polished flat and parallel to 1/10 of the elastic preload deflection, will be lubricated to prevent bonding and permit small movements between the glass and metal at relatively low friction load. The preload will be confined to the glass extension. Only the friction loads in the other two rotation fixtures will be carried through the mirror substrate.



MIRROR MOUNT FIXTURE



MOUNT ELASTIC MODEL FOR ONE AXIS

Figure 83 view B illustrates the elastic model for one axis of freedom for the fixture of view A. The mirror extension and Invar interface form a stiff spring, K_I . The natural frequency of the coupling system, neglecting damping, is:

$$\omega_n = \sqrt{\frac{K_s + K_I}{M}}$$

where,

M = mirror mass.

The relative movement of the mirror and structure is:

$$X_m - X_s = \frac{\omega_s^2}{\omega_n^2 - \omega_s^2} A_s \sin \omega_s t$$

where,

ω_s = support vibration frequency

ω_n = natural frequency of coupling

A_s = amplitude of support vibration.

Figure 83. Mirror Mount.

From an elastic solution for flat 3:1 rectangular plates in contact:

$$K_I = \frac{F_p}{\delta_p} = \frac{\sqrt{A}}{0.88 \left[\frac{1 - \nu_G^2}{E_G} + \frac{1 - \nu_m^2}{E_{ir}} \right]}$$

where,

F_p = preload

δ_p = static mirror deflection due to preload

A = interface area

ν = Poisson ratio

E = Young's modulus.

Figure 84 illustrates an example for a 10 pound mirror subjected to a 7.5g support vibration. The maximum preload, 125 pounds, required to maintain mirror/Invar contact at

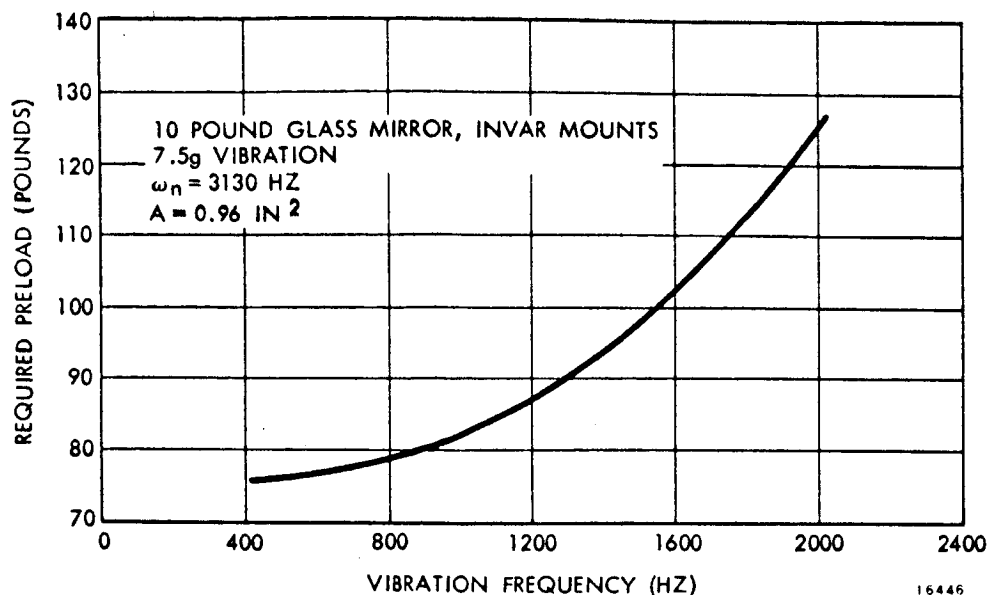


Figure 84. Mount Preload Required to Retain Glass Mirror in Invar Compression Mount.

2000 Hz will not cause material failure. However, creep and friction problems might make it desirable to isolate the scanner from the inputs above 1000 Hz and decrease the preload.

Structural Distribution.—The 24-probe scanner size and weight parameters demand a low density structural solution. A welded tubular truss design using a total of 18 tubes is necessary to obtain the required strength from Invar. A maximum design stress of 6,000 psi for the 30g centrifuge, and 10,000 psi at 10g vibration levels yield an average tube size of 0.75 inch outside diameter by 0.035 inch wall thickness. After optimizing the tube properties for uniform stress, the tubular weight is 6 pounds. The combined gusset plate and mirror mount weights are 4 pounds. The synthesized structure is shown in figure 85. The scan wheel, momentum compensator, and spectrometer interfaces with the body structure at tube junctions. Moments between the scan wheel and compensator are carried by the large diameter structural tubes which act as closed torque tubes. The large tube diameters are permissible from a thermal standpoint. The total radiation blockage is minimized by minimizing the number of truss members.

Spectrometer Housing.—The optical and sensory elements in the spectrometer are too closely grouped to permit the use of a low blockage housing. It was decided to mount the elements in a closed thin sheet tubular container. The spectrometer will be mounted to the side of the body housing at tube junctions per figure 85. The package is vertically oriented with its longest dimension parallel to the scanner optical axis to minimize vertical thermal radiation blockage. Adjustment of the spectrometer location, relative to the scanner output light beam, will be accomplished at the two mounting points.

Scan Wheel Systems.—The preliminary wheel system contained 24 optical probes, was 27 inches in diameter, and was placed on edge in the primary optical path. The major study effort for that design centered around building a thin stiff wheel to minimize optical blockage and weight while maintaining suitable optical tolerance and geometric fidelity.

The subsequent tilted scan wheel relaxed the weight and stiffness problems. The study of the tilted scan wheel concept dealt with the design tradeoffs between the effects of scan focus curvature, wheel speed, and geometry. In the tilted scan wheel concept, the scanner wheel

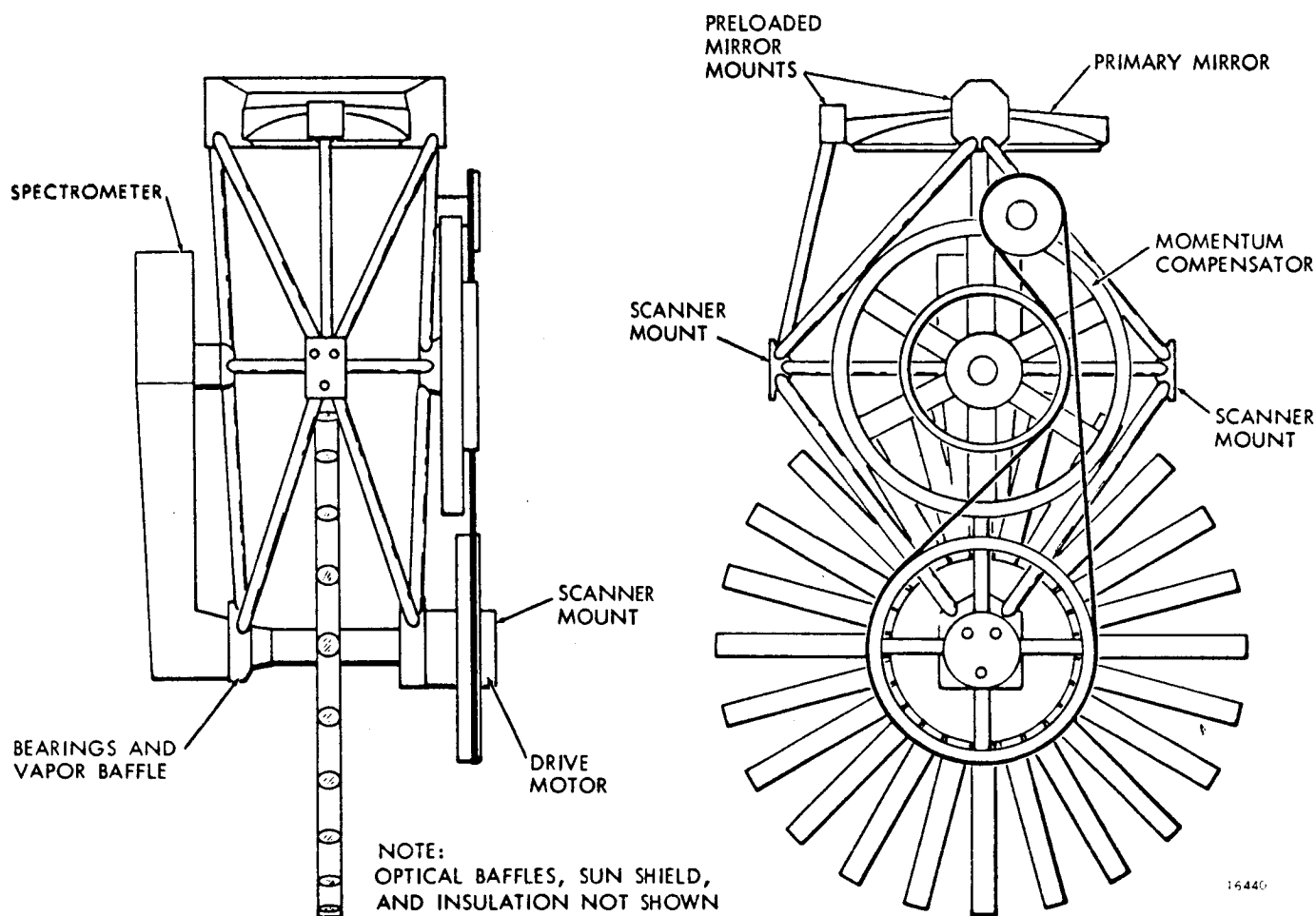


Figure 85. Invar Tube Scanner Structure.

was completely removed from the optical path by a folding mirror. In this manner, blockage was considerably reduced.

Dynamics and Design Considerations (24-Probe Wheel). -The thermal requirement of a low blockage structure combined with high structural efficiency, demanded by the scanner weight/size parameters, suggested the structural forms of figure 86. A peripheral hoop design analysis was included to assess the value of tangential stiffening.

Since the wheel was to be placed on edge in the incoming parallel light beam, the total wheel area (blockage) within the 8-inch aperture had to be minimized. Blockage is composed of two items, wheel thickness and axle thickness. Figures 87 and 88 illustrate the blockage problem in terms of the wheel thickness, W . The axle thickness was fixed by the probe output light cone. Various cantilever axle designs were studied and rejected due to body structure weight. The maximum permissible wheel thickness is limited by the optics to 1 inch. This yielded 40 percent blockage.

The basic deformation modes for the spoked wheel are illustrated in figure 89. In figure 89 view A, a wheel spinning about the Z-axis and rotated about the Y-axis will deform, as shown, due to gyroscopic forces. The axial deformation shown in figure 89 view B is of the form caused by the lowest wheel axial vibration mode. The effect of a rigid peripheral hoop is illustrated on the bottom spoke of each view. The predominant effect of the hoop for

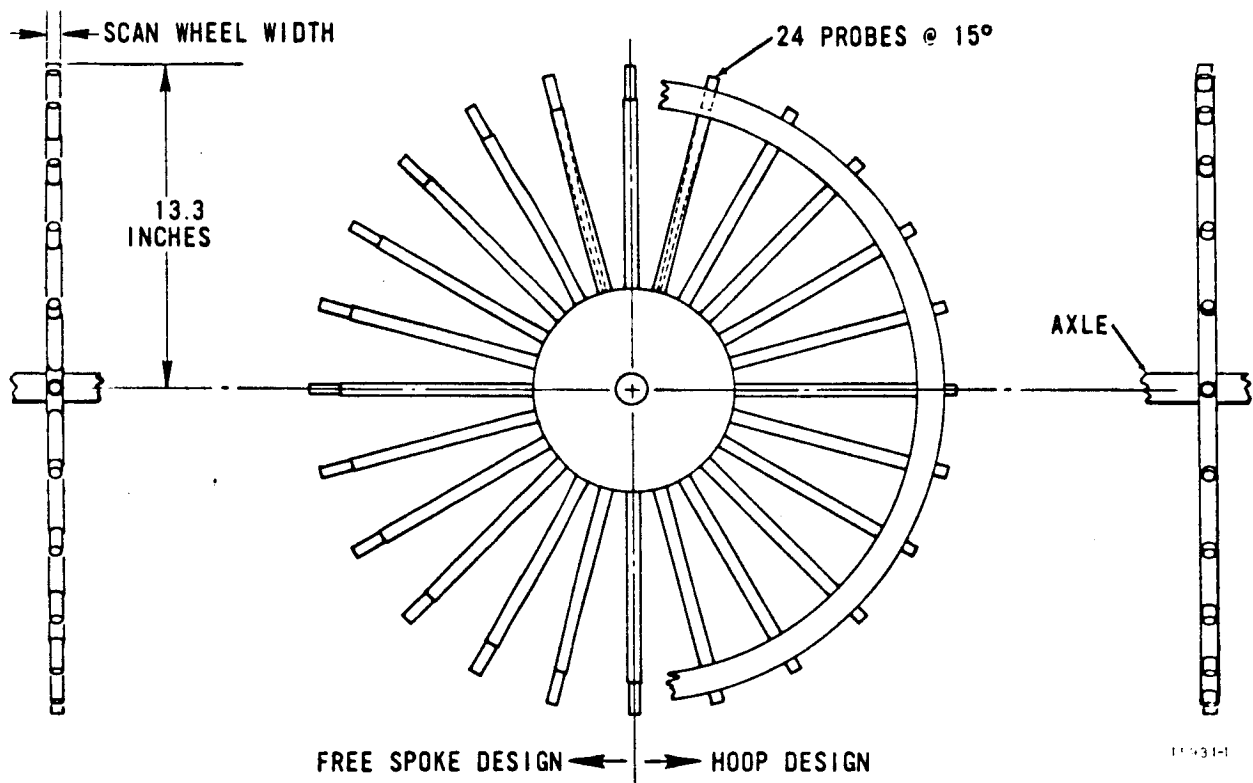


Figure 86. Preliminary Scan Wheel Forms.

these modes is to constrain the spoke tip angle, thus effectively increasing the stiffness of the spoke.

The gyroscopic deflections for spoked wheels with and without hoops were explored extensively. A summary of the resulting equations is included in appendix III. The gyroscopic mode is important because it describes the basic dynamic stability of the disk. It was determined that if the Y-axis secondary rotation suddenly ceased, as in transient excitation, the disk normal vector, N , would remain deflected at angle ϕ and would begin to orbit the Z-axis in a cone at characteristic frequency ω'_p . The warped disk would introduce a cyclic sinusoidal skewing of the image scan line. The effect would die away at a rate proportional to ω'_p , and to the material damping characteristics.

The effect of a peripheral hoop on gyroscopic and vibration deformation was found to depend on the hoop section efficiency and material properties. The ratio of torsional and bending stiffness to hoop weight determined whether the hoop would increase or diminish the deformation. Time did not permit a complete study of the hoop phenomena, but initial calculations indicated that a 1-inch wheel thickness would not permit an efficient hoop section design. Consequently, the hoop design approach was dropped and subsequent design examples are for free spoke designs.

The axially deflected vibration mode is important during launch due to the highly resulting spoke stresses. It was previously shown that sinusoidally varying spoke stresses should be limited to 10,000 psi or less to avoid plastic distortion. A material distribution study was performed for the wheel spokes. The most efficient sections for the present case are square and circular tubes. A comparison of the two sections, figure 90 show that the circular tube is superior to the square tube for thin wall sections having a ratio of inner to outer dimensions of 0.576 or greater.

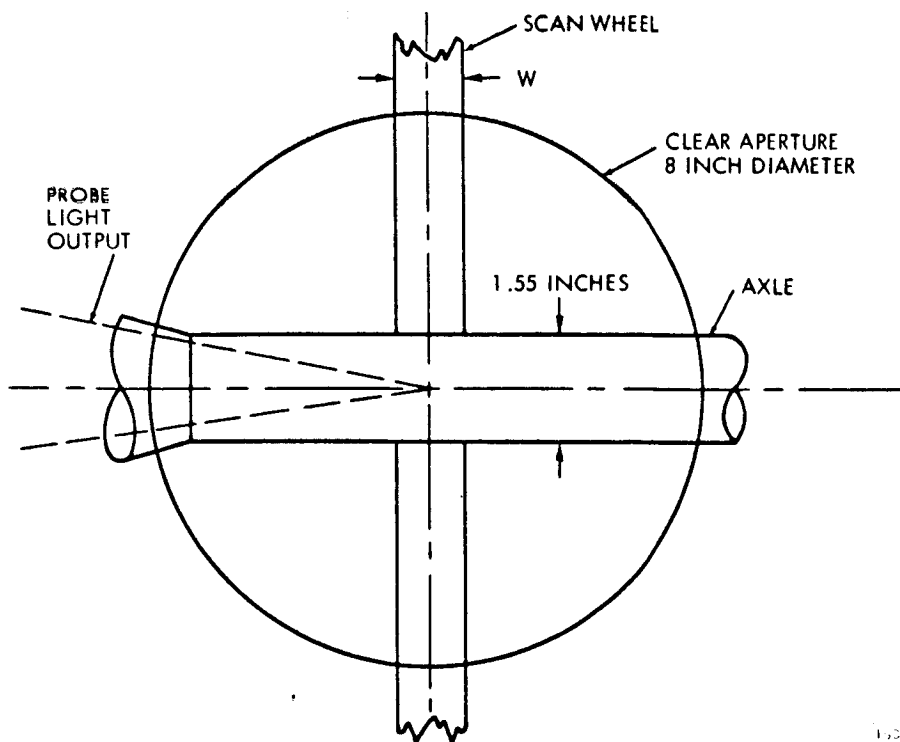


Figure 87. Primary Optical Blockage.

A vibration and stress study for a free spoke system was performed to determine the required amount of structural optimization. The high frequency lateral vibration direction was studied first because that mode was less dependent on wheel hub configuration than the axial mode. Figure 91 indicates the results of subjecting nontapered spoked wheels of various materials and thicknesses to 200g resonant conditions. Beryllium wheels are superior due to the superior material properties. The aluminum and Invar wheels are similar in response due to the similarity of E/ρ properties (see paragraph on materials). The 5,500 psi

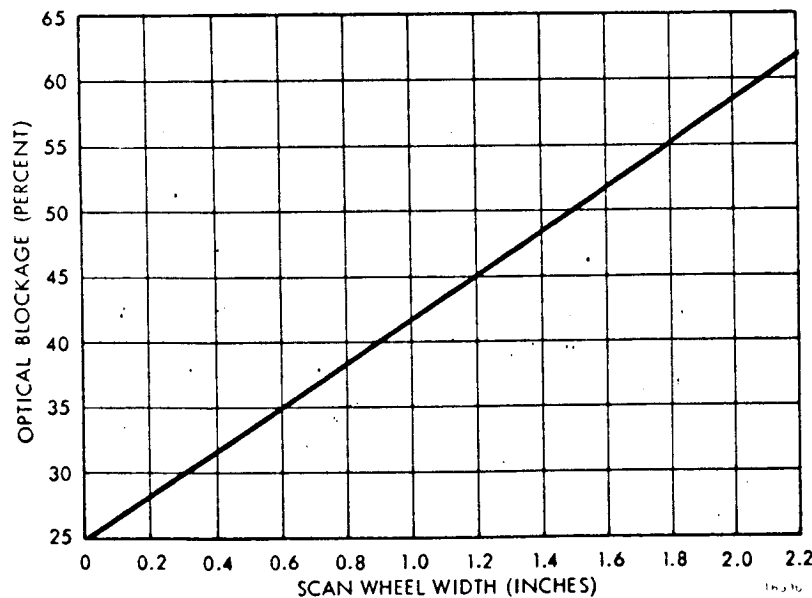


Figure 88. Optical Blockage Due to Scan Wheel in Primary Field-of-View.

stress level for the 1-inch tube diameter nontapered Invar wheel indicates that a more efficient tapered radial material distribution is necessary for a wheel subjected to axial and lateral vibration. The axial mode of vibration, figure 89, would include the stress due to hub compliance, which is not prominent in the lateral vibration example of figure 90.

The basic difference between the Invar and aluminum tube designs of figure 91 is the cross section wall thickness. The Invar tube walls are about one-third the thickness of the aluminum walls for similar weight and stiffness properties. Tapered designs for Invar, where the tubes are thin at the tip and thick at the root, are limited by manufacturing tolerance problems at the tip. A tapered aluminum 10-pound wheel having a 1-inch hub thickness was

designed using the equations summarized in appendix III. Similar dynamic results would have been achieved with Invar by substituting thinner wall sections. The interesting problem of determining the optimum taper function to minimize stress and compliance was not

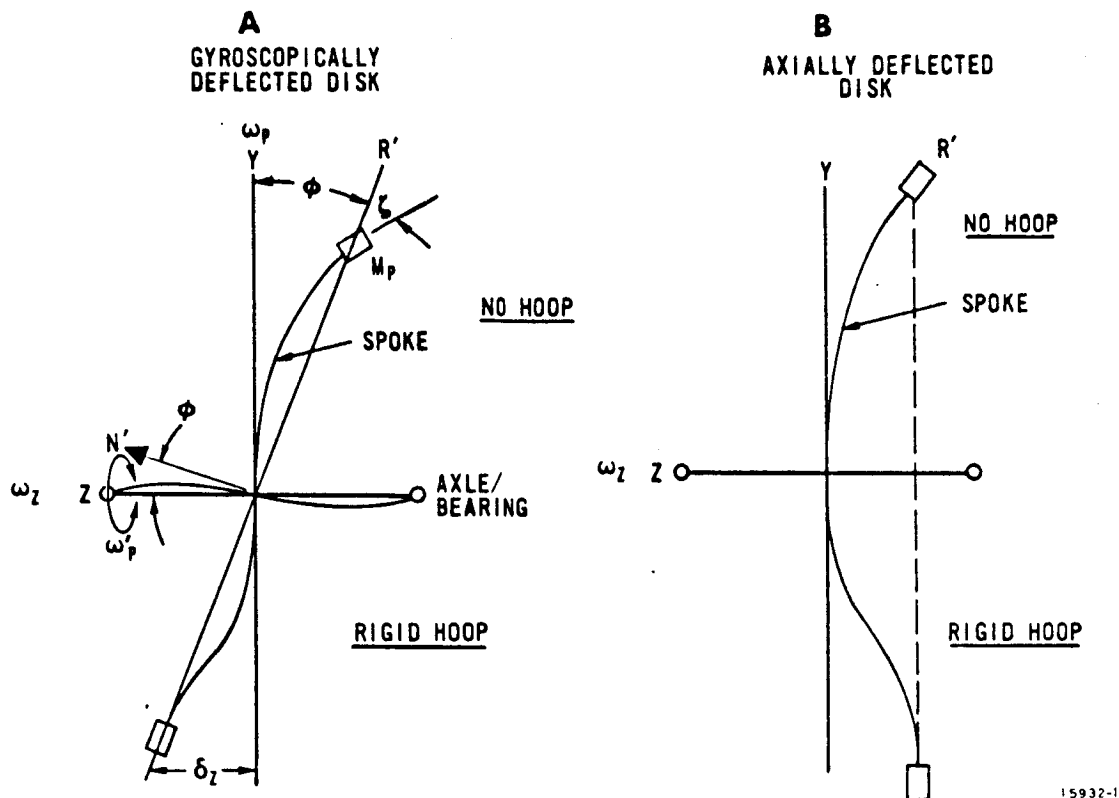


Figure 89. Scan Wheel Fundamental Deformation Modes.

completely solved due to lack of time. The strongest simple function which will yield a feasible tip wall thickness is of the form:

$$I = I_t X^n$$

where,

I_t = tip section area moment of inertia

X = distance from spoke tip

n = exponent determining taper rate.

For $n = 2$, the tip wall thickness is 0.01 inch for aluminum (figure 92). The 1g deflection plot of figure 92 shows that the major source of compliance is the axle interface hole in the hub. The resulting 150 Hz resonant frequency could be raised by redesigning the hub ring. The stress plot shows that stresses at 200g resonance are within the design limit of 10,000 psi.

A gyroscopic analysis of the tapered aluminum wheel yielded the results of figure 93. The maximum expected in-flight rotational perturbation is the 0.087 radian per second vehicle reacquisition rate. This rate will result in a wheel deformation of approximately the one-tenth resolution element tolerance limit defined for that type of geometric error.

The natural frequency at which the perturbed wheel would precess after gyroscopic excitation is 1450 Hz. That value is sufficiently high to guarantee rapid structural damping of the

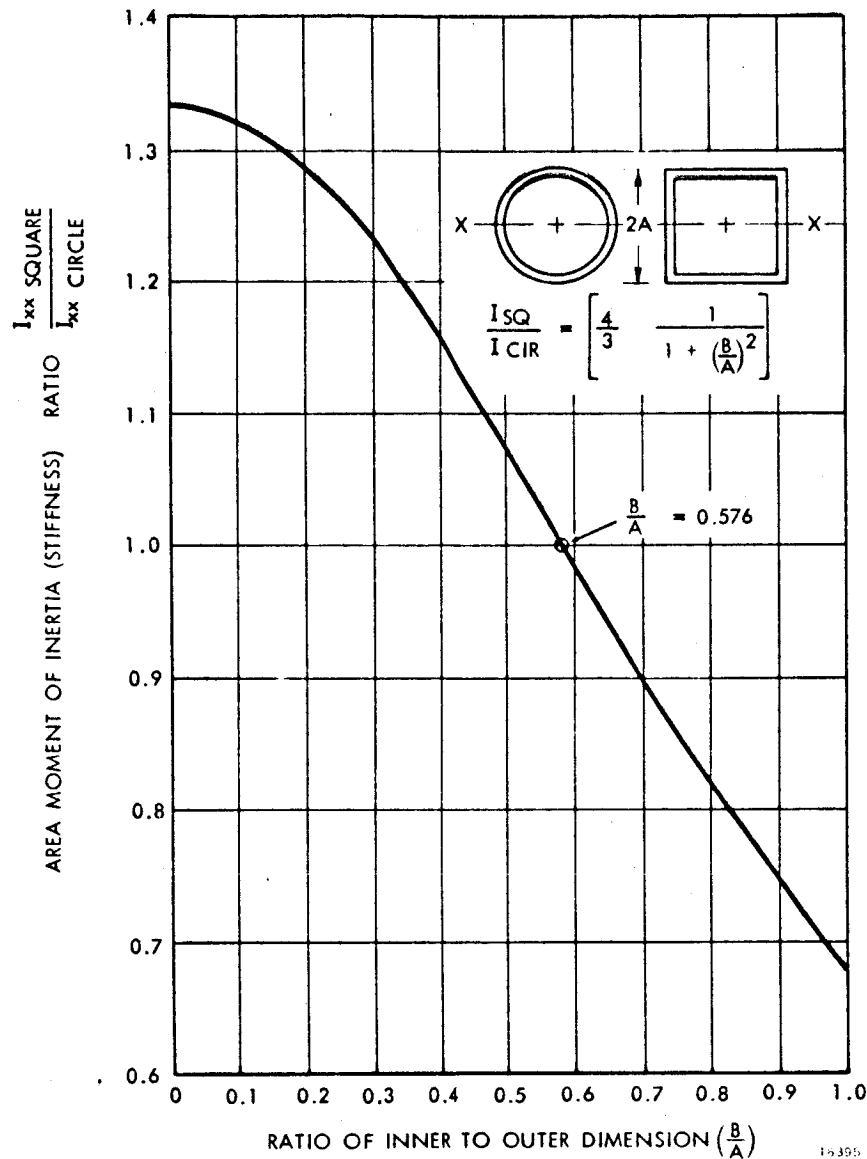


Figure 90. Stiffness Comparison at Same Weight and Outside Dimension for Square and Rolind Tubes.

perturbation. It is apparent that the vehicle orbit rate (one orbit every 100 minutes) will not cause noticeable wheel deflections.

A slightly modified design to stiffen the wheel hub would permit a thicker tube wall at the wheel periphery. An Invar wheel based on the above aluminum design, would thus be feasible from a manufacturing standpoint, and would reproduce the dynamic properties of the aluminum wheel.

Great Circle Scanning. - The 24-probe scan wheel is designed to scan a portion of the image sphere in a manner which defined a straight line on the ground. The scan wheel disk is the same diameter as the image sphere. The disk perimeter contacts the sphere on a great circle.

Great circle scanning was found to be a special case from a versatile family of tilted scan wheels. The geometry of the tilted wheel scanner is discussed in detail in the following paragraphs.

Tilted Wheel Spherical Scan System (Additional Study Area). -A scan system was developed which reduced the length of the scanner by a factor of 2 and reduced the effective thermal path length by a factor of 2.5. Figure 94 illustrates the relative decrease in package size accomplished with no compromise in optical performance.

The thermal and size problems in the present application dictated the necessity of folding the original scan system to fully use the advantages of image plane scanning. The search for a folded image scan system was guided by the following reasoning (figure 94).

A scanning probe, focused on F, must be held within the depth of focus, $\pm\delta$, by a structural path connecting the scan disk to the primary mirror. The thermal path length which controlled focus in the original system was $\overline{FO} + \overline{DO}$, approximately 40 inches.

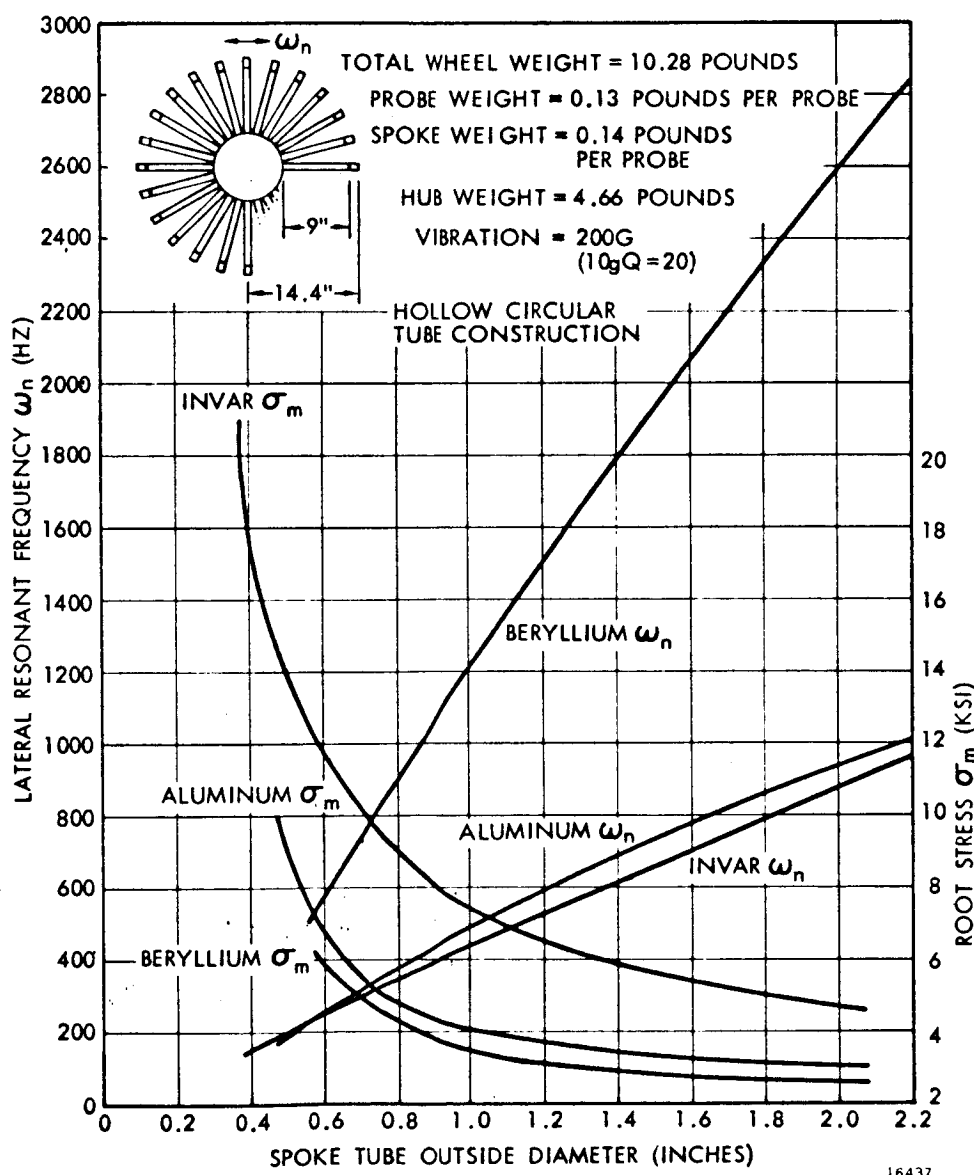


Figure 91. Nontapered Spoke Properties in High Frequency Lateral Direction.

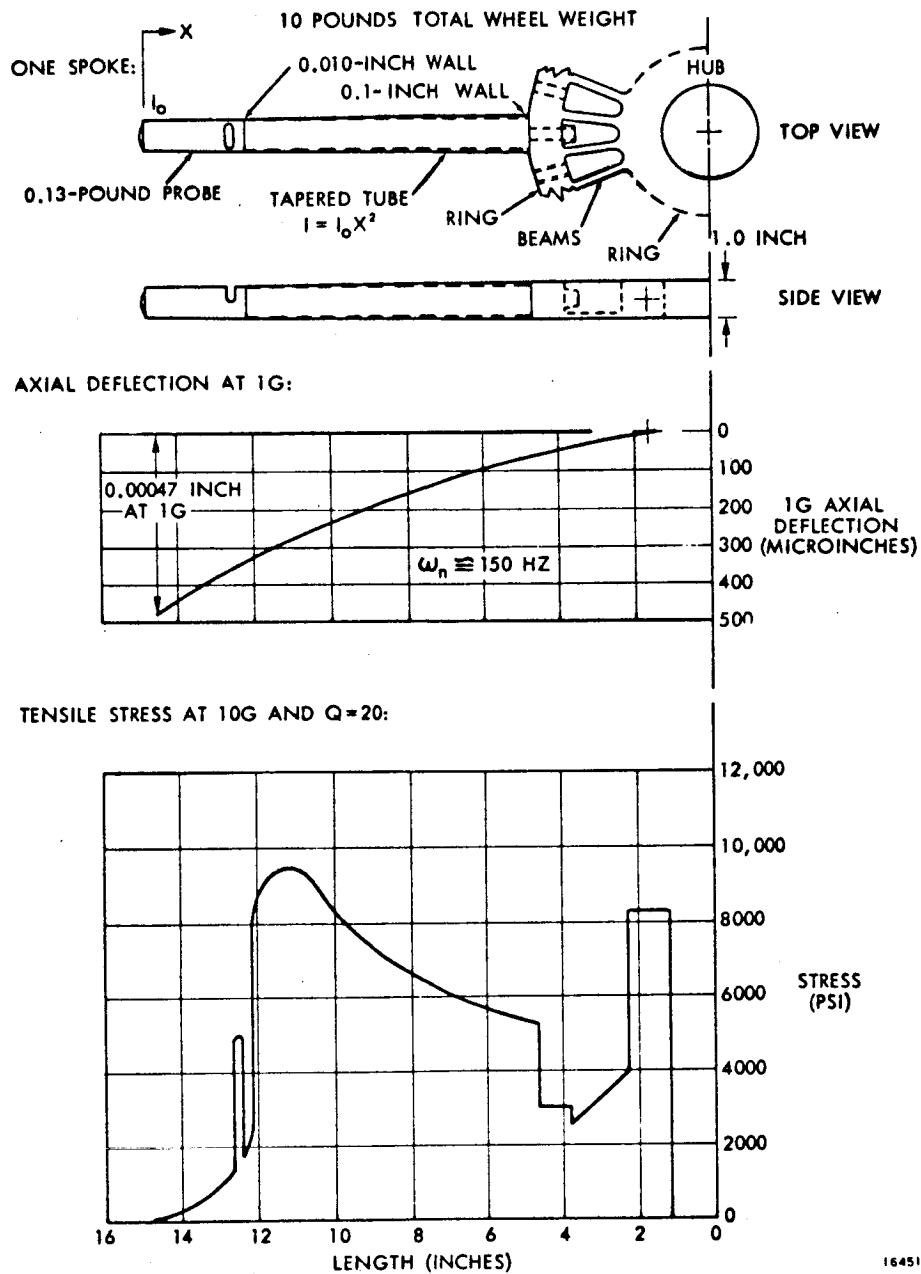


Figure 92. Stress and Deflection for Tapered Aluminum 24-Probe Scan Wheel, 1-Inch Wide.

Let

$$\overline{FO} + \overline{DO} = nR = \text{total thermal path length}$$

also,

$$2\delta = \frac{BR^2}{A} = \text{depth of primary focus}$$

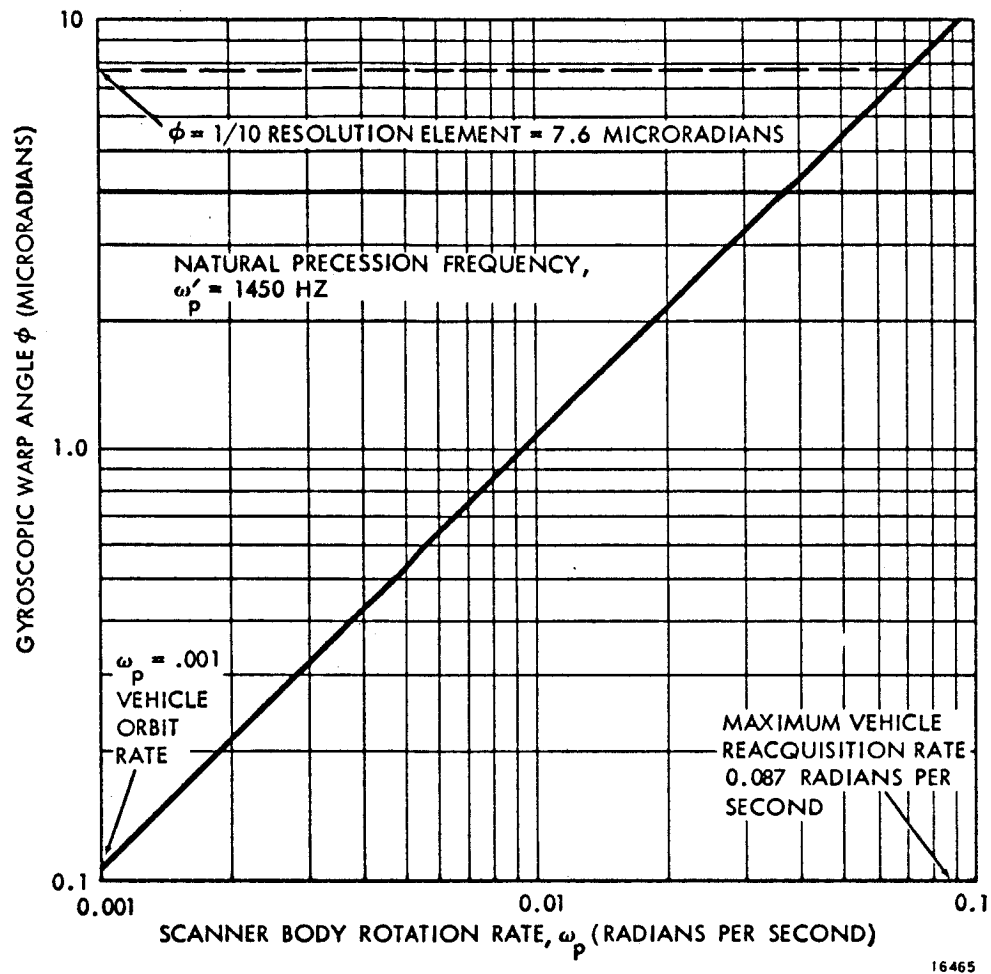


Figure 93. Scan Wheel Gyroscopic Deformation
(Tapered Aluminum 24-Probe Wheel).

where,

R = primary focal length

B = primary angular blue diameter fixed by performance specification

A = primary aperture

n = thermal path length coefficient.

In the folded system, it was desired to minimize the ratio of thermal length to depth of focus. Namely:

$$\frac{nA}{BR} = \frac{n}{B (f/\text{number})} = \text{ratio of thermal path length to depth of focus (minimize this ratio)}$$

where,

$f/\text{number} = R/A$ = focal ratio (f/number) of the primary.

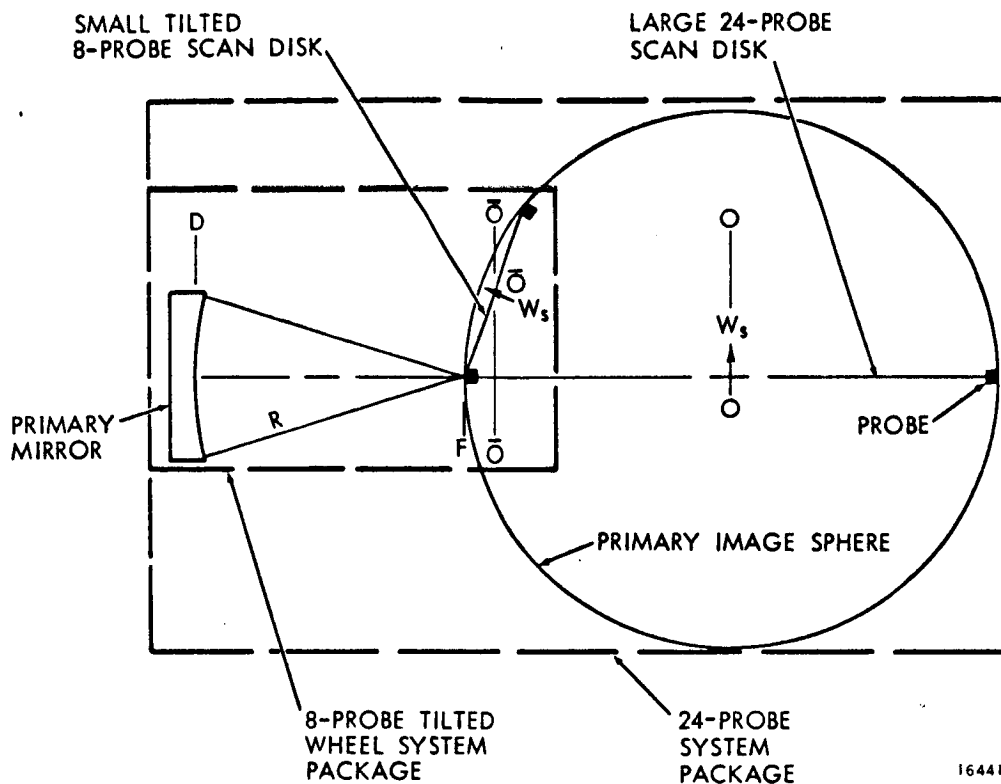


Figure 94. Reduced Package Size for Tilted Scan System.

It was thus necessary to either increase the old f /number or reduce the new thermal path length coefficient, n . Increasing the f /number would have increased the system structural weight, so the f /number was maintained at the previous value of 1.67.

The coefficient, n , was reduced by moving the scan rotation center, O , closer to the focal surface at F . This was accomplished by tilting the scan disk. The new system put O at \bar{O} , with a new path length, $\bar{FO} + \bar{DO}$, reduced by a factor of 2.5 over the previous length, $FO + DO$.

The large reduction in thermal length produced substantial improvements in the passive thermal control system safety factor. In addition, by cutting the total scanner volume in half, it was estimated that structural stiffness and strength would improve by a factor of at least 4.

The infinite family of tilted wheel scan geometries was found to contain the original 24-probe wheel as a special case. Figure 95 illustrates the relation of the scan wheels to the image sphere. The periphery of each of the wheels lies entirely on the spherical surface. A correctly spaced set of optical probes attached to the wheel periphery, focused on the peripheral circle, and aligned with rays extending from the probes to the sphere center at O will scan the ground image if the wheels are properly located. After assigning a 100 nautical mile equivalent image width, a family of scan wheels was generated in terms of axle tilt angle, ϕ , measured in the XZ plane. The wheel diameter and tilt angle is determined uniquely by the image width and number of optical probes, figures 96 and 97. The optical f /number, 1.67, and focal length, 13.33 inches, is the same for each case.

The cycle time for one probe to pass across the calibration sources and the image of the 100 nautical mile track length was determined. Cycle time is fixed by the 0.01 second time

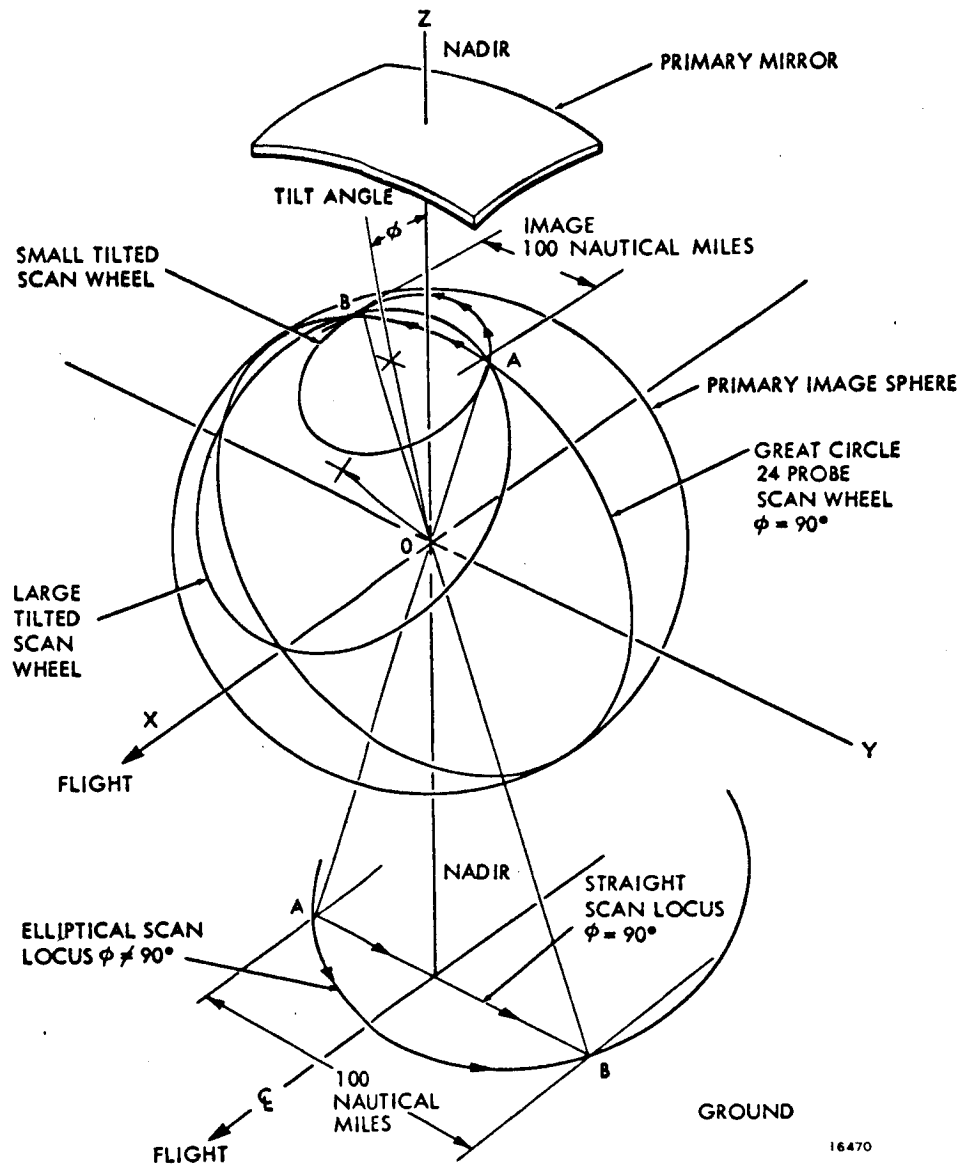


Figure 95. Tilted Wheel Scan Geometry.

for the vehicle to cross the 228-foot track width and the number of detectors per channel. The cycle time, and the number of scan wheel probes, determine the scan wheel rotation speed. Figure 98 shows that rotation speeds increase rapidly as the number of probes decreases.

A tilted wheel scanner scans ellipses on the ground. Figure 99 shows that the curvature of the active portion of the scan locus is small for wheels with eight or more probes. The curvature, calibration length, and number of detectors per channel determines the resolution element dwell time. The dwell time, for a 0.82-inch calibration length, is not appreciably reduced by scan curvature for wheels having eight or more probes (figure 100).

The high scan efficiency inherent in the 24-probe wheel was not sacrificed in the tilted systems. A probe is maintained in the field-of-view at all times, except for a short calibration time. The ratio of calibration length to active scan length determines the scan efficiency.

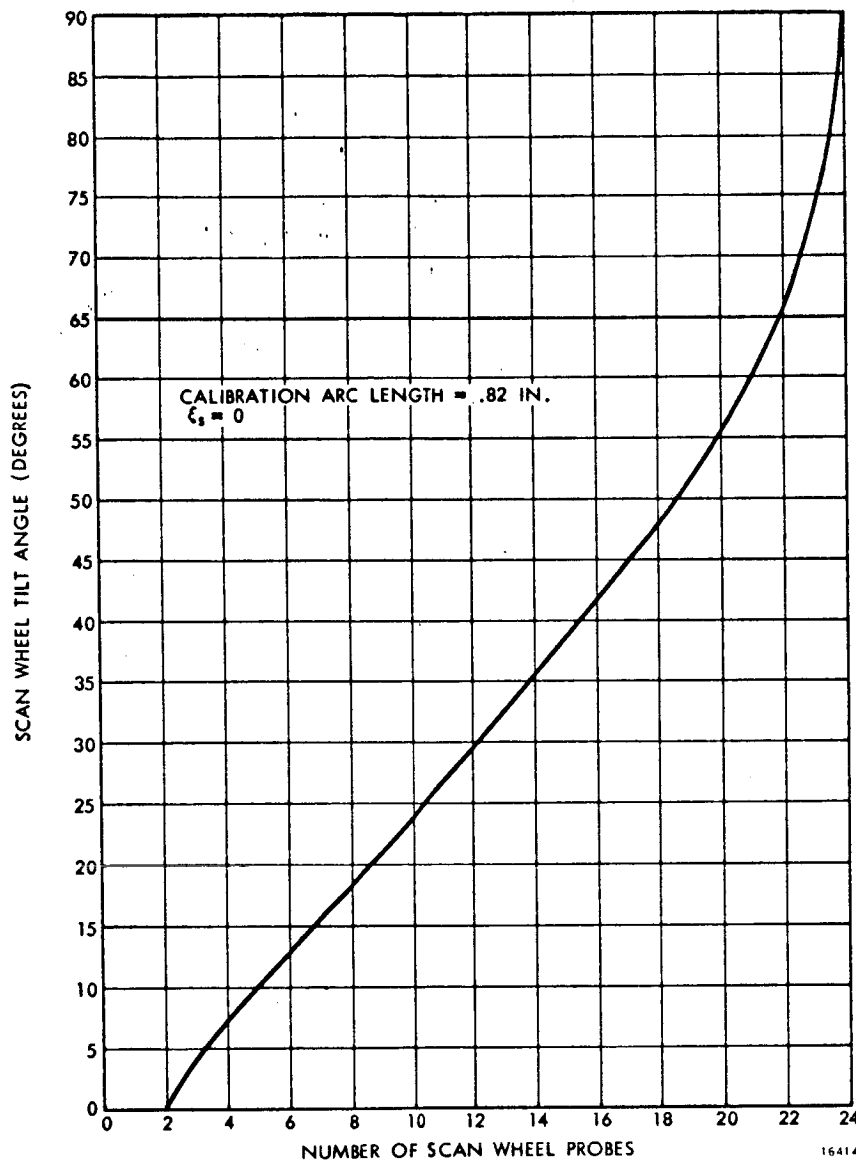


Figure 96. Scan Wheel Tilt Angle.

Figure 101 shows that calibration lengths less than 0.4 inch would yield efficiencies greater than 90 percent.

The apparent anomaly, evidenced by the rising scan efficiencies and decreasing dwell times for wheels having less than eight probes, resulted from the effects of increasing scan curvature. The dwell times were correct for all cases, but the efficiency values for the highly curves loci were misleading. High scan efficiency, based on the length or time ratios of calibration to active scan, does not correctly predict dwell times for wheels having less than eight probes.

A tradeoff study was made to determine the most suitable scan wheel size. From the thermal, structural, and material analyses, it was evident that the thermal path length should be as short as possible. The path length reduction for a decreasing number of probes is

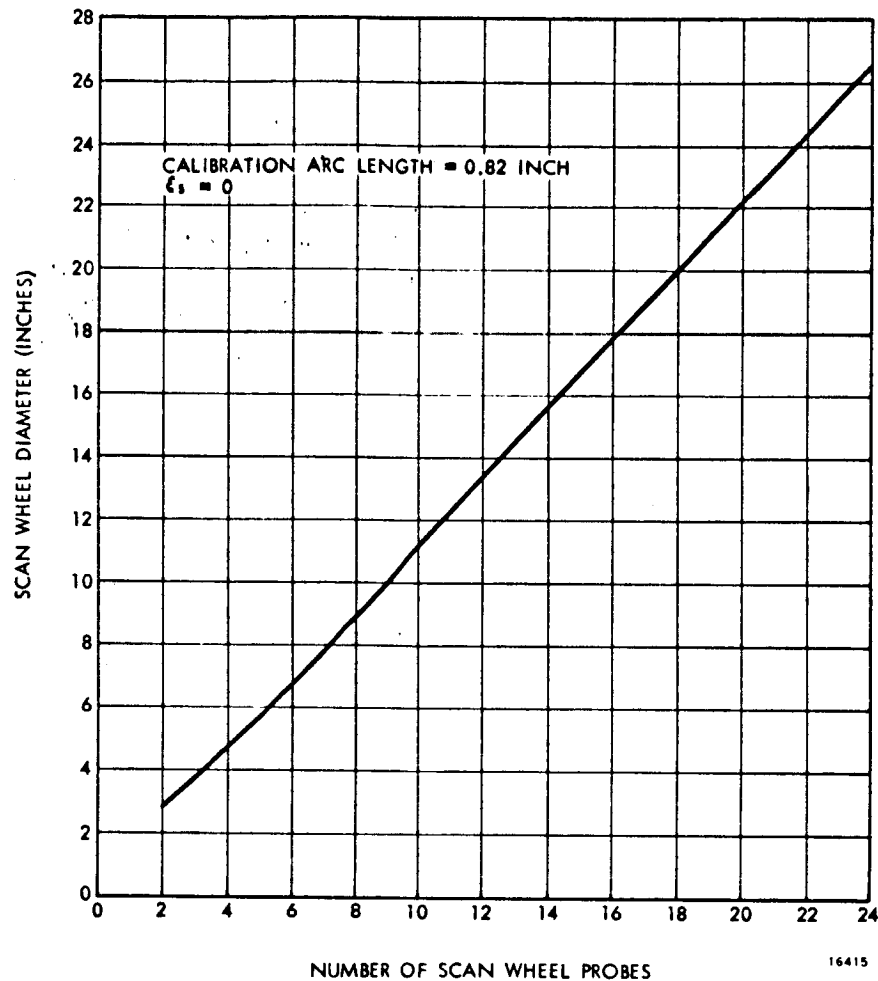


Figure 97. Scan Wheel Diameter.

evident from figure 102. An adverse effect of reducing the probe number was apparent in the plot of scan wheel peripheral acceleration, figure 103. The probe elements would have to maintain figure and location for 1 year in the indicated centrifugal acceleration field. The dwell times of figure 100, and probe matching and alignment tradeoffs, were considered.

A scan wheel containing eight probes was chosen. Short dwell times were avoided and the centrifugal acceleration was limited to 60g's. The structural thermal path length was reduced to 16 inches.

The benefits of increasing the number of detectors per channel for the eight-probe wheel are evident in figures 100 and 103. The use of two detectors per channel (two ground lines scanned per probe pass) would reduce the centrifugal acceleration to 15g's and double the dwell time.

The scan loci of figure 99 can be moved fore or aft along the flight path by varying the forward view angle, ξ_s . The above graphs were all plotted for $\xi_s = 0$, which placed the scan chord on the nadir intersect. Complete families of tilted wheels can be derived for other angles using the complete equations in appendix V.

Scan overlap and dwell time variation in the scan cycle were analyzed using the equations in appendix V. Scan errors were found to be negligible for the eight-probe system.

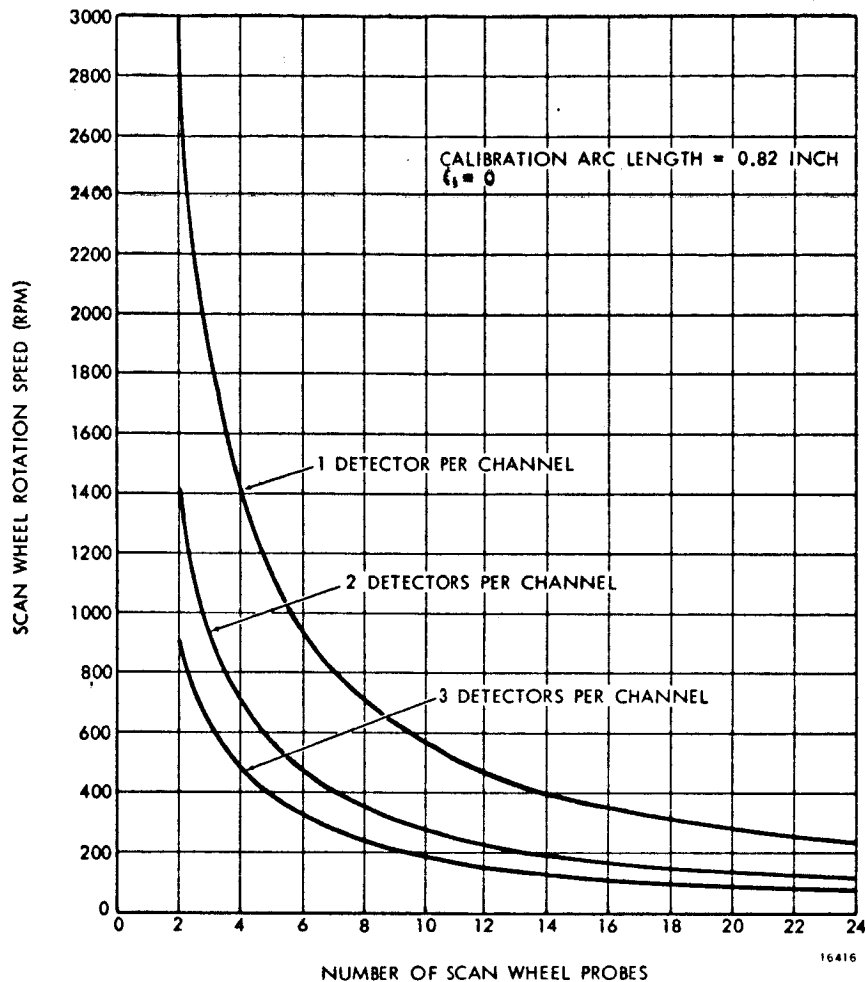


Figure 98. Scan Wheel Rotation Speed.

Scan Wheel Drive System. -The function of the drive system described in this paragraph is to rotate the scan wheel in a manner to create a uniform cross track scan velocity, which can be reproduced by the ground based reproduction system. In addition, the drive system must not degrade scanner geometric performance.

The scanner geometric requirements include maintenance of focus, line to line continuity in the reconstructed image equal to \pm one-tenth of a resolution element width, and mapping accuracy of 1 percent in a 100 nautical mile section. Mapping accuracy is a function only of spacecraft motion over the ground if the scan wheel disk is held in a fixed position relative to the spacecraft flight direction. Spacecraft motion stability depends on the effect on the spacecraft of the uncompensated angular momentum of the on-board systems. The scanner drive system includes a momentum compensation device which is described in subparagraph on momentum compensation.

The selected mechanical system is shown in figure 104. The scan wheel and synchronous motor are supported on a common shaft by the scan wheel bearing set. It may also be desirable to mount a shaft encoder on this shaft to provide synchronization signals. The motor is synchronized to the spacecraft clock and powered through a suitable inverter and filter system by the spacecraft primary power. Power for the momentum compensator is taken off the scan wheel axle at the drive wheel and transmitted to the rotation reversing wheel by a seamless Mylar or Kapton belt.

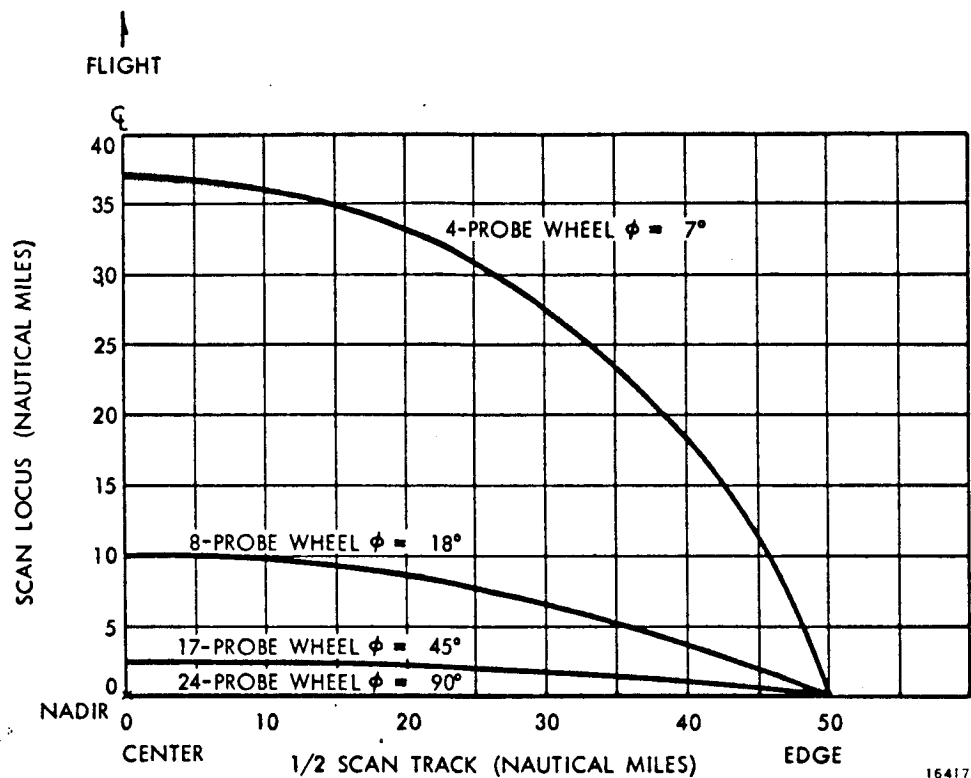


Figure 99. Scan Curvature.

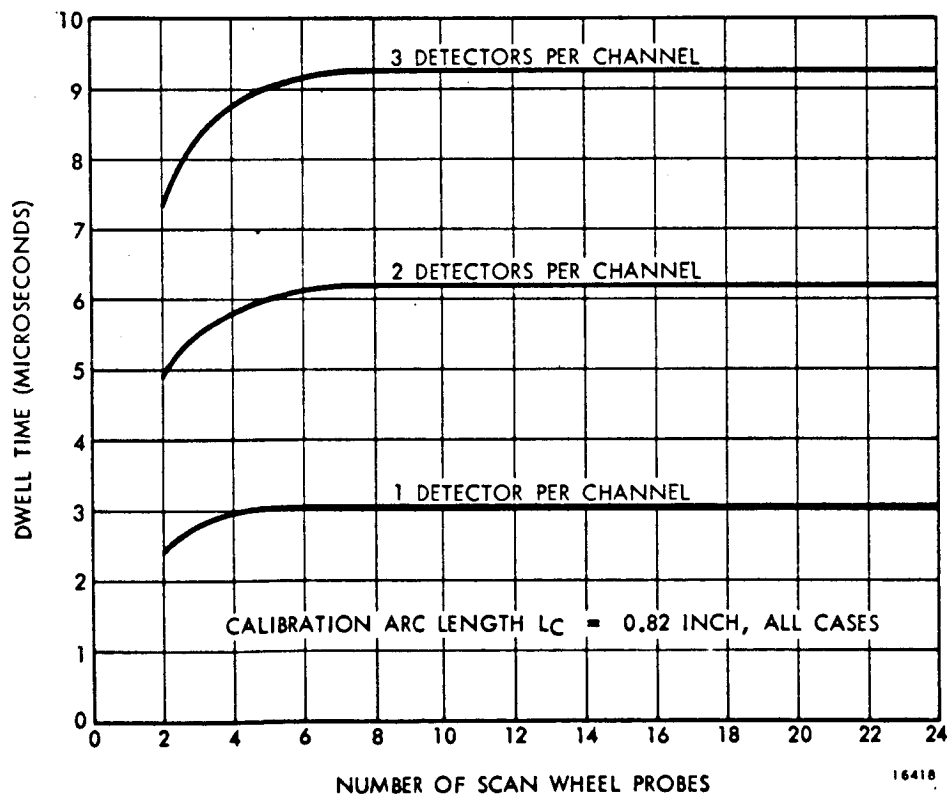


Figure 100. Resolution Element Dwell Time.

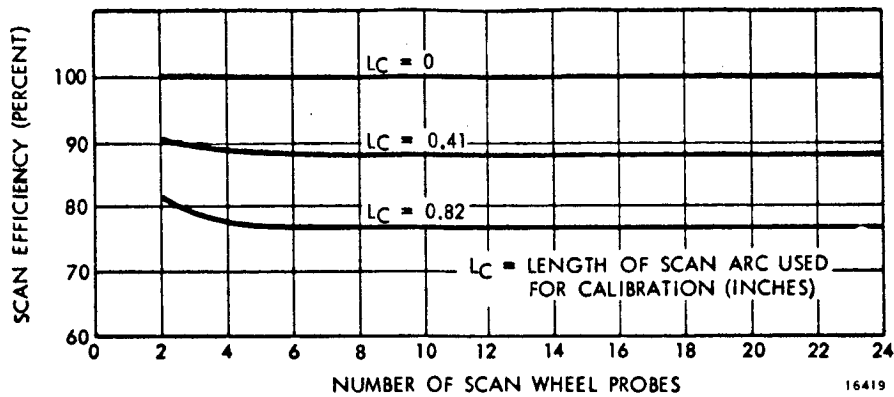


Figure 101. Scan Efficiency.

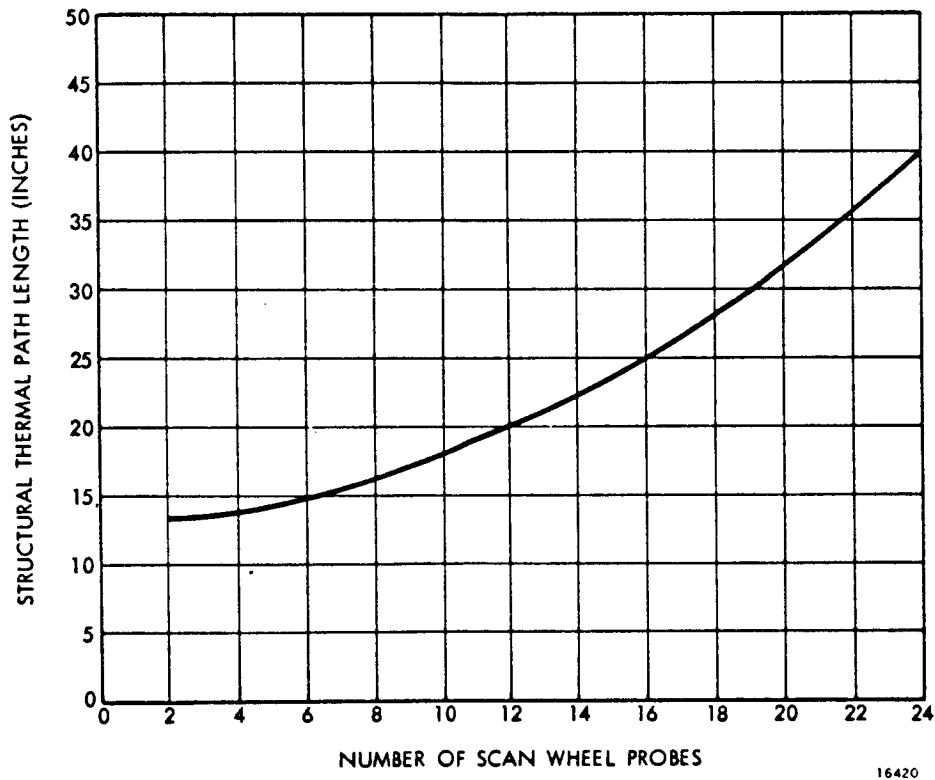


Figure 102. Thermal Path Length.

Maintenance of focus and the lateral component of resolution element contiguity is performed by the structural system. Thus, the only requirement imposed on the drive system in the lateral and radial wheel directions is low noise vibration. A lightweight drive belt, without gear teeth, provides the necessary quiet power transmission. The lateral wheel resonant frequency is 150 Hz. At this frequency, it would require a lateral drive belt oscillation greater than achievable to excite the 0.25g amplitudes required for the one-tenth resolution element tolerance.

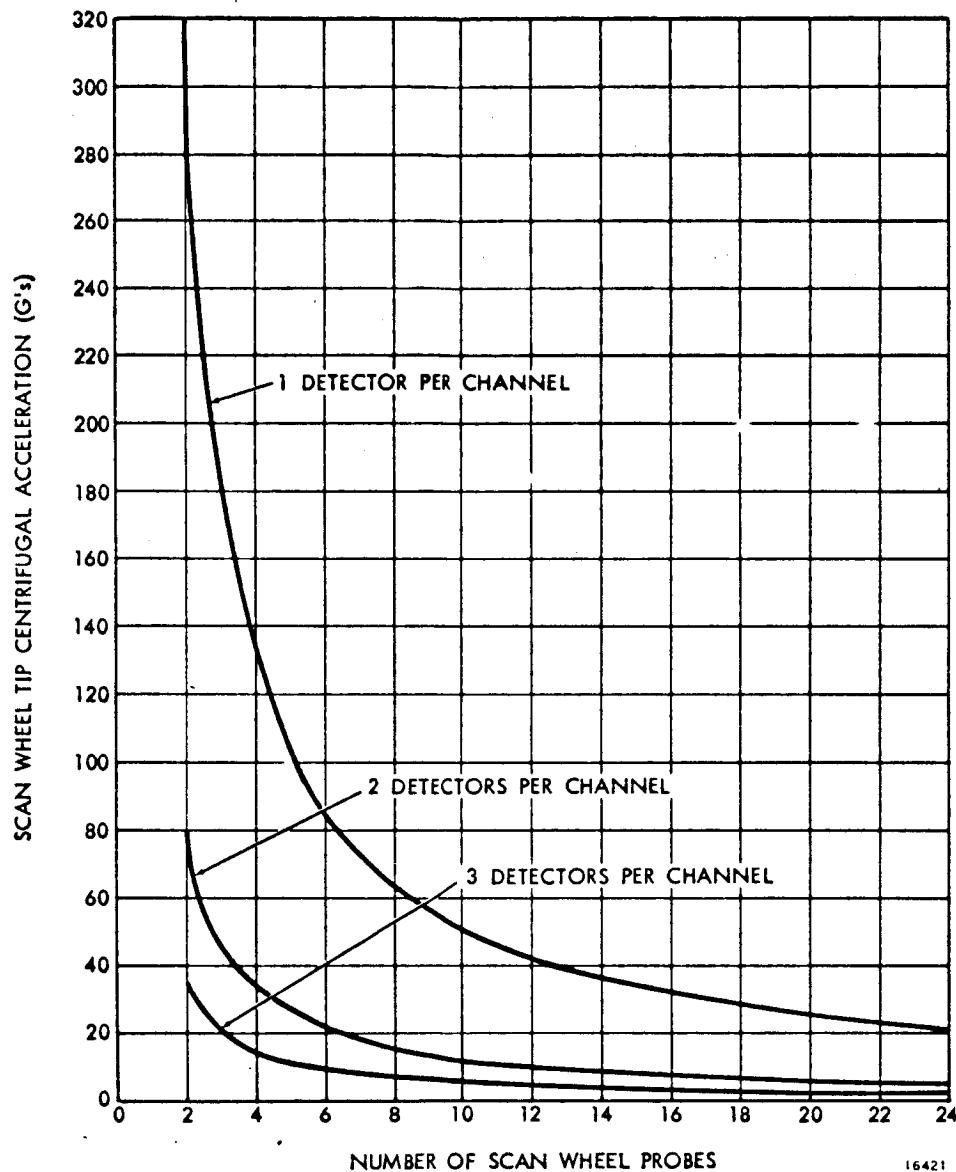


Figure 103. Scan Wheel Centrifugal Acceleration.

The relation of the drive system rotation rate parameters to the one-tenth resolution element contiguity depends on the method of synchronizing the tangential scan wheel probe position to the ground based recording and readout printing system. If the printer is synchronized to the scan wheel perfectly and continuously by the shaft encoder signals, the wheel rotation rate can wander without distorting the reconstructed image. With such a system, doubling the wheel speed would result in a 50 percent overscan, but with no distortion. A better synchronization system would register the printer at the start and end of a scan line, and infer interim position by integrating the long term mean scan wheel speed. The latter system provides the strongest existing constraint on the drive system accuracy. The rotation rate must be sufficiently uniform within a scan line (1/24 of a wheel rotation) to provide an element to element tangential indexing accurate to one-tenth of the 76-microradian resolution element width. The following analysis shows that the proposed system will provide that accuracy.

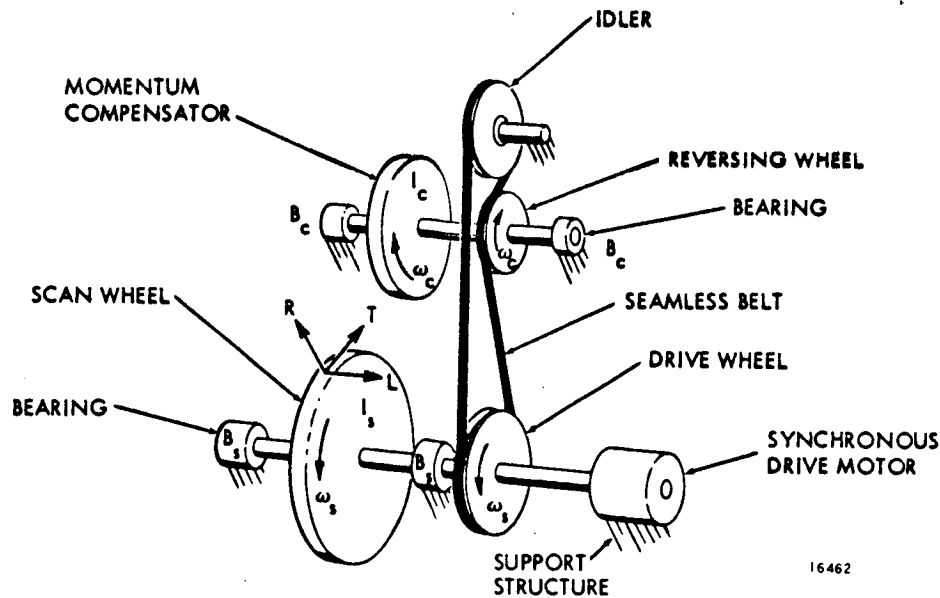


Figure 104. Scan Wheel and Momentum Compensation Rotary Drive System.

The rotational errors of the system of figure 104 result from its dynamic properties. The two disks, having significant rotational inertia, are coupled by a stiff elastic belt. The wheel and belt system is connected to a motor, which exhibits large magnetic compliance. The belt and the bearings provide noise sources which excite two natural vibration modes. The high frequency rotation mode is due to the belt compliance. The noise sources are of sufficiently low amplitude and frequency that the high frequency mode amplitude is negligible. The low frequency mode due to the motor magnetic compliance will be discussed in detail.

Consider the drive and reversing wheel to have radii R_s and R_c , respectively. Their ratios defines the system nominal speed ratio, S_o :

$$S_o = \frac{R_s}{R_c}$$

where,

R_s = scan drive wheel radius

R_c = compensator reversing wheel radius.

Momentum compensation requires that the moments of inertia of the two-wheel, namely I_s and I_c , be in the same ratio so that:

$$\frac{I_s}{I_c} = S_o.$$

The fundamental frequency can then be written in terms of the known scan wheel inertia and variable motor and speed ratio properties:

$$\omega_n = \frac{NT}{16 \pi I_s (1+S_o)} \text{ radians/second}$$

where,

ω_n = system natural frequency (rad/sec)

N = number of motor magnetic poles

I_s = scan wheel mass moment of inertia (in-lb-sec)

T = motor pullout torque (oz-in).

A plot of natural frequencies is shown in figure 105. Note that the natural frequencies are below 1/4 Hz for a 20 oz-in. motor. The system requires approximately 10 ounce-inches of motor torque.

The total scan wheel and momentum compensation system response to a sinusoidal torque input at the scan wheel is given by:

$$\theta_s = \frac{\pi \tau}{8NT} \left[\left(\frac{1}{1 - \left(\frac{\omega_f}{\omega_n} \right)^2} \right) \right] \text{ radians} \quad (12)$$

where,

θ_s = maximum amplitude of scan wheel rotation oscillation (radians)

τ = maximum amplitude of sinusoidal disturbing torque (oz-in)

ω_f = frequency of disturbance (rad/sec).

The maximum value of θ_s will develop from the lowest forcing frequencies. First, consider the forcing function caused by the scan wheel bearings. The balls rotate at $1/2 \omega_s$. The lowest forcing frequency is a function of the number of balls passing a race imperfection:

$$\omega_f = \frac{\omega_s}{2n}$$

where,

n = number of balls in bearing.

The error ratio, θ_s/τ , for a 24-pole, 20-oz-in. motor is plotted in figure 106. For an example of system oscillation induced by bearing noise, let $S_o = 3$ and $n = 8$. Then from

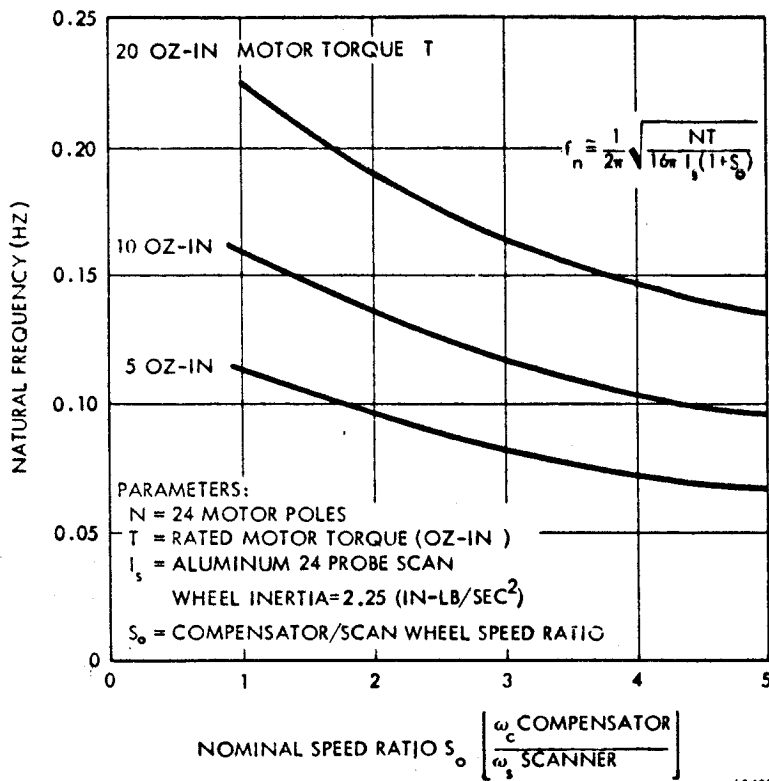


Figure 105. Fundamental Natural Frequency for Momentum Compensated Belt Coupled System Due to Magnetic Motor Compliance.

The lowest frequency change in speed ratio due to a sinusoidally varying belt thickness is:

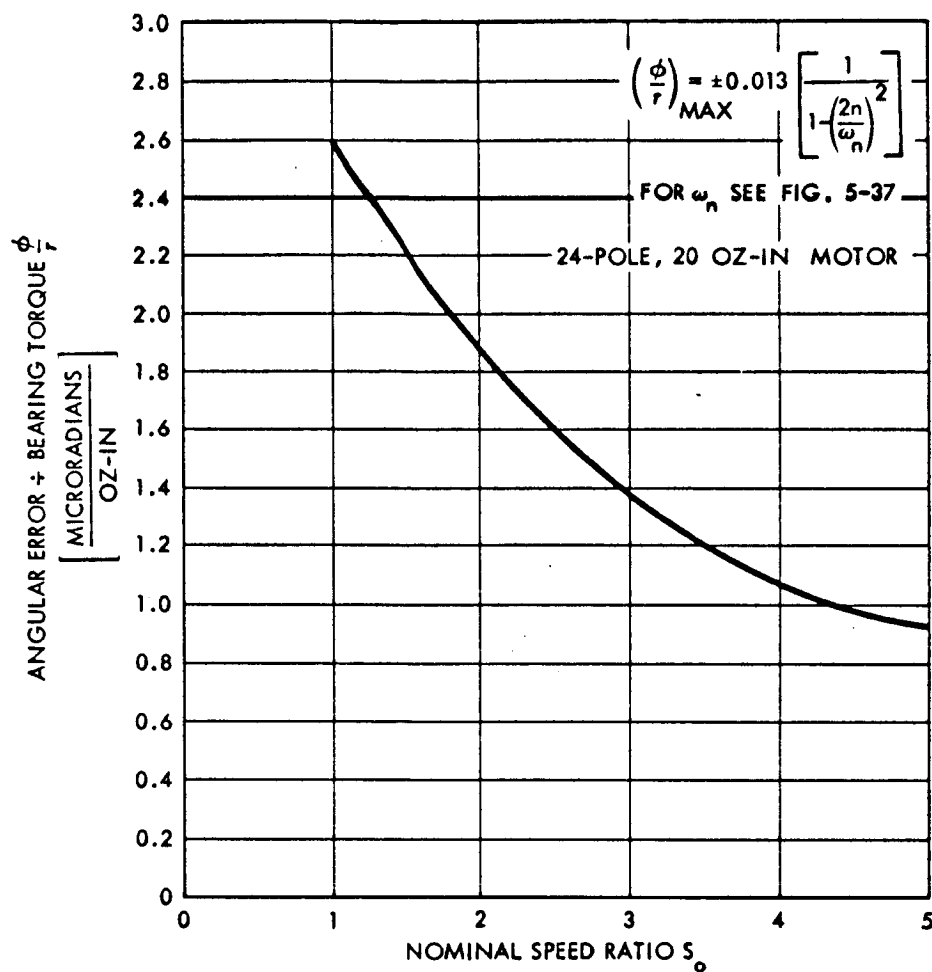
$$S(t) = S_o + \Delta S \sin \omega_b t$$

$$S(t) = S_o + \Delta S \sin \left[\frac{\pi^2 R_s A}{15 L_b} \right] t \quad (13)$$

$$S_{\max} = S_o + \Delta S \quad (14)$$

figure 106, $\theta_s/\tau = \pm 1.4$ microradians per oz-in. For an extreme disturbance, τ , equal to 1 oz-in., θ is only ± 0.02 resolution elements every 12 scan wheel revolutions. This error is negligible.

Next, consider the forcing function presented by the drive belt. This is the lowest frequency forcing function occurring in the system. To increase belt life, the belt is made as long as possible. As the belt length increases, the time it takes to traverse the entire system also increases. A 40-inch belt in the drive system would have a natural frequency of approximately 8 rad/sec. This is considerably nearer the system natural frequency ($\omega_n = 1$ rad/sec) than was the case for the bearing noise example. A drive belt of Mylar or Kapton can be made to have a thickness variation as small as ± 0.0001 inch. If this small variation is distributed sinusoidally around the belt length so as to place the thin section at one end and the thick section at the other end, a significant rotational oscillation can occur in the scan system.



16466

Figure 106. Ratio of Scan Wheel Angular Rotation Error to Bearing Generated Disturbing Torque.

where,

$S(t)$ = speed ratio as a function of time

A = scan wheel rotation speed (rpm)

ω_b = belt frequency (rad/sec)

L_b = total belt length (inches)

ΔS = maximum change in speed ratio

S_{max} = maximum instantaneous speed ratio.

For a flat belt, Δ_s is:

$$\Delta_s = \frac{(R_c + R_s) \Delta B}{2R_c^2}$$

$$\Delta_s = \frac{S_o (1 + S_o) \Delta B}{2R_s} \quad (15)$$

where,

ΔB = change in belt thickness (inches).

Equation (15) is plotted in figure 107 for the case where $\Delta B = \pm 10^{-4}$ inches. The maximum speed ratio change is very small. However, larger oscillations result as a by product of these small perturbations.

For a system with a belt flutter induced variable speed ratio occurring at a frequency near the fundamental resonant frequency, a sustained form of oscillation, similar to motor hunting, will occur. Equation (12) can be used to determine the amplitude of the response. Considering the belt to be rigid for the frequencies of interest, there are no potential energy storage mechanisms in the system. Thus, during variable speed rotation, such as described by equation (13), kinetic energy must be conserved. Using equation (14), and equating the kinetic energies at the nominal and extreme speed ratios during the belt cycle, yields an expression for the maximum scan wheel speed variation due to belt flutter. The expression, which does not yet include the amplification effects of resonance, is:

$$\frac{\omega_{s_{\max}}}{\omega_s} = \frac{S_o (1 + S_o)}{S_o + \left[S_o + \frac{S_o (1 + S_o) \Delta B}{2R_s} \right]}$$

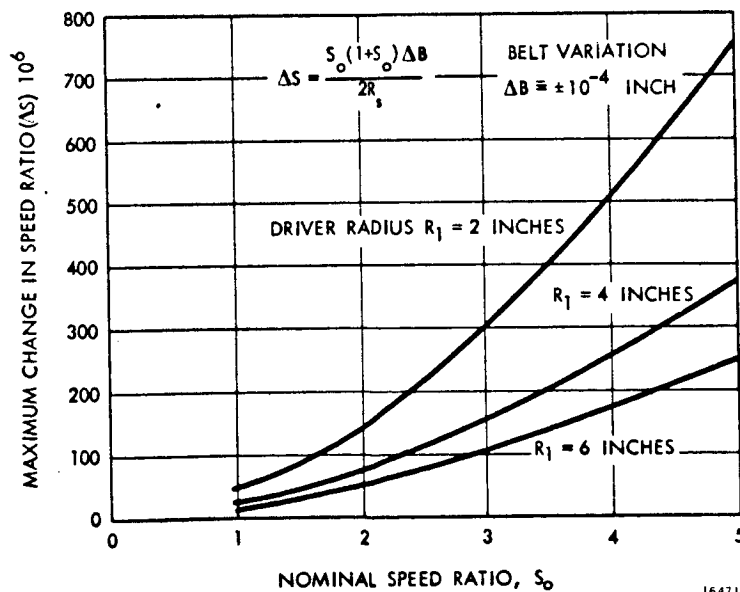


Figure 107. Speed Ratio Change Due to a Variable Thickness Belt.

From (14) we have:

$$\frac{\omega_{s_{\max}}}{\bar{\omega}_s} = \left[\frac{S_o + (S_o)^2}{S_o + (S_{o_{\max}})^2} \right]^{\frac{1}{2}} \quad (16)$$

where,

- $\omega_{s_{\max}}$ = maximum instantaneous scan wheel rotation speed
- $\bar{\omega}_s$ = nominal scan wheel rotation speed
- S_o = nominal ratio of compensator to scan wheel rotation speed
- S_{\max} = maximum instantaneous speed ratio.

Equation (16) describes the maximum speed amplitude ratio of the oscillating scan wheel due to belt thickness variation. The oscillating scan wheel drives the systems natural vibration mode as follows. By integrating the sinusoidally varying scan wheel speed, (16), the maximum change in motor torque during a belt rotation cycle is:

$$\Delta T = \tau = \frac{NT (\omega_{s_{\max}} - \bar{\omega}_s)}{16 \pi \omega_b} \quad (17)$$

Inserting equation (17) into (12) yields the final system oscillation amplitude:

$$\theta_s = \pm \frac{2 (\omega_{s_{\max}} - \bar{\omega}_s)}{\omega_b} \left[\frac{1}{1 - \left(\frac{\omega_b}{\omega_n} \right)^2} \right] \quad (18)$$

where,

- θ_s = maximum scan wheel angular oscillation amplitude due to belt thickness variation (radians)
- $\omega_{s_{\max}}$ = maximum scan wheel rotation speed from equation (16)
- $\bar{\omega}_s$ = average or nominal scan wheel rotation speed
- ω_b = belt rotation frequency
- ω_n = total system natural frequency.

Equation (18) describes the maximum rotational error for the drive system. For example, consider a system having a speed ratio $S_o = 3$, scan wheel drive disk radius $R_s = 2$ in., and a 20 oz-in., 24-pole motor. From figure 107, the maximum speed ratio change due to a belt

having a ± 0.0001 inch thickness variation is $(300) 10^{-6}$. Then from (16) we find $\frac{\omega_s \max}{\omega_s}$

$= 0.999925$ for the nonresonant condition. This yields a nonresonant scan wheel speed error of 0.001885 rad/sec which is small compared to the nominal value of 25.1 rad/sec. However, when the dynamic condition of equation (12) is computed for a 40-inch belt length, the rotational position error is $\theta_s = \pm(72) 10^{-6}$ radians. This amounts to two resolution elements every 1.6 wheel revolutions. This error is much larger than any of the other anticipated drive system dynamic errors, including motor torque variations and bearing noise. When the error is spread over the 38 scan lines in the 1.6-wheel revolutions, it becomes negligible.

Belt life was investigated for mylar materials. These materials will sustain 10^8 belt rotation cycles prior to failure, as long as the ratio of largest pulley diameter to belt thickness is greater than 150. For the above example, using a 4-inch diameter drive wheel and 1.33-inch reversing wheel, belt life was estimated at 2.5 years.

Momentum Compensation. -The drive system of figure 104, paragraph on scan wheel drive system, includes an integral momentum compensating system. The system cancels the scan wheel angular momentum with an accuracy adequate to achieve the 0.06 in-lb-sec spacecraft tolerance. Momentum compensation is required by the spacecraft to conserve attitude control fuel. Fuel must be expended to create the torques necessary to correct for uncompensated angular momentum and keep the spacecraft nadir pointing.

Referring to figure 108 view A, the scan wheel rotates in a direction opposite to that of the momentum compensator wheel. For an ideal system, the moments of inertia of the disks would be proportional to the inverse of the rotational speed ratio, and the products of inertia with respect to the spin axis would be zero, i.e.:

$$\frac{I_{yyc}}{I_{yys}} = \frac{1}{S_o}$$

$$I_{xy} = I_{xz} = I_{yz} = 0$$

The angular momentum vectors would be the same magnitude, but opposite in direction. If in addition the spin axes, Y_c and Y_s , are parallel (but not necessarily colinear), complete compensation will result (figure 108 view B) providing the axle bearings are connected by a rigid structure. For the perfect system, a rotation, $\vec{\omega}_z$, applied to the scanner body will result in scan wheel and momentum compensator torques equal to $(\vec{H}) (\vec{\omega}_z)$. Since $(\vec{H}_c) (\vec{\omega}_z)$ is equal and opposite to $(\vec{H}_s) (\vec{\omega}_z)$, the torques will be cancelled in the rigid structure and the spacecraft will not sense the scan wheel angular momentum.

Errors in cancellation are of two types, sinusoidal and constant. The sinusoidal errors arise from failure to balance the wheels, bearing runout, wheel gyroscopic deformation, drive belt thickness variations, etc. The constant errors result from axle misalignment, speed ratio error, and moment of inertia ratio error. In practice, the momentum vectors will be of slightly different magnitude and will not be perfectly parallel. In addition, they will vary in time. The resulting maximum vector error, ΔH , figure 108 view C, must be less than 0.06 in-lb-sec.

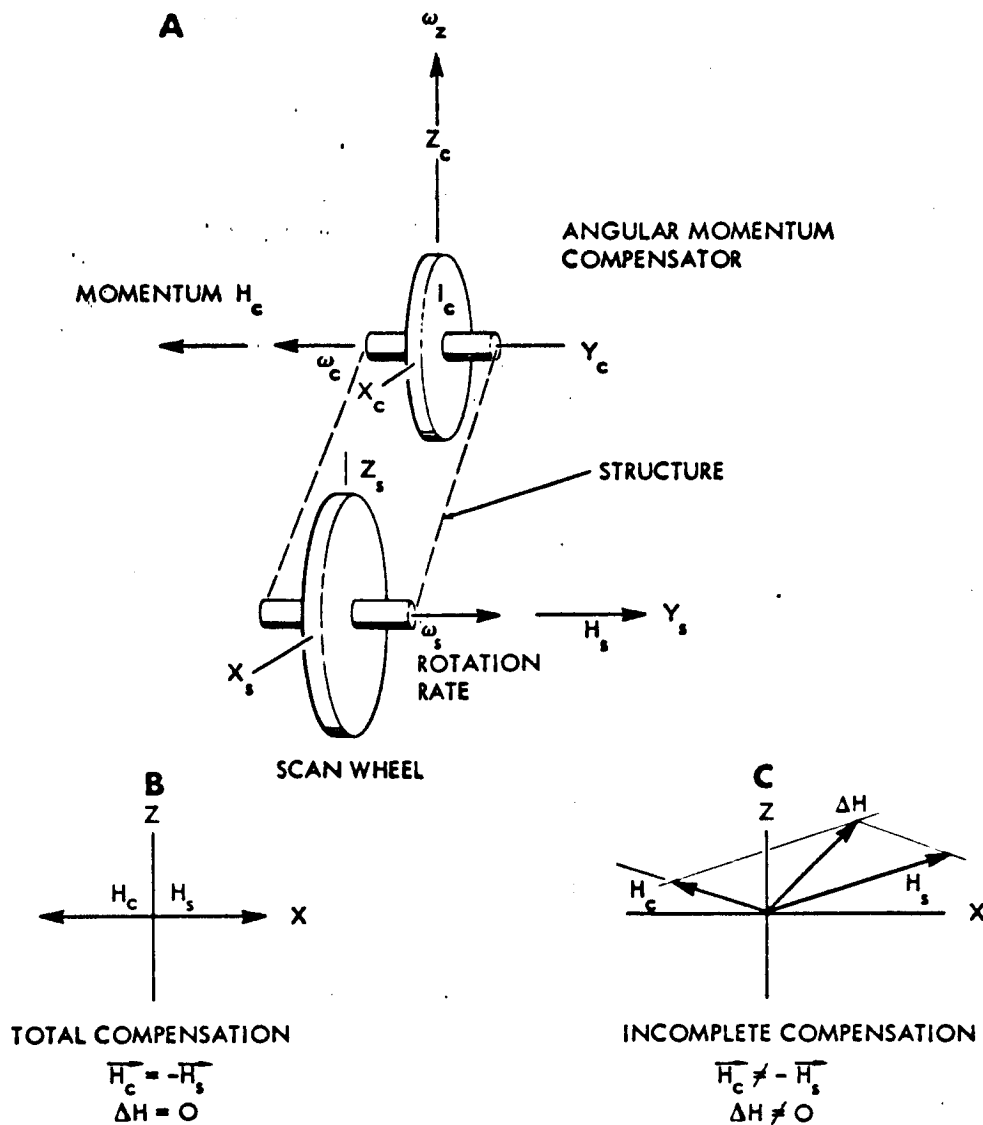


Figure 108. Momentum Compensation.

Consider the effects of inertia error. A 26-inch diameter scan wheel rotation rate is 25.1 radians per second. Allotment of the total 0.06 inch-pound-second error to a change in wheel inertia would be the equivalent of adding or subtracting an amount of peripheral material equal to 0.02 cubic inch of Invar. In practice, much better wheel balance and adjustment can be achieved.

Axle misalignment of 0.001 radian would create the 0.06 in-lb-sec error tolerance. For a 10-inch axle length, this requires locating the bearings to within a ± 0.01 inch bore tolerance. Careful alignment should provide 10-times closer tolerances without difficulty.

Variation in speed ratio affects the momentum balance as follows:

$$\frac{H_c}{H_s} = \left(\frac{I_c}{I_s} \right) \left(\frac{\omega_c}{\omega_s} \right) = \frac{S_o + \Delta S}{S_o} = \frac{S_o'}{S_o}$$

where,

H_c = compensator momentum (in-lb-sec)

H_s = scan wheel momentum (in-lb-sec)

I = mass moment of inertia (in-lb-sec)

ω = rotation speed (rad/sec)

S_o = nominal or average ratio of compensator speed to scan wheel speed

Δs = change in speed ratio

S_o' = speed ratio resulting from the Δs change.

Then we have:

$$\Delta H = H_s - H_c = H_s \left(1 - \frac{S_o'}{S_o} \right).$$

For $H = 0.06$ in-lb-sec and $H_s = 56.5$ in-lb-sec (Invar spoked 24-probe wheel):

$$\left(1 - \frac{S_o'}{S_o} \right)_{\text{minimum permissible}} = 1 - 0.00106$$

Belt creep provides the largest anticipated speed ratio change. The speed ratio variation due to belt creep can be shown to be:

$$\frac{S_o'}{S_o} = 1 - \frac{C}{16R_s A_b E_b}$$

where,

C = torque being applied by belt to drive pulley (oz-in)

R_s = drive wheel radius

A_b = belt cross sectional area

E_b = belt material elastic.

For example, consider a mylar belt with a 0.5 by 0.01-inch cross section. The anticipated torque is approximately 1 oz-in. If that figure doubled, then creep would change the speed ratio to:

$$\left(\frac{S_o'}{S_o} \right) = 1 - 0.00,0011.$$

Again the error is negligible.

The momentum compensation system thus appears to be feasible if care is exercised in fabricating and balancing the hardware.

Bearings. -The scan wheel requires close tolerance bearings to maintain the probes within the prescribed scan focus. It was estimated that since the thermal system required most of the ± 0.0004 inch primary depth of focus, the total bearing runout and noise production should not be more than ± 0.00005 inch during the 1-year orbit life. Bearings can be obtained with 0.00005 peak-to-peak runout by proper selection for class 7 production units. The latter runout would permit a 100 percent increase in runout to occur before the arbitrary limit was reached.

The use of an Invar axle permits the wheel to be supported by three stationary deep groove bearings. Deep groove bearings exhibit lower torque at low speeds than do angular contact bearings. A duplex preloaded pair (1.3125 inches outside circumference, 0.875 inch inside diameter, 0.25 inch wide) will support the motor driven shaft end. A single spring loaded bearing (2.875 inches, outside diameter, 2.3125 inches inside diameter, 0.25 inch wide) will stabilize the shaft at spectrometer interface.

The values of torque and compliance, listed in tables 20 through 25, were based on a friction coefficient of 0.1 and a 0.125-inch ball diameter (16 balls per small bearing, 36 for large bearing). Power requirements for the oil lubricated bearings, neglecting drag due to oil seals, are plotted in figure 109. It is apparent that the power requirements and starting torques are not prohibitive.

Bearing lubrication methods were considered. It was determined that a combination of F-50 oil and G-300 grease (General Electric) would be preferable over other fluids and ion plated solid lubricants. The bearings would be vacuum impregnated with F-50 oil, centrifuged to remove the excess, and filled 20 to 35 percent with G-300 grease. The grease will provide the required elasto-hydrodynamic (EHD) protection, and the oil will presaturate the retainer.

A launch survival tradeoff exists between bearing torque and stress as affected by preload and lubricant viscosity. In general, a bearing under low preload will become unloaded during a launch vibration half cycle. The succeeding half cycle will reload the bearing with large resulting dynamic stresses. A solution to the plastic damage caused by the large dynamic stresses would be to increase the lubricant viscosity (thus increasing bearing drag) and/or increase the preload to prevent unloading (thus increasing the probability of wear failure during the 1-year orbit life). A phenomenon peculiar to a nonpreloaded, highly stressed bearing is that lateral excursions bring the balls to rest on a portion of the race which is removed from the normal preload running region. Thus, dynamic plastic damage will only result in secondary flow effects in the useful portion of the race. It was estimated that by using a moderate 15-pound preload, to uniformly unload the bearings during peak vibration,

Table 20. Preload vs Torque (Single Bearing)

Preload (pounds)	Average Torque (gram-centimeter) at 240 rpm with oil (300 centistokes at 70° F.)	Starting Torque (gram-centimeter) (Bearing-Dry)
5	296	6
10	300	10
15	306	18
20	310	30
25	316	42

and a grease lubricant, to raise the EHD film strength and reduce material transfer from race to ball, it will be possible to survive launch without bearing degradation. The 15-pound preload system applied to the 10-pound, 24-probe scan wheel will produce an axial resonant frequency of 500 Hz and a radial frequency of 870 Hz. The G-300 grease will approximately double the power requirements indicated in figure 109.

A baffle system will be necessary to retard the loss of the F-50 oil in the bearing in vacuum. The baffle would be of the labyrinth diffusion barrier type, for which design equations are readily available. The baffle and bearing dust seals will be designed to minimize lubricant flow onto the optical elements. Suitable use of barrier films would be desirable to inhibit creep of the silicone oil.

Table 21. Preload vs Torque (Duplex Pair).

Preload (pounds)	Average Torque (gram-centimeter) at 240 rpm with oil (300 centistokes at 70° F.)	Starting Torque (gram-centimeter) (Bearing-Dry)
5	84	6
10	90	19
15	98	36
20	108	55
25	119	71

It was estimated that the bearing requirements for the tilted wheel scan system would be similar to those for the 24-probe system.

Table 22. Thrust Load Versus
Axial Deflection
(Single Bearing).

Bearing Preload (pounds)	Thrust Load (pounds)	Axial Deflection (10 ⁴ inches)
10	10	0.4
	20	0.8
	30	1.2
	40	1.6
	46	Unload Point
15	10	0.3
	20	0.65
	30	0.95
	40	1.4
	50	1.6
	60	1.9
	68	Unload Point
20	10	0.25
	20	0.55
	30	0.8
	40	1.1
	50	1.4
	60	1.6
	70	1.9
	80	2.2
	90	Unload Point

Table 23. Thrust Load Versus
Axial Deflection
(Duplex Pair).

Bearing Preload (pounds)	Thrust Load (pounds)	Axial Deflection (10 ⁴ inches)
10	10	0.55
	20	1.15
	30	1.7
	40	2.25
	49	Unload Point
15	10	0.45
	20	0.95
	30	1.4
	40	1.8
	50	2.35
	60	2.8
	69	Unload Point
20	10	0.4
	20	0.8
	30	1.2
	40	1.65
	50	2.05
	60	2.45
	70	2.85
	80	3.3
	90	Unload Point

Table 24. Radial Load Versus
Radial Deflection
(Single Bearing).

Bearing Preload (pounds)	Radial Load (pounds)	Radial Deflection (Micro-inches)
10	20	32
	40	62
	60	94
	80	126
	100	158
	120	190
	140	220
	160	250
15	20	28
	40	54
	60	82
	80	110
	100	138
	120	164
	140	190
	160	218
	180	246
	200	274
20	20	24
	40	48
	60	74
	80	98
	100	122
	120	146
	140	172
	160	198
	180	220
	200	246

Table 25. Radial Load Versus
Radial Deflection
(Duplex Pair).

Bearing Preload (pounds)	Radial Load (pounds)	Radial Deflection (Micro-inches)
10	20	35
	40	52
	60	80
	80	105
	100	130
	120	158
	140	184
	160	210
15	180	236
	200	262
	20	24
	40	48
	60	70
	80	96
	100	118
	120	142
	140	166
	160	190
	180	212
	200	236
	20	22
	40	43
	60	65
	80	86
	100	108
	120	130
	140	152
	160	172
	180	194
	200	216

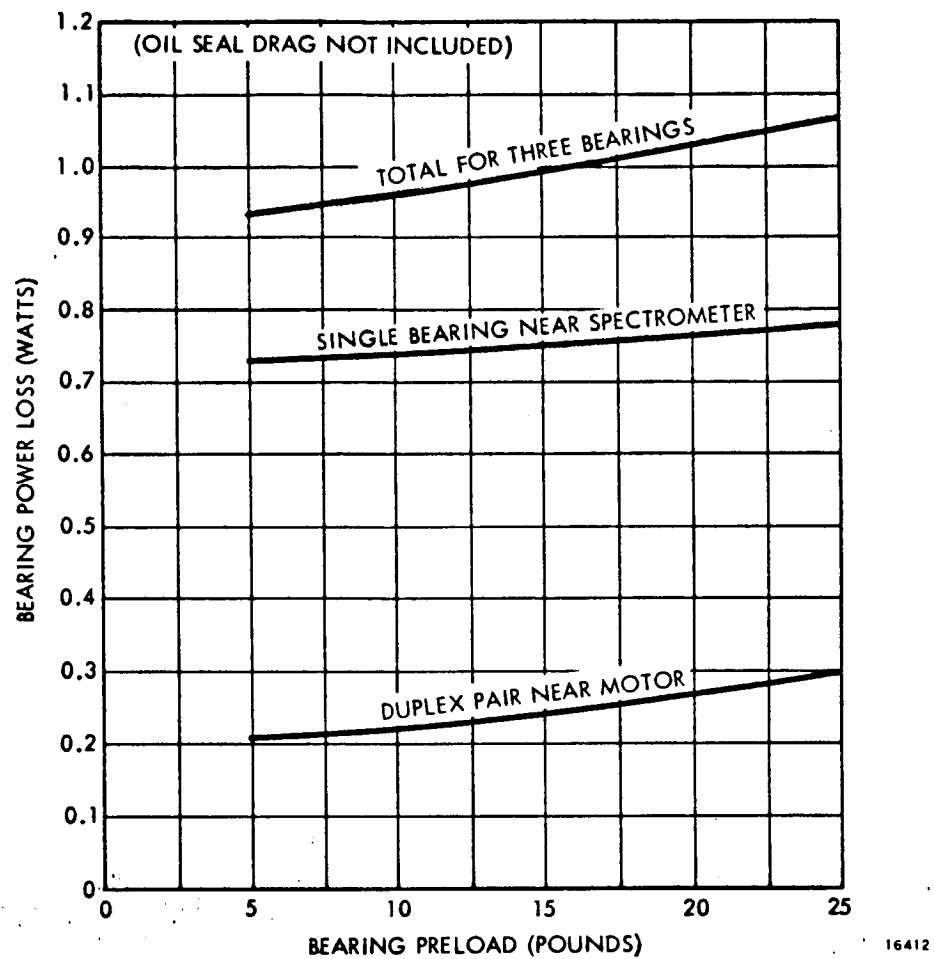


Figure 109. Oil Lubricated Bearing Power Loss.

SYSTEM PERFORMANCE

This section presents results analysing MSPS system performance and its variation with design parameters. The factor that best defines system performance is signal-to-noise ratio, S/N . First, a meaningful definition of S/N is formulated and its effect on spatial and spectral resolution discussed. The variation of S/N with certain parameters is then reported.

Signal-To-Noise Ratio and Noise Equivalent Reflectance

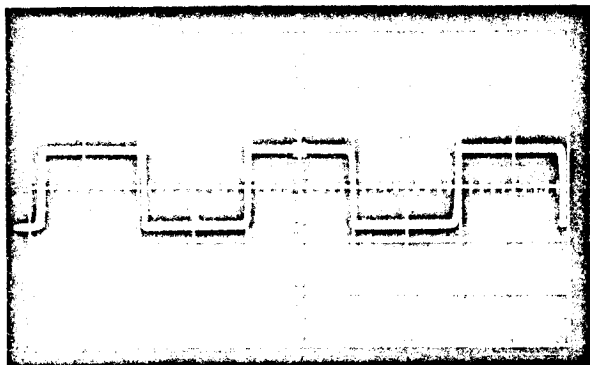
In previous sections, the range of signal amplitude for various terrain targets, and the data channel noise as a function of input, were calculated. It is a simple matter to combine these results and compute an S/N . A difficulty arises in trying to decide which of the many possible definitions of S/N to use or, once calculated, to determine the adequacy of the resultant S/N for the present purpose. Peak highlight signal-to-rms noise is a convenient parameter to compare the performance of different system designs, but represents an unlikely combination of actual operational signals. In addition, since the present system is photon noise limited, the rms noise depends on the signal level. This makes the use of a single noise figure for large dynamic range signals questionable.

A parameter related to S/N that has some meaning with respect to actual operational use is noise equivalent delta reflectance, $NE\Delta R$. This is the change in terrain reflectance which produces a signal change just equal to the rms noise of the system. The units of $NE\Delta R$ are percent, which leads to some ambiguity over meaning. As used here, a change in reflectance of 1 percent signifies a one-unit change of reflectance, not a 1 percent change in signal level. For example, if the terrain reflectance changes from 2 to 3 percent, the signal level may have changed by 50 percent. This is a convenient parameter since the reflectances of various terrain features has been tabulated (see paragraph titled Scene Reflectances) making it possible to estimate the difference in reflectance between targets of interest. This reflectance difference can then be directly compared to $NE\Delta R$ to determine if those targets will produce resolvably different signals and to estimate the quality of reproduced imagery.

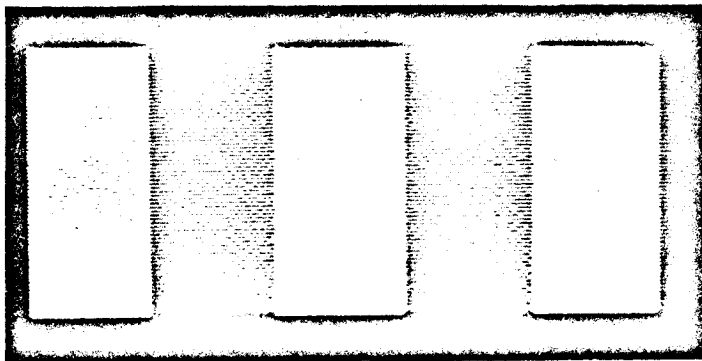
As an aid to estimating the quality of imagery obtainable with various noise levels, the photographs in figures 110 through 112 were made. These photographs of oscilloscope presentations of a square wave bar pattern degraded by varying levels of noise. The signal source was a photomultiplier tube illuminated by a light emitting diode driven by a square wave source. Noise, representing true photon noise, was injected by adding a constant level flux from a separate light source. In all cases, the peak-to-peak signal amplitude is constant, the only difference being in the amount of added noise. The bar width is 20 microseconds, equivalent to 6 resolution elements (230 feet wide each). A resolution element is defined as the area encompassed by the instantaneous field-of-view of the MSPS. The noise bandwidth for all photos is 200 KHz. The results should be representative of actual operating parameters. S/N is defined as the peak-to-peak signal to the rms noise. The results for a S/N of 1 are indicative of that scene illumination condition for two bars (adjacent areas) whose reflectance difference is just equal to the $NE\Delta R$; for $S/N = 2$, a reflectance difference of twice $NE\Delta R$, and so on. The photos show that even for $S/N = 1$, the bar pattern is visible and area density measurements could be made to quantize the reflectances of the two bars.

One reason for the relatively useful results at even a low S/N is that for an extended object, several measurements can be made and averaged either by the observer's eye or by actual computation. This technique improves the effective S/N over the instantaneous value. This effect is demonstrated in figure 113 where individual line scans are visible. For this figure, the signal is a triangular wave of period 6.6 microseconds, which is equivalent to a bar target degraded by system response, one resolution element wide. At a S/N of 1, the signal

A



ANALOG

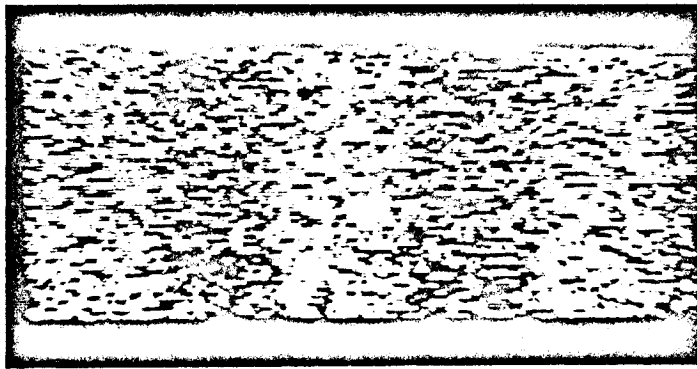


VIDEO

B

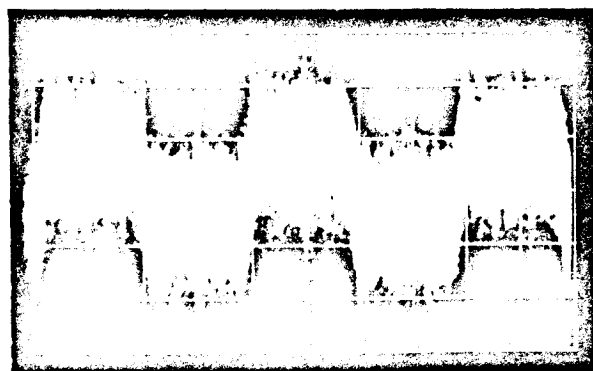


S/N = 1

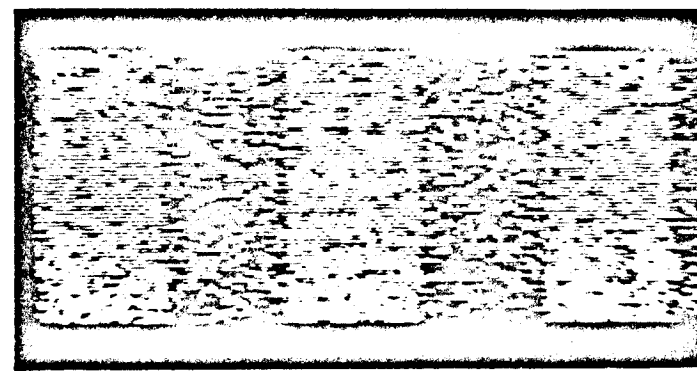


S/N = 1

C



S/N = 2

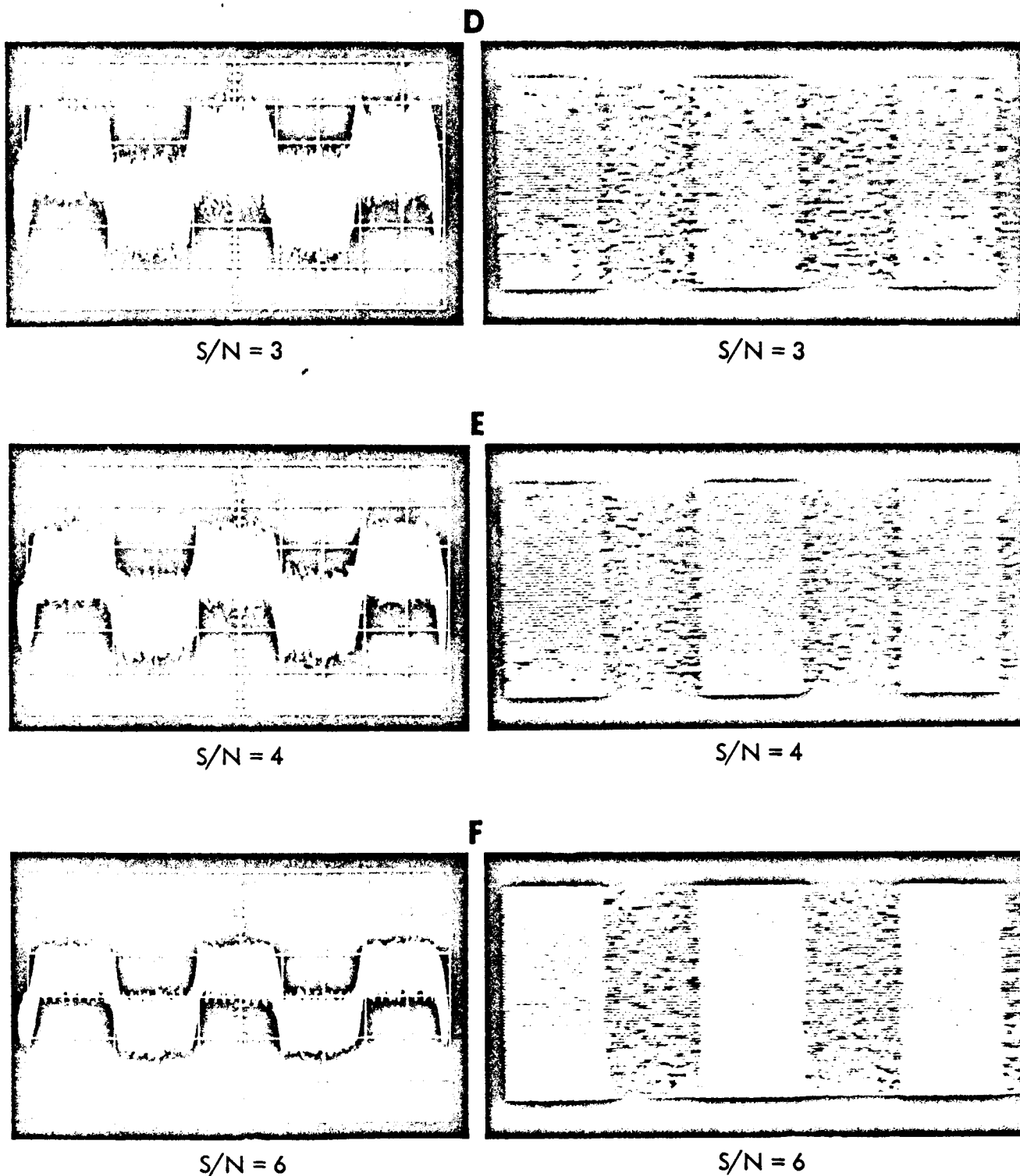


S/N = 2

HORIZONTAL SCALE: 10 MICROSECONDS PER CENTIMETER
NOISE BANDWIDTH: 200 KHZ

16448

Figure 110. Effect of S/N on Analog Signal (Left) and Reproduced Imagery (Right).

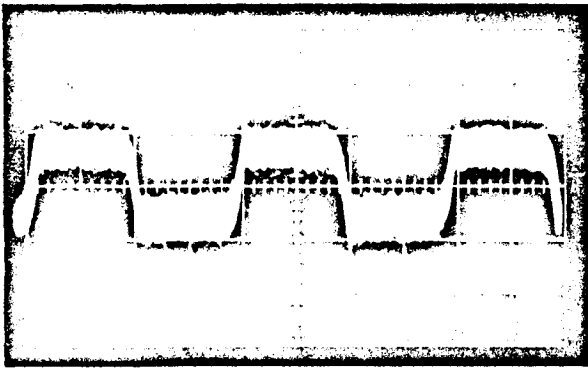


HORIZONTAL SCALE: 10 MICROSECONDS PER CENTIMETER
 NOISE BANDWIDTH: 200 KHZ

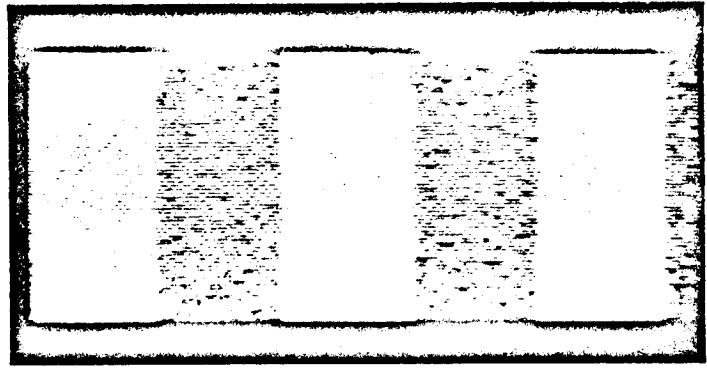
16449

Figure 111. Effect of S/N on Analog Signal (Left) and
 Reproduced Imagery (Right).

G

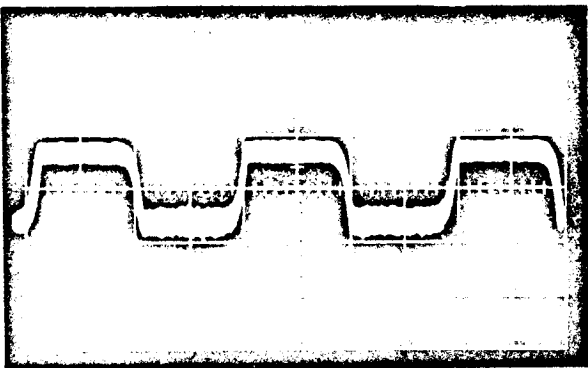


S/N = 10

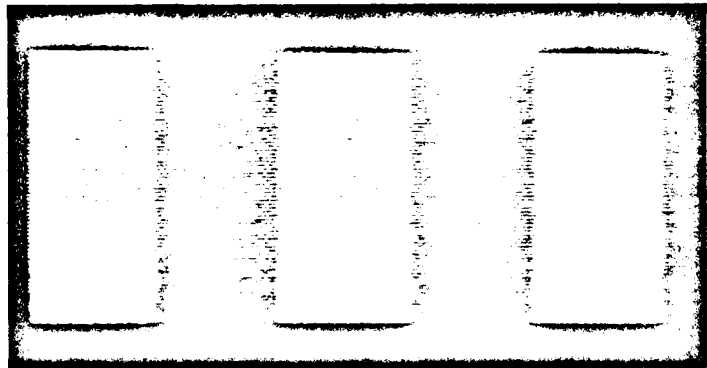


S/N = 10

H

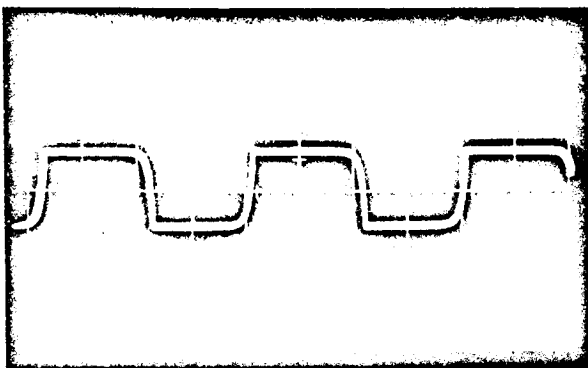


S/N = 20

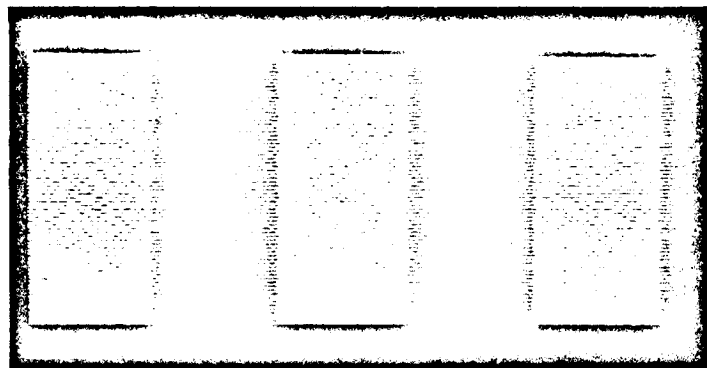


S/N = 20

I



S/N > 100

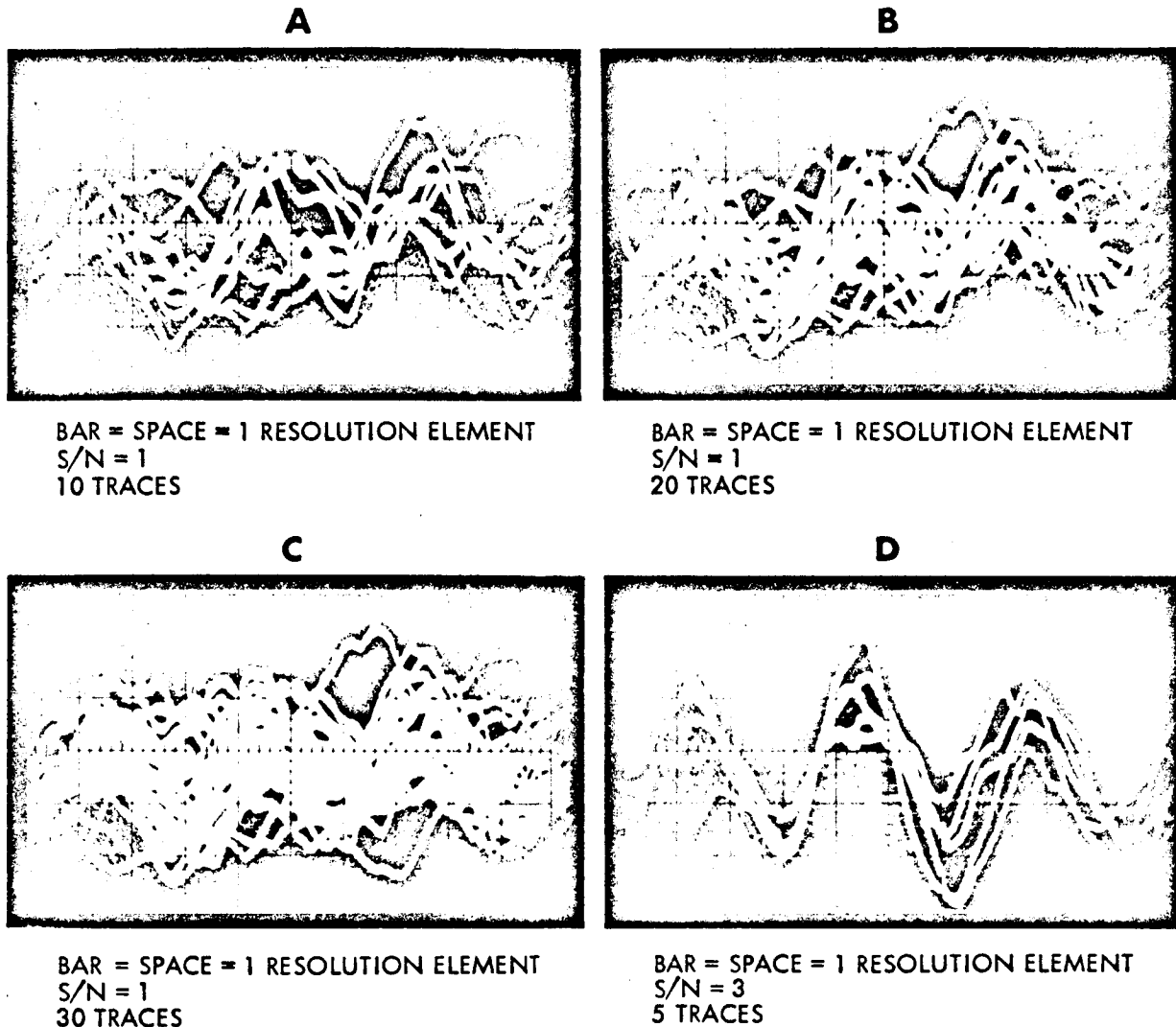


S/N > 100

HORIZONTAL SCALE: 10 MICROSECONDS PER CENTIMETER
NOISE BANDWIDTH: 200 KHZ

16450

Figure 112. Effect of S/N on Analog Signal (Left) and Reproduced Imagery (Right).



SIGNAL IS TRIANGLE WAVE OF PERIOD 3.3 CENTIMETERS
EQUIVALENT TO ONE RESOLUTION ELEMENT
WIDE BAR.

HORIZONTAL SCALE: 2 MICROSECONDS PER CENTIMETER

NOISE BANDWIDTH: 200 KHZ

16447

Figure 113. Effect of Multiple Traces on Ability to Distinguish Signal in Presence of Noise.

shape is not discernible in single traces even when 10 traces are superimposed. When 20 traces are superimposed, a band with roughly triangular shape emerges, and for 30 traces, the effect is reinforced. Clearly shown in the next photo is the effectiveness of even a small increase in instantaneous S/N. Increasing the instantaneous S/N from 1 to 3 provides a dramatic improvement in signal quality.

From these figures, it is concluded that terrain targets with reflectance differences of two to three times the system NEAR will produce definitive imagery and quantitative signals

of great value. For reflectance differences equal to $NE\Delta R$, useful imagery will be produced, although the size of the targets becomes significant in the recognition process.

There are several ways to calculate $NE\Delta R$. The significant point is that the incremental signal resolvable by the scanner is fixed by scanner parameters while the terrain reflectance difference which will produce this just resolvable signal depends on several external factors, such as solar zenith angle and atmospheric conditions. Therefore, although it is possible to calculate a unique value for rms noise, no unique value for $NE\Delta R$ exists.

Because linearity is assumed, the incremental change in input radiant energy caused by a 1 percent change in terrain reflectance is just $P_s (100\%)/100$ where $P_s (100\%)$ is the signal, exclusive of backscatter, due to 100 percent terrain reflectance. To calculate $NE\Delta R$ it is now necessary to compare this 1 percent signal with the actual total noise level. Since the sensor is photon noise limited, the noise depends on the total radiant energy, including backscatter, and can be expressed in the form:

$$ENI \left[P_T(R) \right] = \sqrt{K P_T(R)} \text{ (watts)}$$

where $P_T(R)$ is the total input power for terrain reflectance, R , and K is a constant depending on the spectral band, noise bandwidth, and other system parameters. For a noise bandwidth of 200 KHz and other previously described system parameters, the value of K is given below (see paragraph titled Data Channel Noise):

<u>Band</u>	<u>k</u>
1	$(1.20) 10^{-6}$
2	$(1.56) 10^{-6}$
3	$(2.47) 10^{-6}$
4	$(7.80) 10^{-6}$

Noise equivalent delta reflectance is then given by:

$$NE\Delta R = \frac{ENI \left[P_T(R) \right]}{\frac{P_s (100\%)}{100}} = 100K \frac{P_T(R)}{P_s (100\%)}$$

Notice that $NE\Delta R$ depends on $P_T(R)$, which in turn depends on terrain reflectance; the larger the terrain reflectance, the larger the noise level and, therefore, the larger (worse) the value for $NE\Delta R$. Values for P_T and P_s have been estimated for various assumptions of atmospheric conditions (see paragraph titled Atmospheric Model and Radiant Energy) and the resulting $NE\Delta R$'s plotted as a function of solar zenith angle in figures 114 through 117. These results are valid only for the assumptions listed in the figures. Two curves are shown, one for a terrain reflectance of 100 percent, which represents the worst case for the atmospheric conditions used, and one for the median agricultural reflectance in each band. Increased atmospheric scattering will result in degraded (larger) values for $NE\Delta R$.

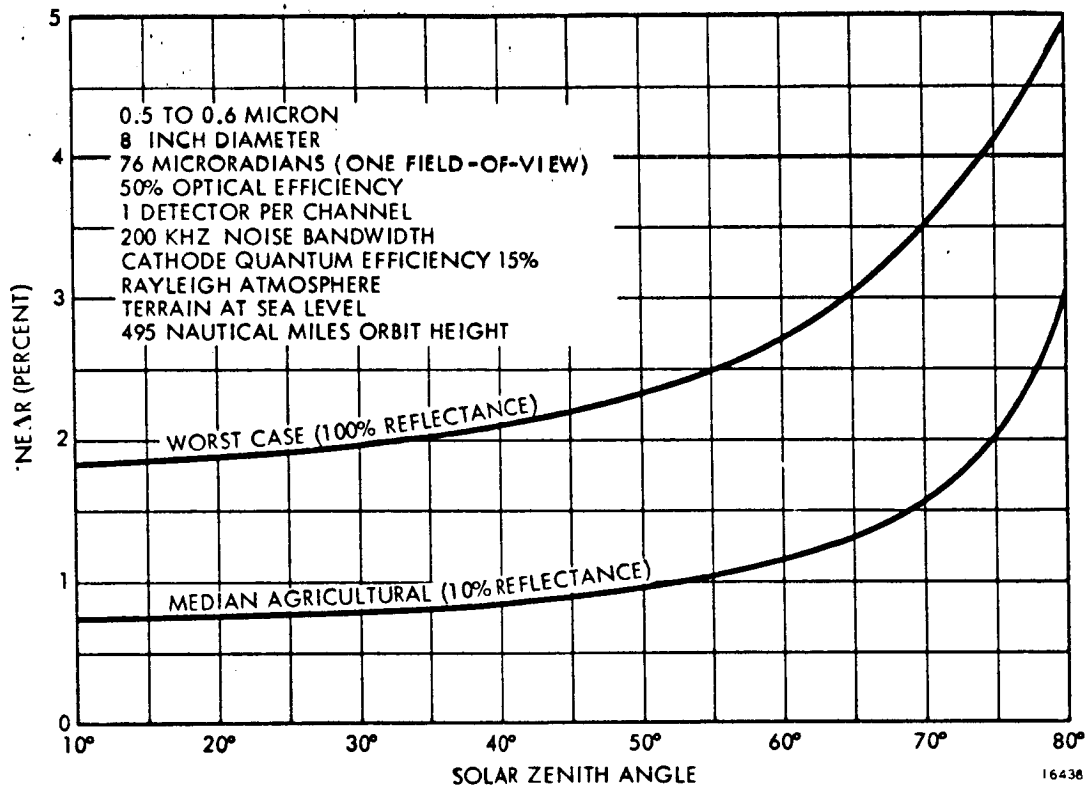


Figure 114. NEAR for Band 1.

System Performance with Parameter Variations

Multispectral scanner performance can be changed by altering any one of the many parameters, such as objective diameter, orbit height, etc. Some of these parameters are significant in that they produce large changes in performance for relatively small parameter variations. Other parameters are not so significant. An example of a relatively insignificant parameter is the number of detectors used per channel, since this affects only the noise bandwidth and that affects performance only as the one-half power. Thus, doubling the number of detectors and halving the attendant reliability results in only a 40 percent improvement in S/N performance. A relatively powerful parameter is the objective mirror diameter, since signal power level increases as the square of the diameter. However, the noise level for a photon noise limited system also increases linearly with signal level, so that overall gain in S/N is proportional only to aperture diameter.

One of the most significant parameters is instantaneous field-of-view, which corresponds to spatial resolution. Increasing the field-of-view has several effects on the system. Signal is increased as the square of the increase in field-of-view. Again the noise density increases, but the required analog bandwidth decreases concurrently, so that overall the rms noise level does not change. Therefore, S/N increases as the square of the field-of-view. The number of bits per sample required to encode the more accurate signal increases slowly as S/N improves, but the number of samples per second drops because of the decrease in bandwidth. The number of bits per second and telemetry rate decreases, but not as fast as analog bandwidth. Another important parameter is the quantum efficiency of the detectors, especially for band 4 when the efficiency of a S-1 surface is very low.

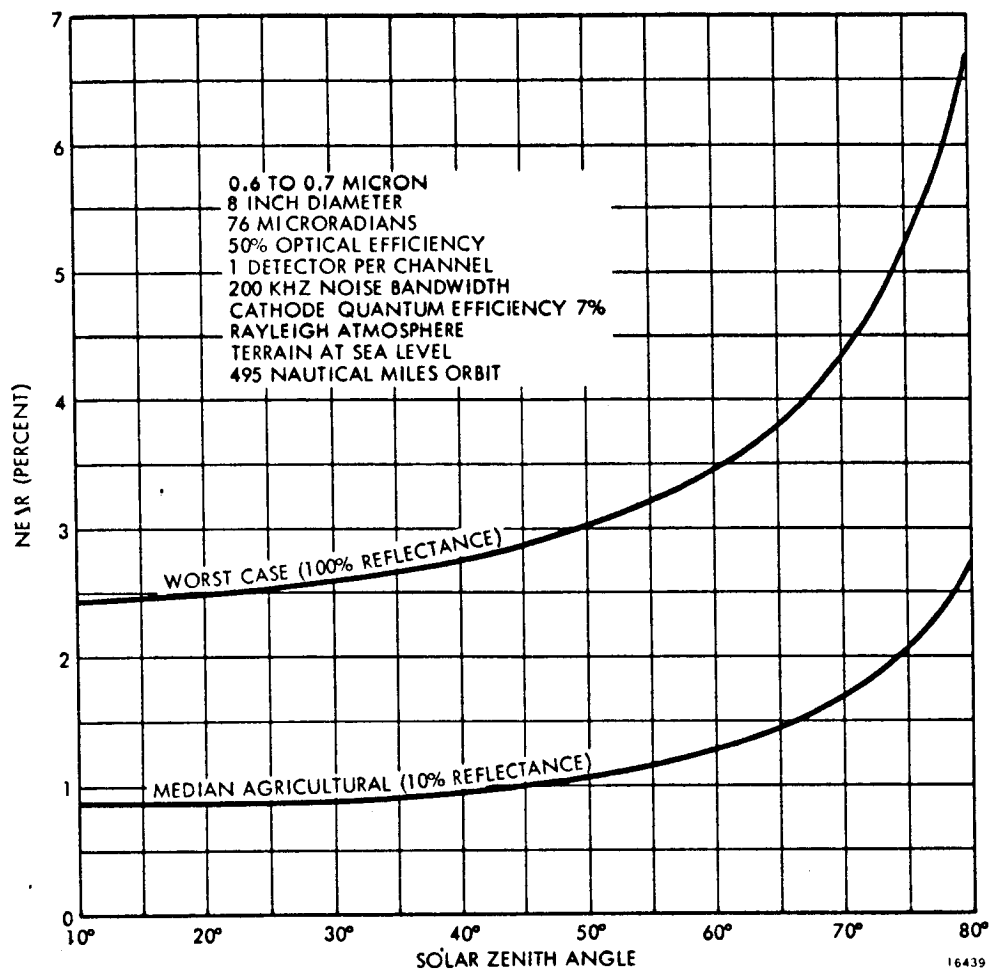


Figure 115. NEAR for Band 2.

These general statements are shown quantitatively in figures 118 through 124. All of the curves shown are relative to a value of 1 at a 200-foot field-of-view, except for the number of bits per sample which cannot be expressed in a relative fashion. To calculate the required number of bits per sample, it was assumed that there are about 100 quantizer levels required at a 200-foot field-of-view and that the number of levels changes directly with S/N. All results are for contiguous scan lines.

Table 26. Parameter Change vs Weight Change.

Parameter	Effect on Weight
Instantaneous field-of-view Detector per channel	None Less than 1 pound per detector added
Objective diameter	3rd or 4th power of the ratio of the diameter change
Orbit height	None
Quantum efficiency	None

These curves are included in this study report to illustrate the effect on the system if any of these parameters are changed. A difficult parameter to estimate without detail design is the effect on weight of these various changes. A qualitative judgment on this effect is given in table 26 only as a guide to the magnitude of the change.

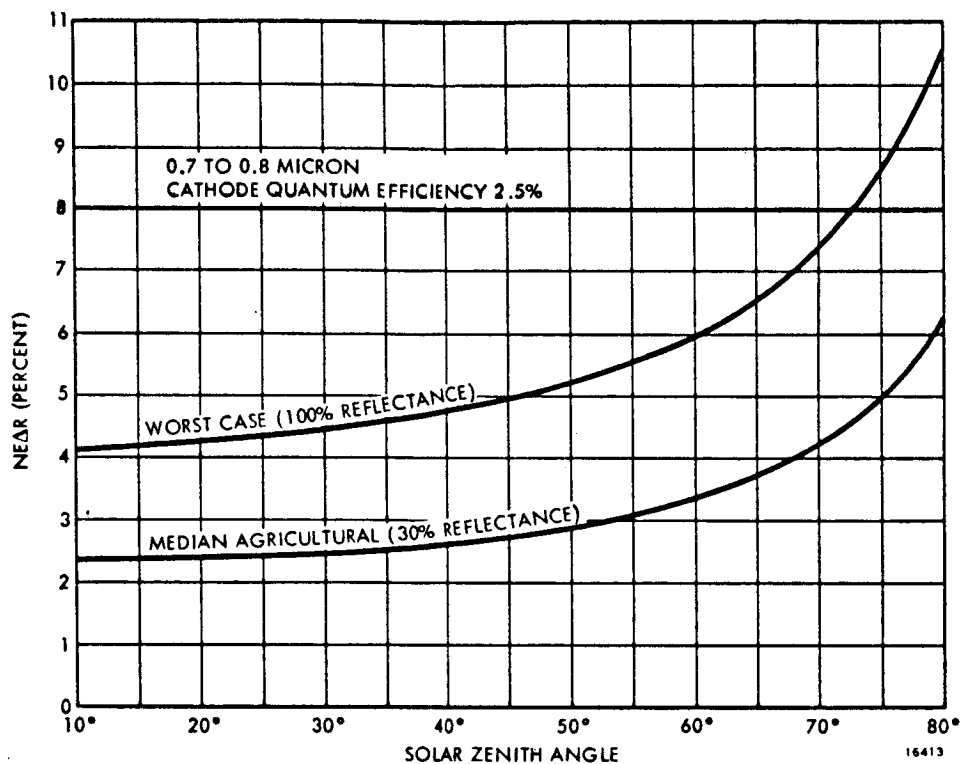


Figure 116. NEAR for Band 3.

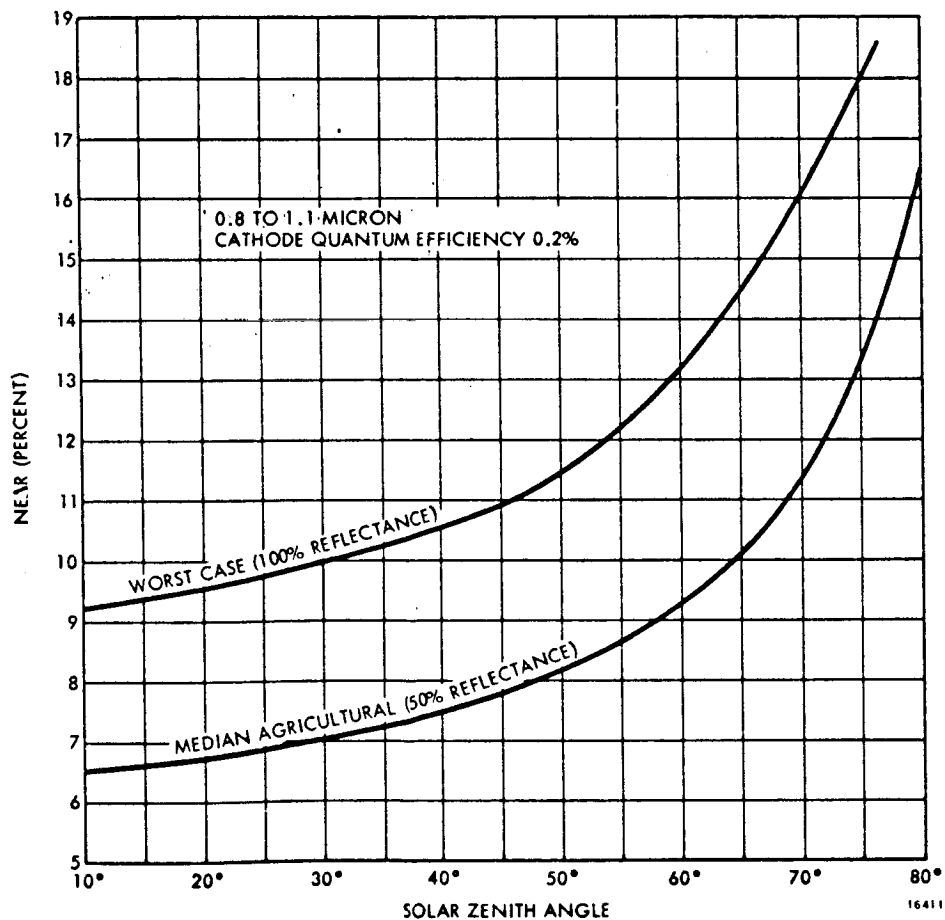
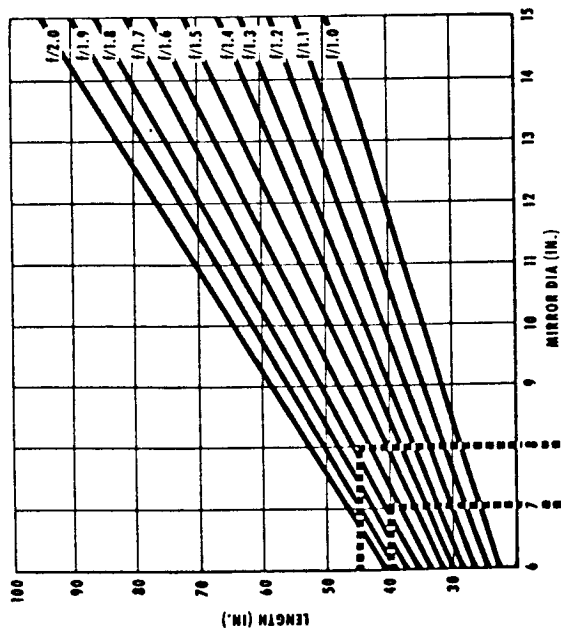


Figure 117. NEAR for Band 4.



$$SN \propto DIA, (FOV)^2, \sqrt{\# \text{ DET/CH}}$$

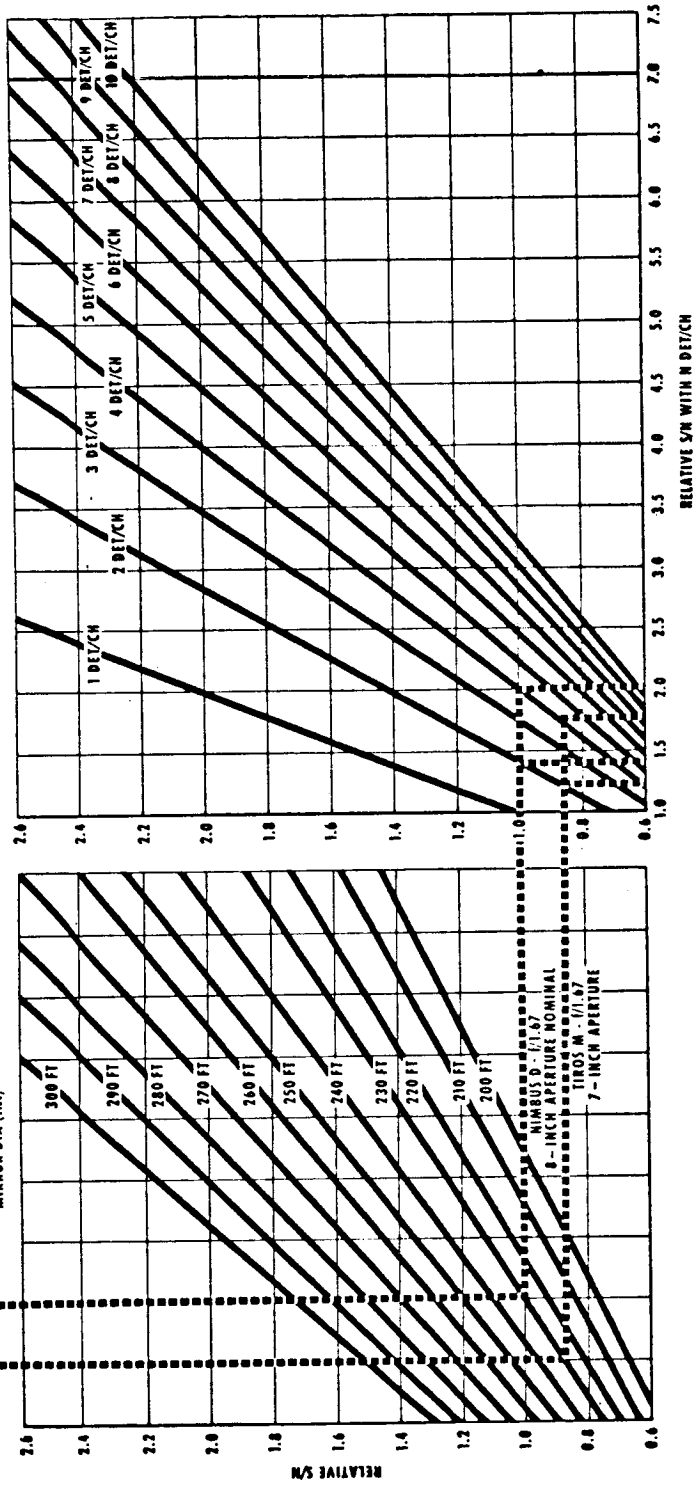


Figure 118. Variation of Scanner Performance with Overall Length, F/Number, Field-of-View, (FOV) and Number of Detectors per Channel.

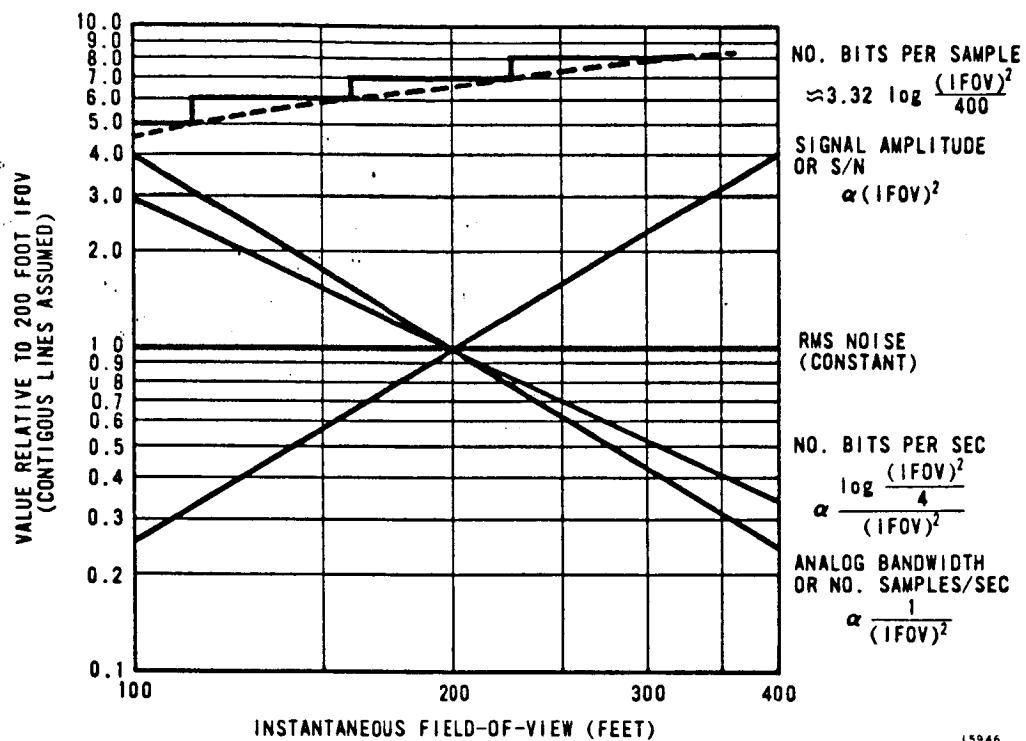


Figure 119. Variation of Parameters Relative to 200-Foot Field-of-View.

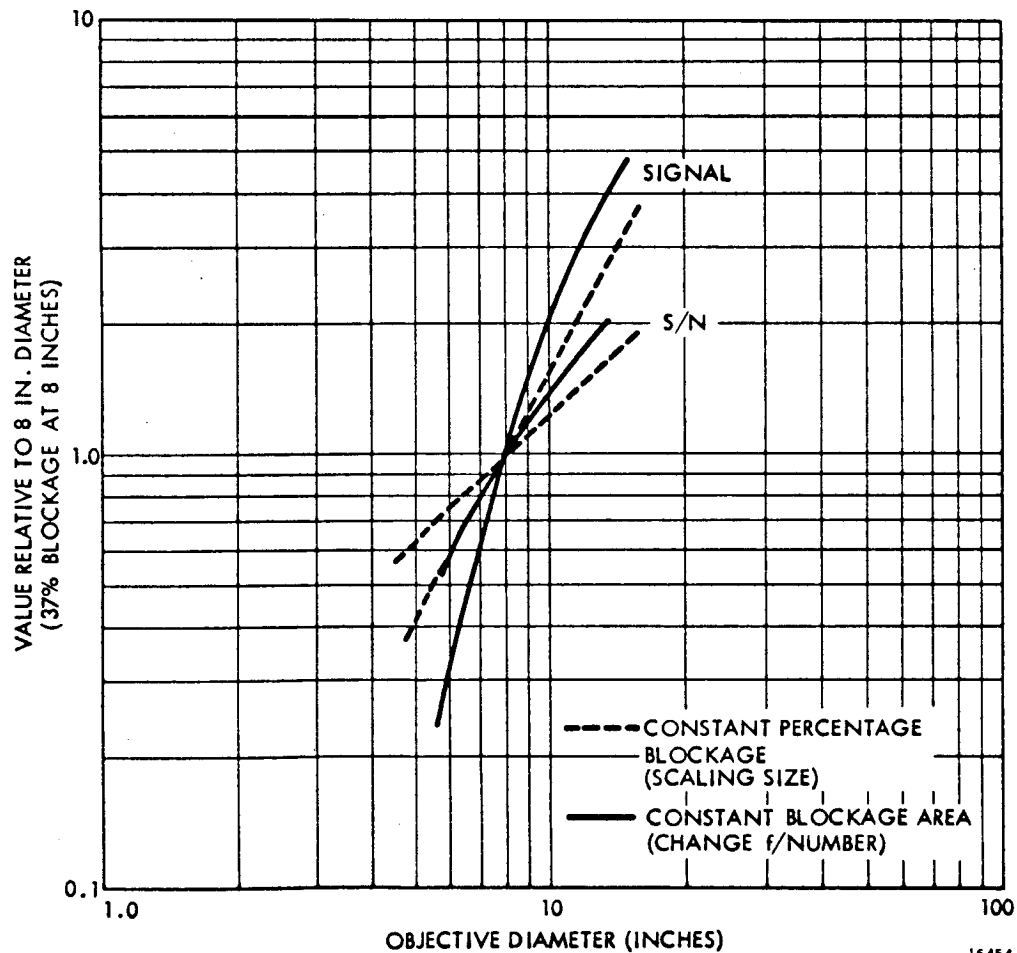


Figure 120. Variation of Parameters with Objective Diameter.

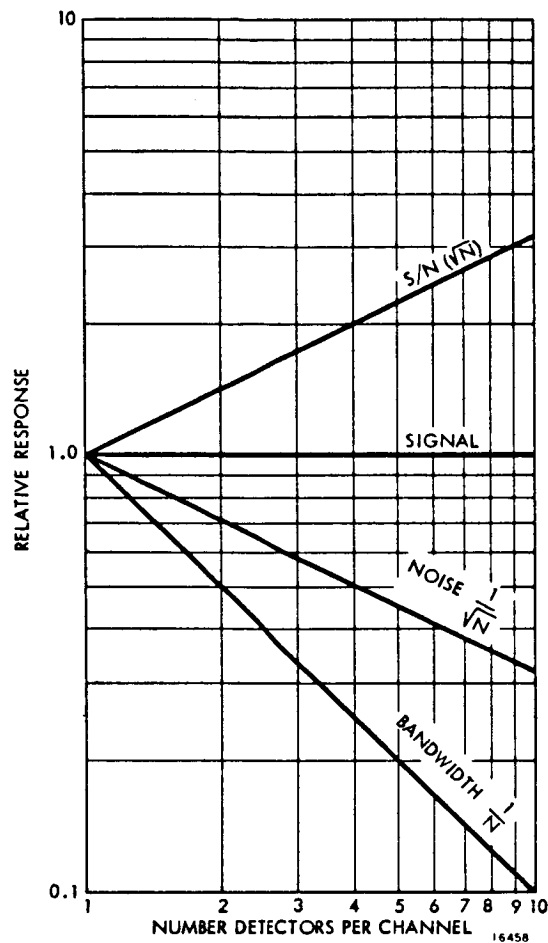


Figure 121. Variation of Parameters with Number of Detectors per Channel Relative to One Detector per Channel.

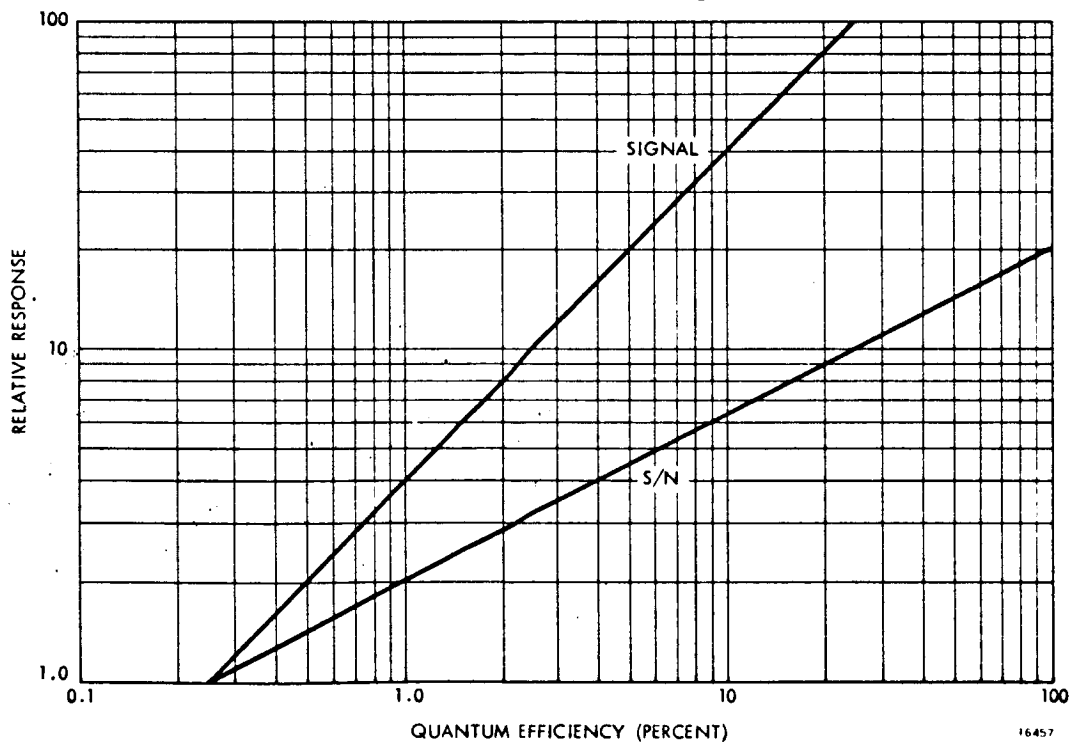


Figure 122. Variation of Parameters Quantum Efficiency Relative to 0.25 Percent (Band 4).

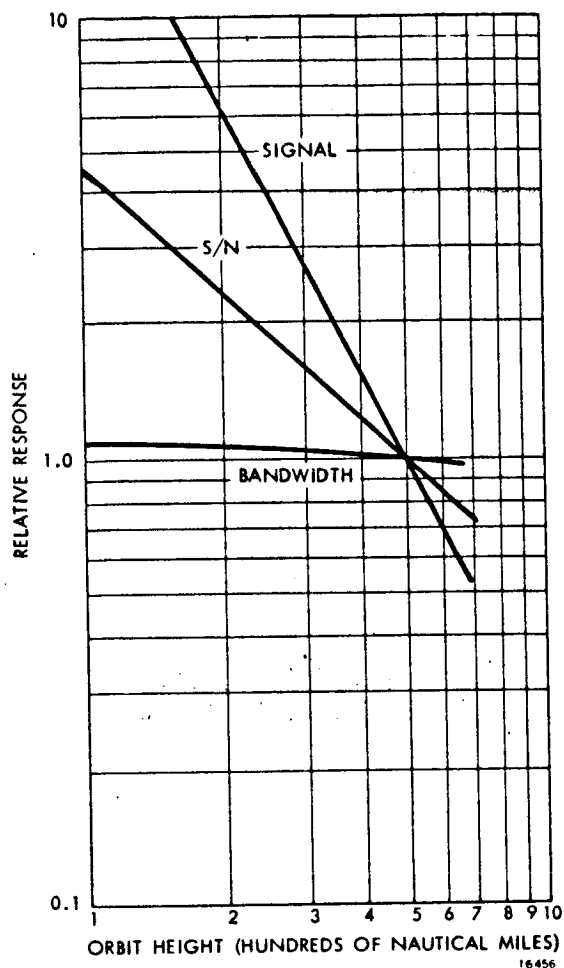


Figure 123. Variation of Parameters Orbit Height Relative to 500 Nautical Miles.

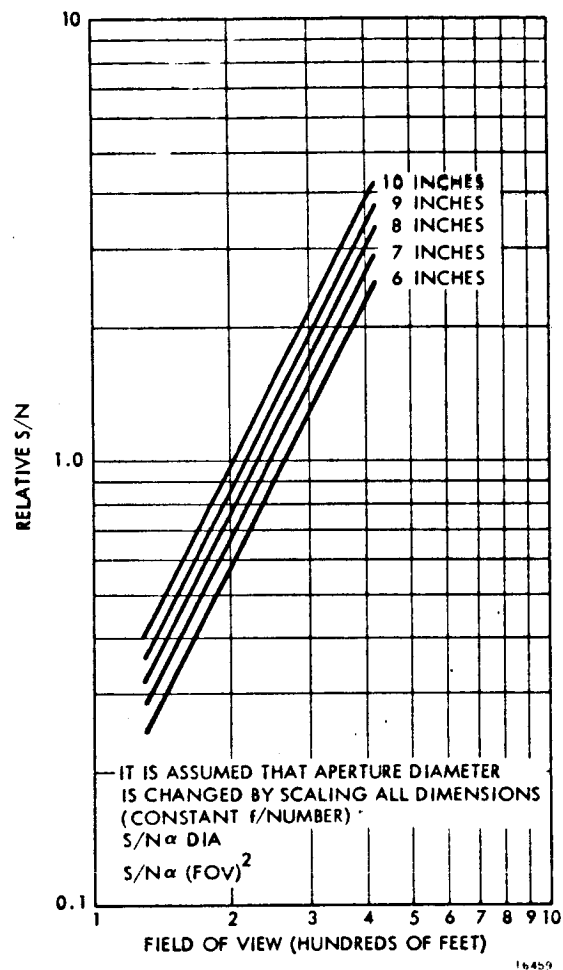


Figure 124. Relative S/N vs. Field-of-View for Various Aperture Diameters.

BIBLIOGRAPHY

- (1) University of Michigan, Target and Background Characteristics, Air Force Avionics Laboratory, Wright Patterson Air Force Base, July 1966, AD489968.
- (2) Gultman, A., Extinction Coefficient Measurements on Clear Atmospheres and Thin Clouds, Applied Optics, Volume 7, Number 12, December 1968.
- (3) Robinson, N., Solar Radiation, Elsavior Publications, New York, 1966, Pp. 214ff.
- (4) Coulson, D., and S., Tables Related to Radiation Emerging from a Planetary Atmosphere with Rayleigh Scattering, University of California Press, 1969.
- (5) Radio Corporation of America, RCA Phototube and Photocells, Technical Manual PT-60, Electronic Components and Devices Division, Lancaster, Pa., 1963.
- (6) Schatt Optical Glass Inc., Color Filter Glass, #365E, Duryea, Pennsylvania.
- (7) Doraning, J., Modulation Systems and Noise, Prentice Hall, P. 91, 1964.
- (8) Feldman, J. R., An Analysis of Frequency Shift Keying Systems, Proceedings of the National Electronics Conference, Volume 17, Pp. 530-542, 1961.
- (9) Cahn, C. R., TRW Report M110-9U5.
- (10) Rosin, S., Inverse Cassegrainian Systems, Applied Optics, Volume 7, Number 8, Pp. 1483-1497, 1968.

GLOSSARY

Following is a list of terms and their abbreviations used in this report.

A/D	analog-to-digital
AM	amplitude modulation
BWN	noise bandwidth
EFL	effective focal length
EHD	elasto-hydrodynamic
ENI	equivalent noise input
ERTS	earth resources technical satellite
FFT	fast Fourier transform
FM	frequency modulation
FOV	field-of-view
FSK	frequency shift keying
HPI	high performance insulation
MEV	million electron volts
MSPS	multispectral point scanner
MTF	modulation transfer function
MYS	microyield stress
NASA/GSFC	National Aeronautics and Space Administration/ Goddard Space Flight Center
NMI	nautical miles
ORA	Optical Research Associates
PCM	pulse code modulation
PM	phase modulation
PMT	photomultiplier tube
PSD	power spectral density
PSI	pounds per square inch
PSK	phase shift keying
S/N	signal-to-noise ratio
VCXO	voltage controlled crystal oscillator

Appendix I

IMAGE ORIENTATION ANALYSIS

When square or rectangular apertures are used, great care must be exercised to prevent image rotation with scan in a system containing folding flats. Analyzing such systems is most conveniently treated using matrix algebra. Consider a series of plane reflectors. Absolute space position can be handled separately so only the direction cosines will be considered. The effect of optical power would be to simultaneously reverse both directions perpendicular to the optical axis.

Consider the following three left matrix operators which transform the spacial orientation of any (column) unit vector. For a rotation through an angle σ about the X-axis:

$$\vec{R}_\sigma = \begin{bmatrix} 1 & 0 & 0 \\ 0 & \cos \sigma & -\sin \sigma \\ 0 & \sin \sigma & \cos \sigma \end{bmatrix}.$$

Evidently:

$$\vec{R}_\sigma^{-1} = \vec{R}_{-\sigma}.$$

For rotation through an angle σ about the Z-axis:

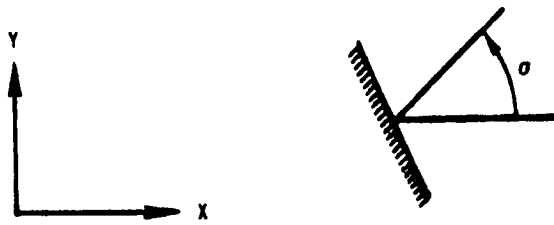
$$\vec{S}_\sigma = \begin{bmatrix} \cos \sigma & -\sin \sigma & 0 \\ \sin \sigma & \cos \sigma & 0 \\ 0 & 0 & 1 \end{bmatrix}.$$

Finally, reflection by a mirror orthogonal to the X-axis is characterized by:

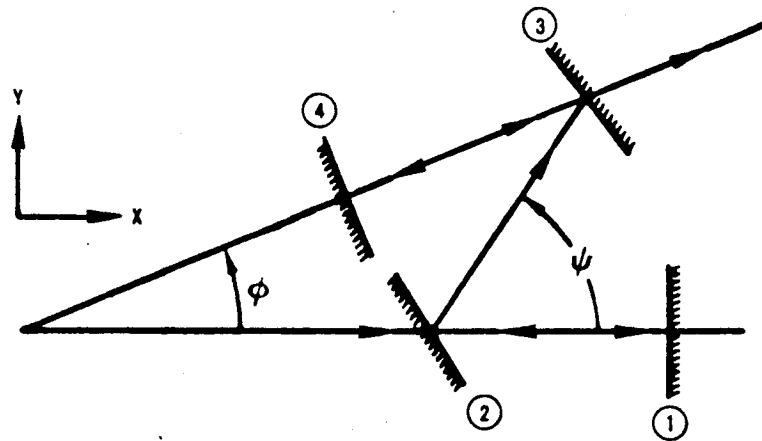
$$\vec{M} = \begin{bmatrix} -1 & 0 & 0 \\ 0 & 1 & 0 \\ 0 & 0 & 1 \end{bmatrix}$$

Thus, a mirror rotated on the Z-axis will result in a transformation:

$$\vec{A}_\sigma = \vec{S}_\sigma \vec{M} \vec{S}_\sigma^{-1} = \begin{bmatrix} -\cos 2\sigma & -\sin 2\sigma & 0 \\ -\sin 2\sigma & \cos 2\sigma & 0 \\ 0 & 0 & 1 \end{bmatrix}$$



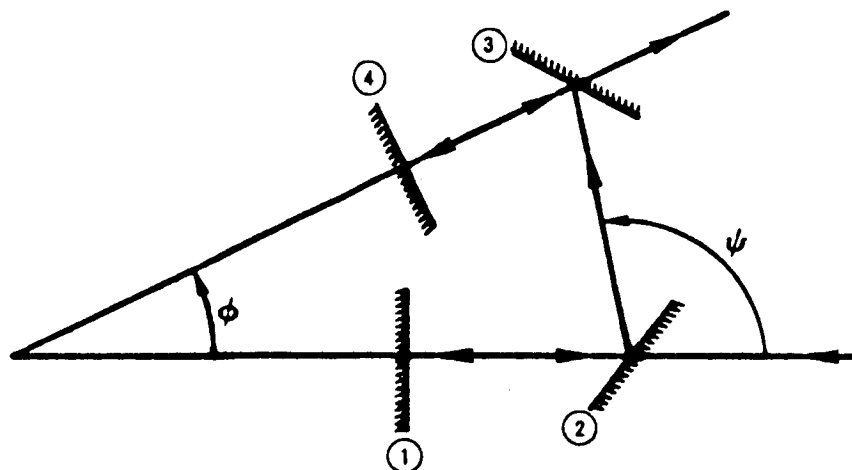
Consider the planar system:



This system performs the transformation:

$$\vec{T}_1 = \vec{A}_\phi \cdot \vec{A}_{\frac{\psi + \phi}{2}} \cdot \vec{A}_{\frac{\psi}{2}} \cdot \vec{A}_0$$

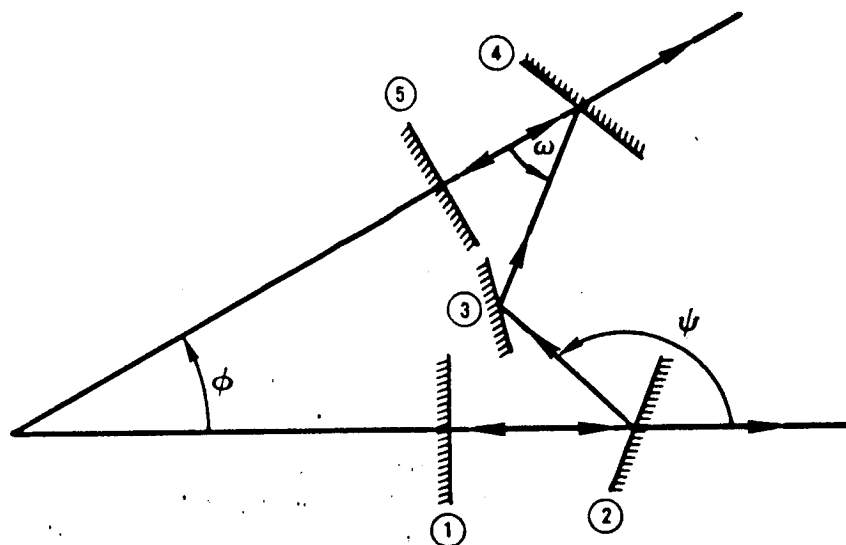
Another system is:



Here:

$$\vec{T}_2 = \vec{A}_\phi \vec{A}_{\frac{\psi + \phi}{2}} \vec{A}_{\frac{\pi + \psi}{2}} \vec{A}_0$$

Finally, consider:.



$$\vec{T}_3 = \vec{A}_\phi \vec{A}_\omega \vec{A}_\psi \vec{A}_0$$

It is obvious that:

$$\vec{A}_\alpha \vec{A}_\beta = \begin{bmatrix} \cos(2\alpha - 2\beta) & -\sin(2\alpha - 2\beta) & 0 \\ \sin(2\alpha - 2\beta) & \cos(2\alpha - 2\beta) & 0 \\ 0 & 0 & 1 \end{bmatrix} = \vec{B}_{\alpha - \beta}$$

so,

$$\begin{cases} \overrightarrow{T_1} = \overrightarrow{B_{\frac{\Phi-\psi}{2}}} \cdot \overrightarrow{B_{\frac{\psi}{2}}} \\ \overrightarrow{T_2} = \overrightarrow{B_{\frac{\Phi-\psi}{2}}} \cdot \overrightarrow{B_{\frac{\pi+\psi}{2}}} \\ \overrightarrow{T_3} = \overrightarrow{B_{\frac{-\omega}{2}}} \cdot \overrightarrow{B_{\frac{\Phi+\omega}{2}}} \cdot \overrightarrow{A_0} \end{cases}$$

Now also:

$$\overrightarrow{B_{\alpha}} \cdot \overrightarrow{B_{\beta}} = \overrightarrow{B_{\alpha+\beta}}$$

And thus:

$$\overrightarrow{T_1} = \overrightarrow{B_{\frac{\Phi}{2}}} = \begin{bmatrix} \cos \Phi & -\sin \Phi & 0 \\ \sin \Phi & \cos \Phi & 0 \\ 0 & 0 & 1 \end{bmatrix}$$

$$\overrightarrow{T_2} = \overrightarrow{B_{\frac{\Phi}{2} + \pi}} = \begin{bmatrix} -\cos \Phi & \sin \Phi & 0 \\ -\sin \Phi & -\cos \Phi & 0 \\ 0 & 0 & 1 \end{bmatrix}$$

$$\overrightarrow{T_3} = \overrightarrow{B_{\frac{\Phi}{2} - \pi}} \cdot \overrightarrow{A_0} = \begin{bmatrix} -\cos \Phi & -\sin \Phi & 0 \\ -\sin \Phi & \cos \Phi & 0 \\ 0 & 0 & 1 \end{bmatrix}.$$

We now rotate the entire system through an angle ϵ about the X-axis. Then we obtain:

$$\overrightarrow{T_i'} = \overrightarrow{R_{\epsilon}} \cdot \overrightarrow{T_i} \cdot \overrightarrow{R_{\epsilon}}^{-1}$$

Finally to orthogonalize the solution in the region of interest, we go to:

$$\overrightarrow{T_i''} = \overrightarrow{T_i}^{-1} \overrightarrow{T_i'} = \overrightarrow{T_i}^{-1} \cdot \overrightarrow{R_\epsilon} \cdot \overrightarrow{T_i} \cdot \overrightarrow{R_\epsilon}^{-1}$$

For compactness:

$$\begin{cases} \cos \Phi = c \\ \sin \Phi = s \\ \cos \epsilon = u \\ \sin \epsilon = v \end{cases}$$

then,

$$\overrightarrow{T_1''} = \begin{bmatrix} c^2 + us^2 & usc(u-1) + v^2s & vsc(u-1) - uvs \\ sc(u-1) & u(s^2 + uc^2) + v^2c & v(s^2 + uc^2) - uvc \\ vs & uv(c-1) & u^2 + v^2c \end{bmatrix}$$

$$\overrightarrow{T_2''} = \begin{bmatrix} c^2 + us^2 & usc(u-1) - v^2s & vsc(u-1) + uvs \\ sc(u-1) & u(s^2 + uc^2) - v^2c & v(s^2 + uc^2) + uvc \\ -vs & -uv(c+1) & u^2 - v^2c \end{bmatrix}$$

$$\overrightarrow{T_3''} = \begin{bmatrix} c^2 + us^2 & usc(1-u) - v^2s & vsc(1-u) + uvs \\ sc(1-u) & u(s^2 + uc^2) + v^2c & v(s^2 + uc^2) - uvc \\ -vs & uv(c-1) & u^2 + v^2c \end{bmatrix}.$$

Since ϵ is reasonably, small, then the second order in ϵ_i is:

$$\overrightarrow{T_1''} = \begin{bmatrix} 1 & 0 & 0 \\ 0 & 1 & 0 \\ 0 & 0 & 1 \end{bmatrix} + \begin{bmatrix} 0 & 0 & -s \\ 0 & 0 & 1-c \\ s & c-1 & 0 \end{bmatrix} \epsilon + \begin{bmatrix} -1/2s^2 & s(1-1/2c) & 0 \\ -1/2sc & c-1/2-1/2c^2 & 0 \\ 0 & 0 & c-1 \end{bmatrix} \epsilon^2$$

$$\overline{T_2''} = \begin{bmatrix} 1 & 0 & 0 \\ 0 & 1 & 0 \\ 0 & 0 & 1 \end{bmatrix} + \begin{bmatrix} 0 & 0 & s \\ 0 & 0 & 1+c \\ -s & -c-1 & 0 \end{bmatrix} \epsilon + \begin{bmatrix} -1/2 s^2 & -s(1+1/2 c) & 0 \\ -1/2 s c & -c-1/2-1/2 c^2 & 0 \\ 0 & 0 & -c-1 \end{bmatrix} \epsilon^2$$

$$\overline{T_3''} = \begin{bmatrix} 1 & 0 & 0 \\ 0 & 1 & 0 \\ 0 & 0 & 1 \end{bmatrix} + \begin{bmatrix} 0 & 0 & s \\ 0 & 0 & 1-c \\ -s & c-1 & 0 \end{bmatrix} \epsilon + \begin{bmatrix} -1/2 s^2 & s(1/2 c-1) & 0 \\ 1/2 s c & c-1/2-1/2 c^2 & 0 \\ 0 & 0 & c-1 \end{bmatrix} \epsilon^2$$

These expressions show that for reasonable values of Φ , $\overline{T_1''}$ and $\overline{T_3''}$ are equivalent, and both yield significantly less space rotation of the image about the look direction axis than does $\overline{T_2''}$.

Appendix II

BURCH MICROSCOPE OBJECTIVES

The two-element reflective probes for the MSPS are essentially Burch microscope objectives. (Rosin⁽¹⁰⁾ calls them "inverse cassegrainian systems", D. Grey, "Schwarzschild mirrors.") Fundamentally, the family consists of two mirrors of radii, r_1 and r_2 , separated by a distance $t_p = d$. All first-order properties can be derived from these three parameters. For the third-order properties, the position of the stop is important for all aberrations except spherical. Also, the conic constants and the fourth-order aspheric coefficients must be specified if the two mirrors are permitted to be aspheric.

Rosin provides a complete algebraic description of Burch microscope objectives composed of spherical elements and mentions the possibility of extending the analysis to cover aspheric surfaces. This extension is developed in this short note in general terms, but all examples are specific to the probe problem.

The algebraic method provides a powerful insight into such systems, not afforded by optimization programs. All solutions meeting a given set of conditions can be found and evaluated. Such systems, having the desired first- and third-order characteristics, provide excellent starting configurations for the automatic programs.

Theory

First-order properties of the system are specified by three quantities, r_1 , r_2 , and d . Generally, three equations are required in these three unknowns (figure 125). Following Rosin, first define new parameter α

$$\alpha = \frac{h_2}{h_1},$$

where h_1 and h_2 are the paraxial (axial) ray heights on the two mirrors. Then select a scale factor equal to the object distance, s_1 , measured from the first mirror. The curvatures are thus expressed as the dimensionless parameters

$$\kappa = \frac{s_1}{r_1}$$

$$\lambda = \frac{s_1}{r_2}$$

(For an infinite object image distance, s_2' should be used as the scale factor.)

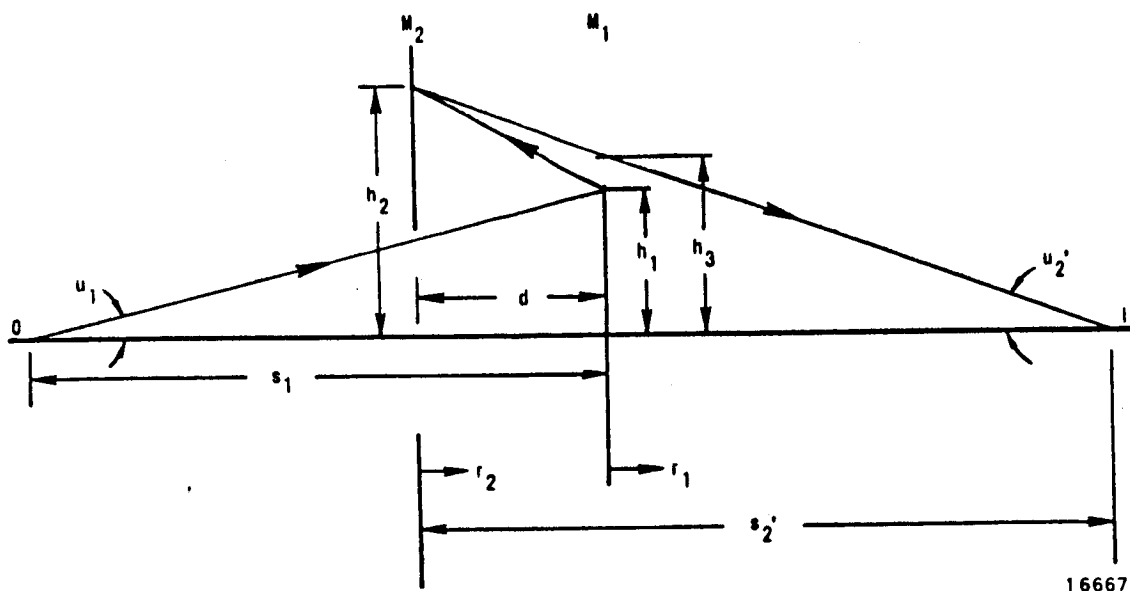


Figure 125. Burch Microscope Objective.

These three variables completely determine the system, since the normalized separation is given by

$$\frac{d}{s_1} = \left(\frac{1 - \alpha}{2\kappa - 1} \right). \quad (1)$$

Conventional ray-tracing sign conventions are used so that d is negative, as is s_1 for real objects. In figure 125, if a mirror is convex to the left, its radius is positive.

First-Order Relationships. -Depending on the given conditions, there are a large number of first-order equations relating α , κ , and λ . Suppose that the desired angular magnification μ is known, then

$$\mu = \frac{u_2'}{u_1} = -\frac{F_1^\#}{F_2^\#} = 2\alpha\lambda - 2\kappa + 1 \quad (2)$$

or,

$$\alpha\lambda = \kappa + \frac{(\mu - 1)}{2}$$

where u_1 and u_2' are the incident and emergent angles, respectively, of the marginal paraxial ray. Focal ratios $F_1^\#$ and $F_2^\#$ are for the corresponding cones. Likewise, if focal length f of the system is specified, then

$$\frac{f}{s_1} = -\frac{(2\kappa - 1)}{2(\lambda - \mu\kappa)}.$$

Another such condition is for the case of known total track, ℓ , from object to image, which is given by

$$\frac{\ell}{s_1} = -1 + \frac{d}{s_1} + \frac{\alpha}{\mu}. \quad (3)$$

Equation (1) for d/s_1 and (2) for μ can be inserted into equation (3), if necessary.

Two other equations based on specified obscuration ratios are derived by Rosin. Suppose the configuration is as in figure 125, so that the blockage is provided by the first mirror. The obscuration factor φ for the exiting bundle is then:

$$\varphi = \frac{h_3}{h_1} = \alpha + \mu \left(\frac{d}{s_1} \right) = \alpha + \frac{\mu(1 - \alpha)}{(2\kappa - 1)}. \quad (4)$$

Notice φ is inversely proportional to the linear obscuration. Suppose the configuration is reversed as shown in figure 126. Then the incident bundle is obscured and can be described by the obscuration factor φ^* , given by

$$\varphi^* = \frac{h_4}{h_2} = \frac{(2\kappa + \alpha - 2)}{\alpha(2\kappa - 1)}.$$

This completes the list of common first-order relationships.

Third-Order Relationships. -If the mirrors are permitted to assume conic forms, specified by eccentricities ϵ_1 and ϵ_2 , then longitudinal spherical aberration q can be written as

$$q = \frac{h_1 u_1}{\mu^2} \left[\kappa(\kappa - 1)^2 - \epsilon_1^2 \kappa^3 - \alpha^2 \lambda (\alpha \lambda - 2\kappa + 1)^2 + \epsilon_2^2 \alpha^4 \lambda^3 \right],$$

where $u_1 = 1/2F_1^\#$ is the paraxial entrance angle of the rim ray.

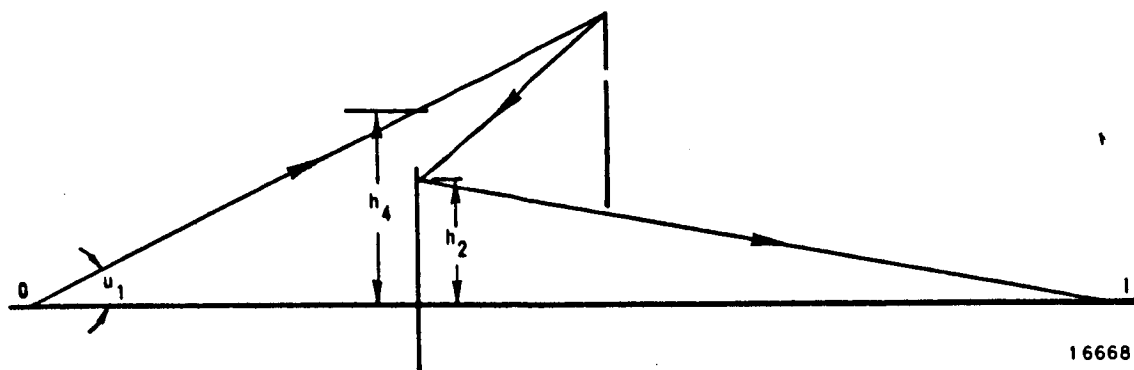


Figure 126. Burch Microscope Objective (Reversed).

For spherical surfaces, $\epsilon_1 = \epsilon_2 = 0$ so that the condition for zero spherical aberration becomes

$$\kappa(\kappa - 1)^2 = \alpha^2 \lambda [\alpha \lambda - 2\kappa + 1]^2. \quad (5)$$

Where the objective is to be used with an optical system that produces an image with spherical aberration $-q^*$, then the total system can be free from spherical aberration if

$$q = \frac{q^*}{\mu}$$

that is, if q^* satisfies

$$q^* = h_1 u_1 \left\{ \kappa(\kappa - 1)^2 - \alpha \alpha \lambda (\alpha \lambda - 2\kappa + 1)^2 - \epsilon_1^2 \kappa^3 + \epsilon_2^2 \alpha^4 \lambda^3 \right\}. \quad (6)$$

Extension of the theory to cover coma is outside the scope of this report. Note that for spherical mirrors which have no spherical aberration, i.e., whose parameters satisfy equation (5), then the relationship required for simultaneously correcting both third-order coma and astigmatism is

$$\lambda(\kappa \alpha + \kappa - 1) = \kappa(2\kappa - 1).$$

This equation actually expresses the concentricity of the two mirrors, so that it is equivalent to

$$r_2 = r_1 - d.$$

Note that this is independent of the stop position.

MSPS Probe: Spherical Surfaces. -It is desired to scan the primary image that formed by the spherical primary mirror, with a set of identical catoptric probes. A two-element Burch microscope objective is an obvious simple choice for the probe optics. One possible MSPS configuration is shown in figure 127. (The optical ray is reversed in direction from the usual convention so that the probe is shown as in figures 125 and 126.) The probe, consisting of secondary and tertiary, scans the primary image by rotating about C, the center of curvature of the primary mirror and image. The final image is at C.

The first-order requirements for the probe are governed by the primary mirror and the scanning geometry. Since most versions of the MSPS considered have very small fields-of-view (about 0.1 milliradian), spherical aberration is the most important of the third-order effects.

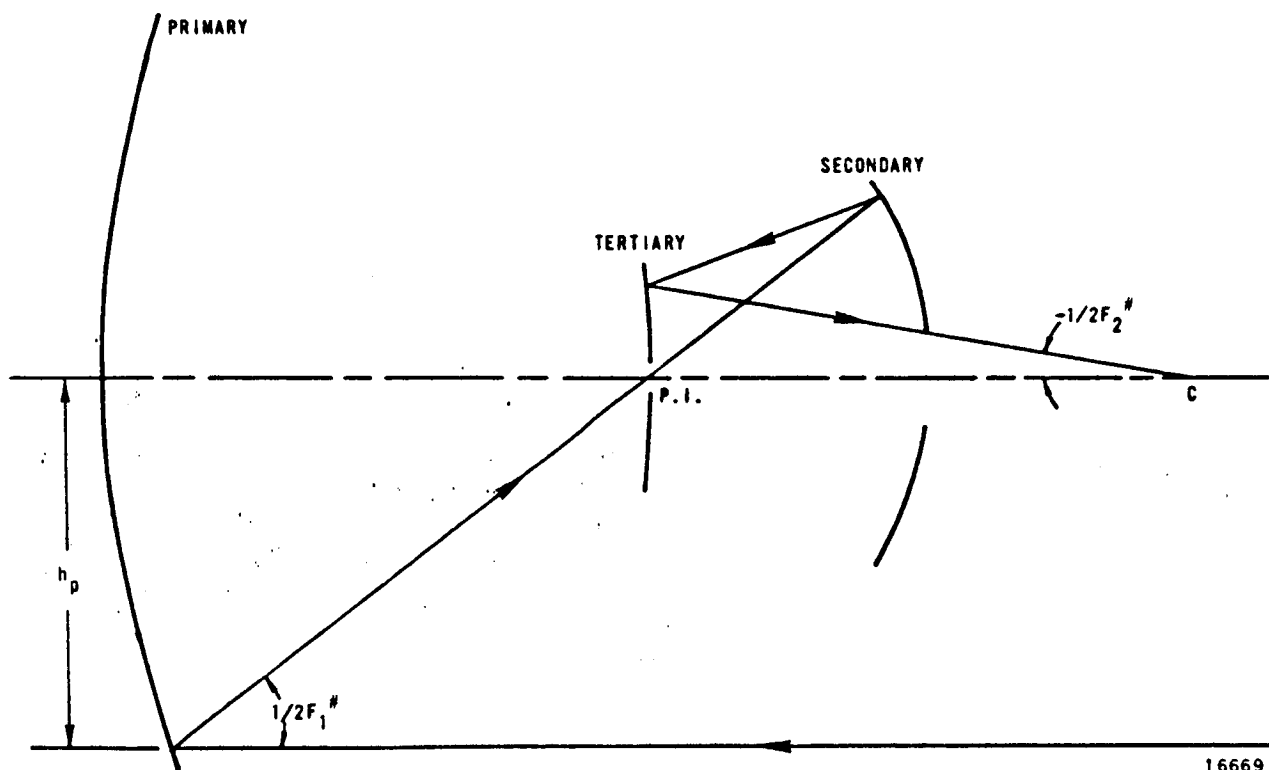


Figure 127. Catoptric MSPS Configuration.

A major system tradeoff concerns the amount of spherical aberration correction to be afforded by the probe. The spherical aberration of the primary mirror can be written

$$q^* = \frac{h_p^2}{4r_p} = -\frac{h_p}{16F_1^\#}$$

where h_p , r_p (< 0) and $F_1^\#$ (> 0) are, respectively, the semiaperture, the radius of curvature, and the focal ratio of the primary mirror. Since $h_1 = h_2/\alpha$, and if all correction of spherical aberration are to be accomplished in the probe, then the relationship

$$\frac{\kappa(\kappa-1)^2}{\alpha} - \alpha\lambda(\alpha\lambda - 2\kappa + 1)^2 - \frac{\epsilon_1^3 \kappa}{\alpha} + \epsilon_2^3 \alpha^3 \lambda^3 = -\frac{h_p}{8h_2} \quad (7)$$

must hold.

For first-order parameters, examine the case where there is no blocking of the incident ray bundle, i.e.,

$$\varphi^* = h_4 = 0,$$

and the light is introduced into the probe through a small hole in the tertiary mirror. This leads to

$$d = s_1$$

so that equation (1) becomes

$$\alpha = -2(\kappa - 1). \quad (8)$$

If the probe's angular magnification μ is specified, then

$$\alpha\lambda = \kappa + \frac{(\mu - 1)}{2}. \quad (9)$$

As a first effort, examine the family of Burch objectives composed of spherical mirrors which, with the primary, produce zero spherical aberration. Then, after substitution, equation (7) becomes

$$-\kappa^2 + \kappa - 2(\kappa + \beta)(\beta + 1 - \kappa)^2 = -\frac{h_p}{4h_2}, \quad (10)$$

where,

$$\beta = \frac{(\mu - 1)}{2}.$$

For generating numbers, examine systems which use an f/1.5, 12-inch primary. With this geometry, $h_p = 6''$ and $h_2 = 6\mu$.

Equation (10) is a cubic in κ and can be written

$$p_1 \kappa^3 + p_2 \kappa^2 + p_3 \kappa + p_4 + \gamma = 0 \quad (11)$$

with,

$$p_1 = -2$$

$$p_2 = 2\beta + 3$$

$$p_3 = 2\beta^2 - 1$$

$$p_4 = -2\beta(\beta + 1)^2$$

$$\gamma = \frac{h_p}{4h_2} = -\frac{0.25}{\mu}.$$

All cubic equations have at least one real root. Systems corresponding to imaginary roots and systems which have positive d (and s_1) must be discarded. The latter condition implies a virtual object.

The condition that s_1 is negative demands that h_1 be positive, since

$$s_1 = -2h_1 F_1^\#$$

and $F_1^\#$, the f/number of the input cone, is positive. Hence, α must have an algebraic sign opposite to μ .

From equation (9), note that for negative μ , $\kappa > 1$, and for positive μ , $\kappa < 1$.

The cubic for the case $\mu = 0.25$ is plotted in figure 126. There are no physically realizable solutions for this case, since the only real root $\kappa = 1.195 > 1$. Omitting the γ term in equation (11), the cubic is found to be a slowly varying function of μ without a physically realizable solution, at least in the region $-0.5 < \mu < 0.5$. No Burch objectives, composed of spherical surfaces, were found which would completely correct the spherical aberration of the primary.

In figure 128, the line marked $\gamma = 0$ represents a spherical-aberration-free Burch microscope objective. Solution $\kappa = 0.86$ is physically realizable, but separation $d = -16.1''$ is too large to be of much use, since the total track is only 18 inches. In the region $0.86 \leq \kappa \leq 1$, some correction of undercorrected spherical aberration is provided. However, systems from this region would tend to be unhandy.

MSPS Probe: Conic Surfaces. -Since spherical surfaces cannot correct the primary collecting mirror spherical aberration, the next logical step is to allow the first mirror of the objective to assume a conic shape. This can be done by inserting the term involving ϵ_1 into equation (10) to obtain the following equation.

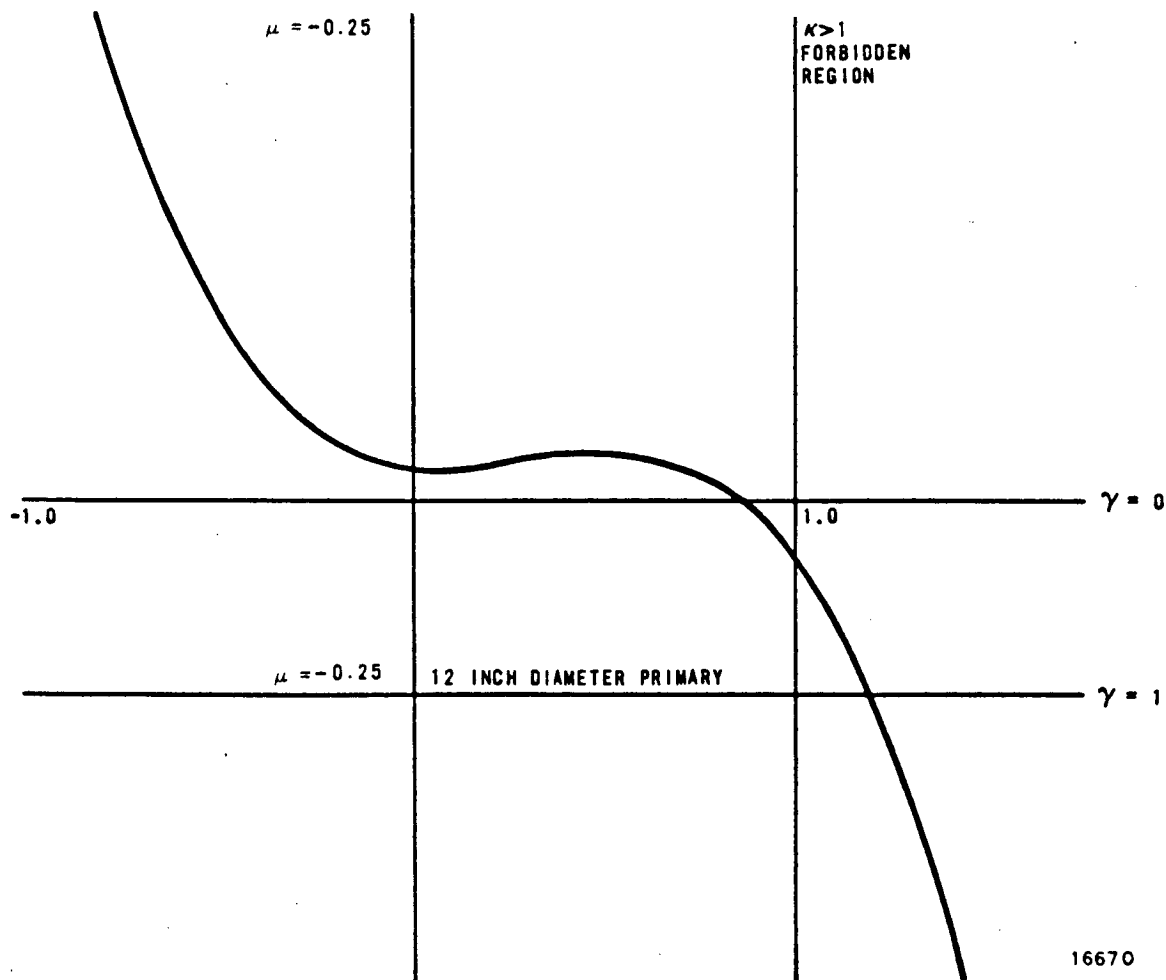


Figure 128. Spherical Aberration Cubic.

$$\epsilon_1^2 = \frac{\alpha}{2\kappa^3} \left[-\kappa^2 + \kappa - 2(\kappa + \beta)(\beta + 1 - \kappa)^2 + \frac{h_p}{4h_2} \right] = \frac{\alpha}{2\kappa^3} (p_1 \kappa^3 + p_2 \kappa^2 + p_3 \kappa + p_4 + \gamma).$$

Now an additional first-order equation is needed, since there are now four unknowns. Among the possible choices is equation (4) shortened to read

$$\varphi = \frac{h_3}{h_1} = \alpha + \mu.$$

For this case, h_3 is the radius of the hole in the secondary (first mirror of the objective) so that φ is the permissible linear obscuration. Another possible choice would be to specify $d = s_1$ on the basis of mechanical considerations.

Several short computer programs were written to generate families of all reflective relays. For input one, the program used semiaperture h_p and focal ratio $F_1^\#$ of the MSPS primary and the total track ℓ . In a vertical-plane scanner $\ell = 2h_p F_1^\#$ and the specification for ℓ is redundant unless folding mirrors are introduced. For a tilted-plane scanner, ℓ is some specificable fraction of the primary focal length. Possible configurations were then generated for various magnifications, μ , and obscurations, φ .

Selection of a configuration must be made on the basis of fabricability, system requirements, etc., as all have zero spherical aberration. One MSPS system, selected for further study, had the prescription given in table 27. (The column labeled n is the index of refraction, a change in sign between successive indices indicating reflection.) This system uses an $f/1.5$ primary, 12-inch diameter. The probe operates at a magnification of -0.25 , has an obscuration ratio of 0.25 , and a total track of 6 inches. When inputted into the POSD computer program, this configuration proved to have zero spherical aberration. This system is only an example and should not be considered optimum for this application. The secondary mirror is an $f/1.0$ aspheric and will be extremely difficult to fabricate. Its concavity does ease the testing problem somewhat.

Table 27. 12-Inch, $f/1.5$ Primary
Catoptric MSPS

	$r(\text{in.})$	$t(\text{in.})$	n	ϵ^2
Primary	-36	-21	-1	0 sphere
Secondary	4	3	1	-1.868 (hyperboloid)
Tertiary	12	-6	-1	0 sphere

Another possible method for achieving zero spherical aberration would be to allow all corrective power to reside in the tertiary mirror. To do this, take $\epsilon_1 = 0$ and solve equation (6) for ϵ_2 . With equation (8) we obtain

$$\epsilon_2^2 = -\frac{1}{2}(\alpha\lambda)^3 \left[p_1 \kappa^3 + p_2 \kappa^2 + p_3 \kappa + p_4 + \gamma \right] \quad (12)$$

For the same first-order system as given in table 27, a conic constant of $-\epsilon_2^2 = 807$ was calculated. This surface is an ellipsoid about the minor axis with an eccentricity too large to represent a feasible solution. Not only would such a surface be nearly impossible to accurately fabricate, but such a system would pass only the true, geometric, rays near the axis. This was also found to be true, to a lesser degree, with the system in table 27. The higher order aberrations of this system are too large to be vanquished by a third-order solution. However, the table 27 configuration did prove an excellent starting point for automatic design.

It is also possible to split the corrective load between the secondary and tertiary. For simplicity in fabrication, it was decided to try a paraboloid for the secondary, i.e., the conic constant $-\epsilon_1^2 = 1$. (The secondary of table 27 would then have a focal ratio of $f/1.0$ and would be difficult to fabricate.) The remaining correction was then assigned to the tertiary. The only change in formula (12) would be to redefine p_4 as

$$p_4 = 2 - \frac{2}{\alpha}.$$

For the system of table 27, $-\epsilon_2^2$ was found to decrease from 807 to 375. This does not represent a significant advantage for this system over one having just one aspheric surface, the secondary.

Summary

The first- and third-order design of Burch microscope objectives can be accomplished algebraically. This permits the generation of families of objectives having the proper properties. Selection of an individual member from a family will then depend on other than first- and third-order grounds, i.e., on mechanical considerations, fabricability, etc.

The algebraic method was used to design a family of catoptric probes for use with an image-plane scanner. In addition to fulfilling first-order requirements, the probe fully corrected the spherical aberration of the fast spherical primary mirror.

Appendix III

THERMAL STUDY

Based on the results of the thermal study, an insulation design was established to provide the necessary thermal protection for the optical structural system.

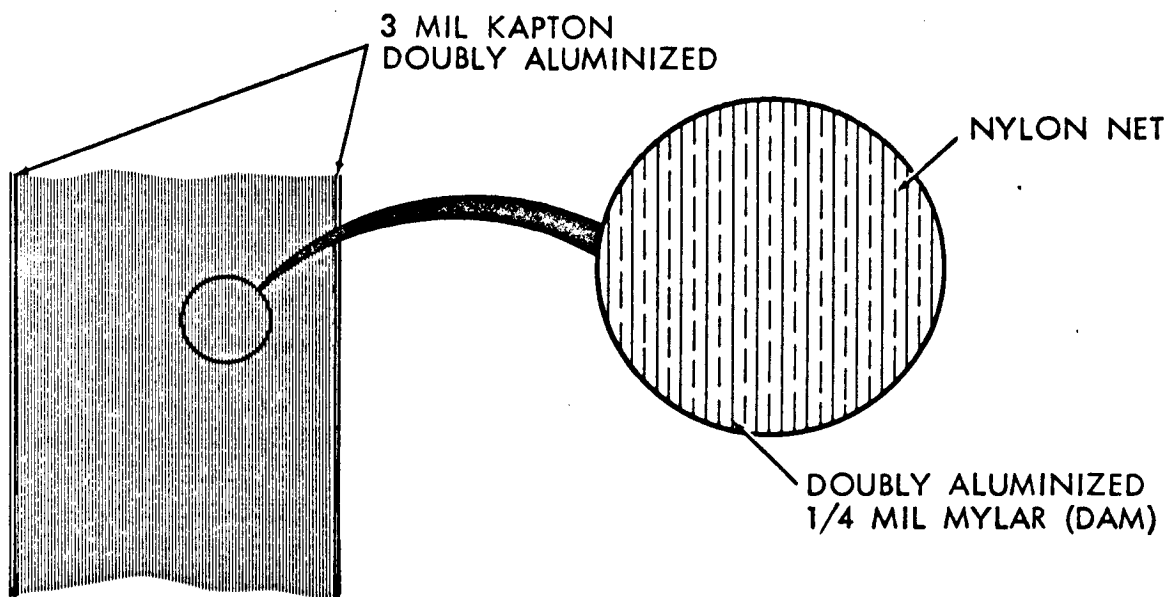
The type of insulation best suited for the passive thermal control system was the radiation barrier type or high performance insulation (HPI). This class of insulation is basically polyester material (Mylar, Kapton) with highly reflective coatings (silver, gold, or aluminum) deposited on either one or both sides. The thickness of the coatings vary from 300 to 1200 angstrom units depending on the properties required.

Based on previous studies of spacecraft thermal protection systems, the basic designs shown in figure 129 were chosen. The top sketch shows a blanket made of Kapton, Mylar, and nylon net, and the second is made of Kapton and NRC-2. Both systems would provide approximately the same thermal protection per pound of insulation. The NRC-2 system would eliminate the necessity of spacers, since NRC-2 is a singly aluminized material that is crinkled to provide minimum contact between sheets.

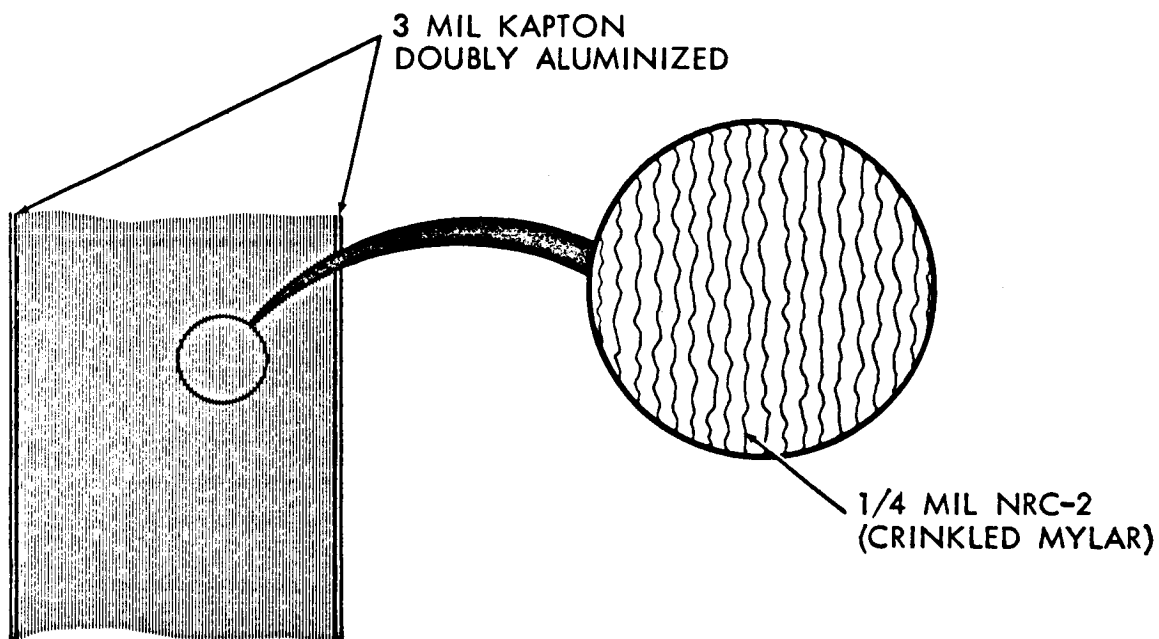
Kapton is used as the outer layer for both systems since the outside temperatures are higher than the limits suggested for Mylar. Kapton can also be used in a relatively thick material size to give the blanket a greater degree of rigidity. It is possible, within limits, to control the coating on the outer Kapton layer and thereby vary the absorptivity, α , and emissivity, ϵ , values. By increasing the thickness of the aluminum, it is possible to obtain values between 0.1 and 0.6 without changing the emissivity. It is further possible to coat the aluminum with silicon oxide. By increasing the thickness of the silicon oxide coating, emissivity values of 0.1 to 0.6 are obtainable, virtually independent of absorptivity. It is possible to obtain a wide range of outside surface temperatures. The limit values of α and ϵ are difficult to obtain but are not required for the present application.

Based on previous experimental results on operating spacecraft, a value for the heat transfer coefficient through the blanket was assumed to be 0.02 Btu/hr-ft²-°R. The actual value for the final hardware design is not easily obtainable by analysis, since it is intimately related to penetrations, mounting method, and blanket design. The insulation system should be mounted as far away from the scanner structural members as possible. Ideally, the blankets should be suspended from the spacecraft structure. If this is not possible, then long nonconducting standoffs from the scanner structure would be the second choice.

The temperature results from the computer orbital model are tabulated in tables 28 and 29 and figures 130 through 134.



30 SHEETS DAM - 32 LAYERS NYLON NET (APPROXIMATE)
DENSITY APPROXIMATELY 80 SHEETS/INCH



40 SHEETS NRC-2 (APPROXIMATE)
DENSITY APPROXIMATELY 65 SHEETS/INCH

16469

Figure 129. Two Acceptable Insulation Systems.

Table 28. Thermal Input to Spacecraft, Btu/hr - ft².

Time of Orbit (Min)	Surface 1			Surface 2			Surface 3			Surface 4		
	S	A	IR	S	A	IR	S	A	IR	S	A	IR
0	0	19.0	14.4	312	0	0	312	25.7	14.4	107	9.8	6.3
10		15.0		256			312	21.7		0	6.9	
20		4.6		106			312	11.0		0	1.7	
30		0		0			312	0		0	0	
40		0		0			0	0		0	0	
50		0		0			0	0		0	0	
60		0		0			0	0		0	0	
70		0		0			0	0		0	0	
80		0		0			312	0		221	0	
90		12.5		54.1			312	7.2		308	3.5	
100		18.8		221			312	19.2		283	8.2	
0 (103)	0	19.0	14.4	312	0	0	312	25.4	14.4	156	9.9	6.3
								25.7		107	9.8	
Time of Orbit (Min)	Surface 5			Surface 6			Surface 7			Surface 8		
	S	A	IR	S	A	IR	S	A	IR	S	A	IR
0	0	61	39	107	9.8	6.3	0	61	39	0*	85.0	54.1
10	0	41		256	9.1		0	53			69.5	
20	0	17		313	5.1		132	25			29.2	
30	0	0		256	0		271	0			0	
40	0	0		0	0		0	0			0	
50	0	0		0	0		0	0			0	
60	0	0		0	0		0	0			0	
70	294	0		0	0		0	0			0	
80	179	15		0	0		0	8.6			15.9	
90	0	46		0	5.6		0	40.2			60.0	
100	0	61		54	9.3		0	59.5			83.5	
0 (103)	0	61	39	107	9.8	6.3	0	61	39	0	85.0	54.1

S---Solar A---Earth Reflected IR---Earth Emitted
 *Solar shielded from surface 8

Table 29. Orbit Average Temperature Ranges
vs. Surface Coating.

Absorptivity α	Emissivity ϵ	T_{ave} ($^{\circ}R$)	
0.1	0.1	519	
0.2		609	
0.3		671	
0.4		719	
0.5		759	
0.6		793	
0.1	0.2	449	
0.2		519	
0.3		570	
0.4		609	
0.5		642	
0.6		671	
0.1	0.3	416	This range plotted in fig- ure 77.
0.2		476	
0.3		519	
0.4		555	
0.5		584	
0.6		609	
0.1	0.4	396	
0.2		449	
0.3		488	
0.4		519	
0.5		547	
0.6		570	
0.1	0.5	382	
0.2		430	
0.3		466	
0.4		495	
0.5		519	
0.6		542	
0.1	0.6	372	
0.2		416	
0.3		449	
0.4		476	
0.5		499	
0.6		519	

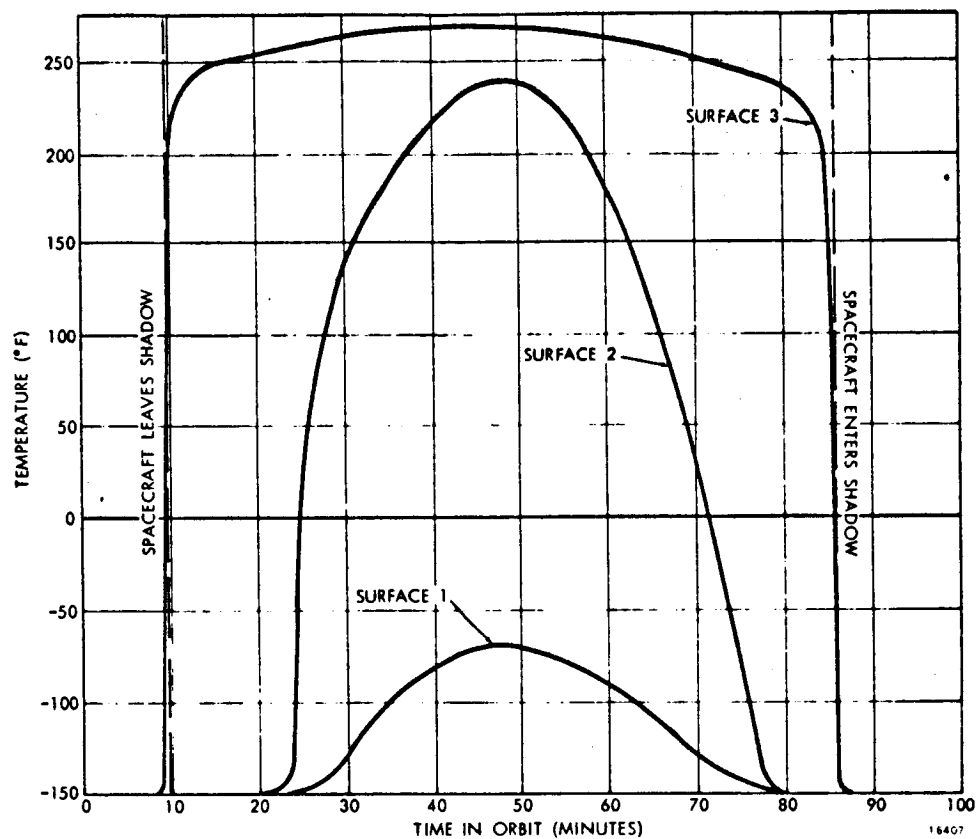


Figure 130. Exterior Surface Temperatures of HPI Surfaces 1, 2, and 3.

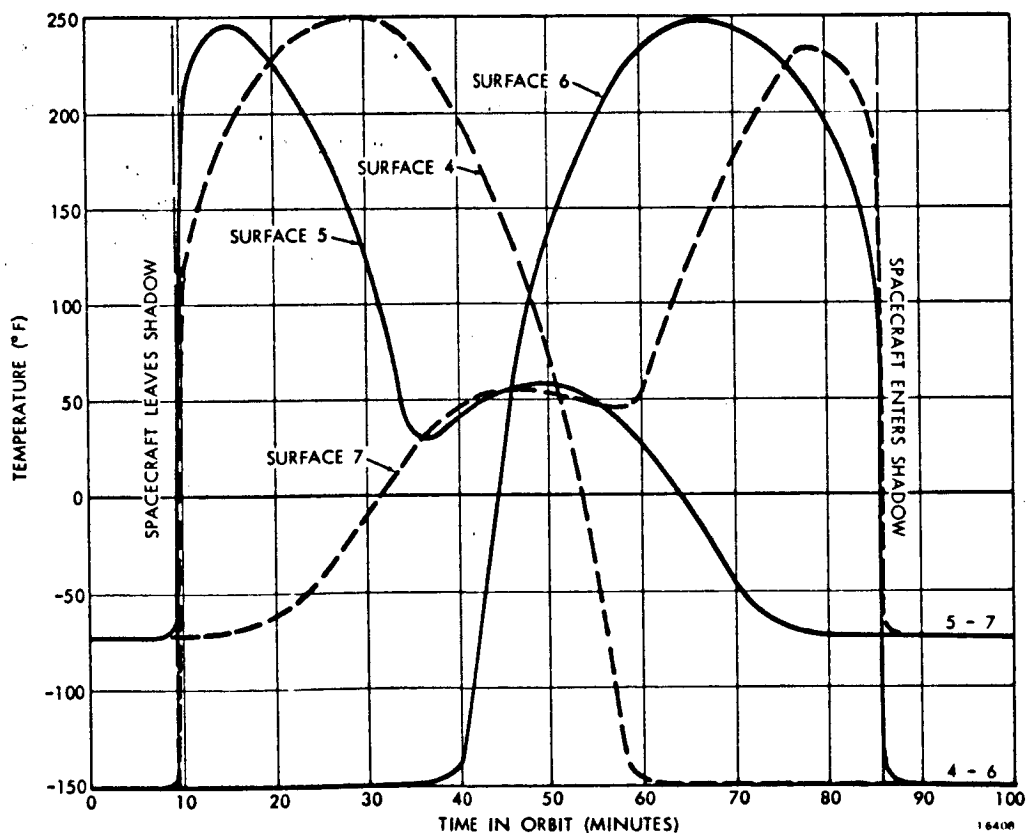


Figure 131. Exterior Surface Temperatures of HPI Surfaces 4, 5, 6, and 7.

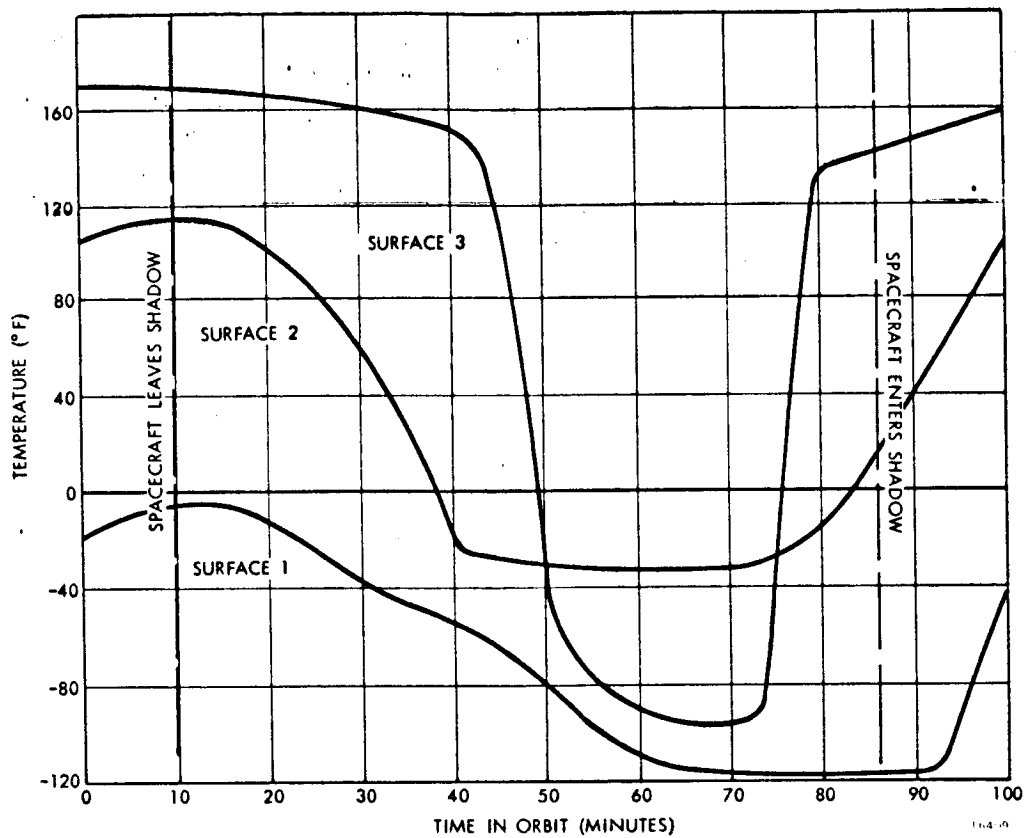


Figure 132. Interior Surface Temperatures of HPI Surfaces 1, 2, and 3.

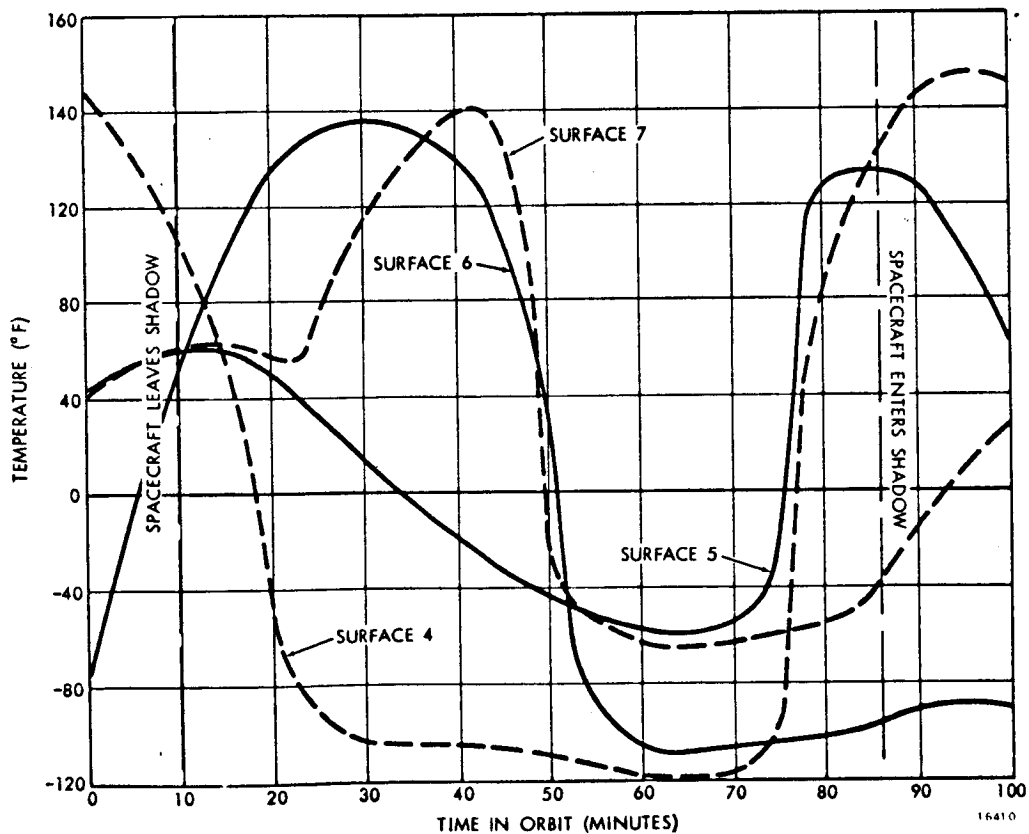


Figure 133. Interior Surface Temperatures of HPI Surfaces 4, 5, 6, and 7.

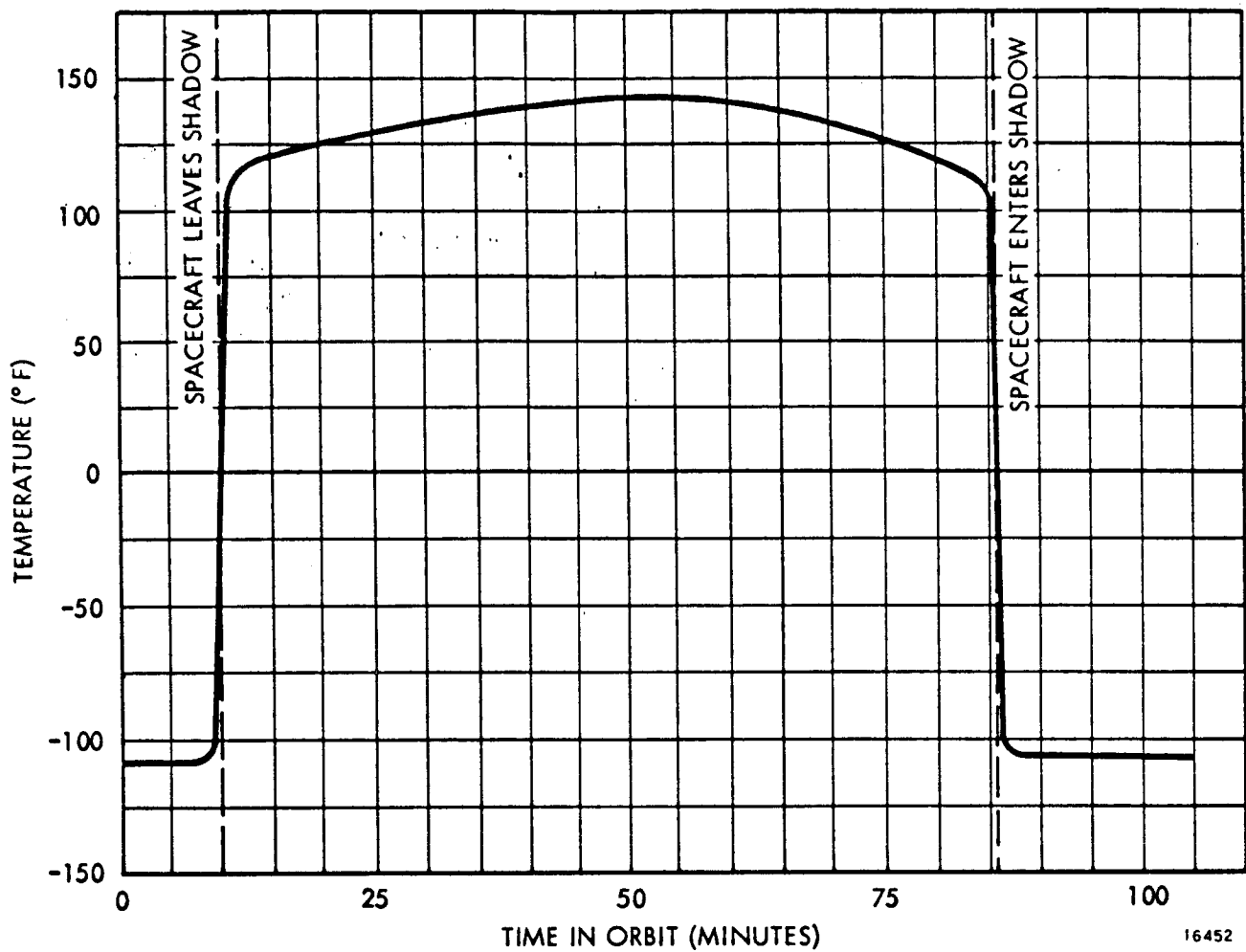


Figure 134. Exterior HPI Surface Temperature Averaged.

Appendix IV

MATERIAL STUDY

ISOTROPIC SYSTEM DIMENSIONAL SCALING (24-PROBE SYSTEM)

It will be shown that a system composed of materials having the same temperature coefficient of expansion will simply undergo a scale change if subjected to a uniform change in mean temperature.

Thermal strain λ is given by:

$$\lambda = \epsilon \Delta T,$$

where,

ϵ = linear coefficient of thermal expansion (a function of temperature)

ΔT = change in mean temperature.

The change in length, ΔL , is found by integrating the strain over the length L , i.e.,

$$\Delta L = \int_0^L \lambda dL = L \epsilon \Delta T.$$

Refer to figure 135, the change in primary focus ΔF , is:

$$\Delta F = \frac{1}{2} \Delta L_m - \Delta L_s + \Delta L_w$$

with

L_m = radius of primary mirror

L_s = length of structure

L_w = radius of scan wheel,

so that ΔF becomes:

$$\Delta F = \frac{1}{2} L_m (\epsilon_m \Delta T_m) - L_s (\epsilon_s \Delta T_s) + L_w (\epsilon_w \Delta T_w) \quad (1)$$

where ϵ_m , ϵ_s , and ϵ_w are coefficients corresponding to L_m , L_s , and L_w , respectively.

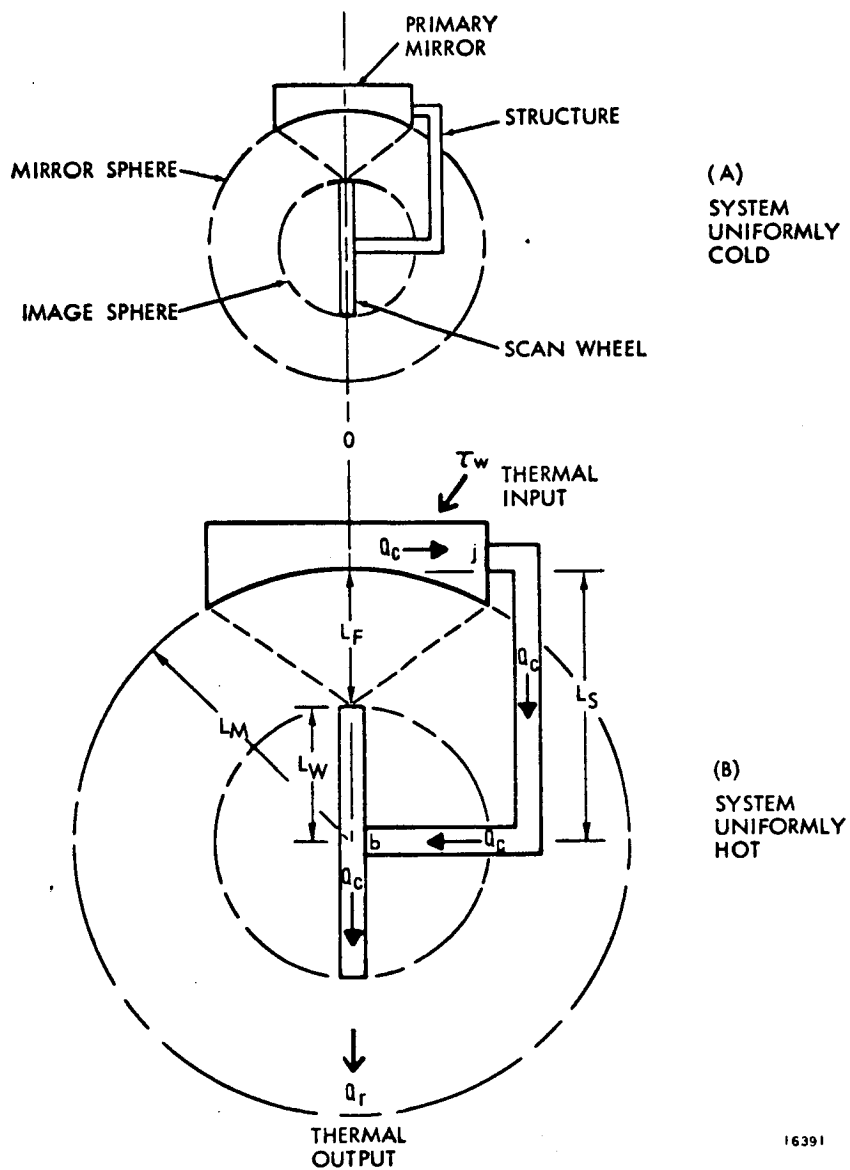


Figure 135. Isotropic System Dimension Scanning.

For the 24-probe great circle scan geometry we have:

$$L_m = L_s = 2L_w,$$

giving

$$\Delta F = L_m \left[\frac{\epsilon_M \Delta T_M}{2} - \epsilon_s \Delta T_s + \frac{\epsilon_w \Delta T_w}{2} \right]. \quad (2)$$

Thus, a system will remain in focus if the condition:

$$\epsilon_m \Delta T_m = \epsilon_w \Delta T_w = 2\epsilon_s \Delta T_s, \quad (3)$$

holds. A special case solution for equation (3) is:

$$\epsilon_m \Delta T_m = \epsilon_w \Delta T_w = \epsilon_s \Delta T_s.$$

Equation (1) shows a system can be initially focused for any arbitrary combination of static $\epsilon \Delta T$ values. The effect of subsequently changing the temperature of an initially focused system can be found from equation (2) for any temperature profile. The case for a perfectly isotropic system $\epsilon_m = \epsilon_s = \epsilon_w$ shows that two temperature profiles will preserve focus if we have for a uniform temperature change:

$$\Delta T_m = \Delta T_w = \Delta T_s \text{ (no gradients),}$$

or for a controlled change such that:

$$\Delta T_m + \Delta T_w = 2\Delta T_s \text{ (controlled gradients).}$$

Example 1

Consider a perfectly isotropic aluminum system with a fixed 2° F gradient between mirror and wheel. For numerical constants we take:

$$\epsilon_m = \epsilon_s = \epsilon_w = \frac{11.8 \times 10^{-6}}{\left(\frac{\text{in.}}{\text{in.}^\circ \text{ F}}\right)}$$

$$L_m = 26.66 \text{ inches.}$$

and

$$\left. \begin{array}{l} \Delta T_m = +1.0^\circ \text{ F} \\ \Delta T_s = 0 \\ \Delta T_w = +1.0^\circ \text{ F} \end{array} \right\} 2^\circ \text{ F gradient}$$

$$\Delta F = 26.66 (11.8 \times 10^{-6})$$

$$\Delta F = 0.00032 \text{ inches.}$$

This should be compared to the depth of focus, ± 0.0004 inches.

Isotropic System Dimensional Scaling (Tilted Wheel System)

Due to the general scan geometry requirement of viewing along a radius of the image sphere, it is apparent that the geometry of figure 136 is invariant for the entire scan cycle. It can thus be demonstrated that the tilted system obeys the isotropic scaling equations after redefining the lengths to give:

$$\Delta F = \frac{1}{2} \Delta L_m - \Delta L_s + \Delta(L_w \sin \theta).$$

The tilt angle θ can be made invariant with temperature by proper distribution of the axle bearings and support structure.

For invariant θ we find:

$$\begin{aligned} \Delta F &= \frac{1}{2} \Delta L_m - \Delta L_s + \Delta L_w (\sin \theta) \\ &= \frac{1}{2} L_m \epsilon_m \Delta T_m - L_s \epsilon_s \Delta T_s + L_w \epsilon_w \Delta T_w \sin \theta. \end{aligned}$$

Example 2

We substitute the tilted wheel parameters for an isotropic aluminum system, namely:

$$\epsilon_m = \epsilon_s = \epsilon_w = \frac{11.8 \times 10^{-6}}{\left(\frac{\text{in.}}{\text{in.}^\circ \text{F}} \right)}$$

$$L_m = 26.66 \text{ inches}$$

$$L_s = 14.73 \text{ inches}$$

$$L_w = 4.4 \text{ inches (8 probes)}$$

$$\theta = 18.5^\circ$$

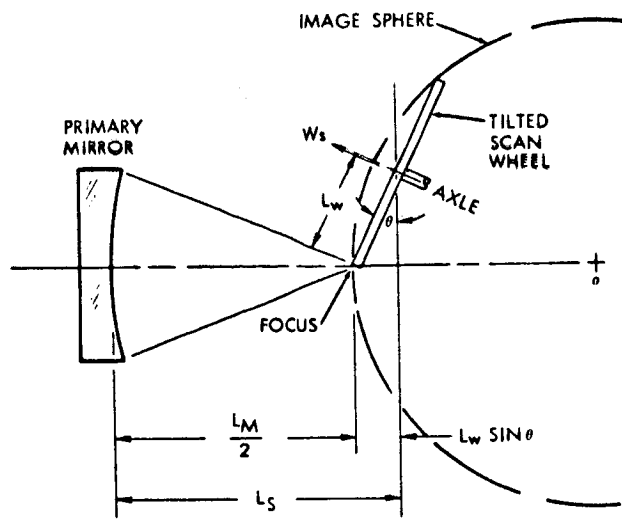


Figure 136. Shortened Thermal Path of Tilted Wheel System.

$$\Delta T_m = +1.0^\circ \text{ F}$$

$$\Delta T_s = 0$$

$$\Delta T_w = 1.0^\circ \text{ F}$$

to give

$$\Delta F = \left(\frac{26.66}{2} + 4.4 \sin 18.5 \right) 11.8 \times 10^{-6} = 0.000174 \text{ inch.}$$

Isotropic System Response to Variable Solar Heating (24-Probe System)

The purpose of this analysis was to explore the effect of material properties on system dimensional response to a steady-state principal thermal gradient. The type of gradient considered was one which would result from a heat flow from the insulation surface above the mirror to the scan window by conduction through the structure.

The material distribution and system size was found to determine both the thermal gradients and the system response to those gradients. In addition, a tradeoff in material properties was found to depend on structural joint and bearing thermal resistances. A material distribution solution was found which yields perfect axial focus with or without thermal gradients.

Consider the circuit of figure 137 consisting of the path R_I , R_s , R_m , R_j , R_s , R_B , R_w , R_g , and R_j . This path represents the most probable principal thermal path in simplified form. Considering the radiative coupling through R_6 to be small compared to heat transfer through the bearings, the path was rewritten per figure 138.

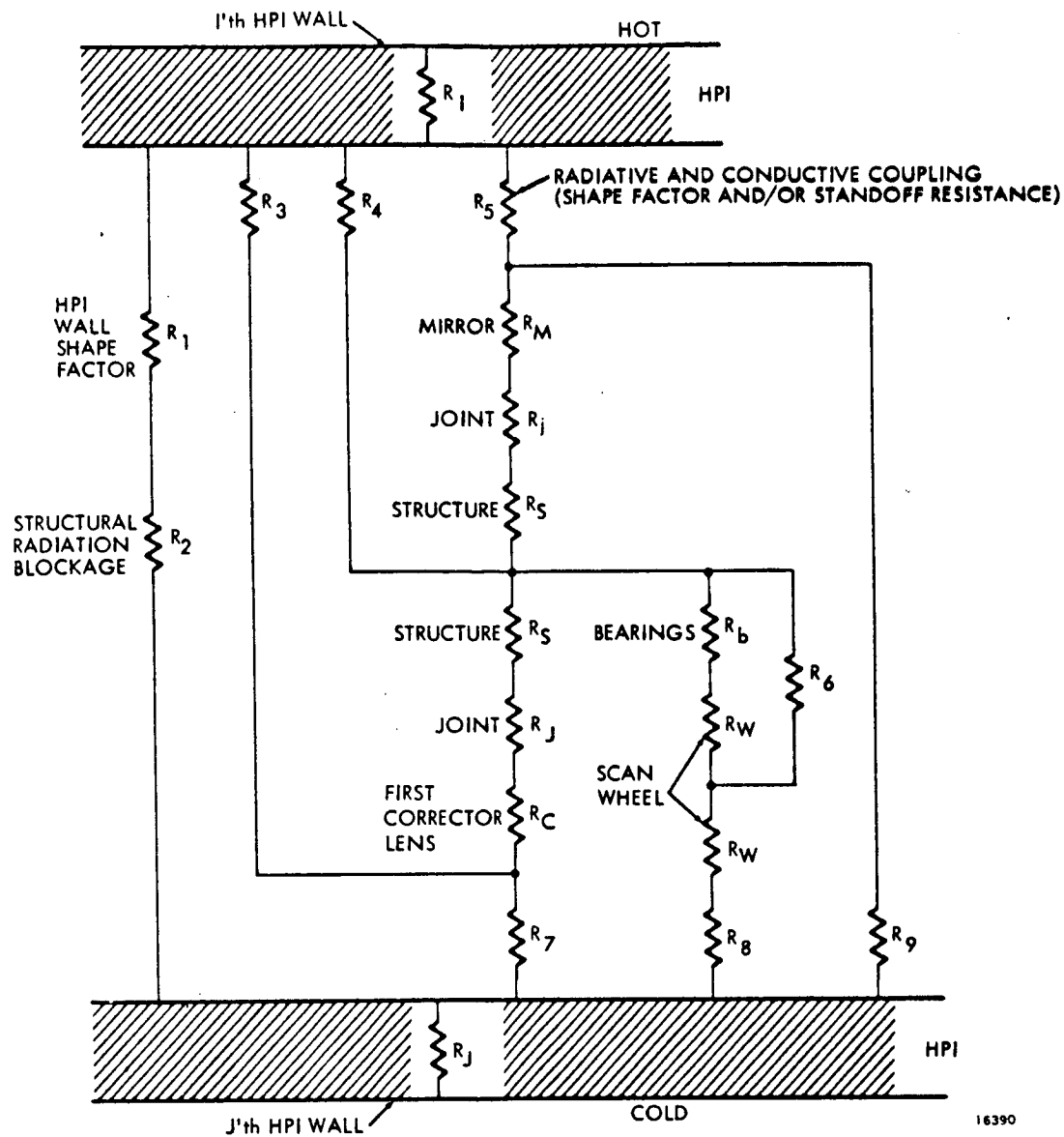


Figure 137. Simplified Element of the Passive Thermal Control Circuit for One HPI Wall Zone Pair.

For a passive material the heat flux is given by:

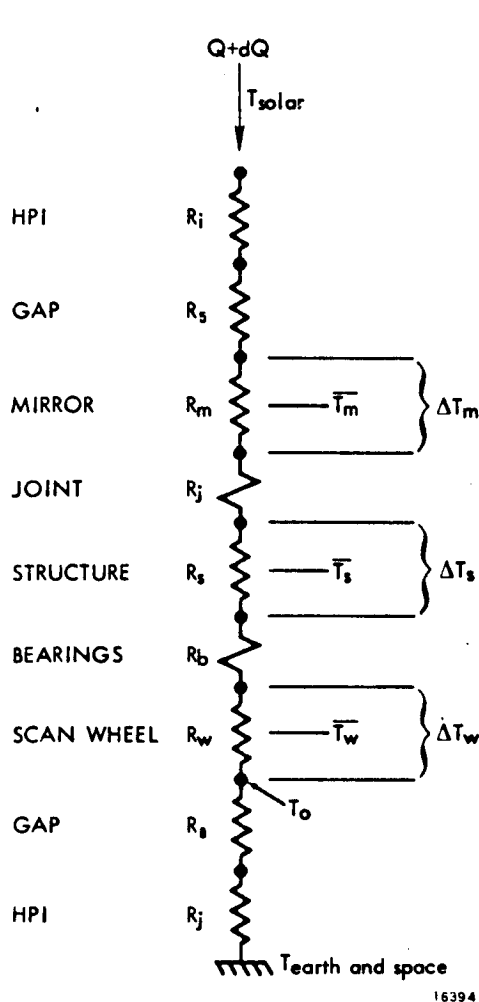
$$Q = \frac{KA \Delta T}{L} = \frac{\Delta T}{R}$$

where,

Q = heat flux (Btu/hr)

K = thermal conductivity (Btu/ft hr $^{\circ}$ F)

A = effective cross sectional area (ft²)



L = thermal path length (ft)

ΔT = thermal gradient across element ($^{\circ}\text{F}$)

$R = L/KA$ = thermal resistance ($\text{hr } ^{\circ}\text{F/Btu}$).

To clarify the various possible initial conditions, the thermal flux, including step "Q" and a subsequent small perturbation "dQ", can be written as:

$$(Q + dQ) = \frac{(KA \Delta T + d(\Delta T))}{L}$$

We rewrite equation (2) in the form:

$$\begin{aligned} dF &= \frac{1}{2} dL_m - dL_s + dL_w \\ &= \frac{1}{2} L_m \epsilon_m d\bar{T}_m - L_s \epsilon_s d\bar{T}_s + L_w \epsilon_w d\bar{T}_w, \end{aligned} \quad (4)$$

where,

$d\bar{T}$ = component average temperature change after introduction of $(Q + dQ)$

Figure 138. Principal Thermal Path.

$$\begin{aligned} d\bar{T}_m &= \left(\Delta T_w + d\Delta T_w \right) + \left(\Delta T_s + d\Delta T_s \right) + \frac{1}{2} \left(\Delta T_m + d\Delta T_m \right) \\ &\quad + (\Delta T + d\Delta T)_{R_b} + (\Delta T + d\Delta T)_{R_j} \end{aligned} \quad (5)$$

$$d\bar{T}_s = \left(\Delta T_w + d\Delta T_w \right) + \frac{1}{2} \left(\Delta T_s + d\Delta T_s \right) + (\Delta T + d\Delta T)_{R_b} \quad (6)$$

$$d\bar{T}_w = \left(\frac{1}{2} \Delta T_w + d\Delta T_w \right) \quad (7)$$

$$d\bar{T}_i \equiv (\Delta T + d\Delta T)_i = (Q + dQ) \left(\frac{L}{KA} \right)_i \quad (8)$$

Inserting equation (8) into equations (5), (6), and (7) and defining the mirror thermal path length as $N L_m$ yields:

$$d\bar{T}_m = (Q + dQ) \left[\left(\frac{L}{KA} \right)_w + \left(\frac{L}{KA} \right)_s + \frac{1}{2} \left(\frac{NL_m}{KA} \right)_m + R_b + R_j \right] \quad (9)$$

$$d\bar{T}_s = (Q + dQ) \left[\left(\frac{L}{KA} \right)_w + \frac{1}{2} \left(\frac{L}{KA} \right)_s + R_b \right] \quad (10)$$

$$d\bar{T}_w = (Q + dQ) \left[\frac{1}{2} \left(\frac{L}{KA} \right)_w \right] \quad (11)$$

Substituting equations (9), (10), and (11) into equation (4), we find:

$$dF = (Q + dQ) \left\{ \frac{1}{2} L_m \epsilon_m \left[\left(\frac{L}{KA} \right)_w + \left(\frac{L}{KA} \right)_s + \frac{1}{2} \left(\frac{NL_m}{KA} \right)_m + R_b + R_j \right] - L_s \epsilon_s \left[\left(\frac{L}{KA} \right)_w + \frac{1}{2} \left(\frac{L}{KA} \right)_s + R_b \right] + L_w \epsilon_w \left[\frac{1}{2} \left(\frac{L}{KA} \right)_w \right] \right\} \quad (12)$$

In addition, from equation (1), for a uniform change ΔT in all system element temperatures we have:

$$dF = (\Delta T) \left(\frac{1}{2} \epsilon_m L_m - \epsilon_s L_s + \epsilon_w L_w \right) \quad (13)$$

It was desired to determine whether a system could satisfy both equation (12) and equation (13) simultaneously for $dF = 0$. Such a system would be capable of maintaining focus for arbitrary changes in uniform mean temperature and/or arbitrary changes in thermal flux.

For a perfectly isotropic system the material thermal properties are equal, that is:

$$\epsilon_m = \epsilon_s = \epsilon_w \quad \left[K_m = K_s = K_w \right]$$

so that equation (13) becomes:

$$dF = \epsilon \Delta T \left(\frac{1}{2} L_m - L_s + L_w \right) = 0.$$

Since $\epsilon \Delta T$ is nonzero we must have:

$$\frac{1}{2}L_m - L_s + L_w = 0, \quad (14)$$

which is the complete isotropic solution for focal stability at uniform temperature.

We rewrite equation (12) to give:

$$dF \equiv 0 = (Q + dQ) \left(L_m \right)^2 \left(\frac{\epsilon}{K} \right) \left\{ \frac{1}{2} \left[\frac{1}{2A_w} + \frac{1}{A_s} + \frac{N}{2A_m} + K \left(\frac{R_b + R_j}{L_m} \right) \right] - \left[\frac{1}{2A_w} + \frac{1}{2A_s} + K \frac{R_b}{L_m} \right] + \frac{1}{8A_w} \right\},$$

which, since $(Q + dQ) \left(L_m \right)^2 \left(\frac{\epsilon}{K} \right)$ is nonzero, has for solution:

$$0 = \frac{1}{2} \left[\frac{1}{2A_w} + \frac{1}{A_s} + \frac{N}{2A_m} + K \left(\frac{R_b + R_j}{L_m} \right) \right] - \left[\frac{1}{2A_w} + \frac{1}{2A_s} + K \frac{R_b}{L_m} \right] + \left[\frac{1}{8A_w} \right]$$

or

$$0 = \frac{N}{2A_m} - \frac{1}{4A_w} + K \left(\frac{R_j - R_b}{L_m} \right)$$

We multiply by L_m to obtain:

$$0 = \frac{NL_m}{A_m} - \frac{L_w}{A_w} + 2KR_j - R_b, \quad (15)$$

the axial solution for focal stability with Q-dependent gradients.

The solution indicated in equation (15) requires a particular form of material distribution but does not relate material properties among the structural elements. The solution is compatible with the uniform temperature solution of equation (14), i.e., if the system is initially at uniform temperature and focused per equation (14), it will be focused for a Q gradient and will remain focused if the gradient subsides independent of the new equilibrium temperature,

providing that the system is constructed per equation (14). Closer examination of the isotropic gradient solution to equation (12) indicates that it creates an on-axis focus by solving an equation of the form

$$C_1 \left(\frac{1}{2} L_m \right) - C_2 \left(L_s \right) + C_3 \left(L_w \right) = 0 \quad (16)$$

where

$$C_1 \neq C_2 \neq C_3. \quad (17)$$

From figure 139, a solution such as equation (17) which, although isotropic, uses nonequal C values can only hold for the vertical scan position. Nonequal C's readjust the lengths to preserve axial focus, but displace the center of the wheel from the center of the mirror image sphere. The resulting defocusing for the nonvertical scan positions is less than would occur without invoking equation (15). A complete isotropic solution does not exist for the thermal gradient case.

The off-vertical focal error can be computed as follows: Let δ_L = displacement of wheel center from mirror image sphere center, i.e.,

$$\delta_L = \frac{1}{2} \Delta L_m - \Delta L_w.$$

From equation (12) it was apparent that initial gradient conditions did not affect solution (15). Let $dQ = 0$ in equation (12), then δ_L becomes:

$$\delta_L = \frac{Q}{2} \frac{\epsilon}{K} \left\{ L_m \left(\left(\frac{L}{A} \right)_w + \left(\frac{L}{A} \right)_s + \frac{1}{2} \left(\frac{NL_m}{A_m} \right) + K (R_b + R_j) \right) - L_w \left(\frac{L}{A} \right)_w \right\},$$

which invoking equation (15) simplifies to:

$$\delta_L = Q \frac{\epsilon}{K} L_m^2 \left[\frac{1}{4A_w} + \frac{1}{2A_s} + K \frac{R_b}{L_m} \right] \quad (18)$$

which is the wheel/mirror center displacement for gradient Q.

From figure 137 the maximum off-vertical focal error dF, correspond to δ_L , is:

$$dF = \frac{L_m}{2} - \delta_L \cos \frac{\theta_s}{2} - \sqrt{\left(\frac{L_m}{2} - \delta_L \right)^2 - \left(\delta_L \sin \frac{\theta_s}{2} \right)^2}$$



For $L_w \gg \delta_L$ we make the approximation:

which when written out yields:

At a constant weight W :

The thermal resistance R is:

IV-11

so that the off-vertical focal shift becomes:

$$\begin{aligned} dF &= \left(1 - \cos \frac{\theta_s}{2}\right) Q L_m \epsilon \left[\frac{1}{2} \left(\frac{\rho L^2}{KW} \right)_w + \frac{1}{2} \left(\frac{\rho L^2}{KW} \right)_s + R_b \right] \\ &= \left(1 - \cos \frac{\theta_s}{2}\right) Q L_m^3 \left[\frac{\rho \epsilon}{K} \left(\frac{1}{8W_w} + \frac{1}{2W_s} \right) + \frac{\epsilon R_b}{L_m^2} \right]. \end{aligned}$$

The off-vertical focal shift for isotropic system was predicted on the basis of equation (15).

Appendix V

SCAN WHEEL SYSTEM

Scan Wheel Dynamics

Consider the spoked scan wheel of figure 140. The wheel rotates at speed ω_z in the XY plane about the Z-axis. Momentum vector, H, is initially coincident with the Z-axis. If an additional rotation, ω_p , occurs about the Y-axis, the Coriolis acceleration of each i'th mass element exerts a torque in the minus X direction given by:

$$\begin{aligned} T_{-x} &= \sum_{i=1}^N M_i (2\omega_p v) y_i \\ &= M_i 2\omega_p \omega_z R_i \sin \theta_i (\text{lb-in.}). \end{aligned}$$

The torque will displace the disk in the minus X direction until the buildup of bearing, axle, and spoke restoring moments cancels the force. At cancellation, the disk normal is rotated by the angle ϕ out of the XZ plane. If the disturbing rotation, ω_p , is ceased, conservation of elastic energy will cause the disk normal to precess about the Z axis at rate ω'_p . The effect will then subside due to material damping. The scan wheel could be constructed with or without a peripheral hoop. A hoop with finite mass and stiffness would modify the dynamic properties of the wheel in proportion to the hoop properties. Hoop bending stiffness would raise the ϕ -mode wheel stiffness by coupling the spokes in torsion. Hoop mass would tend to increase the magnitude of ϕ .

The cases for hoops having zero or infinite stiffnesses are amenable to rapid analysis, but the intermediate cases require analyses which were beyond the time limited scope of the work. It was estimated that the section properties of a hoop designed for a thin wheel would not be effective in overcoming the hoop mass effects.

We summarize the equations for nontapered spoked scan wheels neglecting bearing, hub, and axle compliance. First, the orbit precession rate is:

$$\omega'_p = \frac{K}{H} \left(\frac{1}{\text{sec}} \right), \quad (1)$$

where,

K = wheel stiffness coefficient in ϕ deflection mode (lb-in./rad)

H = scan wheel momentum (in. lb sec).

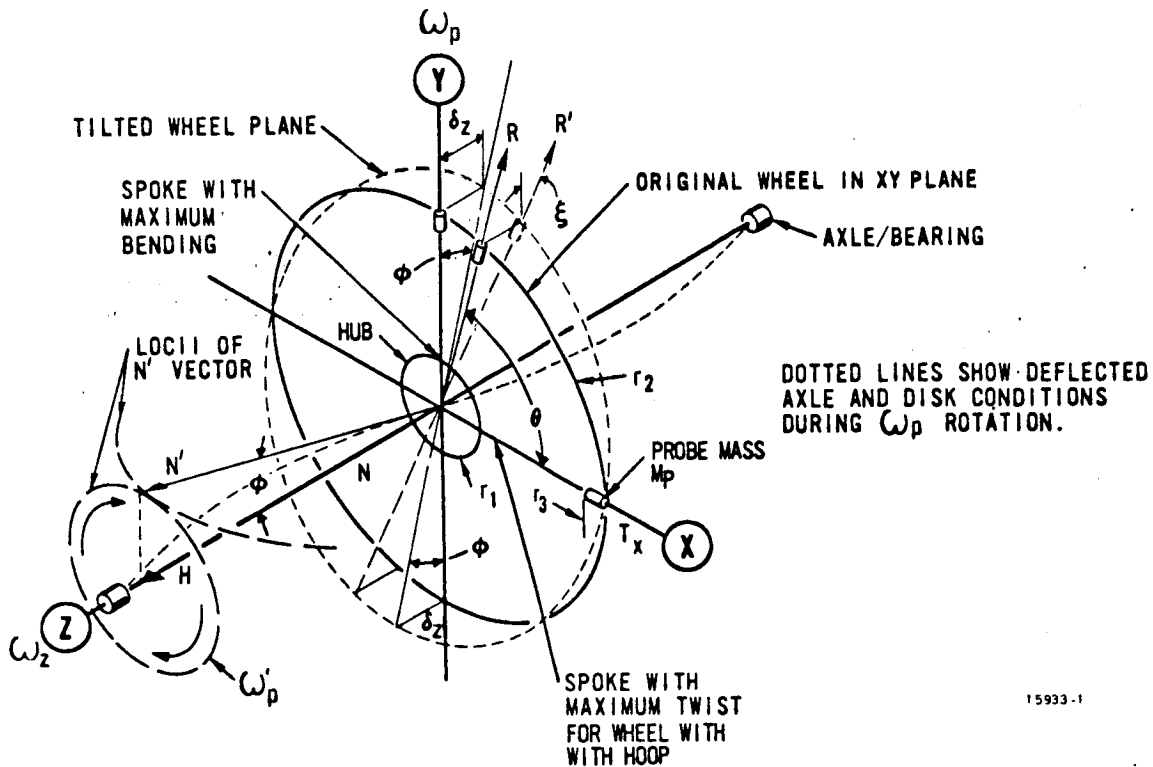


Figure 140. Scan Wheel Precessional Deformation.

The restoring torque, T_x is given by:

$$\begin{aligned}
 T_x &= K\omega = (K_B + K_T)\phi = \omega_p H \\
 &= \omega_z \omega_p \left\{ \left[2\pi r_2 (\rho_h A_h) + \eta M_p \right] (r_2)^2 \right. \\
 &\quad \left. + \frac{\eta}{3} \rho_s A_s r_3^3 \right\} \left(\frac{\text{lb-in.}}{\text{rad}} \right)
 \end{aligned} \tag{2}$$

where,

- K_B = ϕ -mode stiffness due to spoke bending
- K_T = ϕ -mode stiffness due to spoke torsion
- η = total number of spokes
- $\rho_h A_h$ = hoop mass density x area
- $\rho_s A_s$ = spoke mass density x area.

Rigid Hoop

The bending stiffness in the φ -mode for a wheel having a rigid hoop is given by:

$$K_B = \frac{E_s I_s (r_2 + r_1) \left\{ \left[2\pi r_2 (\rho_h A_h) + \eta M_p \right] r_2^2 + \frac{\eta}{3} \rho_s A_s r_3^3 \right\}}{2 (r_2 - r_1)^3 \left[0.166 (M_p r_2 + 2r_2^2 \rho_h A_h \Delta\theta) \right]} \quad (3)$$

$$+ \frac{E_s I_s (r_2 + r_1) \left\{ \left[2\pi r_2 (\rho_h A_h) + \eta M_p \right] r_2^2 + \frac{\eta}{3} \rho_s A_s r_3^3 \right\}}{0.0832 \left(r_1 (r_2 - r_1) \rho_s A_s + 0.0584 (r_2 - r_1)^2 \rho_s A_s \right)} \left(\frac{\text{lb-in.}}{\text{rad}} \right)$$

where,

- I_s = spoke area moment of inertia
- M_p = mass of one probe
- $\Delta\theta$ = angle between spokes = $2\pi/\eta$.

Wheel torsional stiffness in the φ -mode is given by:

$$K_T = K_{\varphi_i} \sum_{i=1}^{\eta} \cos^2 \theta = \frac{G I_{p_s}}{(r_2 - r_1)} \sum_{i=1}^{\eta} \cos^2 \theta_i \left(\frac{\text{lb-in.}}{\text{rad}} \right)$$

where,

- G = shear modulus
- I_{p_s} = spoke polar moment of inertia.

We have for the wheel displacement, φ_{total} :

$$\varphi_{\text{total}} = \frac{1}{\frac{1}{\varphi_B} + \frac{K_T}{I_z \omega_p \omega_z}} \text{ (radians),}$$

where the bending component, ϕ_B , is:

$$\phi_B = \frac{2(r_2 - r_1)^3 \omega_z \omega_p}{EI_b(r_2 + r_1)} \left[0.166 r_2 (M_p + 2r_2 \rho_h A_h \Delta\theta) + (r_2 - r_1) (\rho_s A_s) (0.0832 r_1 + 0.0584 (r_2 - r_1)) \right]$$

For the rigid hoop the spoke tip angle, ξ , is given by:

$$\xi \equiv \phi$$

Hoop with Zero Rigidity

When the hoop has zero rigidity there is no spoke torsional restraint, and for the wheel displacement, we obtain:

$$\phi_{\text{total}} = \frac{(r_2 - r_1)^3 \omega_p \omega_z}{r_2 (EI)_s} \left[\frac{2}{3} r_2 M_p + \frac{4}{3} r_2^2 \Delta\theta \rho_h A_h + \left\{ \frac{1}{4} r_1 (r_2 - r_1) + \frac{11}{60} (r_2 - r_1)^2 \right\} \rho_s A_s \right], \quad (4)$$

where,

$\Delta\theta$ = angle between spokes (radians)

M_p = mass per probe (lb sec²/in.)

r_2 = probe centroid radius (in.)

r_1 = hub junction radius (in.).

The spoke tip angle at the i'th spoke is found from:

$$\xi_i = \frac{(r_2 - r_1)^2 \omega_z \omega_p \sin \theta_i}{(EI)_s} \left[r_2 M_p + 2r_2^2 \Delta\theta \rho_h A_h + \left\{ \frac{2}{3} r_1 (r_2 - r_1) + \frac{1}{4} (r_2 - r_1)^2 \right\} \rho_s A_s \right]. \quad (5)$$

For the case of a wheel with no hoop, set the hoop density area product $\rho_h A_h$ equal to zero in equations (3) and (4).

Wheel mass moment of inertia about Z axis, I_z , for rigid or compliant hoops is given by:

$$I_z = \left[2\pi r_2 \rho_h A_h + \eta M_p \right] r_2^2 + \frac{\eta}{3} \rho_s A_s r_3^3 \quad (6)$$

where, r_3 is the wheel radius to the probe base.

Example 1

Consider the tapered aluminum system of figure 92. To use the linear equations for a tapered system, the median value of I_s was conservatively chosen as:

$$I_s = 0.02 \text{ in.}^4 = \text{value at } 1/2 \text{ spoke radius.}$$

The remaining numerical constants for this example are:

$$\rho_s A_s r_3 = \frac{\text{wheel mass}}{24} = \frac{6.94}{(24)(386)} = 750 \times 10^{-6} \left(\frac{\text{lb sec}^2}{\text{in.}} \right)$$

$$M_p = \frac{3.12}{(24)(386)} = 337 \times 10^{-6} \left(\frac{\text{lb sec}^2}{\text{in.}} \right)$$

$$\omega_z = 240 \text{ rpm} = 25.1 \left(\frac{\text{rad}}{\text{sec}} \right)$$

$$r_1 = 0$$

$$r_2 = 13.5 \text{ (in.)}$$

$$r_3 = 12.15 \text{ (in.)}$$

$$E_s = 10.5 \times 10^6 \text{ (psi)}$$

$$\Delta\theta = 15^\circ = 0.262 \text{ (radians).}$$

From equation (4) we obtain:

$$\phi_{\text{total}} = \frac{r_2^3 \omega_p \omega_z}{E_s I_s} \left[\frac{2}{3} M_p + \frac{11}{60} \rho_s A_s r_2 \right] = 1.06 (10^{-4}) \omega_p \text{ (radians).}$$

For $\phi = 10\%$ of a resolution element, i.e., 7.6μ radians, the maximum disturbing angular frequency is:

$$(\omega_p)_{\text{max}} = 0.072 \left(\frac{\text{rad}}{\text{sec}} \right) = 0.68 \text{ rpm.}$$

The wheel moment of inertia is found from equation (6) as:

$$I_z = \eta r_2^2 \left[M_p + 0.243 \rho_s A_s r_2 \right] = 2.25 \text{ (in. -lb-sec}^2\text{)}.$$

From equations (2) and (4) we find the ϕ -mode bending stiffness to be:

$$K_b = \frac{\omega_p I_z \omega_z}{\phi_b} = 0.514 \times 10^6 \text{ (lb in./rad).}$$

Now the angular momentum is:

$$H = 56.5 \text{ (in. -lb-sec),}$$

so that the precessional rotation rate, as determined from equation (1), is:

$$\omega'_p = \frac{K_B}{H} = 9100 \left(\frac{\text{rad}}{\text{sec}} \right) = 1450 \text{ Hz.}$$

24-Probe Tapered Aluminum Scan Wheel Design Outline

Example 2

Let us consider the probe system as shown in figures 141 and 142. The probe tubes, themselves, are internally cylindrical and externally tapered. Given:

Probe weight = 0.13 pounds each

Total wheel weight = 10 pounds.

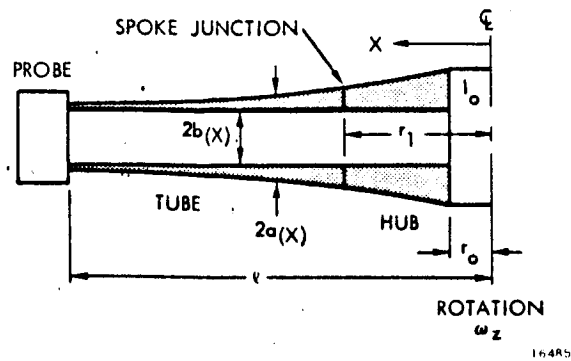


Figure 141. One Spoke Plus Hub Segment.

Let area moment of inertia be:

$$I_s \equiv K_1 (\ell - x)^2 = \frac{A(x)}{4} (a_{(x)}^2 + K_2) \text{ (in.}^4\text{)} \quad (7)$$

where,

$$K_1 = \frac{I_o}{\ell^2}$$

$$K_2 = b^2$$

$$K_3 = b^4$$

$$K_4 = \frac{\pi K_3}{4K_1}$$

$$A(x) = \text{cross sectional area (in.}^2\text{)}$$

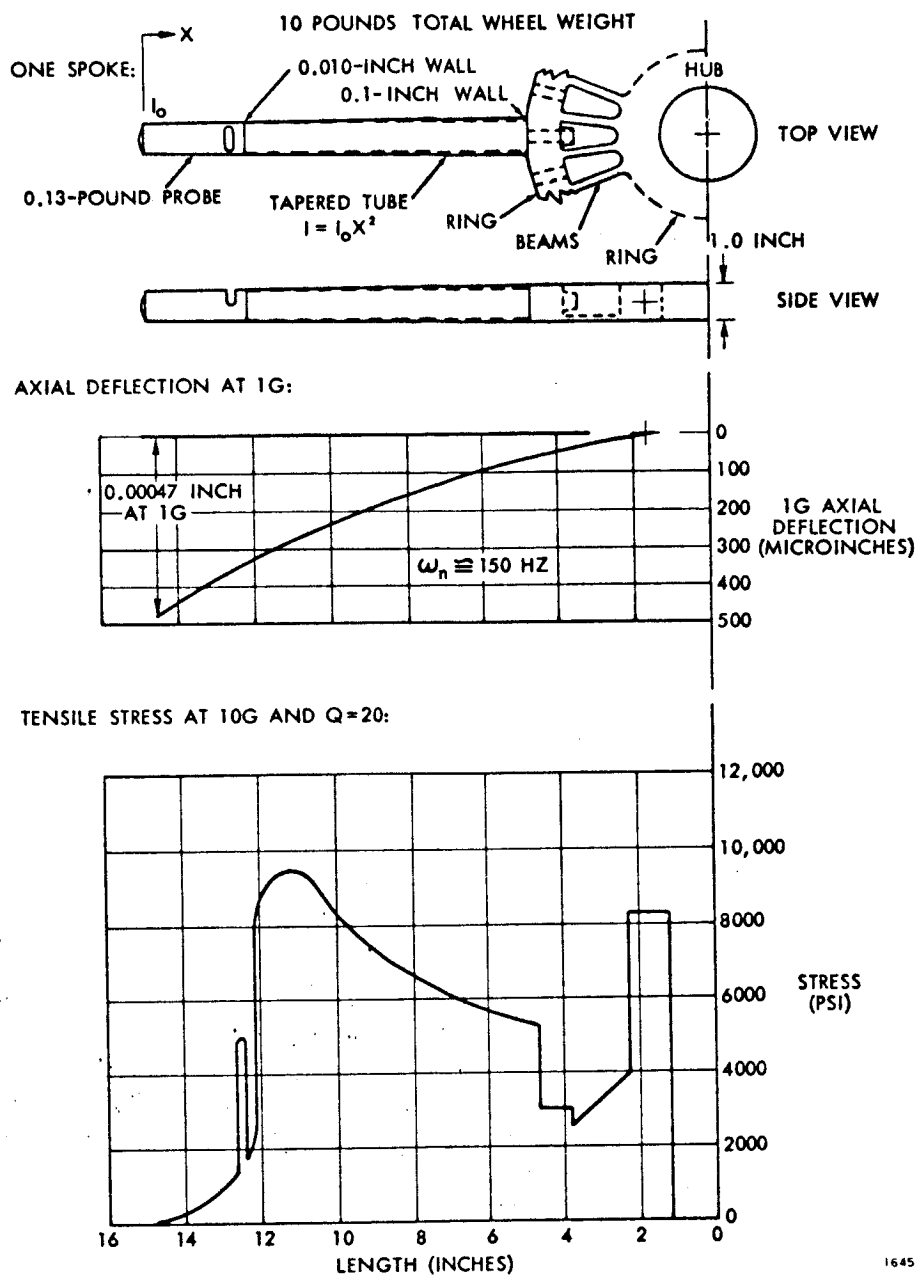


Figure 142. Stress and Deflection for Tapered Aluminum 24-Probe Scan Wheel, 1-Inch Wide.

$$\begin{aligned}
 \text{Weight (tube + hub)} = & \left[\rho - \pi K_2 \ell - \pi \left(\frac{4K_1}{\pi} \right)^{\frac{1}{2}} \frac{K_4^2}{2} \ell \ln K_4 + \pi \left(\frac{4K_1}{\pi} \right)^{\frac{1}{2}} \left\{ \frac{\ell}{2} \left(\ell^2 + K_4^2 \right)^{\frac{1}{2}} \right. \right. \\
 & \left. \left. + \frac{K_4^2}{2} \ell \ln \left(\ell + \left(\ell^2 + K_4^2 \right)^{\frac{1}{2}} \right) \right\} \right] \quad (8)
 \end{aligned}$$

Solving equations (7) and (8) yields:

$$b = 0.4 \text{ yields } 6.94 \text{ pounds metal total.}$$

So that

$$\text{Total weight} = 6.94 + 3.12 = 10.06 \text{ pounds.}$$

$$K_1 = 270 \times 10^{-6} \text{ in.}^2.$$

The tube outer radius is given by:

$$a_{(x)} = \sqrt{\frac{4K_1(\ell - x)^2}{A(x)} - K_2} \quad (9)$$

where

$$A(x) = \pi \left[\left(\frac{4K_1}{\pi} \right)^{\frac{1}{2}} \left\{ (\ell - x)^2 + K_4^2 \right\}^{\frac{1}{2}} - K_2 \right].$$

From equation (9) we have:

$$\text{At } x = 4.02, a = 0.50 \text{ (hub junction)}$$

$$x = \ell, a = 0.010 \text{ (spoke tip).}$$

Axial Resonance

The total deflection curve for spokes was found graphically. The deflection curve for the hub was found by summing solutions for rings and tapered beams simultaneously. A check was performed by summarizing the hub forces in figure 143 to give:

$$\Sigma M_o = (V_{34} + W_3)(r_2 - r_1) + M_{34} - M_{r_3} \frac{\pi r_2^2}{12} + \bar{W}_{22} X_{22} - M_{r_1} \frac{\pi r_1^2}{12} = 2.323 - 2.335 \cong 0.$$

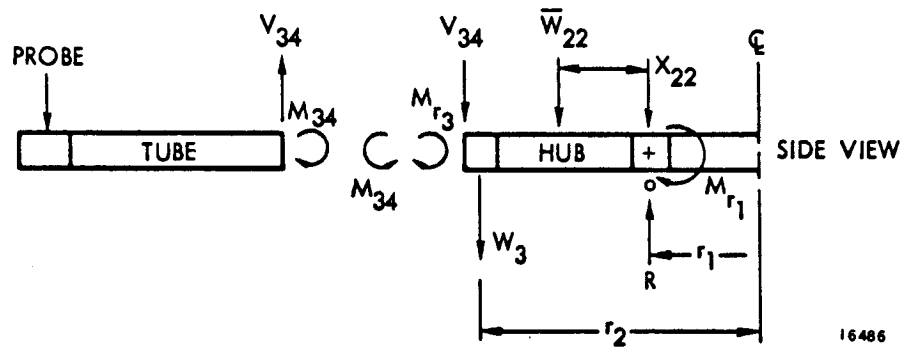


Figure 143. Hub Forces.

- $V_{34} = 0.234$ lbs - spoke shear at hub junction
 $M_{34} = 1.467$ lb in. - spoke moment at hub junction
 $M_{r3} = 0.491$ lb in./in. - ring restoring moment
 $r_2 = 4.16$ in. - outer ring average radius
 $r_1 = 1.75$ in. - inner ring average radius
 $W_3 = 0.0766$ lbs - outer ring weight per spoke
 $\bar{W}_{22} = 0.0978$ lbs - hub beam weight
 $X_{22} = 1.2$ in. - hub beam centroidal distance
 $M_{r1} = 3.92$ lb in./in. - ring restoring moment.

The natural frequency was found by integration to be:

$$f_{\eta} = \frac{1}{2\pi} \sqrt{\frac{g \int_0^l \rho A \delta dx}{\int_0^l \rho A \delta^2 dx}} = 150 \text{ Hz.}$$

where,

- f_{η} = natural frequency
 g = acceleration of gravity
 A = cross section area
 δ = deflection
 ρ = mass density of the material.

Appendix VI

GEOMETRICAL STUDY

General Spherical Imaging

A brief review of the geometry of general spherical imaging will introduce the geometry of the special case family of circular scan loci used in the tilted wheel concept. Referring to figure 144, the $X' Y'$ ground plane is being scanned by a spherical system moving at vehicle velocity, V , in the $-X$ direction at altitude H . The primary mirror sphere of radius $2R$ forms a real image at the image sphere of radius R . Both spheres are centered at O . The image sphere consists of the focused light; there is no actual material surface. For the purpose of explanation, consider the primary reflector to be a complete sphere, neglecting self-blockage problems, so that the complete image of the ground plane can exist at one time on the image sphere. Since the ground is assumed to be a flat plane, the horizon is mapped onto the equator of the image sphere, and the entire ground plane is mapped onto the upper half of the image sphere. To transfer a general ground point G' to the image sphere, draw a straight line from G' through the image sphere center O . Where the line pierces the upper half of the image sphere, point G' will be imaged as G .

Consider the arbitrary parallel ground lines K' and J' to be aligned with the X -axis flight direction and separated by a constant ground distance W'_g . Since these lines appear to meet at the ground plane horizon at points $X' = \pm \infty$, they also appear to meet on the image sphere equator at $X = \pm \infty$. Note that all points in the spherical image of any straight ground line lie in a plane containing the particular ground line and the origin O of the spherical system. Thus, all straight lines on the ground image as great semicircles of radius R , centered on O , and variously oriented, depending on the position of the ground line being imaged.

The uniform motion, V , of the vehicle is mapped as a nonuniform image motion in spherical area scanning, due to the variation in object range. This property is inherent in all wide angle imaging systems. Any general stationary ground point, G' , will have a relative ground velocity $V' = -V$ due to vehicle motion. The straight line motion of G' is parallel to the X' -axis for the assumed X -direction vehicle velocity. All points, G' , form at $X' = -\infty$ and vanish at $X' = +\infty$ on the ground. Hence, all vehicle induced image motion paths originate at $X = -\infty$ and end at $X = +\infty$ on the image sphere equator. The magnitude of the image velocity in the image coordinate system, $|\dot{G}_v|$, due to vehicle forward motion is given by:

$$|\dot{G}_v| = R\dot{\zeta} = \frac{RV}{H} \cos \alpha \cos^2 \zeta \quad (1)$$

where α and ζ are the angular coordinates of G' in the roll and pitch directions, respectively. The image velocity is usually much less than the scan velocity.

The geometry of spherical imaging dictates two properties of any valid spherical scanning mechanism. The scan direction must lie on a great circle in the upper image hemisphere. The scanning optics must maintain their focus in the image hemispherical shell of thickness 2δ , where $\pm\delta$ is the primary depth of focus. A third property, based on a desire for uniform subresolution element dwell time, would have the resolution element field-stop boundaries always normal to the sum of the ground image and scan velocities. This condition cannot easily be met due to problems in creating cyclic field-stop motion. The resulting banding

for a simple field-stop is diminished by the fact that the ground image component, equation (1), is small compared to the scan velocity.

Since any radius, R , is a valid viewing axis, a radius vector can be made to pivot about O , and the tip of R will trace out a valid scan locus in the image shell. A set of 24 of these radii, rotating in the $Y Z$ plane with angular velocity, ω_L , in the X direction, was the scanning device in the great circle scanner. The useful scan locus consisted of the image line ab , which on the ground represented the straight line $a'b'$ of length W'_S equal to 100 nautical miles.

If the radius, R , is constrained to pivot about O in a conic section with axis, ω_S , tilted from vertical at some angle ϕ , the resulting scan locus is a circle of radius, R , on the image surface, and either a circle or an ellipse on the ground plane. The useful scan locus is now $c'e'd'$. There are an infinite number of valid circular scan loci. The original scanner is a special case of this infinite family, i. e., $\phi = \pi/2$; $r = R$. One valuable property of tilted circular scanning is that the rotating scan disk need not be centered at \bar{O} . The tilted disk center, \bar{O} , can be brought close to the image shell, with the resulting large decrease in structural thermal path length.

Tilted Wheel Geometry

The tilted wheel family of present interest is that which is generated by tilt angles $\pi/2 > \phi \geq 0$, figures 144 and 145. The scan rotation axis, ω_S , for this family lies in the $X Z$ plane. The scanning probes, P_i , are arranged on a rotating scan wheel so that their foci lie on the image sphere surface and scan an image disk of radius r . The probe optical axes form a cone of half-angle β given by:

$$\beta = \sin^{-1}\left(\frac{r}{R}\right)$$

The total number of probes, N , must fit evenly into the scan circle with equal angular subdivisions λ so that:

$$N = \sum P_i$$

$$N\lambda = 2\pi \quad (2)$$

The image scan path consists of a calibration arc-length, L_C , and an active scan arc-length, L_S . Hence we find:

$$\lambda = \frac{L_S + L_C}{r} = \theta_S + \theta_C \quad (3)$$

where, θ_S and θ_C are the active scan plus calibration angles.

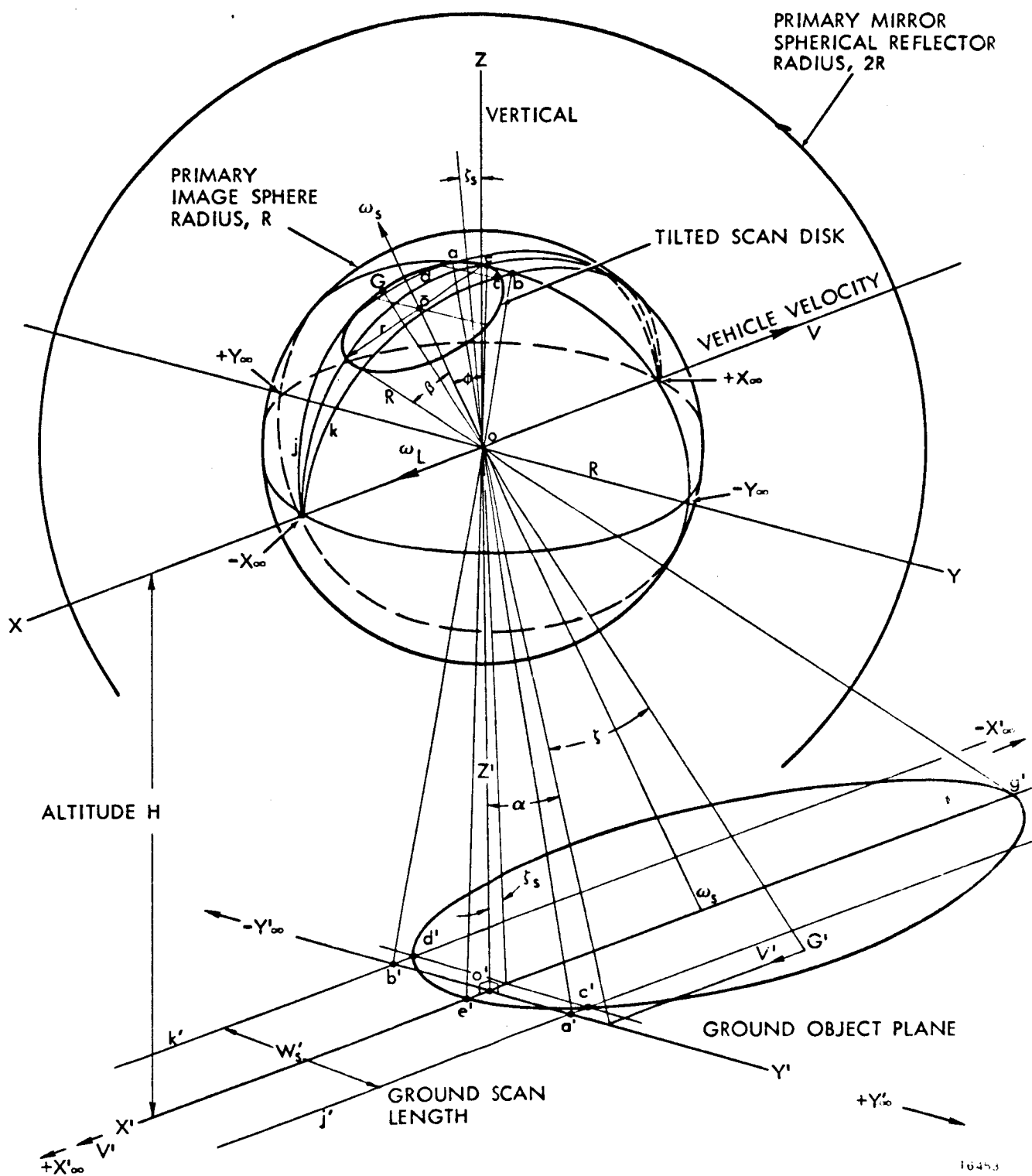
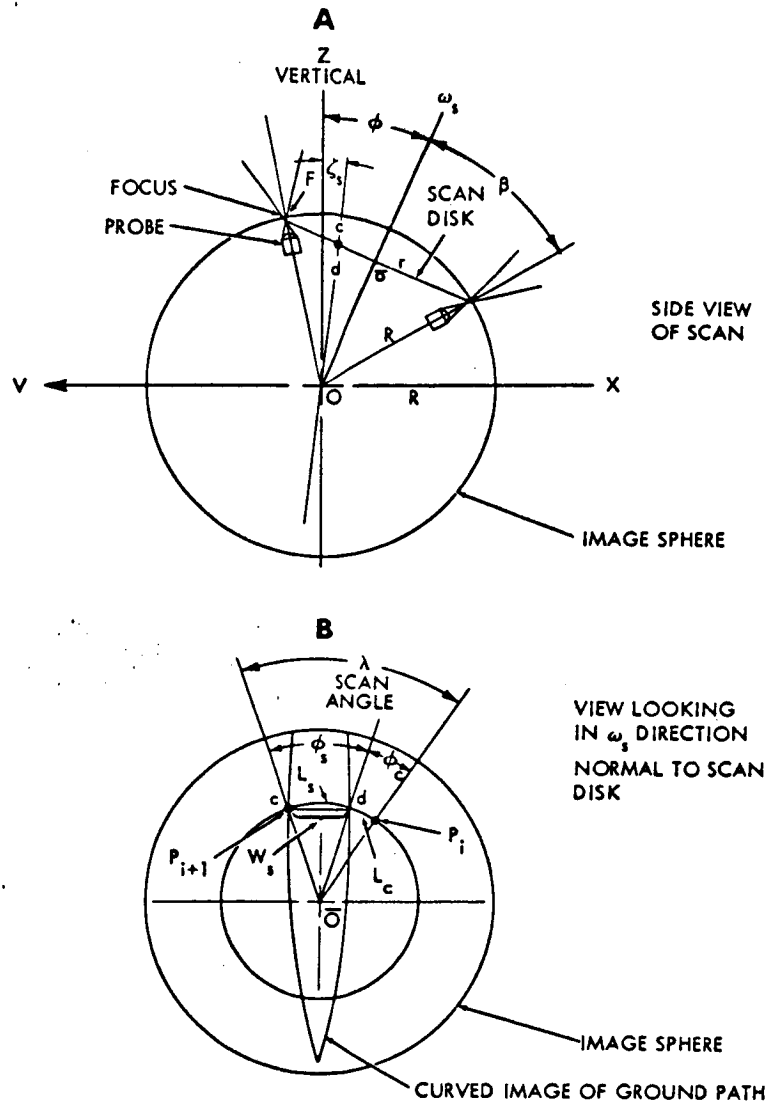


Figure 144. Spherical Imaging.



16461

Figure 145. Scan Wheel Geometry.

For continuous ground coverage, the λ scan angle must be completed in cycle time T_s , which is the time it takes for the vehicle to travel K ground resolution element widths, i.e.,

$$T_s = \frac{KW_r}{V}$$

where,

- K = number of lines scanned per probe pass
- W_r = width of ground resolution element
- V = vehicle velocity.

The cycle time and the number of probes determine the scan wheel angular velocity, ω_s , as:

$$\omega_s = \frac{\lambda}{T_s} = \frac{2\pi}{NT_s} = \frac{2\pi V}{NKW_r}.$$

The active scan arc, L_s , must include, as a chord, the image scan length chord $W_s = \overline{cd}$. The chord length W_s varies with tilt angle ϕ , since the image of the constant width ground path $j'k'$ is curved. For clarity, the image length, W_s , can be expressed in terms of a forward viewing angle, ξ_s (figure 144), as:

$$W_s = \frac{RW_s'}{\sqrt{\frac{H^2}{\cos^2 \xi_s} + \frac{(W_s')^2}{4}}}$$

From figure 144, view B, we have:

$$r \sin \frac{\phi_s}{2} = \frac{W_s}{2} = \frac{RW_s'}{2\sqrt{\frac{H^2}{\cos^2 \xi_s} + \frac{(W_s')^2}{4}}} \quad (4)$$

Combining equations (2), (3), and (4) yields:

$$\lambda = \frac{2\pi}{N} \left[\frac{L_c}{r} + 2 \sin^{-1} \left\{ 2r \sqrt{\frac{H^2}{\cos^2 \xi_s} + \frac{(W_s')^2}{4}} \right\} \right]$$

$$\lambda \leq \pi,$$

where,

- N = total number of probes (Integers > 1)
- L_c = required calibration scan arc length
- r = scan disk radius
- R = image sphere radius
- W_s' = constant length of scanned ground path
- H = vehicle altitude
- ξ_s = maximum forward viewing angle component in $X'Z'$ plane.

Equation (5) describes a family of scan systems for each angle ξ_s . For a particular family, as the number of probes increases, the wheel speed and scan curvature decrease. Decreased scan curvature tends to raise the resolution dwell time.

Scan efficiency η_s is determined directly by the ratio of calibration arc-length, L_c , to total scan length, that is:

$$\eta_s = 100 \left(1 - \frac{L_c}{\lambda_r} \right) \text{ percent.}$$

Dwell time T_D is determined by cycle time, scan arc-length and resolution element width by:

$$T_D = \frac{T_s W_r}{\lambda_r}.$$

The scan rotation axis is tilted away from vertical by angle ϕ in the X Z plane (refer to figure 146) given by:

$$\phi = \xi_s + \tan^{-1} \left(\frac{r \cos \frac{\lambda}{2}}{R \cos \beta} \right).$$

Ground Scan Geometry

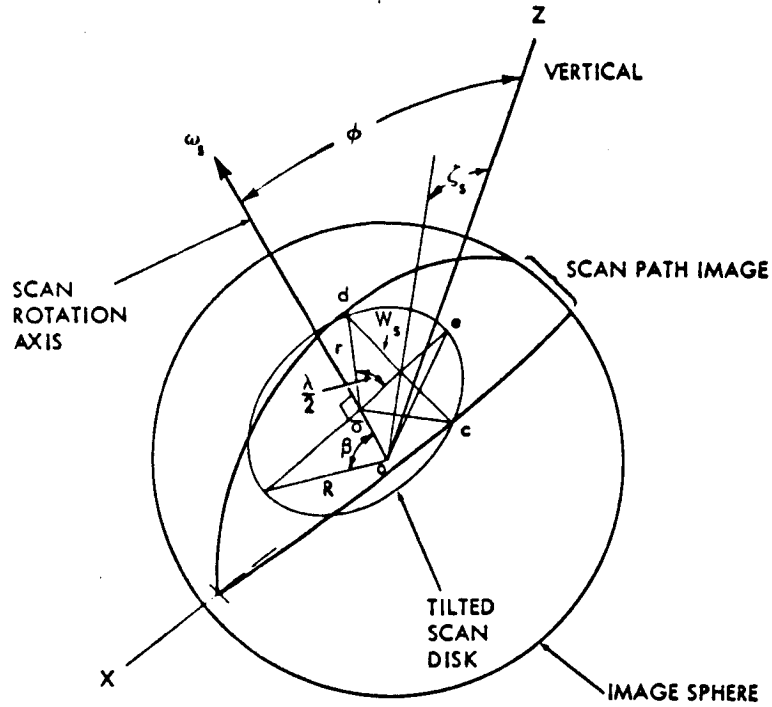
For the cases where tilt angle $\phi = 0$ and $\phi = \pi/2$, the ground scan locus is a circle and a straight line, respectively. For all the intermediate cases, $\pi/2 > \phi > 0$, the loci consist of various ellipses. Considering the elliptical loci, figure 147, it is apparent that the elliptical centers, O_i and O_e , do not lie on the ω_s spin axis. Furthermore, if a resolution element stop of width W_r is effectively placed at the probe location on the scan wheel (resulting in an ω_s synchronous rotating scan element), the resulting differential scan angle, $\Delta\beta$, will not scan a constant sized ground element. This latter effect can be shown to be small, and completely tolerable for most useful ground scan geometries.

It is convenient to refer to the scan boundaries generated by $\Delta\beta$ as the internal and external ellipses. Since tilt angle, ϕ , is the same for each of these ellipses, the major and minor axis equations can be derived in terms of β and evaluated for internal and external values, β_i and β_e .

Considering triangle O - e' - g' of figure 147, we find the major semiaxis A to be:

$$A = \frac{H}{2} \sqrt{\frac{1}{\cos^2(\beta + \phi)} + \frac{1}{\cos^2(\beta - \phi)} - \frac{2 \cos 2\beta}{\cos(\beta + \phi) \cos(\beta - \phi)}}.$$

We can then insert β_i to get A_i or β_e to get A_e .



16463

Figure 146. Scan Rotation Axis.

From figure 148, view A, the minor semiaxis B can be obtained for the circle centered on P:

$$\begin{aligned}
 B &= \sqrt{\overline{PS}^2 - \overline{PO}_e^2} \\
 &= \sqrt{(\overline{O}_e - \overline{PO}_e)^2 - \overline{PO}_e^2} \\
 B &= \sqrt{\overline{O}_e(\overline{O}_e - 2\overline{PO}_e)}
 \end{aligned}$$

From figure 147, we have:

$$\overline{PO}_e = A_e \cos \varphi - e'Q = A_e \cos \varphi - \frac{H \sin \beta}{\cos(\beta_e - \varphi)} \quad (6)$$

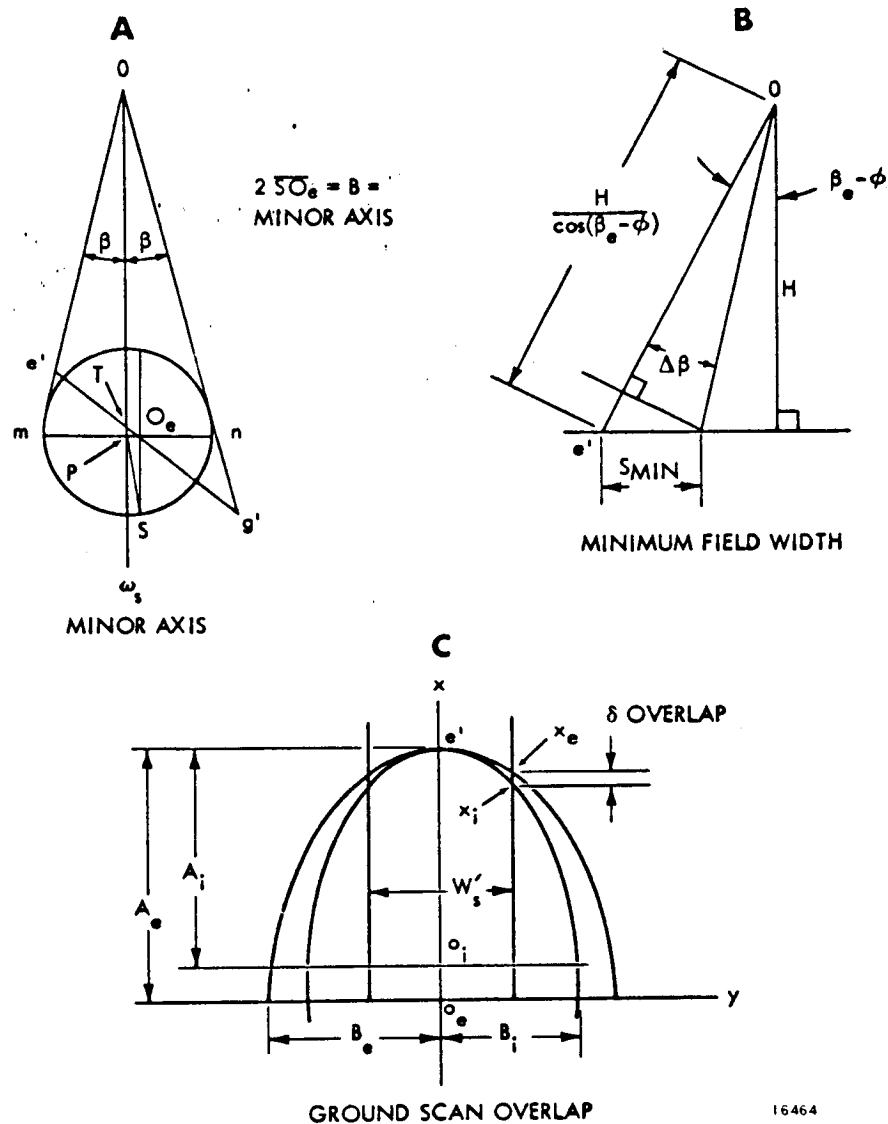


Figure 148. Geometrical Constructions.

Then we can write the minor semiaxis as:

$$B = \sqrt{\left(\frac{A \sin\left(\frac{\pi}{2} + \beta - \phi\right)}{\sin\left(\frac{\pi}{2} - \beta\right)} \right) \left(\frac{A \sin\left(\frac{\pi}{2} + \beta - \phi\right)}{\sin\left(\frac{\pi}{2} - \beta\right)} - 2A \cos \phi - \frac{H \sin \beta}{\cos(\beta - \phi)} \right)}$$

The displacement of the scan centerline, ω_s , from the elliptical center, O_e , is necessary in the determination of overlap. From equation (6) we obtain:

$$\overline{TO_e} = \frac{\overline{PO_e}}{\cos \varphi} = A_e - \frac{H \sin \beta}{\cos \varphi \cos(\beta - \varphi)}$$

Since the elliptical centers, O_e and O_i , are not coincident, the ground scan resolution element width, S , varies during a scan. The maximum width, S_{MAX} , occurs at g' , figure 147, and the minimum, S_{MIN} , occurs at e' . Exact values for S_{MIN} can be (figure 148, view B) found from:

$$S_{MIN} = H \left[\tan(\beta_e - \varphi) - \tan(\beta_e - \varphi - \Delta\beta) \right].$$

Exact values for S_{MAX} can be obtained from

$$S_{MAX} = 2A_e - S_{MIN} - 2A_i.$$

For the case where $\Delta\beta \ll \beta$, the following approximations are valid:

$$S_{MIN} \approx \frac{H \Delta\beta}{\cos^2(\beta_e - \varphi)}$$

$$S_{MAX} \approx \frac{H \Delta\beta}{\cos^2(\beta_e + \varphi)}$$

The approximate scan element width at the minor axis, S_B , is useful for overlap calculations and can be found from:

$$S_B \approx \frac{\Delta\beta \sqrt{B_e^2 + H^2 + \left(A_e - \frac{H}{\tan(\beta_e - \varphi)}\right)^2} \cos \left\{ \tan^{-1} \left[\frac{A_e}{B_e} - \frac{H \sin \beta_e}{B_e \cos \varphi \cos(\beta - \varphi)} \right] \right\}}{\cos \left[\frac{\pi}{2} - \sin^{-1} \left\{ \frac{H \sin \beta}{\cos \varphi \sqrt{\left(A_e - \frac{H \sin \beta}{\cos \varphi \cos(\beta - \varphi)}\right)^2 + B_e^2}} \right\} \right]} \quad (7)$$

The pattern of ground scans is not perfectly contiguous for the circular or elliptical loci due to the mismatch between internal and external boundaries of adjacent scan lines. As shown above for the elliptical loci, the internal and external ellipses are dissimilar. Since

the adjacent scan lines can be moved fore and aft with respect to each other, the error in contiguity can be made to be either underlap, overlap, or some combination of the two. The total mismatch will remain a constant, δ . We will compute the error as underlap for convenience. Refer to figure 148, view C. The internal and external ellipses are constructed tangent at e' . Thus, the line segment $X_i X_e$ is a measure of the maximum underlap or overlap. The equation of the external ellipse is:

$$\frac{y^2}{B_e^2} + \frac{x^2}{A_e^2} = 1.$$

The internal ellipse is given by:

$$\frac{y^2}{B_i^2} + \left(\frac{x - (A_e - A_i)}{A_i} \right)^2 = 1.$$

At $y = W_s'/2$ we have

$$x_e = A_e \sqrt{1 - \frac{W_s'^2}{4B_e^2}} \quad (8)$$

$$x_i = A_i \sqrt{1 - \frac{W_s'^2}{4B_i^2}} + A_e - A_i. \quad (9)$$

So that the maximum overlap is given by:

$$\delta_{\text{MAX overlap}} = A_e \sqrt{1 - \frac{W_s'^2}{4B_e^2}} - A_i \sqrt{1 - \frac{W_s'^2}{4B_i^2}} - (A_e - A_i).$$

For approximate values we can use:

$$A_i = A_e - \frac{W_s \text{ MIN} + W_s \text{ MAX}}{2}$$

$$B_i \cong B_e - S_B \text{ (Refer to equation (7)).}$$